UNIVERSITY OF KWAZULU-NATAL

SCHOOL OF MECHANICAL ENGINEERING

HOWARD COLLEGE

In fulfilment of the degree of

Master of Science in Mechanical Engineering

At the University of KwaZulu-Natal

FUSED DEPOSITION MODELLING (FDM) TO FABRICATE A TRANSITIONAL VERTICAL TAKE-OFF AND LANDING (VTOL) UNMANNED AERIAL VEHICLE (UAV) FOR TRANSPORTATION OF MEDICAL SUPPLIES IN UNDERDEVELOPED AREAS.

Matt Harcus

NOVEMBER 2020

As the candidate's supervisor, I agree to the submission of this dissertation.

Dissertation supervisor: Professor Glen Bright

DECLARATION 1 – PLAGIARISM

I, ……………………Matt Brandon Harcus………………………., declare that

1. The research reported in this thesis, except where otherwise indicated, is my original research.

2. This thesis has not been submitted for any degree or examination at any other university.

3. This thesis does not contain other persons data, pictures, graphs, or other information, unless specifically acknowledged as being sourced from other persons.

4. This thesis does not contain other persons writing, unless specifically acknowledged as being sourced from other researchers. Where other written sources have been quoted, then:

a. Their words have been re-written, but the general information attributed to them has been referenced

b. Where their exact words have been used, then their writing has been placed in italics and inside quotation marks and referenced.

5. This thesis does not contain text, graphics or tables copied and pasted from the Internet, unless specifically acknowledged, and the source being detailed in the thesis and in the References sections.

Signed: …………………………………………………Date: 27 November 2020
………………………

DECLARATION 2 – PUBLICATIONS

DETAILS OF CONTRIBUTION TO PUBLICATIONS that form part and/or include research presented in this thesis (include publications in preparation, submitted, *in press* and published and give details of the contributions of each author to the experimental work and writing of each publication)

Publication 1 (Published): PRASA-RobMech 2020

Harcus, M. & Bright, G., "Fused Deposition Modelling for fabrication of a hybrid Vertical Take-Off and Landing Unmanned Aerial Vehicle", *2020 International SAUPEC/RobMech/PRASA Conference.*

Published March 2020, 6 Pages

The paper was published and presented in March 2020, in Cape Town, South Africa

Matt Harcus was the lead author of this paper and conducted all research and experimental investigations under the supervision of Professor Glen Bright.

Publication 2 (Accepted): ICINCO 2020

Harcus, M. & Bright, G., "Aerodynamic and propulsion performance optimization for an Unmanned Aerial Vehicle (UAV)", *17th International Conference on Information in Control, Automation and Robotics.*

Accepted April 2020, 8 Pages

The paper was accepted in March 2020, in Paris, France

Matt Harcus was the lead author of this paper and conducted all research and experimental investigations under the supervision of Professor Glen Bright.

Publication 3 (Accepted): IECON 2020

Harcus, M. & Bright, G., "Aerodynamic and propulsion performance optimization for an Unmanned Aerial Vehicle (UAV)", *46th Annual Conference of the IEEE Industrial Electronics Society.*

Accepted July 2020, 8 Pages

The paper was accepted in July 2020, in Singapore

Matt Harcus was the lead author of this paper and conducted all research and experimental investigations under the supervision of Professor Glen Bright.

27 November 2020

Signed: ……………………………….Date: …………………….……………. Mr Matt Harcus

27 November 2020

Signed: …………………………………Date: …………………….…………. Professor Glen Bright

ACKNOWLEDGEMENTS

"Drones overall will be more impactful than I think people recognise, in a positive way to help society."

~ Bill Gates ~

ABSTRACT

This dissertation's work has focused on the design and development of a prototype UAV that aims to facilitate the delivery of emergency medical aid supplies to remote locations within South Africa (SA). This research has conducted a conceptualized design of a tilt-rotor VTOL UAV named *Airslipper*, which was entirely fabricated using FDM methods. Identification of key performance parameters within the vehicle's mechatronic design enabled this research to conduct a simultaneous optimization on the propeller-based propulsion system and aerodynamic configuration. Execution of MATLAB's 'gamultiobj' function on two parametrically formulated objective functions resulted in a UAV setup that increased flight endurance by $58\ s$. This improvement amplified the effectiveness of this system and expanded the service radius distance by $1.51\ km$.

The outcome of a stability and sensitivity analysis performed on the *Airslipper's* aerodynamic surfaces provided critical information that contributed towards the vehicle's flight characteristics. Findings indicated a stabilized design that exhibited appropriate frequency plots for both longitudinal and lateral stability modes. The addition of a plane analysis, which included viscous and inertial effects, offered essential drag and pressure coefficients, which aided in the final design. This research correspondingly conducted several CFD simulations on an *Airslipper* model, which allowed this work to examine further the fluid behaviour characteristics endured on the vehicle in both VTOL and Fixed Wing (FW) modes. Simulation findings revealed standard pressure distributions, which confirmed thrust and lift forces for the relevant components without performance compromise.

This research proposed to experimentally investigate a correction factor for an FDM fabricated aerofoil that aimed to determine what structural effects were apparent for a printed part with varying FDM parameters. Outcomes demonstrated greater resilience to failure for parts that had reduced layer heights and increased infill percentages. Fabrication of the *Airslipper* comprised of 99 individually printed parts that encompassed a specific parameter combination which pertained to the design's importance. Validating the prototype's functionality was achieved through a series of hover tests that generated suitable data logs plots for the control response, actuator output signals, vibration metrics, and power. This research concluded by discussing the *Airslipper's* design and fabrication method with further mentioning of recommendations for potential improvements.

TABLE OF CONTENTS

LIST OF FIGURES

LIST OF TABLES

NOMENCLATURE – UNITS

A	Ampere
°	Degree
g	Gram
g/W	Gram per watt
h	Hour
Hz	Hertz
kHz	Kilohertz
J	Joule
kJ	Kilojoule
kg	Kilogram
kg/m^3	Kilogram per metre cubed
kg/m^2	Kilogram per metre squared
kg/m	Kilogram per metre
km	Kilometre
km/h	Kilometre per hour
$[mxn]$	Matrix
mm	Millimetre
m	Metre
m^2	Metre squared
m^3	Metre cubed
m/s	Metre per second
m/s^2	Metre per second squared
mr/s^2	Metre radian per second squared
μs	Microsecond
mAh	Milliamp-hour
N	Newton
Nm	Newton metre
Ω	Ohm
rpm	Revolution per minute
rps	Revolution per second
s	Second
$[m]$	Vector matrix
V	Volt
W	Watt
Wh	Watt-hour
W/kg	Watt per kilogram

NOMENCLATURE – SYMBOLS

~ Chapter 2: Propeller theory ~

A_{disk}	m/s^2	Disk area
$p_2 - p_1$	-	Pressure difference
v_i	m/s^2	Induced velocity
v	m/s^2	Axial velocity
v_∞	m/s^2	Atmospheric velocity
P_i	W	Induced power
P_o	W	Profile power
C_{Pi}	-	Induced power coefficient
C_{Po}	-	Profile power coefficient
C_T	-	Thrust coefficient
C_Q	-	Torque coefficient
C_P	-	Power coefficient
M	-	Figure of merit
λ	-	Inflow factor
σ	-	Solidity factor
r	m	Radius
c	m	Chord length
N	-	Number of blades
n	rpm	Rotation rate
d	m	Diameter
C_L	-	Lift coefficient
C_D	-	Drag coefficient
k	-	Empirical factor
η_{prop}	-	Propeller efficiency
J	-	Advance ratio
T	N	Thrust
Q	Nm	Torque
P	W	Power

~ Chapter 2: UAV modelling ~

G	-	Centre of mass
m	m	Mass
R	$[mxn]$	Rotation matrix
R^T	$[mxn]^T$	Transformed rotation matrix
V_B	m/s^2	Body velocity
T_B	N	Body thrust
v	m/s^2	Linear velocity
ω	mr/s^2	Angular velocity

$\mathcal{L}$	-	Laplace transformation
E_{ktrans}	J	Translational kinetic energy
E_{krot}	J	Rotational kinetic energy
E_p	J	Potential energy
q	-	Generalized coordinates
f_ξ	N	Generalized non-conservative forces
τ_η	Nm	Generalized non-conservative moments

~ Chapter 2: UAV control ~

$u(t)$	μs	Control signal
$e(t)$	-	Error
k_P	-	Proportional gain
k_I	-	Integral gain
k_D	-	Derivative gain
Γ	-	Performance index
$P(t)$	$[mxn]$	Riccati matrix
R	$[mxn]$	Real positive weighting matrix
Q	$[mxn]$	Real positive weighting matrix
$x(t)$	$[m]$	State vector
$u(t)$	$[m]$	Control input vector
A	$[mxn]$	System matrix
B	$[mxn]$	Control matrix

~ Chapter 3: *Airslipper* design and optimization ~

g	m/s^2	Gravitational constant
ρ_{air}	kg/m^3	Air density
$W_{estimated}$	N	Vehicle estimated weight
$D_{estimated}$	N	Vehicle estimated drag
T_{VTOL}	N	Vehicle thrust in VTOL mode
T_{FW}	N	Vehicle thrust in FW mode
$T_{flight,VTOL}$	s	Vehicle flight time in VTOL mode
$T_{flight,FW}$	s	Vehicle flight time in FW mode
$T_{flight,Transition}$	s	Vehicle transition time
$T_{flight,TOTAL}$	s	Vehicle total flight time
$T_{flight,OPTIMAL}$	s	Vehicle optimal total flight time
Alt_{max}	m	Vehicle maximum altitude
R_{flight}	km	Vehicle flight range
γ_{VTOL}	-	Vehicle thrust-to-weight ratio in VTOL mode
γ_{FW}	-	Vehicle thrust-to-weight ratio in FW mode
W	N	Vehicle weight

L	N	Vehicle lift
D	N	Vehicle drag
V_{climb}	m/s	Vehicle climb velocity in VTOL mode
V_{cruise}	m/s	Vehicle cruise velocity in FW mode
$V_{optimal}$	m/s	Vehicle optimal velocity
$C_{L,vehcile}$	-	Vehicle lift coefficient
$C_{D,vehcile}$	-	Vehicle drag coefficient
$J_{aerodynamic}$	-	Aerodynamic objective function
$J_{propulsion}$	-	Propulsion objective function
R_n	-	Number of propellers
ψ	W/kg	Propeller power-to-thrust ratio
d	m	Propeller diameter
n_{VTOL}	rpm	Propeller rotation rate in VTOL mode
n_{FW}	rpm	Propeller rotation rate in FW mode
$n_{required}$	rpm	Propeller required rotation rate
$n_{optimal}$	rpm	Propeller optimal rotation rate
c	m	Propeller blade chord
J_{VTOL}	-	Propeller advance ratio in VTOL mode
J_{FW}	-	Propeller advance ratio in FW mode
$Q_{propeller}$	Nm	Propeller torque
$P_{propeller}$	W	Propeller power
$C_{D0,propeller}$	-	Propeller profile drag coefficient
P_{motor}	W	Motor power
I_{servo}	A	Servo motor current
I_{motor}	A	Motor current
V_{motor}	V	Motor voltage
Q_{motor}	Nm	Motor torque
I_0	A	Motor no-load current
R	Ω	Motor resistance
KV	-	Motor rotation constant
ϖ	-	Motor rotation constant correction factor
l	m	Aerofoil span
S	m^2	Aerofoil area
AR	-	Aerofoil aspect ratio
λ	-	Aerofoil taper ratio
Λ	$\circ$	Aerofoil sweep angle
C_r	m	Aerofoil root chord
$C_{D0,aerofoil}$	-	Aerofoil profile drag constant
e	-	Oswald efficiency factor
$e_{theoretcial}$	-	Theoretical Oswald efficiency factor
$k_{e,F}$	-	Empirical factor for fuselage drag
$k_{e,D0}$	-	Empirical factor for profile

$k_{e,M}$	-	Empirical factor for Mach number
K	-	Aerofoil induced drag constant
AoA	°	Aerofoil angle of attack
R_e	-	Reynolds number
$C_{L,aerofoil}$	-	Aerofoil life coefficient
$C_{M,aerofoil}$	-	Aerofoil pitching moment coefficient
GR	-	Aerofoil glide ratio
$B_{capacity,min}$	mAh	Battery pack minimum capacity
$B_{capacity,servo}$	mAh	Battery capacity for servo motor
$B_{capacity,actual}$	mAh	Battery pack actual capacity
$B_{capacity,cell}$	mAh	Battery cell capacity
$B_{cell,parrallel}$	-	Number of battery cells in parallel
$B_{cell,series}$	-	Number of battery cells in series
$B_{cell,mass}$	kg	Battery cell mass
P_{out}	W	Battery pack output power
$V_{battery}$	V	Battery voltage
d_f	-	Battery design margin
t_f	-	Battery temperature factor
c_f	-	Battery charge factor
a_f	-	Battery ageing factor
$E_{battery}$	W	Battery energy
f_{DOD}	-	Battery depth of discharge
$\rho_{battery}$	kg/m^3	Battery density
$P_{required,VTOL}$	W	Required power VTOL mode
$P_{required,FW}$	W	Required power FW mode
$P_{propulsion}$	W	Propulsion required power
P_{misc}	W	Miscellaneous power
$\eta_{propulsion}$	-	Propulsion efficiency factor
$\eta_{discharge}$	-	Battery discharge efficiency factor
η_{motor}	-	Motor efficiency factor
$\eta_{propeller}$	-	Propeller efficiency factor
$\eta_{electrical}$	-	Electrical efficiency factor
$M_{propulsion}$	kg	Mass of propulsion system
$M_{battery}$	kg	Mass of battery
$M_{fuselage}$	kg	Mass of fuselage
$M_{aerofoil}$	kg	Mass of aerofoil
$M_{payload}$	kg	Mass of payload
M_{misc}	kg	Mass of miscellaneous

ACRONYMS

ABS	Acrylonitrile-Butadiene-Styrene
AM	Additive Manufacturing
AOA	Angle of Attack
API	Application Programming Interface
AVL	Athena Vortex Lattice
BEC	Battery Eliminator Circuit
BLDC	Brushless Direct Current
BMS	Battery Management System
B-VLOS	Beyond Visual Line of Sight
CAD	Computer-Aided Design
CATS	Civil Aviation Technical Standards
CD	Controller Distribution
CF	Carbon Fibre
CFD	Computational Fluid Dynamics
COG	Centre of Gravity
CPU	Central Processing Unit
DFM	Design for Manufacture
EA	Evolutionary Algorithm
EMF	Electro-Magnetic Force
ESC	Electronic Speed Controller
FC	Flight Controller
FDM	Fused Deposition Modelling
FEA	Finite Element Analysis
FFT	Fast Fourier Transform
FishBAC	Fishbone Active Camber
FW	Fixed Wing
GA	Genetic Algorithm
GCS	Ground Control Station
GG	Global Goal
GNU	General Public License
GPS	Global Positioning System
HALE	High Altitude Long Endurance
ICAO	International Civil Aviation Organization
IDEX	Independent Dual Extrusion
IMU	Inertial Measurement Unit
Li-Ion	Lithium-Ion
LiPo	Lithium Polymer
LLT	Lifting Line Theory
LQR	Linear Quadratic Regulator
MALE	Medium Altitude long endurance
MC	Multicopter
MDO	Multidisciplinary Design Optimization

MFC	Macro Fibre Composite
M-FC	Model-Free Controller
MIT	Massachusetts Institute of Technology
MOEA	Multi-Objective Evolutionary Algorithm
MOP	Multi-Objective Problem
MTOW	Mean Take-Off Weight
NACA	National Advisory Committee for Aeronautics
NSGA II	Non-Dominated Sorting Genetic Algorithm 2
OCV	Open Circuit Voltage
OSD	On-Screen Display
PID	Proportional-Integral-Derivative
PDB	Power Distribution Board
PLA	Polylactic Acid
PTFE	Polytetrafluoroethylene
PWM	Pulse Width Modulation
QGC	QGround Control
RC	Remote Control
RPAS	Remotely Piloted Aircraft System
RTO	Remote Training Organization
R-VLOS	Radio Visual Line of Sight
SA	South Africa
S-A	Spalart-Allmaras
SACAA	South African Civil Aviation Authority
SANBS	South African National Blood Service
SISO	Single Input Single Output
SOC	State of Charge
SPEA	Strength Pareto Evolutionary Algorithm
TECS	Total Energy Control System
TR	Test Run
UART	Universal Asynchronous Receiver-Transmitter
UAV	Unmanned Aerial Vehicle
UAVCAN	UAV Controller Area Network
UTS	Ultimate Tensile Strength
VLM	Vortex Lattice Method
VLOS	Visual Line of Sight
VTOL	Vertical Take-Off and Landing

1. INTRODUCTION

An estimated two billion people around the world do not have immediate access to primary and essential medications such as blood and vaccines [1]. These individuals are predominantly located in remote areas that incur rapid population growths, often resulting in extreme deficiency, disease, and illness. However, the advancement of technical proficiency within the current 4th industrial revolution has created opportunistic breakthroughs which could benefit the well-being of these areas. These potential prospects are apparent in specific mechanization systems which possess capabilities that are crucial for sustaining welfare and health within more impoverished districts. The success of these 'technological tools' forms a necessary task that ensures continual prosperity and growth of both communities and individuals for future generations.

UAV technology and FDM printing are amongst the most influential types of consumer machinery within today's society. Utilized by professionals, enthusiasts and research organizations, these systems have provided countless solutions to several challenges at a fraction of the price and time when compared to traditional methods. The implementation of UAV's as an emergency delivery system for medical aid supplies has ignited the humanitarian side of corporations and government organizations. This generosity has led to increased funding for research projects and has exposed their full potential. However, execution of this strategy on a global scale required addressing of certain performance aspects, to guarantee this method was viable from an economical and practical standpoint. Therefore, this research explored the feasibility of FDM as a proposed solution to the manufacturing of UAVs, as factors such as sustainability, modularity, affordability, and accessibility all contribute to the success of this fabrication method for aerial vehicle production.

To obtain the operational characteristics of an FDM fabricated UAV delivery system, particular features such as on-demand delivery with simple deployment capabilities needed to be satisfied. Reachable and approachable payload compartments were required to carry at least $2.5\ kg$, whilst providing sufficient protection for these supplies. Accuracy and consistency of payload drop-off formed a critical aspect for emergencies and confirmed reliability for future use. Integration and communication with a Ground Control Station (GCS) was necessary for ensuring safety protocols and compliance with the relevant aviation bodies. A flight speed of at least $80\ km/h$ was necessary, as operating below this point would yield adverse aerodynamic effects. Replacement parts and mechanical components used in this solution required a cost-effective approach with the purpose of being expendable and replaceable. Due to continual exposure of these systems to harsh environmental conditions, these attributes were essential for maintaining the longevity of the vehicle. These critical characteristics formed the basic requirements for deploying and operating a medical aid delivery system within the remote areas of South Africa.

Integrating the FDM fabrication method within UAV systems has provided significant qualities that cannot be achieved through orthodox practices. Progression of this manufacturing technique in the last decade has radically improved rapid and flexible prototyping, which has set itself apart from convention whilst being affordable and accessible to end consumers. This has allowed designers to freely express their innovative ideas, which has

enabled further development in this field. Implementation of FDM has also promoted the sustainability of UAV's, as biodegradability and reusability of an FDM material such as Poly Lactic Acid (PLA), has enabled part recycling which gives this manufacturing technique an eco-friendly footprint. These traits, when correctly applied, have ultimately enhanced the operational strategies and overall functionality associated with the UAV industry.

The need for a reliable, economical, practical, and sustainable method of delivering medical aid supplies to remote areas was apparent. Satisfying the requirements of this application was necessary for maintaining a functional and operational UAV that persists for several years. This research showed the capabilities of using a flexible manufacturing method such as FDM within the extensive UAV system to develop and fabricate a transitional VTOL UAV for medical aid delivery purposes.

1.1 Research Question

Can FDM be used to fabricate a transitional VTOL UAV for aiding the transport of emergency medical aid supplies in underdeveloped areas?

1.2 Aim

The work conducted within this research proposed to design, manufacture, test and evaluate a VTOL UAV prototype named *Airslipper*. This dissertation aimed to combine the unique characteristics of FDM printing with the capabilities of UAV's, in order to conceptualize a solution that assisted the delivery of medical aid supplies to underdeveloped areas within SA. Achieving this result required a thorough and fundamental investigation of both UAV and FDM technologies, to provide a comprehensive understanding of their extensive applicational uses. Literature pertaining to these technologies gave insights towards the development of a functional delivery system which deliberated the challenges, benefits and impacts of this solution. A suitable design approach that considered the relevant factors was necessary to conduct a preliminary selection of UAV compatible modules that ensured operability. This systematic strategy needed to allow the intended design to undertake an optimization of its key performance parameters with the purpose of impacting the UAV's flight characteristics by increasing the vehicles flight endurance.

An aerodynamic analysis of the optimized design was required for confirming vehicle stability and control in different flight modes. This assessment, along with additional Computational Fluid Dynamic (CFD) simulations, needed to demonstrate the impact of fluid interference surrounding the *Airslipper* design so that performance is not hindered. An evaluation of the FDM method, with regards to the printed components, necessitated the correct setup strategies were implemented and ensured mechanical robustness and aerodynamic efficiency was unaffected within the final assembly. This research aimed to validate the completed prototype's performance through a controlled hover test in VTOL mode. Appraisal of the vehicles flight characteristics needed to satisfy applicational requirements so as to consider the test a success. Review of the *Airslipper's* qualities and attributes certified vehicle effectiveness for the intended application and manufacturing method. Recommendations on potential design improvements were required, and final thoughts of this research needed to be concluded.

1.3 Objectives

The objectives of this research provided the underlying guidance for attaining a complete dissertation that answered the research question. Each objective outlined the most important aspects of aerial vehicle design and offered a comprehensive array of results and findings that contributed to the operation of an FDM fabricated medical aid delivery system.

1.3.1 Research the fundamentals of UAV and FDM technologies and explore their potential in medical aid delivery systems

The continual impact of UAV systems on modern civilization has created increased challenges, such as legislation. This problematic area has been accentuated by the delivery of blood and vaccines, which has been considered dangerous goods by several health organizations. However, the benefits of medical aid delivery systems have become more significant as the outcomes of this technology progresses. Therefore, the literature of this research detailed the current legislative regulations associated with UAV's in South Africa and provided categories which the South African Civil Aviation Authority (SACAA) uses to classify these systems. This research also reviewed existing medical aid delivery systems and the impacts they have on the biopharmaceutical industry. These literature findings aided the operational strategies used in this dissertation and provided the necessary information for deploying an unmanned vehicle.

The implementation of FDM technology within UAV fabrication has formed a relatively new ideology, and due to limited research surrounding this topic, possibilities arose for fabricating a VTOL UAV using this method. The flexible capabilities and enhanced characteristics of FDM have made this technique desirable for manufactures, operators, and designers. However, certain limiting factors and harmful qualities associated with FDM hinder its implementation. This research showed extended literature for combatting these qualities and revealed what precautionary steps were considered to minimize the adverse effects these qualities had on defined UAV modules.

This objective additionally provided the fundamentals of UAV technology and explored aircraft aerodynamics with relevance to the characteristics of aerofoils and aerodynamic analysing platforms. A theoretical background check and investigation on propeller-based propulsion systems provided the necessary information for attaining critical performance parameters for this research. These principal UAV elements supplied this research with possibilities for attaining an enhanced UAV configuration using literature obtained from various Multidisciplinary Design Optimization (MDO) techniques and execution methods. This objective further addressed specific aspects such as the control and modelling of unmanned systems, which aided the design of this technology and offered awareness to the operation and functionality of UAV systems.

1.3.2 Design a prototype UAV and optimize its critical parameters to enhance flight endurance

The design of an electrically powered aerial vehicle proved to be a challenging task that required contribution from multiple research fields. This multidisciplinary effect is a result of the mechatronic nature within UAV propeller-based propulsion systems and their operating fundamentals. This objective acknowledged the working

principles of UAV technology and employed a design approach that considered the vehicles fabrication method and application. This research further revealed the design requirements, hardware limitations and legislation regulations of the system, which supported a preliminary structure for the *Airslipper's* conceptual design.

The initial selection of design parameters formed a systematic approach that addressed the UAV elements individually to achieve the desired outcome. This process considered the restrictions and provided a methodical technique for choosing the appropriate electronic components and their performance parameters. This objective developed the propulsion system setup for the *Airslipper* and offered the essential performance values that assessed the vehicle's capabilities in VTOL flight mode.

The research of this dissertation also aimed to ascertain an optimized parameter combination that enhanced the *Airslipper's* endurance. Accomplishing this outcome required the identification and recognition of the most influential parameters associated with the vehicles aerodynamic design and propulsion system. This objective utilized the fundamental elements of UAV design for the creation of two parametric fitness functions that were specifically formulated for increasing the vehicle's endurance. The constrained functions required a suitable evolutionary algorithm that ensured a Pareto front was obtained. This objective revealed the solution of this MDO and provided the corresponding set of optimized parameters that improved flight endurance and flight service radius.

1.3.3 Analyse and simulate the prototype UAV to ensure functionality in the different flight modes

Due to the unmanned operation of the *Airslipper* UAV, factors such as controllability, sensitivity, and response characteristics were vital to understanding the aerodynamic capabilities of the design. These considerations were necessary to ensure the vehicle preserved functionality and operability when subjected to disturbances and other undesired environmental effects. This research conducted a series of aerodynamic analyses on the *Airslipper* prototype using a suitable analysing program that included viscous and inertial effects for solution accuracy. A stability analysis of the aerodynamic surfaces provided vital data that confirmed the vehicle remained in a stable position at its cruise velocity, thus minimizing power consumption and maximising endurance. Assessing this critical information guaranteed that the influence of external conditions had no impact on vehicles flight modes.

This objective further examined the aerodynamics of the *Airslipper's* modules by CFD simulating a 3D model of the design. Vorticity, pressure distributions and velocity effects were apparent on the individual subassemblies and reinforced the fluid behaviour experienced by the previous analyses. Due to the *Airslipper's* fabrication method and design, this research explored the impact of fluid shearing potential on the aerofoil's structural integrity. Discoveries made in this objective negated any design concerns that were apparent and underlined the full potential for this prototype as a useful UAV in both VTOL and FW flight modes.

1.3.4 Fabricate, assemble, and test UAV to validate key characteristics

As with any aircraft design strategy, reducing weight was crucial for maintaining peak performance. The implementation of FDM fabrication for the *Airslipper* prototype considered the mass of each part whilst aiming

to preserve the structural integrity, robustness, and durability of the design. Due to the literature attained in this research, it was noted that FDM printed parts exhibited anisotropic properties. Therefore, this objective proposed to obtain a correction factor for this fabrication method by experimentally investigating the shear strength capabilities of an FDM printed aerofoil with varying parameters. These findings were combined with a selection matrix that allowed each part of the *Airslipper* to ascertain the optimal parameter combination that best suited the vehicles flight characterises.

Prior to the *Airslipper* assembly, this objective performed several propulsion tests which revealed indispensable data associated with the propeller and motor setups. Results matched the simulations and confirmed the optimization results. Due to a segmented design, the *Airslipper's* fabricated parts were assembled using a combination of bolt connectors and epoxy. This objective revealed the completed assembly and showed how each part interacted to achieve the VTOL and FW flight modes. Testing the *Airslipper* UAV was achieved through a simple hover test that was executed three times to confirm flight consistency. The vehicle successfully completed the testing and provided essential flight log data based on its performance. This objective supplied these findings and offered an array of plots pertaining to the control, vibration, and power consumption of the vehicle. Based on these results, this objective concluded by evaluating the design and fabrication method of the *Airslipper* against factors such as sustainability, maintenance, deployment, and cost.

1.3.5 Discuss, conclude, and make recommendations on this research

The design, analysis, manufacturing, and testing of an FDM printed medical aid delivery UAV was a comprehensive process that considered multiple factors for each development phase. This research yielded a method of manufacturing a VTOL UAV in a cost-effective, practical, and sustainable manner. Characteristics of the *Airslipper* UAV proved useful in both VTOL and FW flight modes, which ultimately confirmed the design and fabrication method. This objective reviewed all aspects of the *Airslipper* UAV and made comparative evaluations between this research and current medical aid delivery systems. Recommendations and potential improvements on this design and fabrication method were addressed, and a critical analysis of the *Airslipper's* performance was completed. This research concluded by commenting on future possibilities within this field.

1.4 Contributions of this research

All results, discoveries and outcomes described in this research pertained to the development and fabrication of an FDM printed VTOL UAV named *Airslipper*. The current literature on using FDM fabricated parts within UAV systems is expansive; however, the implementation of a fully operable VTOL UAV that is entirely fabricated using FDM technology, according to this research, has never been documented.

The unique design of *Airslipper* featured a transitional propulsion system configuration that enabled the vehicle to transition between VTOL and FW flight modes. Each motor arm was individually actuated by servo motors, which increased the overall functionality of the vehicle during both flight modes. The addition of an aerofoil aided the vehicle's endurance and range, which ultimately enhanced the service radius and flight envelope of this design. Due to FDM fabrication and the anisotropic qualities associated with this method, positioning of the aerodynamic control surfaces was located on the motor arms.

This novel setup negated the stress concentrations of traditional control flaps when exposed to wing load forces and high bending moments. This new control surface arrangement allowed for a greater control area and also provided customizability in terms of shape, size, and planform, which significantly increased the response of the vehicle to external disturbances. The design approach adopted for this vehicle highly regarded the fabrication method and application, which allowed this research to undertake a thorough inquiry on how these particular facets integrate within the completed system. These aspects were combined with factors that considered sustainability, cost, maintenance, and repair to develop this design further.

This research conducted a preliminary design of the *Airslipper* and its relevant modules. The initial selection of propulsion parameters, based on an estimated vehicle mass value, proved sufficient for the requirements of the application and yielded a maximum flight time of $0.218\,h$ in VTOL mode. The implementation of the PX4 autopilot firmware within the systems electronic design allowed for the execution of a suitable wireless communication protocol and control design. This setup enabled vehicle telemetry and provided a fully automated system that was capable of operating remotely through a suitable GCS.

By recognizing the importance of this medical aid delivery application, this research noted the benefits for attaining increased endurance. This work identified the cruising phase as the most prolonged and taxing flight period for the vehicle, which corresponded to the maximum energy consumption. Therefore, the research conducted in this dissertation aimed to configure the propulsion system and aerodynamic design for obtaining maximum endurance at the cruise phase. The utilization of MATLAB's 'gamultiobj' function provided a solution to this challenge which returned individually optimized parameter values that resulted in a flight endurance increase of $58\,s$. This outcome enabled the vehicle to have a significantly greater service radius which significantly enhanced the *Airslipper's* capabilities for delivery. This multidisciplinary optimization method provided the propulsion and aerodynamic designs with enhanced parameter combinations that best suited the vehicles cruise phase and revealed the profits of this technique.

The implementation of the FDM fabrication method in this research provided countless design opportunities that offered substantial benefits over traditional UAV manufacturing techniques. FDM also allowed components to become modular and customizable, which significantly improved the functionality of the *Airslipper* design. However, due to the permutations associated with FDM parameters, materials, and equipment, no reliable Finite Element Analysis (FEA) software was found that was capable of performing an accurate analysis of an FDM printed part. Therefore, this research proposed to experimentally investigate the effect certain FDM parameters have on a specific printed parts integrity, robustness, and shear strength.

This work aimed to ascertain a correction factor for an FDM fabricated aerofoil section that can then be applied to the *Airslipper* design, which ensured the bending moments seen by this component did not exceed the shear strength capabilities of the part. Results of the investigation concluded a greater resilience to failure load was apparent for parts that exhibited reduced layer heights and increased infill percentages. It was further noted that layer heights of $0.3\,mm$ or larger did not contribute towards a part's structural integrity and shear strength. These

outcomes revealed the optimal FDM parameter combinations that were then applied to the printed components of the *Airslipper* design.

As desktop FDM equipment has limited build volumes, the *Airslipper* design was partitioned into printable dimensions that required further fastening to complete the assembly. A total of 99 individually printed parts made up the *Airslipper* design at an approximated weight of $\mathbf{5.4\ kg}$ and with a printing time of $\mathbf{589.68\ h}$. Assembly of the vehicle was made straightforward by implementing a mutual fastening system that allowed the relevant modules to become completely secure for flight. This segmented design further enhanced the maintenance and repair strategies, as parts were easily replaced and integrable back into the vehicle. An evaluation of the *Airslipper* design and fabrication method was conducted, and recommendations for potential improvements were made.

1.5 Summary of Chapter 1

This chapter provided a thorough introduction to the challenge at hand and focussed on what steps and actions were required for implementing a VTOL UAV for the delivery of emergency medical aid supplies to these areas. An aim of this research was formulated, and specific objectives for the design, analysis, and fabrication of an FDM printed VTOL UAV were discussed and evaluated. The final part of this chapter provided the outcomes of this dissertation and how specific contributions enhanced the research and development of this industry and application.

2. LITERATURE REVIEW

The literature presented in this research detailed the impact both UAV and FDM technologies have on society and described how each has uniquely influenced modern civilization. This chapter additionally emphasized the various regulatory factors associated with UAV's in SA and explained the implementation of these systems within the biopharmaceutical industry. This literature also discussed the benefits of the medical aid delivery application and further expanded this research to include current strategies and designs employed in this field. An assessment of FDM fabrication challenges was explored in conjunction with some of the innovative techniques adopted by external researchers. These factors revealed the full aptitude of FDM, which further detailed the sustainability and structural integrity of materials such as PLA.

An understanding of aerodynamic fundamentals for FW-based aircraft was established within this work alongside the detailed characteristics of aerofoils operating at reduced Reynolds numbers. Theoretical derivations and expressions for propeller-based propulsion were investigated, and considerations of different propeller setups were observed. This chapter concluded by providing a joint overview of some common mathematical modelling and control techniques used for commercial VTOL UAV operation. The literature of this research offered the underlying knowledge for designing and developing a useful VTOL UAV for medical aid delivery purposes.

2.1 UAV systems and their classification

Initially popularized by the military, for combat and war applications, the UAV has since expanded its capabilities and has seen a complete reconfiguration in terms of its design, functionality, and operational conditions. The first recorded application of a UAV system was in 1930 when the British Royal Navy developed the 'Queen Bee' for aiding pilots in target practice [2]. This vehicle had a maximum flight velocity of $\mathbf{160\ km/h}$ and was the first of its kind to feature refuelling and reuse. Since then, nearly 90 years later, UAV's are able to perform a multitude of applications that serve many industries.

The progression of the 4th industrial revolution has transformed civilization into a productive environment, where efficiency, functionality and aesthetics are everything. Attaining this standard has meant finding technological solutions to challenges that humanity faces on a daily basis. Since the first UAV operation, private corporations, enthusiasts, and educational institutions have found ways to harness the characteristics of these systems for more advanced applications that utilize sophisticated sensors and instrumentation for aiding specific missions. However, typical applications such as wildlife monitoring, security surveillance, videography and delivery services have allowed civilization to seize this opportunity and evolve this automated technology to fit its needs [3]. The operation of an unmanned system is a simple concept that typically involves implementing a mechatronic framework within an aerial vehicle to perform automated flight with precise mission constraints. However, the classification of a particular design for a given mission is a comprehensive procedure that considers individual features and operational elements of the vehicle. Each design has a broad spectrum of classifications, and within that lies the different types of UAVs with their corresponding flight characteristics. *Table 2-1* shows these classifications, which were based on the attributes approved from [4].

Table 2-1: Common UAV classification, revised from _[4]_

	Categories				
Classification	Range (*km*)	Altitude (*m*)	Endurance (*hours*)	MTOW (*kg*)	Size (*m*)
Micro UAV	< 2	< 50	< 0.5	< 3	< 0.5
Mini UAV	< 10	< 80	< 2	< 14	< 3
UAV	> 10	> 120	> 5	> 20	> 4.5
Tactical UAV	70 - 200	30 - 9000	2 - 12	0.5 - 1300	1 - 30
HALE/MALE UAV	> 500	> 14000	24 - 48	> 1000	> 20

2.1.1 The challenge facing the UAV industry

Since the first UAV application, these systems have become a symbol of efficiency, effectiveness, and technological prowess. Development of this technology over the past decade has allowed many industries to adopt the capabilities and standards these tools possess slowly. However, the implementation of new technologies, such as UAV's, comes with a broad set of risk assessed challenges and regulations that must be abided, especially when applications implicate the well-being and privacy of civilization.

2.1.1.1 UAV legislation in South Africa

The globalization of UAV technology has enabled these systems to become more advanced than intended. This commercial interest has led to increased privacy and ethical issues, which has meant industries have struggled to fully utilize these technologies due to legislation and the enactment of various flight restrictions. These governing laws vary according to the UAV's application, configuration, and country of intended use. The drafting of regulations is a difficult task that requires an intense evaluation of the unmanned system and the understanding of potential risks they can cause to the general public. The operation of a UAV for the delivery of medical supplies, specifically in South Africa, has to be licensed through the SACAA [5]. This body is responsible for UAV operating certificates within SA airspace and governs the use of all UAVs for commercial projects. Other concerns facing this application is the regulation behind the transportation of blood, which is classified as a dangerous good which further implicates the use of UAVs for emergency blood delivery.

The SACAA classifies the standard UAV as a Remotely Piloted Aircraft System (RPAS). These types of vehicles are acceptable for personal and private use with no commercial gain. However, applications that involve commercial outcomes must be registered and operated in accordance with Part 101 of the SACAA regulations act [5]. These laws are compliant with the International Civil Aviation Organisation (ICAO) and follow specific technical standards (SA-CATS). For an RPAS to be approved for flight, an organization such as the Remote Training Organization (RTO) needs to verify and conduct theoretical and practical training before the issue of an RPAS license. The vehicle itself needs to be thoroughly investigated and tested to ensure compliance for commercial use. The types of RPAS configurations used by the SACAA are grouped into four classification categories, as seen in _Table 2-2_. The VTOL UAV undertaken in this research follows the Class 1C, which stipulates a maximum flying height of $121.92\ m$ above sea level at a maximum Mean Take-Off Weight (MTOW) of $20\ kg$. This class further states that the maximum energy at impact must be less than $34\ kJ$.

Table 2-2: SACAA RPAS classification categories, revised from [4]

Class	Line-of-Sight	Energy (*kJ*)	Height (*m*)	MTOW (*kg*)
Class 1A	R-VLOS/VLOS	E < 15	H < 122	M < 1.5
Class 1B	R-VLOS/VLOS	E < 15	H < 122	M < 7
Class 1C	VLOS/E-VLOS	E < 34	H < 122	M < 20
Class 2A	VLOS/E-VLOS	E > 34	H < 122	M < 20
Class 2B	Experimental / Research			

E – Indicates the energy at impact

H – Indicates the flying height above ground level

2.2 A UAVs influence in medical aid supply

The ubiquitous nature of UAV development has inspired manufacturers to continually advance the electronic processing power and material handling capabilities of these systems. This progression has enabled UAV technology to be manufactured in a cost-effective and on-demand manner. Depending on the application, these systems may only require specific peripherals, which significantly reduces operating costs and complexities. These advantageous qualities heighten the prospect of UAV delivery and reveal the potential for implementing this strategy as an emergency medical aid delivery system.

2.2.1 The current medical situation in South Africa

Forming an integral part of a South African's basic rights, access to essential and critical medical provisions plays a vital role in basic human health and survival. This governing responsibility is especially true for those within underdeveloped areas and for those living in communities that are distant from metropolitan cities and hospitals. According to the statistics and research given by [6], 84% of South African citizens rely on the public health sector to provide their necessary medical needs. This research also reveals that the public healthcare system of SA comprises of 422 hospital and 3841 clinics and health centres. These numbers reveal the priority of this public sector but also suggest the broadened infrastructure within this country. However, with a rapidly growing population and a vast habitable landscape, SA's demand for immediate and essential medical supplies has increased. This decline in medical assistance is also caused by the extreme poverty of the country and lack of sanitation that is present within rural areas.

Therefore, combatting this demand requires alternative measures to ensure the health of these communities remains a priority, and that livelihood is kept intact. The response to this challenge necessitates a technological solution that is consistently and accurately capable of delivering medical supplies to remote areas within these South African regions. The solution needs to be expendable and cost-effective for ensuring sustainability but must also feature robust qualities to handle the constant and extreme conditions of SA for several years.

2.2.2 Transformation of the biopharmaceutical industry

The supply chain and immediate distribution of basic and essential medical supplies within the 21st century has become a well-established process. The term 'first aid' was not established until 1878, when British soldiers and civilians were trained to treat their fellow countrymen before trained medical physicians arrived [7]. More than a century later, first aid and first response programs have received significant attention due to the advancement in technology and medical science. However, the biopharmaceutical industry of today has become disrupted by the innovation and implementation strategies of UAV's to transport medical supplies efficiently. The persistent deployment tactics of these systems have drastically altered the way in which certain medical supplies are being distributed. This transformation has broadened the capabilities of supplying life-saving vaccines and temperature-sensitive drugs to communities and districts that are affected by natural disasters or epidemic outbreaks [8].

The autonomous functionality of a UAV is exemplified by its simplistic operation yet sophisticated electronics. These systems possess features that are capable of providing immediate relief to remote locations at a fraction of the cost as compared to traditional methods. Besides the physical attributes that make UAV's the best technological solution, research has been conducted to reveal the economic impact and practicality values of these systems for aiding the transport of vaccines. The research shown in [9] shows the numerous challenges that many low-income countries encounter with vaccine supply chains. The authors revealed that the progression of UAV technology within recent years has led to increased distribution methods and has the ability to replace other delivery vehicles whilst reducing overall costs. The results of the study revealed that the UAV provided increased vaccine availability and reduced logistical costs by $0.08 per dosage. It was also noted that the minimum payload capacity required to achieve these cost savings was approximated to be 0.4 litres. These findings offered confidence for future research and suggested that continual use of these systems would cover the initial outlay within a few months.

2.2.3 The benefits of emergency medical aid delivery by UAV

The employment of emergency supply delivery by air was originally performed during the first world war, in 1916, when the British used war aircraft to conduct airdrop resupply missions, in order to deliver food to the starving British soldiers in the town of Kut-al-Amarah [10]. Since then, medical aid delivery systems have included state of the art transport vehicles such as helicopters, aeroplanes and now finally UAVs. Deployment of these modern vehicles has steadily increased the delivery of supplies in a precise and consistent manner within fractions of the time when compared to 1916. The adoption of UAV technology has created new opportunities that were once considered too dangerous or were not cost-effective. This growth has led to the engagement of humanitarian logistics and disaster relief response programs by various governments and private corporations around the world.

The benefits of integrating unmanned technology within emergency medical response programs have facilitated superior operation characteristics at faster deployment times. This implementation has shifted the paradigm for emergency medical aid distribution as it closes the gap on last-mile delivery and distribution to individuals. When it comes to critical medical supplies such as blood, vaccines, anti-venom and even organs, time is of the essence,

and thus the transportation of these supplies requires specific precautionary measures no matter the destination. Compared to the conventional helicopter and plane delivery systems, UAV's dominate a more generous array of capabilities such as faster delivery, on-demand dispatch times and unmanned operations. These features distinguish the UAV system, and factors such as reduced manufacturing time and subdued maintenance costs, substantially increase their effectiveness over other methods.

Furthermore, the cost of operation is radically diminished due to the rechargeability and reusability of battery cells, thus making it a more sustainable method of delivery in the long run. Although the maximum payload, flight range, and flight velocities are reduced due to the electric nature of the system, the intended operation of the system can be achieved without personnel and does not require extensive training. These attributes make the UAV a suitable emergency medical aid delivery system in order to ensure patient survivability in the most extreme situations.

2.2.4 Existing medical aid delivery UAVs

The ongoing research in material science, along with innovative design approaches, has allowed UAV's to have drastically reduced fabrication costs. These advancements have been combined with cutting-edge electronic components to maximize the performance and functionality of these systems. This progressive evolution has inspired researchers to pursue and dedicate resources into creating functional UAV designs for emergency medical aid supplies.

A study was conducted by Johns Hopkins Bloomberg School of Public Health, in which a research team utilized UAV's and supply chain software called HERMES to deliver vaccines across Mozambique [11]. The objective was to develop and analyse an array of scenarios for vaccine delivery that included challenges that a UAV might encounter. The results from the study revealed a savings cost of between 20 and 50 percent as compared to the traditional land-based transport for vaccine delivery within the country. This investigation reveals a practical implementation and shows how logistical savings associated with these systems can be obtained.

2.2.4.1 Zipline

Due to its forward-thinking design and operational network, the American company Zipline is at the forefront of humanitarian relief for emergency medical aid support. The company has a commercial project in Rwanda and is collaborating with its government to help aid the hospitals with on-demand blood transport in a rapid response situation. Zipline's drones feature a fixed-wing design with a single propeller for thrust. The UAV is capable of carrying up to $1.5\ kg$ of payload and has a flight radius of $75\ km$. The deployment procedure utilized by this company is achieved through a zipline catapult system which propels the vehicle to $100\ m/s$ within the space of $3\ m$. This design characteristic allows the vehicle to attain cruising speed faster, and thus increases the design efficiency. The company is looking to the future and considering medical deliveries to areas outside Rwanda, and they are aiming to diversify their payload to include vaccines and diagnostic test kits [12].

2.3   The impact of Additive Manufacturing

With a swiftly growing research backing, Additive Manufacturing (AM) has become an emerging technology that has revolutionized the manufacturing industry. Not only has it significantly influenced the manufacturing sector, but it has also been exploited by various individuals, including entrepreneurs, professionals, and academia. The inception of the stereolithography system for rapid prototyping first appeared in the 1970s, when Dr Hideo Kodama invented a version of this method using the ultraviolet light curing technique [13]. Since then, AM has been manipulated and broadened to fit into a multifaceted industry and has become synonymous with rapid and flexible manufacturing.

The employment of this technology has shifted the workplace environment and has radically altered the way in which many products are fabricated, distributed, and sold. This historical innovation has impacted modern civilization through its disruptive nature and has further diversified its applicational capabilities to fit a number of outcomes. With standard AM technologies such as vat photopolymerization, material extrusion, powder bed fusion and direct energy deposition, AM can produce any product, provided it has been set up accordingly.

The ability to create complex geometries with intricate details at a fraction of the time and cost has made AM a disruptive technology in the manufacturing market [14]. The need for AM within 21st-century manufacturing techniques has resolved undesired features such as Design for Manufacture (DFM), which is a well-established field of study and plays a significant role in traditional fabrication methods. AM has also reduced the overall tooling and moulding costs associated with these methods. This development has influenced the design of products and has allowed designers to minimize waste through the execution of intelligent design approaches and fabrication strategies. Further applicational uses and research on AM technologies have been documented in great detail by various academia such as in [15] and [16].

2.3.1 Fused Deposition Modelling

At the forefront of affordable and readily available AM technologies, FDM possesses characteristics that make it a perfect method for both rapid prototyping and end-consumer use. Attributes such as modularity and customizability make this approach an attractive fabrication tool over the older customary methods. FDM operates by deposing a molten thermoplastic polymer material in a desired two-dimensional shape and is hardened through natural and forced convection methods. This process is then systematically repeated for every specified vertical layer height until a final product is attained.

The most common thermoplastic materials used are Acrylonitrile-butadiene-Styrene (ABS) and PLA [17]. These materials are naturally sourced and are in abundance, which makes them relatively cheap and easy to process. Both materials exhibit similar mechanical properties, but due to PLA's biodegradability and sustainability, it is the favoured material in the FDM industry. With a steady increase in FDM printing over the past few decades, users have seen the progressive evolution of this method and have witnessed the advancements associated with the materials setup strategies and equipment.

2.3.1.1 Challenges of FDM fabrication for UAV's

Although the FDM fabrication method is a cost-effective technique that exhibits countless benefits over traditional techniques, particular challenges hinder its successfulness when creating larger parts. This issue is particularly evident with UAV frames and aerofoils, which can form complex structures that require the utmost accuracy. One of the main constraining factors that contribute to this cause is the minimal build platform associated with FDM printers, specifically desktop variations. This limitation requires bulky parts, such as the aforementioned frames and aerofoils, to be fragmented or partitioned into printable dimensions. Enabling this strategy creates additional design complications, as further assembly is required to combine individual parts to form the desired component. As a result, part integrity degrades and thus becomes inconsistent with the different Computer-Aided Design (CAD) simulations. Part incompatibility and inaccuracy are also susceptible to more extensive printing and may even require unnecessary post-processing.

Another negative feature of FDM that hampers the quality of the desired outcome is the surface finish and surface roughness of a fabricated part. This factor drastically affects the aerodynamic capabilities of an aerial and is directly influenced by explicit processing parameters and the stair-stepping phenomenon associated with sloped and curved parts. Research by [18] proved that minimizing the effect of stair-stepping was achieved through the implementation of a sub-layer in the parts build direction. Results of this research showed better quality prints and improved the surface finish using this method. Other research such as [19] demonstrated how surface roughness could be predicted based on the build direction, setup layout and layer thickness of an FDM printer. Although the literature has shown several methods that try mitigating this undesired effect, specific post-processing techniques such as sanding, and polishing are still the ultimate solution to create the desired surface finish.

Due to the operational qualities of FDM's deposition technique, fabricated parts exhibit the undesired property of an anisotropic structure [20]. This characteristic is particularly important as it affects the parts mechanical strength along the build direction, and further constitutes to the parts surface roughness and inaccuracies. The severity of this behaviour is directly influenced by processing parameters that are used in a parts setup procedure. Research shown in [21] has revealed what parameters physically affect a parts structural integrity and robustness. The authors conducted several experiments to determine which factors significantly contribute to this undesired outcome. Parameters such as layer height and wall thickness along with part setup strategies such as build direction and deposition angle, all contribute to the parts resilience at different loading conditions. This research suggested a parameter combination, that when implemented, can maximise the strength and integrity of a printed part.

2.3.1.2 Research and development in FDM technology

Continual developments in the FDM industry has led to improved equipment, modified material properties and innovative build strategies, which has ultimately enhanced the performance and part outcomes of this technology. Such research can be found in [22], where the authors integrated the capabilities of rapid prototyping and machining. By utilizing a five-axis hybrid FDM printer, the authors were able to attain dimensionally accurate parts whilst being able to significantly reduce the amount of support structure needed, resulting in reduced material

consumption and waste. This hybrid system also demonstrated post-processing and machining of the printed parts, which can be used to achieve greater tolerances for more complicated designs.

Other research shown by [23] aimed to improve the fabrication of large-sized thin-walled structures through the implementation of a laser-assisted heating system. This method proposed to solve the problem of part warping and deformation during printing. Results of the modifications revealed a decrease in surface roughness whilst improving the parts overall mechanical properties and shape accuracy. These research improvements are an example of FDM's customizability which offers an understanding of the possible future developments of this technology. With a sudden surge in desktop printing and constant use of PLA material, researchers have taken this opportunity to investigate the attributes of printed specimens against their properties. The development of focussed material combinations has revealed some extraordinary results in terms of a parts mechanical, chemical and electrical characteristics. Studies such as [24] have shown the various capabilities of filament composites with their ability to conduct electrical current and simultaneously display extreme resilience to torsional stress.

Other research such as [25] provided scientific insights into the behaviour and qualities of PLA from varying sources. This research conducted multiple investigations using several spectroscopy techniques to analyse the change in chemical properties of PLA. Findings revealed variations in additives, pigments, and fillers for the different manufactures of PLA. These changes in material chemistry and processing transformed the chemical behaviour of the filament and thus characterised the material in different ways. The authors provided observations on these results and offered design considerations when using PLA filament. However, the capabilities of FDM printed PLA still lacks the physical attributes that other FDM materials possess. Therefore, the authors of [26] presented an approach to experimentally modify PLA's physical properties through the addition of sustainable additives. Through rheological analysis and dynamic mechanical analysis of printed specimens, results showed that the tailoring of PLA's physical attributes is possible whilst retaining biodegradability and FDM compatibility.

2.3.1.3 Sustainability of FDM fabrication

Describing the sustainability of this technology can be seen from two different perspectives, the recyclability of the material along with the reproduction and reusability of parts. The PLA biopolymer is derived from a renewable resource such as corn and sugarcane, which makes it abundant and accessible. The biodegradability of PLA is far more superior than other materials synthesized from the same source; this is mainly due to its chemical makeup and processing [27]. Besides the use in FDM fabrication, PLA has uses in food packaging and disposable utensils.

The FDM fabrication method features a unique self-replicating trait that sets itself apart from any other. This ability allows a machine to build and fabricate parts that can be used to make others. This phenomenon is known in the FDM industry as a RepRap system [28]. Having this quality allows for a single printer to replicate its components so as to create a print farm, thus reducing part manufacturing costs and logistics. The RepRap system also leads to the development of new and improved machine designs and encourages research and innovation within this field. The FDM printer requires minimal setup and the electro-mechanical parts used to build and maintain this machine are relatively cheap and abundant. With slight modifications to the overall setup, these systems can reuse their old parts as new filament material. This means that the same material used to produce a

part can be repurposed to fabricate another. This reusability allows the fabrication method to become a zero-waste manufacturing technique with an eco-friendly footprint.

2.3.2 Impact of FDM parameters on printed parts

As with any fabrication method, a variety of undesired characteristics plague the FDM technique, as mentioned by the challenges above. However, the successfulness of a printed part, based on the intended design, is centred around a multitude of parameter variations associated with FDM. This dependency falls in-between the parts CAD model and the finished product, known as the slicing parameters. Although each of the many individual variables contributes towards the desired outcome in some way, some particular parameters are more influential and more dominant than others. Within this research, parameters such as infill density, layer height, wall thickness, infill pattern, and print speed form the fundamental framework of a fabricated part. These parameters have a direct impact on a parts weight, surface finish, strength, flexibility, durability, and fabrication time. Additional printing aspects, such as print direction and part setup strategies, also contribute to the overall performance of a part.

When evaluating the functionality of a UAV, factors such as aerodynamics and structural integrity are fundamental areas to consider. Since these factors are dependent on the design materials used for the individual components, it can be noted that FDM parameters have a significant impact on the UAV's performance. Hence, maximizing the efficiency and capabilities of the vehicle requires these components to be lightweight and aerodynamic in shape whilst maintaining structural stability to external forces. Thus, obtaining an optimal combination of printing parameters is necessary for achieving these attributes.

2.3.2.1 Aerodynamic surfaces

The surface of a part produced by desktop FDM printing has shown to be influenced by particular attributes that result in relatively poor finish qualities which further create adverse effects for the aerodynamics and drag of an aerial vehicle [29]. However, due to print setup strategies and parameter combinations, a part can be fabricated in a manner that minimizes these negative attributes. Allowing the requisite elements of a UAV, such as an aerofoil, to be built for minimum drag, means aligning the build direction of this part with the intended forward velocity of the vehicle [30].

This setup strategy is backed by research shown in [31], which shows how this undesired surface roughness can be negated through FDM printing attributes have such as build direction and layer height. The application of these research outcomes aims to help reduce the materials surface roughness and minimize the potential for turbulence, thus decrease the total drag exerted on the aerodynamics surfaces of the vehicle. However, implementing this strategy intensifies the anisotropic behaviour of parts, which creates weak adhesion points between print layers. As a result, the potential for delamination and shearing of the printed parts is heightened. Research conducted in [32] and [33] emphasized these damaging qualities and provided critical information pertaining to this issue.

2.3.2.2 Structural integrity

The PLA and ABS materials used by FDM are adequate for attaining the necessary strength and robustness for prototype manufacturing. However, fabricating parts with increased mechanical properties requires the knowledge of creating complex and compelling supporting structures within a printed part. The use of conventional load and non-load bearing designs were traditionally implemented for increasing strength whilst reducing weight and material waste. However, these methods can be combined within FDM to form a multifunctional hybrid structure approach that adopts the best features without the need for complicated designing. This structure is known as a parts infill, which is an interior geometric construction method within a part. These structures are typically used for supporting overhangs; however, infill patterns known as cubic and gyroid, provide significantly improved mechanical characteristics such as high shearing and compressive strengths. This gyroid pattern was discovered by Massachusetts Institute of Technology (MIT) researchers, who found this pattern embedded in butterfly wings, which itself gave the wings their rigidity and flexural strength [34].

FDM attributes that contribute to the hybrid structure include the deposition angle, infill percentage, wall thickness, and layer height. Research conducted by [35] and [36] analysed these attributes through an experimental investigation. This research demonstrated the impact these attributes had on a part's flexural strength and rigidity. Results showed a statistically significant effect between the parts deposition angle and infill percentage. Other pertinent observations included the impact layer height had on the curvature of a part, which yielded a non-linear relationship. This research revealed a superior resistance to flexural stress for a part that exhibited an infill percentage of 10 % at a deposition angle of 60 degrees. The authors suggested that this combination further reduced build time and maintained the strength of a part whilst minimizing the anisotropic effect. These tests, along with other research in [37] and [38], contribute to the structural strategy for the fabrication of a UAV.

2.4 UAV aerodynamics

The associated lift and drag components of an aerial vehicle form the fundamental attributes of aerodynamic design. These topics require input from multiple research fields and can be expressed by numerous viewpoints. However, this research makes use of a fluid mechanics approach, which breaks down the complexity of physical interaction between the components. The absolute of aircraft design is achieved by minimizing aerodynamic drag whilst maintaining vehicle dynamics, control, and stability. Drag reduction significantly impacts the vehicle's performance and contributes to other factors such as payload carrying capacity and maximum flight endurance. Achieving this standard can be obtained through the design strategies of a vehicle's aerodynamic configuration and propulsion system setup.

2.4.1 Aerodynamic surfaces at low Reynolds numbers

Due to design requirements and material limitations, the aerofoils of a UAV naturally experience low Reynolds numbers as a result of reduced aerofoil chords and flight speeds. The aerofoil of a UAV typically observes Reynolds numbers lower than $Re < 6x10^5$, which impacts the vehicles performance characteristics differently to standard passenger aircraft. Research in this field has shown significantly reduced aerodynamic efficiency when scaling conventional aircraft aerofoils and outcomes of several investigations have also illustrated increased power

consumption due to excessive drag when operating at these values [39]. This effect is a product of airflow interaction, specifically the boundary layer physics of flow separation with sporadic turbulence. It is therefore necessary within this research, to understand the basic geometric design features of an aerofoil to ensure optimal performance in low Reynolds number operation.

Research given in [39] used a CFD solver which coupled a laminar-turbulent transition model with a Spalart-Allmaras (S-A) turbulence model to investigate the effects of low Reynolds numbers on UAV aerofoils. The research showed a correlation between aerofoil performance and Reynolds number for conventional aerofoils such as the National Advisory Committee for Aeronautics (NACA) 0012. This baseline enabled additional findings which illustrated Reynolds numbers below $Re < 1x10^5$ exhibited an increase in drag due to the aforementioned flow separation. This research also provided performance information on aerofoils with varying thickness-to-chord ratio's (t/c) and cambers. Results of these disparities suggested that having a 6-9 % camber on thin-plate aerofoils (t/c of 1%) significantly increased the lift-to-drag ratio.

Further examinations of low Reynolds number behaviour revealed a greater chance of trailing edge separation for thicker aerofoils. This outcome meant that thin plate aerofoils create more lift due to the preservation of the lower surface pressure. This phenomenon is also true for reversed configured aerofoils, where the sharp leading edge allows the separation and reattachment much earlier, similar to that of thin plates. The outcomes of this research recommended the implementation of thin cambered aerofoils as they offered appreciable performance characteristics at lower Reynolds numbers and also generated higher lift-to-drag ratios at lower flight speeds.

2.4.2 Aerofoil optimization

The optimization of an aerofoil has specific implications for the vehicle's performance. By adjusting the aerofoils design, characteristics such as lift, drag, pitching moment, stability, and dynamic response are affected. These alterations further impact the vehicle's payload carrying capacity, flight endurance, flight speed and manoeuvrability. Consequently, when selecting the appropriate aerodynamic configuration, it is essential to identify what vehicle characteristics are of the utmost importance. Therefore, obtaining an optimal aerofoil design is achieved by satisfying the desired outputs of an aircraft whilst subjected to applicational constraints and legislation requirements.

2.4.2.1 Shape and profile optimization

The geometric design of an aerofoil is directly influenced by two key components, the shape and profile of the aerofoil. The profile component of an aerofoil is classically used to gain an understanding of the maximum lift characteristics of the aerofoil, which depends on the vehicle's weight. However, the shape component can be further broken down to facilitate the planform and out-of-plane factors of an aerofoil, which are considered the most important aspects that many designers focus on for achieving increased flight functionality. Each of these components contains numerous influential parameters and are usually chosen based on the vehicle's application, fabrication method and aerodynamic configuration. Therefore, maximizing the effectiveness of an aerofoil can be achieved by optimizing these components for a given flight condition, typically the vehicles cruising phase, where most of the flight is spent and hence most of the consumed energy. These geometrical parameters define the

aerofoils abilities but also dictate the specific limitations for a given operational environment. *Table 2-3* reveals the corresponding design components and shows what parameters are associated with each.

All of these geometrical parameters contribute to the performance of an aerofoil; however, the multidisciplinary nature of aerofoil design hinders the complete optimization of each parameter as some parameters are dependent on others. Therefore, a compromise must be found which provides the most optimal result but still satisfies the flight conditions. Research into the optimization of aerofoil design, specifically the aerofoils of UAV's, has enhanced vehicle performance, functionality and applicational use.

Authors such as [40] proposed to obtain the most optimal aerofoil design for a High-Altitude Long Endurance (HALE) UAV. The authors of this research aimed to maximise both the lift-to-drag ratio and lift of an aerofoil whilst minimising its relevant pitching moment. The implementation of a multi-objective optimization technique and Navier-Stokes equation solver allowed the authors to set up the optimization problem in a manner that offered the best results for the intended application. The use of a Bezier curve technique parametrized the aerofoils lower, and upper surface curves whilst, the sweep and taper ratio parameters were added to reinforce the optimization. Outcomes of this research showed a Pareto front of the optimization problem and revealed sixty-five possible solutions for the aerofoil configuration. Findings revealed a linear dependency for the lift force and lift-to-drag ratio, which allowed the authors to ascertain the utmost performance characteristics of the aerofoil for minimal pitching moments.

Additional research shown in [41] approached an aerofoil design optimization through a MATLAB tool and an aerodynamic solver named XFOIL. This research defined the aerofoil through a combination of PARSEC and Bezier-curve parametrisation functions which described the camber line and thickness distribution, respectively. The formation of an objective function was used to achieve an aerofoil design that exhibited low pitching moments of an aft-swept wing. The authors aimed to achieve the maximum aerodynamic performance of a UAV aerofoil that operates at a Reynolds number of $Re = 5x10^6$. The execution of a genetic algorithm for this problem provided results that revealed a negative relationship between the aerofoils maximum thickness and lift-to-drag ratio. These observations confirmed the behaviour of aerofoils operating at low Reynolds numbers and enabled the selection of a suitable configuration that provided the best outcomes for the author's application.

Table 2-3: Arrangement of geometrical parameters associated with an aerofoil

Profile	Planform	Out-of-Plane
Camber	Sweep	Twist
Thickness	Span	Dihedral
Leading edge radius	Chord	Spanwise bending
Upper surface	Taper ratio	
Lower surface	Aspect ratio	

2.4.2.2 Aerofoil morphing

Due to the manufacturing capabilities of UAV's, the design and optimization of an aerofoil are typically set to the vehicle's cruise flight condition, which corresponds to the maximum performance gain. However, with the diversity of UAV applications and aerodynamic configurations, flight conditions and flight phases are unpredictable. These uncertainties hinder a predefined optimal design and thus require a different approach for attaining maximum performance. Research into aerofoil morphing has revealed some innovative techniques that have enhanced the capabilities of vehicles for many flight conditions. This strategy achieves improved performance by constantly modifying specific aerofoil parameters during flight.

The most common morphing parameters are the aerofoils camber and span, as they yield a more significant influence on the aerofoil's performance at varying flight velocities. Research has revealed several methods and conceptual designs for achieving aerofoil morphing. Authors in [42] showed the significance of trailing edge morphing for various flight conditions of an FW UAV. The authors implemented a Fishbone Active Camber (FishBAC) morphing strategy to aid the vehicle's lift coefficient, which ultimately increases vehicle functionality. Outcomes of this research demonstrated the competency of aerofoil morphing, and the findings illustrated improved lift forces with reduced drag.

Further research shown in [43] proposed to design a novel morphing control surface camber flap by employing piezoelectric Macro Fibre Composite (MFC) actuators as opposed to servo-based actuators. By implementing a bimorph flap, tip deflection occurred in both directions, which allowed for an increase and decrease in lift. After wind tunnel experimental setups, and suitable computer analyses using the aerodynamic program XFOIL, results revealed superior characteristics for MFC actuators as opposed to servo actuators. These findings were apparent in the shape conformity investigation, which resulted in higher lift values and appreciable lift-to-drag ratios for MFC actuation. Along with better reliability and reduced spatial footprint, the MFC actuator requires less operating power and has orders of magnitude better bandwidth capabilities [43]. In conclusion, the aerodynamic efficiency benefits from the employed MFC actuator; thus, by adopting this concept for UAV vehicles that require lift force variations, overall flight performance, and endurance can be improved.

2.4.3 Aerodynamic analysing programs

The rapid growth of the UAV industry has led to significantly improved aerodynamic analysing programs, which are typically used to aid the aerodynamic design and control design of unmanned systems. These tools have evolved into robust and accurate software packages that are capable of analysing advanced aircraft configurations to ensure flight functionality before vehicle fabrication. These programs are released under the General Public License (GNU) and specifically state that there is no guarantee on results. However, research such as [44] has provided performance comparisons for programs such as Athena Vortex Lattice (AVL) and XFLR5 versus known CFD solvers. Findings of this research have revealed minimal deviation between the two analysing platforms for lift, drag and moment curves. These discoveries validate the use of these programs as a reliable and accurate aerodynamic analyser for UAVs and aerodynamic surfaces.

2.4.3.1 AVL

The AVL program is an advanced aerodynamic and flight dynamic analyser for rigid aircraft configurations. Initially established by Mark Drela of MIT in 2004 [45], AVL has become a useful tool for gaining valuable information on various aerodynamic characterises of a given airframe. By implementing an extended vortex lattice model together with a slender-body model, AVL is capable of performing tasks such as dynamic stability analysis and trim calculations.

2.4.3.2 XFLR5

XFLR5 is remarkably similar to AVL in terms of its algorithms methodical approach; however, this platform was developed from the original XFoil code. Mainly implemented for aerofoils operating at lower Reynolds numbers, XFLR5 makes use of the Lifting Line Theory (LLT) in conjunction with a Vortex Lattice Method (VLM) and 3D Panel Method to perform its solution. This program offers a greater variety of graphical results which noticeably aids the users' experience. XFLR5 also incorporates a stability and sensitivity analysis that enables designers to determine the longitudinal and lateral stability modes of their vehicles. These outcomes are critical for control design and ensure natural damping is achieved.

2.5 Propeller propulsion of a VTOL UAV

The progression of UAV systems within modern applications has been considerably influenced by the precision control and effortless implementation of propeller-based propulsion. The execution of propeller setup strategies for UAV design is critical for attaining the necessary thrust of various aerodynamic configurations and ensures controllability at different flight conditions. The propeller is a simple component that impacts the vehicle's capabilities similar to the vehicle's aerofoil, where several performance parameters are responsible for maintaining vehicle functionality. The propulsion system on a UAV is only as effective as its components, and their relationship with each other. Therefore, enhancing the UAV's capabilities can be achieved through the optimization of the propeller's geometrical parameters, configuration, and setup. However, prior to attaining this desired propeller design, one must first grasp the theory behind propeller aerodynamics.

2.5.1 Propeller Theory

Propeller theory is an integral field of study, and its significance is vital to the success of the UAV industry. The propeller is one of the main components that directly impacts flight characteristics of an aircraft; therefore, understanding the theoretical background and fundamental principles is an indispensable step to optimizing a propulsion system. From the research given by [46] and [47], there exist three distinct methods for numerically determining the overall performance and effectiveness of a propeller. All these methods abide by the fundamental principle described by *Equation 2-1* and define a propeller based on its geometrical parameters.

$$Propulsion = Thrust \times Velocity \qquad (2\text{-}1)$$

2.5.1.1 Integral momentum theory

A theory that conceives the propeller as an actuator disc, which rotates at a given rate, whereby a pressure difference is apparent across the region. This concept requires specific assumptions to further breakdown the complexities of propeller aerodynamics. After applying these assumptions to the fundamental principles of propulsion, a resultant thrust force can be expressed as a function of pressure difference, disc area and flight velocity, as shown by *Equation 2-2*.

$$T = A_{disk}(p_2 - p_1) = \rho_{air} A_{disk} v_i v_\infty \tag{2-2}$$

Where v_i and v_∞ represents the induced velocity across the propeller and the atmospheric velocity, respectively. The assumptions also detail a relationship between these velocities, given by *Equation 2-3*.

$$v_\infty = 2v_i \tag{2-3}$$

By noting this velocity relationship, the propellers induced power P_i can be determined by *Equation 2-4*, which represents the change in kinetic energy of the fluid across the propeller.

$$P_i = T(v + v_i) = T^{\frac{3}{2}}\sqrt{2\rho_{air} A_{disc}} \tag{2-4}$$

Therefore, a correlation emerges which relates the thrust coefficient C_T to the induced power coefficient C_{Pi} by *Equation 2-5*.

$$C_{Pi} = \lambda C_T = \frac{C_T^{\frac{3}{2}}}{\sqrt{2}} \tag{2-5}$$

According to momentum theory, the induced power P_i constitutes to the majority of energy consumed; however, there is a secondary component of the power required for flight. This unexpected component is typically referred to as the profile power P_o, which is the power needed to overcome the profile drag associated with the propellers blade shape. A figure of merit M value for the ratio of induced power to profile power can be determined from *Equation 2-6*, which reveals a measure of the propeller's efficiency and effectiveness.

$$M = \frac{P_i}{(P_i + P_o)} = \left(1 + \frac{C_{Po}}{\lambda C_T}\right)^{-1} \tag{2-6}$$

2.5.1.2 Blade element theory

A method of modelling a propeller by analysing a dimensional strip of a foil rotating through space. The strip is assumed to be rigid due to the centrifugal forces, and the use of small-angle approximations is accepted. Integration of the propellers span-wise elementary forces enables key dimensionless parameters to be determined, namely the inflow λ and solidity σ factors, which are essential to this theoretical breakdown and are given by *Equation 2-7* and *Equation 2-8*.

$$\lambda = \frac{(v_c + v_i)}{nR} \tag{2-7}$$

$$\sigma = \frac{blade\ area}{disc\ area} = \frac{Ncr}{A_{disc}} \tag{2-8}$$

This theory makes use of a relationship between the power and torque of a propeller, for which the differential power coefficient dC_p can be represented by *Equation 2-9*.

$$dC_P = dC_Q = dC_{Pi} + dC_{Po} = \frac{1}{2}\sigma C_L \phi r^3 dr + \frac{1}{2}\sigma C_D r^3 dr \qquad (2\text{-}9)$$

Where dC_{Pi} and dC_{Po} are the associated induced and profile differential power coefficients, respectively. Integrating *Equation 2-9* with respect to the propeller's radius r returns an approximated representation of the power coefficient C_P by *Equation 2-10*.

$$C_P = k\lambda C_T + \frac{1}{8}\sigma C_{Do} \qquad (2\text{-}10)$$

Assumptions of uniform flow and a constant profile drag coefficient are made. Therefore, an empirical factor k is applied to the first term to account for additional tip losses.

2.5.1.3 Dimensional analysis

An analysis type for determining the design parameters of a propeller through the implementation of the $[MLT^{-2}]$ method. Applying this technique leads to several performance coefficients which are considered by many industry leaders to be the basis for propeller performance data. After some simple manipulation, the propellers thrust force can be given by *Equation 2-11*.

$$T = C_T \rho n^2 d^4 \qquad (2\text{-}11)$$

Where the thrust coefficient C_T is an expression of the propellers Reynolds number Re, Mach number at the blade tip M_{tip} and the advance ratio J. The variables n and d resemble the propellers rotation speed and diameter, respectively. *Equation 2-12* below shows the advance ratio of a propeller, which is a non-dimensional number that expresses the linear distance the propeller travels in one revolution.

$$J = \frac{v}{dn} \qquad (2\text{-}12)$$

The torque Q and power P equations are derived using the same dimensional technique and reveal the following relationships by *Equations 2-13* and *Equation 2-14*. The overall propeller efficiency $\eta_{propeller}$ is also shown in *Equation 2-15*, and the term v represents the propellers axial velocity.

$$Q = C_Q \rho n^2 d^5 \qquad (2\text{-}13)$$

$$P = C_P \rho n^3 d^5 \qquad (2\text{-}14)$$

$$\eta_{propeller} = J\left(\frac{C_T}{C_P}\right) = \frac{Tv}{2\pi nQ} \qquad (2\text{-}15)$$

2.5.2 Propeller setup

The aerodynamic fundamentals and theoretical principles of propeller design revealed the importance of certain geometric variables and showed the influence they have on a systems thrust generation, power consumption and efficiency. This basic understanding allows the propulsion system to be studied from a setup strategy standpoint

that ensures optimal thrust values is achieved with the necessary controllability for a given application. A propulsion setup strategy is a standard method of gauging vehicle functionality and also outlines the overall propeller configuration for confirming compatibility with the other propulsion components.

2.5.2.1 Pusher versus puller propellers

Research in [48] proposed to investigate the potential improvements a pusher propeller has on the propulsion system of a multirotor UAV. This study conducted an experimental analysis of various propeller designs to ascertain the maximum thrust values of each. The investigation was set up by implementing a disk loading sensor for thrust measurements whilst a 3S Lithium Polymer (LiPo) battery was utilized for power. The use of a Pulse Width Modulation (PWM) control signal for the Electronic Speed Controller (ESC) with incremental pulse width steps of $100\mu s$ provided the results.

Findings showed that pusher propellers improved the efficiency of the propulsion system by approximately 3% for disk loadings between $25\ N/m^2$ and $120\ N/m^2$. The same author proposed to conduct a secondary analysis that determined maximum thrust and efficiency for a specified number of propeller blades. Results revealed that two-bladed pusher propellers had an increase in efficiency and thrust as opposed to the three-blade pusher variants. These results were backed by outcomes of [49] and provided an effective measure on propeller performance for VTOL UAV's as they expose the optimal setup in terms of efficiency for the given propeller designs.

2.5.2.2 Coaxial versus single propellers

The same author of [48] experimented with coaxial propeller setups and aimed to determine the performance gain when implementing this approach. The experiment featured four different coaxial setups that varied in spacings from a conventional configuration to a $150\ mm$ distance. These variations allowed the investigation to benefit from a broader set of results that provided greater accuracy and negated any inconsistencies. The same two-bladed pusher propeller was used for each test, and the execution was identical to the previous. Outcomes revealed a greater efficiency and maximum thrust generation from the conventional contrarotating configuration. From these findings, the authors suggested that coaxial spacing larger than $80\ mm$ did not impact the performance of the propeller; however, spacing less than $35\ mm$ significantly reduced efficiency and yielded increased vibration on the motor arm. Although the coaxial setup is an effective means of producing higher torque and minimizing swirl losses in the slipstream, they require double the motors, hence double the weight, as compared to single propeller alternatives. These observations were backed by [49] and concluded that two-bladed single pusher propellers are best suited for VTOL UAV's as they offer higher thrust-to-weight ratios and are noticeably better for controlling.

2.5.2.3 Influence of propeller arrangement

Due to the substantial payload carrying capacities of modern UAV systems, propeller thrust generation and control has become a distinguished influence in UAV design. This has meant propellers are required to rotate at higher speeds and at faster response times. However, this increase in rotation intensity significantly impacts the generation of aerodynamic vortices at the extreme tips of the propeller blades. These vortices, dependent on the

size and rotation rate of the propeller, can negatively affect the power consumption and thus decrease the overall efficiency of the vehicles flight.

The research conducted in [50] proposed to investigate how these vortices are generated based on rotor-to-rotor interactions, and the authors also explored what measures could be implemented, with the purpose of avoiding this undesired effect. It was evident through experimental results that thrust coefficients of the propellers were independent of the arrangement distances. This outcome also demonstrated a reduction in thrust fluctuations as propeller separation distance increased. The authors further examined the aeroacoustics for rotor interaction and revealed a dramatic increase in noise level as the separation distance decreased. Findings of this research suggested that once the rotor-to-rotor separation distance became greater than twice the diameter of the propeller, the aeroacoustics and performance became null in void. These results provided the necessary information for propulsion system design and multirotor configurations.

2.6 Multidisciplinary Design Optimization

An MDO is an optimization method that allows conflicting design objectives to be solved numerically based on the various disciplines of study. The most common architectures of MDO used for aircraft design include the gradient-based and stochastic search algorithm optimization techniques [51]. Both these techniques offer an array of capabilities that are pertinent to aerodynamic analyses, and their distributed nature allows the problem to be partitioned to form a more comprehensive solution. The authors of [52] evaluated the use of these techniques and demonstrated their effectiveness in solving aerodynamic shape optimization problems. A comparison of the results showed no variation in reliability and convergence for single and multipoint optimization for both mentioned techniques. This research is supported by authors of [53], who have shown consistent results in gradient-based optimization for two-dimensional NACA aerofoils.

Although gradient-based methods show promise in aerodynamic optimization, search algorithms, specifically genetic variants, are the preferred choice when solving Multi-Objective Problems (MOP) simultaneously. This is due to the computational efficiency of search algorithms and the tendency of gradient-based optimizers to converge to local minimums before a final solution is achieved. This decision is backed by the research in [54] and [55], which shows the implementation of a genetic algorithm for attaining various optimized aerodynamic designs. These findings validate the proficiency of search algorithms for aerodynamic design optimization and confirm their reliability and consistency for other uses.

Due to the multidisciplinary nature of a UAV system, the preferred genetic algorithm must employ multiple fitness functions for the solution of an optimized aerodynamic and propulsion design. There exist only a few approaches for MOP's, one of interest is the Multi-Objective Evolutionary Algorithms (MOEA's), which possess features that are capable of computing non-linear objectives and constraints along with attaining an unbiased sampling of Pareto solutions [56]. This approach makes use of candidates that represent individuals of a population and are iteratively modified through a heuristic hierarchy, to increase their fitness for the next generation. The aerodynamic and propulsion designs are linked to the Evolutionary Algorithm (EA) through a set of parametrically defined fitness functions and are coupled with constraints for faster and accurate convergence. Over the past two

decades, several MOEA's have been proposed for solving and optimizing aircraft designs. From which, most have been developed based on the original Non-dominated Sorting Genetic Algorithm-II (NSGAII) [57] and Strength Pareto Evolutionary Algorithm (SPEA) [58]. Although the NSGA-II is a dated algorithm, the parametric objective functions used by aircraft designers requires accuracy and reliability over computational time.

The authors of [59] approached the optimization of UAV aerofoils using this NSGA-II technique. By implementing a two-step approach, accounting for aerodynamic and structural conditions, the author's set up an optimization problem to ascertain the maximum endurance of a two-dimensional aerofoil planform whilst minimising its weight. Aerofoil profile constraints such as leading and trailing edge radii were imposed, and the aerofoils camber and thickness were set as variables. The authors applied the NSGA-II algorithm to solve the problem and replaced the analysing tools by a Kriging meta-model for reduced computational time. Results of the algorithm revealed an optimized set of Pareto points on a Pareto front which provided the maximum endurance for the UAV. These outcomes demonstrated the capabilities of this algorithm and showed potential for optimizing other aerodynamic parameters.

The appropriate algorithm for this research needs to be accessible and robust enough to handle the aerodynamic and propulsion optimization of a UAV design. Therefore, the chosen algorithm is the elitist Genetic Algorithm (GA), which is implemented in MATLAB's optimization toolbox and defined under the 'gamultiobj' function. The elitist GA is a variant of the NSGA-II and predominantly favours individuals with better fitness rank for increased population diversity.

2.7 Mathematical modelling of a UAV

As with any unmanned system, mathematically modelling the dynamics is essential for representing and validating the control behaviour of a system before deployment in the physical world. The operational characteristics of UAV technology requires the modelling of all dynamical forces and resultant torque's experienced by the vehicle. This process is essential for achieving autonomous flight and is implemented within the vehicles control architecture to ensure the correct propulsion forces are applied at different flight conditions.

2.7.1 Co-ordinate reference frames

There are three distinct coordinate systems for which the dynamics of a multirotor UAV system can be modelled, namely Euler angles, quaternions, and vector rotations. These methods are used to define the orientation and displacement of a fixed body from an initial point to a final one in a given domain. The Euler angles approach is the most common method of establishing a coordinate system for aerial robotics, as it describes the orientation of a body by three successive rotations about the three different axes. Each rotation is denoted by a matrix, for which they are multiplied, and a resulting rotation matrix is established. This defines and links the body of the previous position and orientation to the later one within the earth's frame of reference. Although this method involves simpler mathematics, Euler angles suffer from singularities when subjected to a second angle of zero [60]. Although twelve variations of the Euler angles are available, only one can be pursued for a given model.

2.7.2 Dynamic modelling

Newton-Euler and Euler-Lagrange are the two methods for dynamically modelling an aerial vehicle when using Euler angles as the coordinate frame. The Newtonian approach conserves the linear and angular momentum of rigid bodies to solve the problem and describes the system using individual components. However, the Lagrangian approach applies the translational and rotational energies of the system to describe it as a singular body. Both techniques result in the same solution but in a different style, which signifies the customizability of these approaches.

2.7.2.1 Newton-Euler

The model based on the Newton-Euler formalism, which obtains the differential equations of motion for a rigid body, can be derived from first principles using the fundamental theorem of mechanics and Euler's theorem of angular momentum. The basis of this model is established under the assumption that all forces acting on the vehicle, namely gravitational forces, added-mass forces and dissipative aerodynamic forces, are dependent only on the vehicle's linear velocity and the independent variable, time [61]. *Equation 2-16* shows how the body frame balances the acceleration force mV_B and centrifugal force $v(m\dot{V}_B)$ against the gravitational force $R^T G$ and the total thrust of the propellers T_B [62].

$$mV_B + v(m\dot{V}_B) = R^T G + T_B \qquad (2\text{-}16)$$

In the inertial frame, because the centrifugal force is neglected, *Equation 2-17* equates the acceleration of the body $m\ddot{\omega}$ to the gravitational force G and thrust forces RT_B, where the magnitude and direction of the thrust contribute to the acceleration of the vehicle [62].

$$m\ddot{\omega} = G + RT_B \qquad (2\text{-}17)$$

2.7.2.2 Euler-Lagrange

The Euler-Lagrange model is also derived from first principles as like the Newton-Euler method, but this approach describes the dynamics of the system by two scalars, those being the kinetic and potential energies and the non-conservative forces of the vehicle [63]. *Equation 2-18* states that the total energy produced by the vehicle equates to the sum of the translational E_{ktrans} and rotational E_{krot} kinetic energies minus the potential energies E_p of the system.

$$\mathcal{L}(q, \dot{q}) = E_{ktrans} + E_{krot} - E_p \qquad (2\text{-}18)$$

Equation 2-19 represents the lagrangian equation used to obtain the generalized non-conservative forces and moments of the system. This is achieved by taking the time derivative of *Equation 2-18* with respect to the generalized coordinates q.

$$\frac{d}{dt}\left(\frac{\partial \mathcal{L}}{\partial \dot{q}_i}\right) - \left(\frac{\partial \mathcal{L}}{\partial q_i}\right) = \begin{bmatrix} f_\xi \\ \tau_\eta \end{bmatrix} \qquad (2\text{-}19)$$

The above equations represent the lagrangian form equation and equation of motion of a system, respectively. These equations form the basis to deriving the complete non-linear dynamical behaviour of the aerial vehicle [64].

2.8 Control techniques of a UAV

All robotic systems, despite its operational nature, require some form of control to perform as intended. In terms of aerial robotics, control is required for stabilizing the vehicle during the various flight modes. Although UAV control is dependent on the differential equations and dynamics of a mathematically modelled system, it is vitally important to understand the implications of different control architectures.

2.8.1 Linear and Non-Linear feedback control systems

Due to the unique dynamics of UAV systems, control has become highly non-linear when aggressive and rapidly changing operations are required, such as the transition from VTOL hover mode to FW flight mode or when attitudes exceed the minimum angles of attack. Non-linear controllers perform significantly well in a specified operating region and consider the true dynamics of the system which account for nonlinear aerodynamics and kinematic effects, actuator saturation and rate limitations [65]. However, despite the performance of non-linear controllers, linear controllers are still favoured in the UAV industry. This is partly due to the simplistic nature of linear controllers but more so due to the accurate models generated by linear approximations, which are based on countless wind tunnel investigations and measurements from numerous academia and industry leaders [66].

Nevertheless, linear controllers can be utilized within a non-linear system through a linearization process. This form of architecture is achieved by exploiting multiple linear controllers for each horizontal, vertical, and transitional flight modes. This method involves dividing the flight envelope into smaller partitions, whereby each region is linearized about the corresponding steady-state operating point of the UAV's dynamics [65]. However, linear controllers implemented in this fashion are subjected to a limited domain of stability and are based on restrictive assumptions [61]. These limiting conditions, along with an inadequate robustness response from wind sensitive perturbations, of lightweight and small-scale UAV's, becomes a restrictive control method for hybrid VTOL vehicles.

It is understood that both forms of linear and non-linear control architectures have limitations that hinder their implementation, design, and robustness. However, the selection of a controller can become a methodical process once flight conditions and applicational constraints are applied. Thus, control design can become purely based on the mission specifications and environmental factors exposed to the vehicle. There are two main linear controllers, namely the Proportional-Integral-Derivative (PID) and Linear Quadratic Regulator (LQR), that are applicable to VTOL UAV's operating as a transport vehicle. These laws have been extensively researched, and thus utilized in several institutional and commercial projects over the past decade.

2.8.1.1 PID controller

The PID controller is considered the most common linear controller, due to its simplistic integration and reduced design time. This controller utilizes proportional, integral, and derivative gains which are determined through

empirical tuning to manipulate the performance of the system to a desired state of response. The gains can also be estimated to minimise tuning using the Ziegler and Nichols method [65]. Because PID control is a form of linearized control and is only applicable for Single Input Single Output (SISO) systems, independent PID controllers can be used for the implementation of a non-linear system through feedback linearization. The controller makes use of PID, PD and P controllers, to allow for altitude control, attitude control and velocity control, respectively. This adjustability offers incredible opportunities as it can be customized per vehicle configuration. The general mathematical form of the PID controller is given by *Equation 2-20*.

$$u(t) = k_P e(t) + k_I \int_{-\infty}^{t} e(t)dt + k_D \frac{de}{dx}(t) \qquad (2\text{-}20)$$

Where $u(t)$ is the control signal, $e(t)$ is the tracking error and k_p, k_i, k_d are the corresponding proportional, integral, and derivative gains. This type of controller has been implemented in many UAV configurations and allows seamless execution such as in [67] and [68]. Authors of [69] developed and designed the control for a tilt-wing UAV during low-speed manoeuvring, and revealed that through a combination of PID controllers, monitored by a Controller Distribution (CD), sufficient response times and minimal state error was achieved for vertical, horizontal and transitional flight modes. These results demonstrate the capabilities of PID controllers for complex tilt-wing applications, which illustrates the potential when implementing multiple controllers for hybrid vehicles.

2.8.1.2 LQR controller

This form of control is linearly implemented and uses a control input to minimize the performance index of a given mission. This index is given by *Equation 2-21* and is subjected to *Equation 2-22*.

$$\Gamma = \frac{1}{2} \int_{t_0}^{t_f} [\, x^T(t)Qx(t) + u^T(t)Ru(t)\,]dt \qquad (2\text{-}21)$$

$$\dot{x}(t) = Ax(t) + Bu(t) \qquad (2\text{-}22)$$

Where $x(t) \in \mathbb{R}^n$ and $u(t) \in \mathbb{R}^m$ are the state vector and control input vector, respectively. A and B form the systems matrix and control influence matrix respectively, whilst R and Q are real positive weighting matrices. The solution of the general matrix differential Riccati equation provides a Riccati matrix that can be attained and applied to the control signal, which is given by *Equation 2-23*.

$$u(t) = -R^{-1}(t)B^T(t)P(t)x(t) \qquad (2\text{-}23)$$

Where $P(t)$ is the aforementioned Riccati matrix. The LQR controller benefits from the selection of weighting matrices applied to the control signal. This aids the controller's adjustability and is based on Bryson's trial-and-error rule. LQR controllers are robust with respect to process uncertainties and have heightened capabilities for handling multiple actuators of complex dynamics, as seen in research given by [70] and [71].

The research shown in [72] proposed to investigate the differences between a model-based controller and a Model-Free Controller (M-FC) when implemented within a tail-sitter VTOL UAV during different flight modes. A scheduled LQR architecture was used for the model-based controller, and a continuous adaptive controller was employed for the M-FC. The feedback response of these controllers for the vehicles hovering phase revealed a compromised LQR controller when wind perturbations were apparent. The corresponding M-FC provided greater

accuracy for its state estimation errors which significantly improved the vehicle's stability during these disturbed conditions. However, due to the high dynamic sensitivity of the transition phase, the M-FC became computationally expensive and showed weakness in its estimation values. This resulted in superior controllability for the LQR controller. Due to the complicated design and implementation process of an M-FC, a model-based control architecture was the preferred choice for this vehicle setup and overall best suits hybrid VTOL UAV configurations.

2.9 Summary of Chapter 2

The literature attained in this chapter detailed the impact of UAV and FDM technologies within modern civilization. This knowledge offered valuable insights towards implementing UAV's for biopharmaceutical delivery and also revealed some of the current strategies and designs used by existing organizations. This chapter also showed the theoretical principles of propeller-based propulsion and aerodynamic fundamentals, intending to provide a broader understanding of UAV operations for VTOL and FW flight phases. The literature on UAV design and optimization methods such as MDO offered critical information for achieving a more functional design. A basic overview of the different mathematical modelling procedures and control techniques used in many UAV systems was also documented in this chapter.

3. DESIGN AND OPTIMIZATION OF THE AIRSLIPPER UAV

The design of a UAV can become a complicated process due to its highly mechatronic nature and multidisciplinary construction. Performance characteristics of an unmanned vehicle are typically evaluated by the degree of compatibility between two main aspects, the aerodynamic and mechatronic designs. These influential elements can be further broken down to incorporate the stability, controllability, and manoeuvrability of the various aerodynamic surfaces, along with the electronic propulsion, and control system designs. Each of the corresponding designs are responsible for attaining a certain quality and thus significantly contribute to the effectiveness of the vehicle within its applicational constraints. These design aspects are unique to a systems framework arrangement and are subject to the operational requirements, which may necessitate specific strategies to accommodate practical validation.

3.1 Design approach

The preliminary design approach of a UAV is an essential step that considers external factors for achieving the desired outcome. The design approach used in this research reflected the medical aid delivery application and fabrication method to assist the capabilities of the completed design. Although these design tactics and approach strategies may not directly influence the performance of a UAV, other factors such as component reliability, flight accuracy, mechanical robustness and part replaceability aid the design process and ensure a feasible implementation.

3.1.1 Design for medical aid delivery application

The implementation of UAV's for expedited delivery has grown into an exciting industry that has endless possibilities. Developments in this technology have made transporting supplies easier, faster, and more economical, especially in last-mile delivery applications. These aspects have shown an increase in the potential for UAV delivery, and several international companies have already started employing these systems throughout their business models. However, utilizing these systems for on-demand medical aid delivery requires these attributes to be accentuated, to ensure safety and compliance with the relevant aviation bodies. The design of a medical aid delivery system must consider aspects such as dependability and consistency, as the transportation of blood, vaccines, and organs is often a matter of emergency and has extreme value.

To guarantee these central characteristics are met, considerations must be taken throughout the vehicle's design and assembly. Factors such as off-the-shelf components and third-party hardware accessories used within the construction of a vehicle, often impact these attributes, and thus determines the performance of such a vehicle. Therefore, when selecting mechanical or electronic parts, it is essential to verify the stated performance features through experimental setups and external testing. This process is used to measure and evaluate the limitations of the associated components before being fully integrated within the UAV. Performing these controlled tests also aids the calibration of the components and verifies their compatibility to ensure that no bottleneck effect is present.

Aside from the physical components, reflection within the UAV's control architecture and firmware must align with regulations and confirm a successful operation in extreme circumstances or environments. Characteristics of

communication protocols and application interfaces are cardinal attributes for assuring firmware robustness and consistency. These operating system qualities must follow conventional practices when implemented throughout the mechatronic design as not to cause unwanted disturbance or interference with other electronics. Along with a self-adjusting correctly designed control architecture, flawless execution is needed for the integration of an always-connected Global Positioning System (GPS). This employment tactic is particularly important in emergencies as a GPS can take several minutes to locate the necessary satellites before becoming operational. The use of an automated system is vital for maintaining optimal flight characteristics at all times and ensures the vehicles power distribution is aligned with the relevant sensors and controllers.

3.1.2 Design for FDM fabrication

Configuring an aerodynamic design for an aerial vehicle is achieved by identifying what type of propulsion system is going to be employed for attaining the outcomes of the application. For this research, the utilization of a tilt-rotor setup is going to provide the best solution for this fabrication method. Therefore, the relevant structures of the aerodynamic configuration need to be accurate, lightweight, and customizable whilst maintaining mechanical stability and resilience to external forces. The approach of fuselage and aerofoil design was traditionally obtained by generating a streamlined shape that conformed to individual moulds and tools associated with ordinary methods. This conventional method, however, led to restricted design choices and limited design variations, as tooling and moulds were expensive and difficult to adapt for a single design. Therefore, the FDM fabrication technique has allowed these aerodynamic structures to be free from conformity which has permitted the fuselage and aerofoil designs to become adaptable and unique for explicit applications.

This form of fabrication allows greater versatility and enables dynamic design strategies, which enhances the mechanical characteristics of the manufactured parts. By alleviating design conformity, this method facilitates further experimentation and development in this industry, which can ultimately extend the proficiency of FDM fabrication in UAV design. Although the FDM approach is capable of creating accurate and structurally stable parts directly from CAD models, obvious setup requirements are needed. This part setup process is a systematic selection of FDM parameters in conjunction with part layout strategies and material choice. Performing the correct setup is essential for attaining a desired part accuracy, strength, and durability. The FDM fabrication method has become synonymous with flexible and rapid prototyping. However, when the part setup strategy is incorrectly performed, certain imperfections and errors create complications and thus compromise the aerodynamic design. Combatting these undesired effects requires the design to accommodate for slight imperfections in the accuracy and smoothness of a part. Although this fabrication method has become a standard process, the equipment and material used can vary depending on the supplier. This incongruity makes each printer unique, and thus printer accuracies vary from $0.1\ mm$ to $0.5\ mm$. It is therefore essential to account for these values when considering tolerances, clearances, and threaded holes.

3.2 Mechatronic design

The inherent mechatronic framework of a UAV system creates an advanced interface between the relevant modules. The interaction of mechanical, electrical, electronic, and computer disciplines provides a foundation for developing an extremely capable system that can perform autonomously, as intended. The mechatronic design of

a UAV follows the typical methodology associated with *Figure 3-1*, where each of these engineering fields contributes toward the operation of UAV technology in their way.
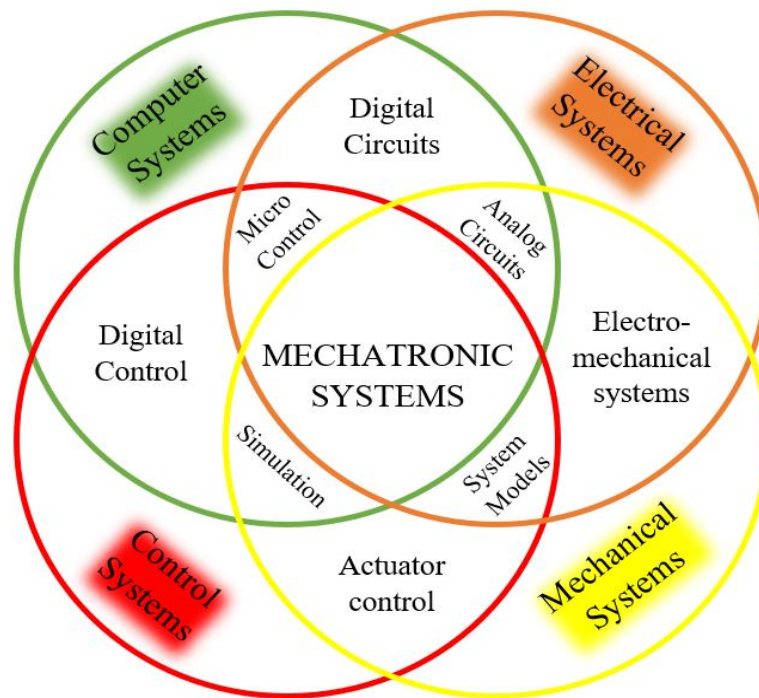
Figure 3-1: Typical mechatronic diagram, adapted from [46]

Figure 3-2 reveals the systematic framework for a typical VTOL UAV design with a tilt-rotor configuration. This diagram follows that of a mechatronic system and combines all factors from the four disciplines. The illustration reveals how aerodynamic control and stability are simplistically achieved and also demonstrates the distribution of electrical power throughout the system. The implementation of analogue and digital command signals within the electronic components allows the relevant subsystems to transfer critical information with the flight controller. This framework of signal manipulation is essential for control response and creates the necessary feedback for operation. The wireless communication network protocols used by the GPS and telemetry components enables the UAV system to perform independently and autonomously with a GCS.

3.3 Preliminary design of UAV modules

UAV component selection is regarded as a comprehensive and intricate design challenge, that requires each submodule to be chosen based on the systems applicational characteristics and constraints. However, the mechatronic nature of UAV design dictates that each component is influenced by the previously selected one, making the design complex yet methodical. Achieving a complete initial design requires a thorough understanding of the design requirements, regulatory compliance conditions and hardware limitations utilized for this UAV. These restrictions provide a foundation for accomplishing the most effective initial design possible that best suits the application. *Table 3-1* shows the applied restrictions for the conceptualized *Airslipper* UAV design, which are based on the medical aid delivery application, SACAA compliance regulatory body, FDM fabrication method and hardware specifications. The values given in the table form the building blocks for the *Airslipper* design and allow for a systematic design of submodules.
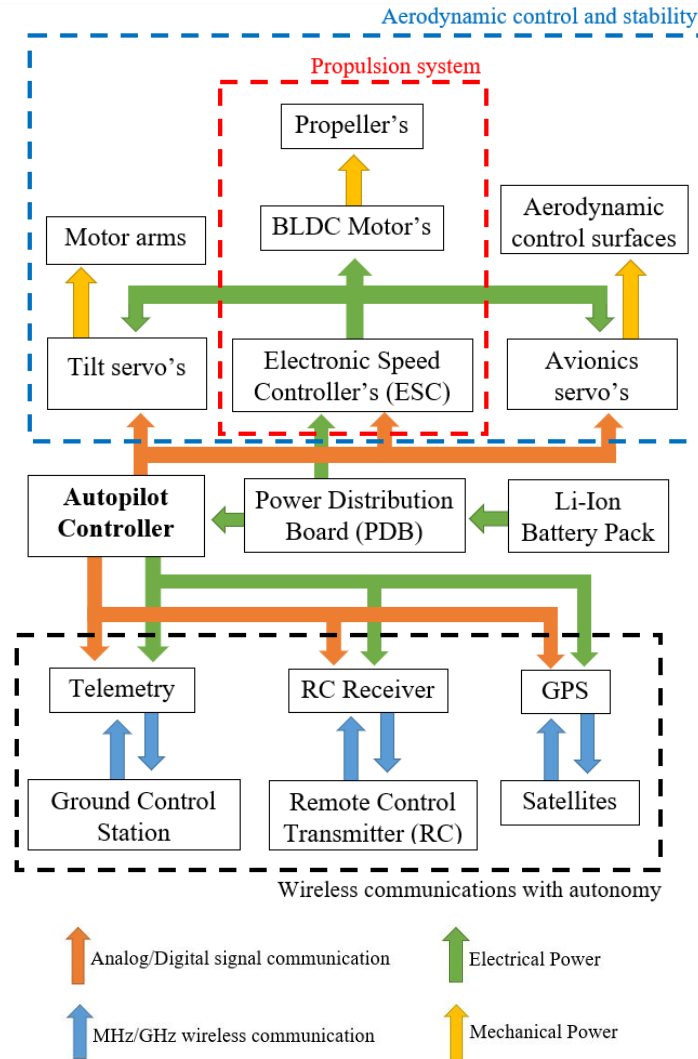
Figure 3-2: Mechatronic framework of a tilt-rotor VTOL UAV design

Table 3-1: Airslipper UAV requirements for the medical aid delivery application

Operational / Design requirement	Value	In accordance with
Minimum service radius	$12000\ m$	Design requirement
Recommended cruise velocity	$28\ m/s$	Design requirement
Maximum operating height	$122\ m$	SACAA Regulations
Operational weight range	$7 < kg < 20$	SACAA Regulations
Maximum system current draw	$140\ A$	Hardware requirement
Electronic system voltage range	$7.4 < V < 44.4$	Hardware requirement
Number auxiliary outputs	8	Hardware requirement
Number motor outputs	8	Hardware requirement
Propeller diameter	$450\ mm$	Design requirement
Maximum motor current	$35\ A$	Hardware requirement
Motor voltage	$24\ V$	Hardware requirement
Recommended aerofoil span	$2.2\ m$	FDM fabrication requirement
Recommended aerofoil reference area	$0.35\ m^2$	FDM fabrication requirement
Recommended aerofoil root chord	$0.28\ m$	FDM fabrication requirement

3.3.1 Propulsion system design

A propeller-based propulsion system design for an aerial vehicle is a highly multidisciplinary process, as seen in Chapter 2. The individual components used in this process are bound via specific parameters that are critical for measuring the vehicles outputs and determining the associated flight characteristics. The following topics reveal the procedure for achieving the initial *Airslipper* UAV propulsion setup and indicate the necessary parameter values for each component. The propulsion design needs to satisfy the requirements of *Table 3-1* whilst yielding the best performance for the application.

3.3.1.1 Propellers

The globalization of UAV's for commercial and industrial use in the past decade has revolutionized propeller designs and efficiencies, which has further improved their thrust maximums. Depending on the application, these components can be manufactured from Carbon Fibre (CF) composites, which provides increased rigidity whilst minimizing the propeller's weight. Although CF is the preferred material, they are expensive compared to their nylon counterparts. However, the performance characteristics of CF propellers make them a superior choice for applications that require the utmost precision and efficiency.

The propeller is considered the most integral component due to its direct influence with the vehicle's propulsion force and is also responsible for providing the necessary control for the different flight modes. The associated parameters of a propeller gauge its functionality and are a result of the propellers manufacturing process, material, and aerodynamic design. The thrust, power, and torque coefficients of a propulsion setup demonstrate the propellers proficiency and are used in a term known as advance ratio . This ratio informs the designer on how competent the propeller is at a given axial flight velocity, which ultimately aids the propulsion design. The selection of a propeller and its parameters must consider the vehicles tilt-rotor transition phase and several other factors that include flight velocity, frame size, weight, and application. *Equation 3-1* reveals an estimated weight given to the *Airslipper* based on its expected design, operation and applicational requirements.

$$W_{estimated} = 100.62 \; N \tag{3-1}$$

This weight needs to be equally distributed across all four propellers $R_n = 4$ whilst accounting for a VTOL thrust-to-weight ratio of $\gamma_{VTOL} = 1.2$. This deliberation yields *Equation 3-2*, which gives the required thrust that each propeller needs to generate for maintaining aerial flight in VTOL mode.

$$T_{VTOL} = \frac{\gamma_{VTOL}(W_{estimated})}{R_n} = \frac{1.2(100.62)}{4} = 30.01 \; N \tag{3-2}$$

As most propeller performance data is unavailable from many manufactures, a value of $\psi = 0.65$ is used for the power-to-thrust coefficient ratio. Therefore, based on the design requirements, the propellers maximum diameter is given as $d < 450mm$, which can be then used to determine the required rotation rate n of each propeller given by *Equation 3-3*.

$$\psi = \frac{(P_{propeller})}{(T_{VTOL})nd} \tag{3-3}$$

For approximation reasons and design purposes, the propeller's power $P_{propeller}$ is equated to the motor's power P_{motor}. This power value can then be calculated by *Equation 3-4*.

$$P_{motor} = P_{propeller} = I_{motor}V_{motor} = 35(24) = 840\ W \tag{3-4}$$

By using the motor power, the propellers rotation rate for VTOL mode can be seen by *Equation 3-5*.

$$n_{VTOL} = \frac{(P_{propeller})}{\psi d(T_{VTOL})} = \frac{840}{(0.65)(30.01)(0.45)} = 95.69\ rps = 5741.67\ rpm \tag{3-5}$$

Therefore, the required advance ratio for VTOL mode can be calculated by using the vehicles climb velocity of $V_{climb} = 2.5m/s$ as seen in *Equation 3-6*.

$$J_{VTOL} = \frac{V_{climb}}{nd} = \frac{2.5}{95.69(0.45)} = 0.058 \tag{3-6}$$

Due to this low advance ratio in VTOL mode, the propeller's efficiency significantly decreases. However, this efficiency changes when the vehicle transitions into FW mode. Given a drag coefficient of $C_{D,vehcile} = 0.7$ for a streamlined body, *Equation 3-7* can be used with the stipulated maximum aerofoil area S and cruise velocity V_{cruise} to determine an estimated aerodynamic drag $D_{estimated}$ value associated with the vehicle.

$$D_{estimated} = C_{D,vehcile}S\left(\frac{\rho_{air}V_{cruise}^2}{2}\right) = 0.7(0.35)\left(\frac{1.225(28)^2}{2}\right) = 117.649\ N \tag{3-7}$$

This drag force can then be assumed to be equally distributed across all propellers. As with the VTOL mode, a thrust-to-weight ratio of $\lambda_{FW} = 1.2$ is implemented for FW flight. This information leads to *Equation 3-8*, which gives the maximum thrust each propeller must produce to ensure stable and steady flight.

$$T_{FW} = \frac{\lambda_{FW}(D_{estimated})}{R_n} = \frac{1.2(117.649)}{4} = 35.29\ N \tag{3-8}$$

The thrust exerted in FW mode yields similar values to VTOL mode. Assuming the propeller power is kept at the maximum, and other parameters are constant, the propellers rotation rate for FW mode flight mode can be given by *Equation 3-9*.

$$n_{FW} = \frac{(P_{propeller})}{\psi d(T_{FW})} = \frac{840}{(0.65)(35.29)(0.45)} = 81.37\ rps = 4882.62\ rpm \tag{3-9}$$

The propellers advance ratio can then be determined in *Equation 3-10*.

$$J_{FW} = \frac{V_{cruise}}{nd} = \frac{28}{81.37(0.45)} = 0.764 \tag{3-10}$$

This new advance ratio signifies an increase in the propeller's efficiency and illustrates the proficiency of these propeller performance parameters.

3.3.1.2 Battery pack

The choice of battery technology used in newer electrically powered industrial and commercial UAV systems is between LiPo or Lithium-Ion (Li-Ion) cells [73]. These lithium-based power storage devices are incredibly power-efficient and possess energy densities that are far more superior amongst all other alternatives. Due to their

manufacturing process and design, these lithium cells are capable of withstanding exceptionally high current loads for prolonged durations. This unique ability increases the C rating associated with these cells, which is paramount for UAV propulsion systems.

Both LiPo and Li-Ion battery technologies have outstanding characteristics for propeller-based propulsion systems. However, the pre-packaged brick-like form of LiPo batteries makes their dimensional size fixed, which further confines their charge capacities. These qualities hinder the selection of an optimal battery configuration and obstruct freedom when designing a compact fuselage. Alternatively, Li-Ion cells are much smaller and are commonly found as singular $3.6\,V$ cells formed into a cylindrical shape. The most ubiquitous type is the 18650 Li-Ion cell, which is fabricated with dimensions of $18\,mm$ in diameter by $65\,mm$ long. The benefit of these cells is apparent when irregular battery packs are required to fit or conform to a given shape. This gives the battery pack increased versatility as the occupied volume can be spatially varied according to the aerodynamic configuration. The advantages of implementing Li-Ion over LiPo is apparent, but the most pertinent is the ability for Li-Ion battery packs to customize the voltage and charge capacity, which can correspond to the application's specifications. This modularity ensures the battery is optimally designed for the intended flight conditions and no energy is wasted.

Designing a lithium battery pack is performed by firstly determining the maximum operating voltage of the propulsion system. This value has a significant influence on the vehicles generated thrust due to its direct relationship between motor and propeller parameters. A higher voltage typically delivers greater power to the propulsion system, but consequently reduces overall flight time. Therefore, a value of $24\,V$, which has total lithium battery cell series configuration of $B_{cell,series} = 6$, should be a reliable voltage for providing sufficient power whilst maintaining acceptable flight endurance. This voltage also falls between the electronic system range and below the maximum motor voltage, as seen in *Table 3-1*.

The following calculations are used to determine the number of parallel cells of the battery pack and hence the total capacity. Based on the requirements, it is assumed that the propulsion system draws the motor's maximum current of $I_{motor} = 35\,A$ for both VTOL and FW modes. These values are accompanied by a climb velocity of $V_{climb} = 2.5\,m/s$ and a maximum cruise velocity of $V_{cruise} = 28m/s$. Noting the vehicles maximum flight range of $R_{flight} = 12\,km$ at the specified flight velocity, *Equation 3-11* reveals the required flight time to achieve this distance.

$$T_{flight,FW} = \frac{R_{flight}}{V_{cruise}} = \frac{12000}{28} = 428.57\ seconds \qquad (3\text{-}11)$$

Calculating the total time required for VTOL mode to reach the maximum altitude of $Alt_{max} = 122\,m$ and back is determined by *Equation 3-12*.

$$T_{flight,VTOL} = (2)\frac{Alt_{max}}{V_{climb}} = (2)\frac{122}{2.5} = 96.8\ seconds \qquad (3\text{-}12)$$

Although these flight times correspond to the respective flight modes, an estimated additional flight time of $T_{flight,Transition} = 120\ s$ accounts for the vehicles transitioning phases. Therefore, the total expected flight time is shown in *Equation 3-13*.

$$T_{flight,TOTAL} = T_{flight,FW} + T_{flight,VTOL} + T_{flight,Transition} = 645.37\ seconds = 10.75\ minutes \quad (3\text{-}13)$$

This total flight time is assumed to have a constant current draw of $I_{motor} = 35\ A$ per motor; therefore, the batteries minimum charge capacity can be given by *Equation 3-14*.

$$B_{capacity,min} = (T_{flight,TOTAL})(I_{motor} x4) = \left(\frac{10.75}{60}\right)(35x4) = 25\ 083\ mAh \quad (3\text{-}14)$$

It is assumed that all control surface and tilt-rotor servo motors draw an equal current of $I_{servo} = 1\ A$ during the vehicles flight period. Thus, *Equation 3-15* can be used to calculate the additional power draw from all eight of these components.

$$B_{capacity,servo} = (T_{flight,TOTAL})(I_{servo}\ x\ 8) = \left(\frac{10.75}{60}\right)(1x4) = 716\ mAh \quad (3\text{-}15)$$

Therefore, adding this value and applying an electrical power loss efficiency factor $\eta_{electrical} = 0.95$, the actual battery capacity can be calculated using *Equation 3-16*.

$$B_{capacity,actual} = \frac{(B_{capacity,min} + B_{capacity,servo})}{\eta_{electrical}} = \left(\frac{25083+716}{0.95}\right) = 27\ 156\ mAh \quad (3\text{-}16)$$

This value demonstrates the battery packs total capacity required to satisfy the necessary flight conditions. Assuming the battery pack consists of 18650 cells, each having a cell capacity of $B_{capacity,cell} = 3000\ mAh$, *Equation 3-17* can determine the total number of battery parallel cells.

$$B_{cell,parrallel} = \frac{B_{capacity,actual}}{B_{capacity,cell}} = \frac{27156}{3000} = 9.052\ \approx 9\ cells \quad (3\text{-}17)$$

By further noting that each genuine 18650 cell has a mass of $B_{cell,mass} = 0.045\ kg$, the total mass of the battery can be determined by *Equation 3-18*.

$$M_{battery} = (\ B_{cell,parrallel}\ x\ B_{cell,series}\ )B_{cell,mass} = (6\ x\ 9)0.045 = 2.43\ kg \quad (3\text{-}18)$$

3.3.1.3 Motors

The advancement in Brushless Direct Current (BLDC) motor design, construction and material selection has significantly improved the performance and efficiencies of this technology. These motors are capable of generating substantial torque values but are also adept at providing extremely high rotation speeds with precision and control. The continual demand for UAV technology has created new research and development opportunities in BLDC production. These improvements have considerably contributed to the successfulness of UAV systems and have enhanced the functionalities of various propulsion designs. The introduction of multiple neodymium permanent magnets in BLDC motors has substantially increased vehicle efficiency and response, which has led to electromagnetism layouts that are commonly found as In-runner and Out-runner variants.

The sizing of a BLDC motor is identified by the stator's dimensions in millimetres, where the first two numbers signify the diameter, and the last two digits reveal the stator's height. These dimensions are an indication of the motor's velocity constant and hence its torque. The velocity constant is what determines the rotation rate of the motor and is typically given as a KV rating, which is then multiplied by the motors supplied voltage to give an rpm value as seen by *Equation 3-19*.

$$n = V_{Battery}(KV) \qquad\qquad (3\text{-}19)$$

The selection of a motor's KV rating is dependent on the vehicles weight, propeller specifications and battery configuration. Knowing this data provides the necessary platform for acquiring a suitable motor and its KV rating. A correction factor of $\varpi = 1.5$ is applied to the KV rating, which can be calculated by *Equation 3-20*. This correction factor considers torque and power loss during operation and assures a sufficient KV rating is attained. *Figure 3-3* shows a simple graphical relationship between motor sizing and vehicle size.

$$KV = \frac{\varpi(n_{VTOL})}{V_{Battery}} = \frac{1.5(5741.67)}{24} \approx 360 \qquad\qquad (3\text{-}20)$$
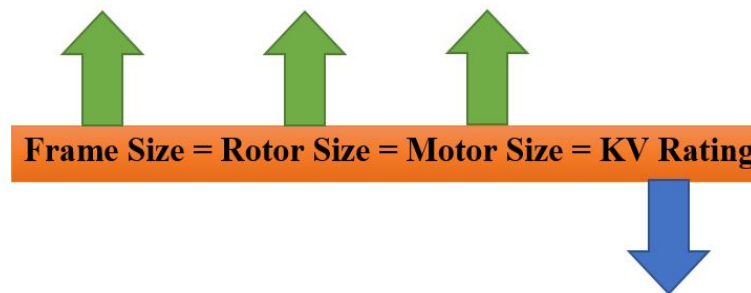
Figure 3-3: Motor sizing selection relationship

3.3.1.4 Electronic speed controller

The ESC is a type of speed controller used for almost all BLDC motors and is fundamentally a microcontroller, consisting of a 32-bit processor. ESC technology typically communicates with PWM signals; however, in recent years, the implementation of faster digital protocols such as One-shot and D-Shot have powerfully impacted their performance. These new and improved protocols use higher sampling rates and faster response times that include features such as telemetry. Commanding these signals is achieved by the controller's firmware, and the most common firmware used in the UAV industry are BLHeli and Kiss. The rating associated with an ESC is based on how much continuous current can pass through the controllers MOSFET's and at what rates it can achieve this. The implementation of electrolytic capacitors is also a gauge of the ECS's capabilities, as they are used as a dampening effect from power spikes generated by the BLDC motors and help reduce electronic noise from cameras and IMU sensors. *Figure 3-4* shows the typical ESC architecture and reveals how each of these circuitries interacts with the BLDC motor and battery, respectively.

Commanding a BLDC motor requires a throttle signal from the UAV's flight controller which gets further processed through the ESC's microcontroller before being sent to the subsequent drive and position circuitry. By utilizing Hall-effect sensors and back EMF, the ESC is able to decode the digital signals and provide the exact

current values to the motors stator for inducing rotation. Depending on the ESC variants, this process operates with an update frequency of $9 < kHz < 75$. These rates are indicative of an efficient controller that can provide precise and accurate current's in a controlled manner. Selection of ESC specifications is dependent on the propulsion systems components and thus must be chosen once all other parts are selected. Given that the motors maximum power rating is $P_{motor} = 840\ W$ at $I_{motor} = 35\ A$, a suitable ESC rating of $40\ A$ should suffice the high current bursts.
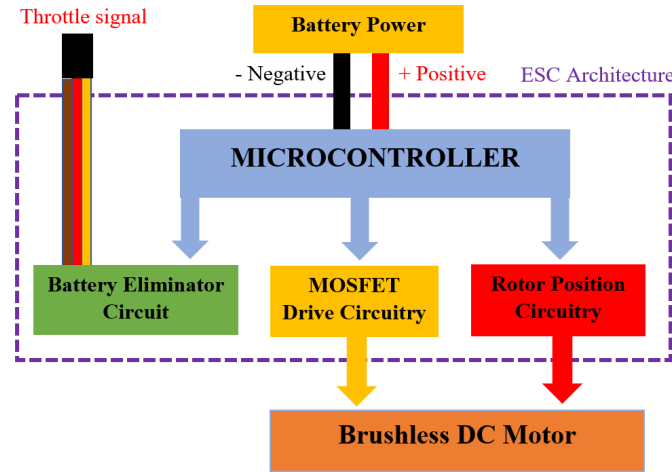
Figure 3-4: Systematic framework of ESC design

3.3.1.5 Calculated Performance for VTOL mode

By focussing around the applicational requirements and initial propulsion system design parameters, an estimated calculation can be conducted on the systems performance in VTOL mode. The approximated vehicle weight, which includes the propulsion system, is used in conjunction with the design variables previously determined. *Table 3-2* displays these values with additional flight information and atmospheric conditions, which is necessary to compute the vehicles range, flight time and power consumption. The calculation was performed by an established online platform called 'eCalc', which is a Dutch-based company with background knowledge in electric propulsion systems [74]. The platform is supported by international brands such as 'Boeing' and 'Airbus', and the creators have several published articles on electric propulsion technology. This experience ensures a reliable and trustworthy service for calculating and evaluating the design performance of electric brushless motor drive systems.

Results of this performance test can be seen in *Figure 3-5*, which reveals motor characteristics at different current values. This figure demonstrates the linear power consumption of the motor with current draw and also shows a peak motor efficiency of $\eta_{motor} = 84.6$ % at $20\ A$. The vehicles estimated range and flight time in VTOL mode are displayed in *Figure 3-6*, which reveals a maximum flight time of $0.218\ h$ with an estimated rate of climb of $V_{climb} = 2.8\ m/s$. *Table 3-3* exposes these performance results and shows some key characteristics associated with this propulsion design. The results of this setup allowed the vehicle to maintain flight in VTOL mode with a thrust-to-weight ratio of $\gamma_{VTOL} = 1.4$ and a specific thrust value of $5.29\ g/W$. These calculated outcomes confirm the design parameter selections and yield results which are appropriate for the application's requirements.

Table 3-2: Input parameters and flight conditions for propulsion system

Atmospheric conditions	
Vehicle elevation	$122\ m$
Air temperature	$25^0 C$
Air pressure	$101.3\ kPa$
General	
Estimated weight of vehicle	$10.2\ kg$
Number of propellers	4
Frame size	$910\ mm$
Battery specifications	
Cell type	*Lithium Ion*
Cell configuration	*6S9P*
Total capacity	$25000\ mAh$
Total voltage	$24\ V$
Depth of discharge	$80\ \%$
ESC rating	
Rated current	$40\ A$
Motor specifications	
Motor constant rating	$360\ KV$
Motor stator size	6008
No load current	$1.4\ A\ @\ 10\ V$
Resistance	$0.05\ \Omega$
Number of magnetic poles	22
Propeller specifications	
Diameter	$450\ mm$
Pitch	$152\ mm$
Number of blades	2
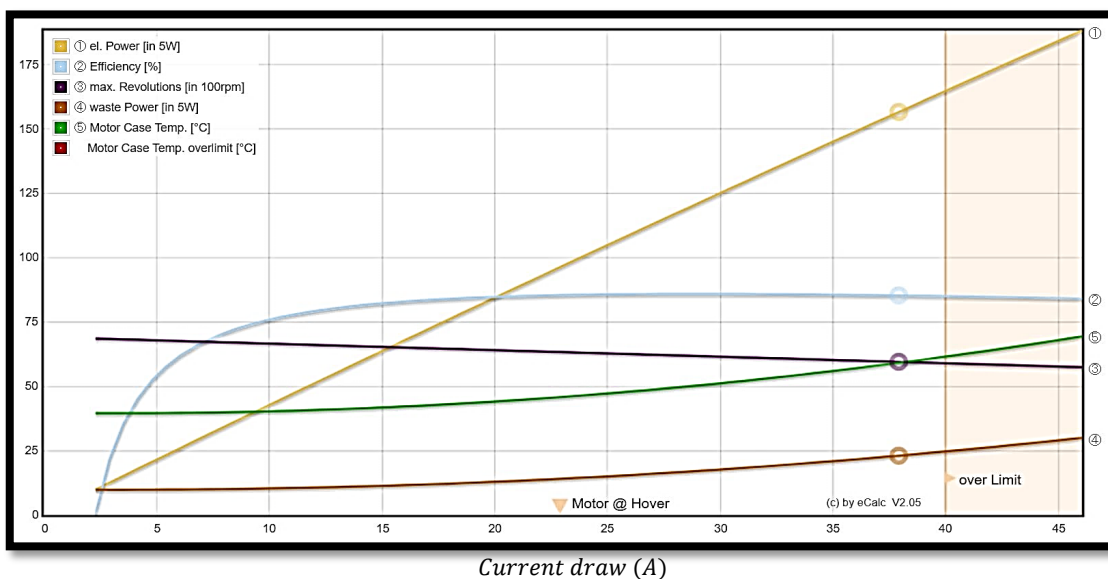
Figure 3-5: Motor characteristics at full throttle in VTOL mode, converted from [74]

Velocity (*km/h*)
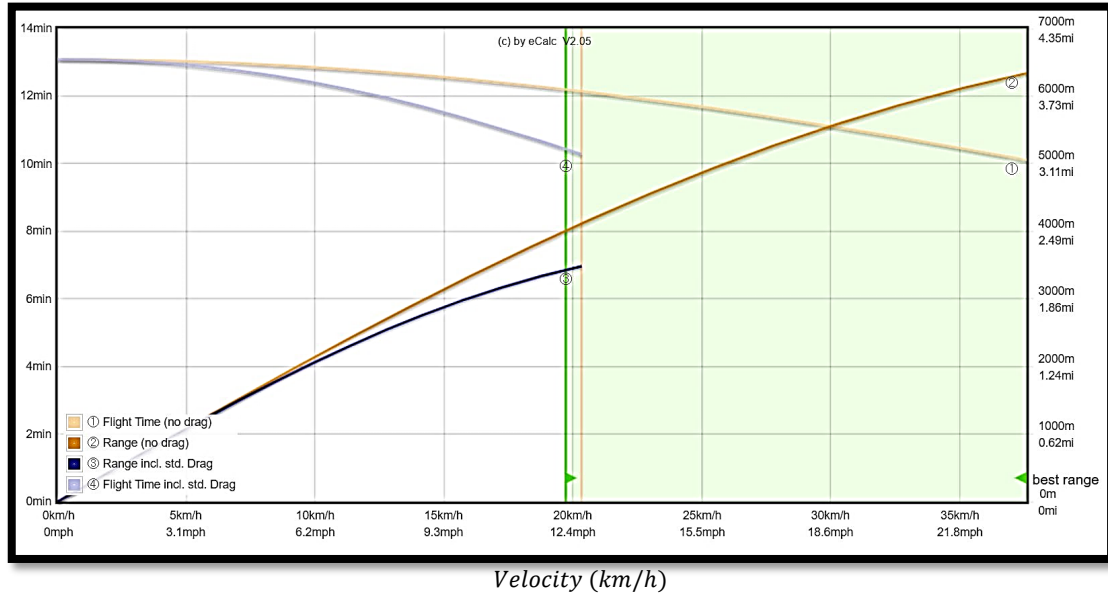
Figure 3-6: Estimated flight range and flight time in VTOL mode, converted from [74]

Table 3-3: Motor and vehicle performance results based on initial input parameters

Motor in VTOL mode	
Battery Load	6.14 C
Current	28.64 A
Voltage	21.02 V
Throttle	79 %
Power-to-Weight ratio	243.2 W/kg
Electrical Power	551.2 W
Mechanical Power	465.3 W
Rotation rate	5621 rpm
Efficiency	84.6 %

Vehicle in VTOL mode	
Max Tilt angle	32^0
Max Speed	38 km/h
Estimated Range	3.48 km
Estimated max rate of climb	2.8 m/s
Flight time	0.218 h
Thrust-weight ratio	1.4
Specific thrust	5.29 g/W
Input Power	1979.7 W
Output Power	1630.5 W

3.3.2 Aerodynamic design

As previously mentioned in Chapter 2, the aerodynamic configuration is directly influenced by the flight characteristics and operational requirements of an aerial vehicle. Due to the on-demand and immediate response required for medical aid delivery systems, achieving VTOL flight with a transition into FW mode is essential for ensuring emergency deployment and extended flight envelopes. This transition phase must be attained aerodynamically through the tilting of propellers and must also account for the payload's importance, so to not cause excessive vibrations or extreme attitudes. Design considerations such as payload accessibility, material sustainability, operation robustness, and vehicle rigidity must form part of this design. Special attention must also be placed on the different modules that make up the final design, and concerns must be mitigated through the particular formerly discussed design approaches. Due to the *Airslipper's* application and deployment strategy, maintenance and repair are vital areas that must be addressed in conjunction with the vehicle's fabrication method and cost in mind. Further emphasis must be placed on the vehicle's size, which must conform to the predetermined propulsion system and legislation standards.

3.3.2.1 Fuselage and motor arms

The fuselage of an aerial vehicle that operates in FW mode is typically associated with 'elongated' and 'round'. These terms describe the shape of a body that is aerodynamically stable and efficient. However, the *Airslipper's* design considered in this research needs to accommodate for the FDM fabrication method, tilt-rotor propulsion setup and requirements of an emergency medical aid delivery system. Therefore, as the Li-Ion battery pack is the largest component in the UAV system, an opportunity arises to create a custom battery spatial configuration that conforms to the vehicle's fuselage. This tactic minimizes wasted space and creates a more compact design that can potentially reduce drag and increase vehicle stability. The design used for the *Airslipper* was influenced by a bullet train, which has a slender profile that is suitable for speed whilst maintaining structural and aerodynamic characteristics. *Figure 3-7* shows a rough initial sketch of this design and illustrates the slender fuselage body with four protruding arms for the tilt-rotor propulsion system.
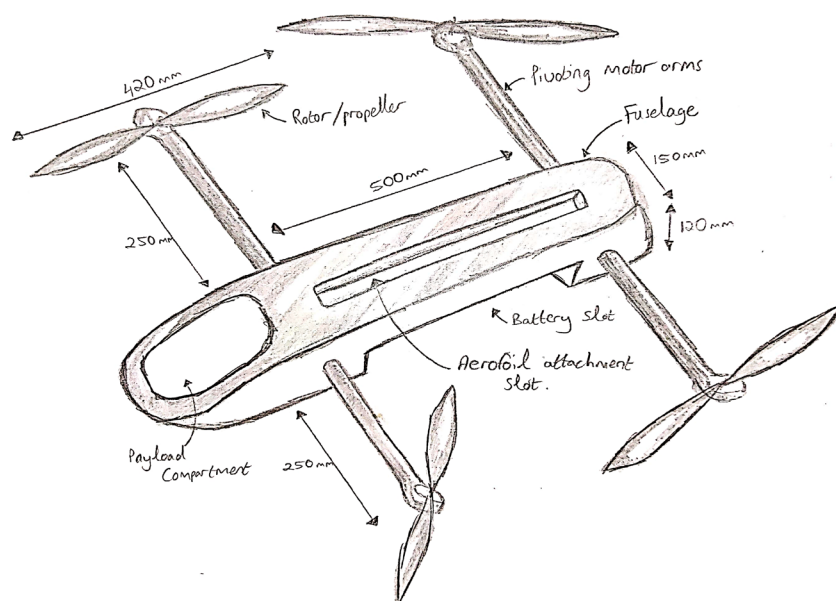
Figure 3-7: Concept of the Airslipper design layout in VTOL mode

A large payload compartment is situated at the front of the vehicle, as this location provides the appropriate accessibility and aids the aerodynamic stability and sensitivity. The conformed battery pack has a dedicated battery slot which is positioned below the electronic compartment. The purpose of this slot enables the battery to be completely detachable to allow for simpler vehicle disassembly and repair. A secondary slot, for the aerofoil, is situated directly atop the fuselage and provides the same benefits as the battery slot. These design features were employed as a result of the FDM fabrication method but mostly contributed to the continuous operation and maintenance of the *Airslipper* UAV.

3.3.2.2 Control surfaces

The control surfaces of an unmanned system are an essential element that enables aircraft stability and control during FW flight modes. Traditional forms of these surfaces are commonly represented by control flaps on the span of an aerofoil, which are actuated in some manner to cause airflow deflection and thus control. Depending on the vehicle's stability derivatives, aerodynamic configuration, and performance characteristics, these flaps may require significant amounts of actuation for increased airflow deviations to maintain steady flight conditions.

As FDM is used as the fabrication method for the *Airslipper's* aerofoil, certain limitations hinder this traditional control flap design strategy. This is due to the compromised structural integrity of an FDM printed wing once slots and hinges are accounted for. Therefore, combatting this challenge required the control surfaces to be placed on the motor arms of the vehicle, making the design unique but functional. By allowing these flaps to hinge on the motor arms, design characteristics such as roll rate and pitch rate can be optimized by modifying the shape, size, and deflection angle of these surfaces. This adjustability is usually restricted on standard aircraft due to control flap placement and the employment of complex mechanics. The implementation of morphing control surfaces was considered in this design; however, the execution of this approach was not possible due to the inadequacies of the fabrication method and actuation force.

3.3.2.3 Aerofoil

An aircraft's aerofoil is purely responsible for providing a sufficient aerodynamic lifting force to counteract the vehicle's mass. Typically used in applications that require extended endurance, this design element allows a vehicle to obtain increased payload carrying capacities with greater flight velocities. As seen in Chapter 2, the shape and profile parameters of an aerofoil have a substantial impact on these characteristics, and when implemented correctly, can enhance the operability of the vehicle.

Since the cruise velocity of the vehicle is constrained to $V_{cruise} = 28\ m/s$ and the aerofoil's root chord is set at $C_r = 0.28\ m$, a suitable profile can be selected that ensures maximum lift-to-drag ratio for increasing the *Airslipper's* endurance. However, before determining the lift capabilities of a profile, it is essential to verify the Reynolds number experienced by an aerofoil section during cruise flight conditions. *Equation 3-21* uses these cruise velocity and root chord values to calculate the maximum Reynolds number of the aerofoil in FW mode, where v is the dynamic viscosity of air at an altitude of $Alt_{max} = 122\ m$.

$$Re = \frac{\rho V_{cruise} C_r}{\mu} = \frac{V_{cruise} C_r}{\upsilon} = \frac{28(0.28)}{1.42x10^{-5}} = 552\,112.67 \qquad (3\text{-}21)$$

This Reynolds number value provides an understanding to what type of aerofoil profile should be selected, and based on the literature attained in Chapter 2; it can be assumed that profiles with reduced thicknesses and increased cambers generate notable performance gains when operating at lower Reynolds numbers. Using this information and a database of aerofoil profiles, the NACA 6412 was determined to be the preferred choice, as it provides a glide ratio above 120 at the specified Reynolds number.

The NACA 6412 is a slender profile with a maximum thickness of 12% at 30% chord and has a maximum camber of 6% at 40% chord. The choice of these profile parameters was strongly backed by the FDM fabrication method, as the profiles thickness and camber are directly proportional to the aerofoils weight. Noting the aerofoils limited area of $S = 0.35\ m^2$ and assuming a spanwise lift coefficient of $C_{L,aerofoil} = 0.65$ for a tapered non-swept aerofoil, *Equation 3-22* can be used to calculate the total lift force of the aerofoil at the specified flight conditions.

$$L = \frac{C_{L,aerofoil} \rho_{air} V_{cruise}^2 S}{2} = \frac{(0.65)(1.225)(28)^2(0.35)}{2} = 109.24\ N = 11.13\ kg \qquad (3\text{-}22)$$

This maximum lift force corresponds to the vehicles estimated weight and thus suffices the fundamentals of aerial flight.

3.3.3 Electronic design

The electronic modules of a mechatronic design are expected to attain the desired communication and response from all contributing components. This process is an essential step for ensuring complete integration and confirms system compatibility. A UAV's electronic framework consists of several vital components that are vital for guaranteeing functionality and safety throughout the vehicles flight modes. These dedicated components are responsible for performing signal and sensor processing, power distribution, battery management and wireless communication. The electronic design is necessary for achieving unmanned operability and forms the fundamental attributes of a UAV that allows for a higher degree of reliability, accuracy, and consistency.

3.3.3.1 Flight Controller

The UAV's Flight Controller (FC) is the brains of the electronic system and is used for analysing sensor data whilst doubling as a signal processor for the mechatronic design. This component is responsible for every command associated with the vehicle's operation and contains onboard sensors such as an accelerometer, gyroscope, and magnetometer, also known as an Inertial Measurement Unit (IMU). Progression of the UAV industry, together with advanced electronic designs, has enabled these components to benefit from faster microprocessors with more integrated memory to allow greater functionality. These technological improvements have critically reduced unexpected latency times between tasks which expands the components abilities to fit different aerodynamic configurations and applications.

Performance of an FC is typically assessed on its features and technical specifications, which is ultimately a measure of computing power and process responsiveness. Additional qualities such as accuracy and repeatability of the IMU and GPS sensors are also an indication of the FC's capabilities. Depending on the design and

implementation, an FC can include On-Screen Displays (OSD), Battery Eliminator Circuits (BEC's), and black-box data logging. These added features are combined with an array of external sensors such as barometers, current sensors, and airspeed sensors to create an advanced controller that has endless versatility.

The *Airslipper's* electronic design considered several FC variations, however, this research settled on the Pixhawk 4 due to its compatibility and interfacing aspects. Based on Pixhawk-project FMUv5 open hardware design, the Pixhawk 4 comprises of a 32-Bit Arm® Cortex®-M7 processor running at 216 MHz with 512 KB ram. This board is manufactured by a company called Holybro and uses the open-source PX4 autopilot firmware from 'Auterion'. With the ability to communicate with companion computers, the Pixhawk 4 is a high-performance controller that provides increased ram capabilities for firmware development. *Figure A-1* shows the interface capabilities of the Pixhawk 4 and gives information on its size.

3.3.3.2 Power distribution and battery management

The power distribution and battery management associated with mechatronic systems have become a crucial consideration for maintaining safety and reliability. This is a result of several electronic components becoming sensitive to voltage and current deviations due to their delicate integrated circuitry. The use of a Power Distribution Board (PDB) within UAV technology has significant advantages, as it allows accurate power regulation across the multiple external components and sensors. With a constant voltage being supplied by the UAV's battery, BEC's within a PDB are necessary to satisfy the individual electronic power requirements.

Due to the standardized operating voltages of familiar UAV sensors, BEC's typically output voltage values of $3.3\ V$ and $5\ V$. The Holybro PM07 PDB used for this research is compatible with the Pixhawk 4 FC and features voltage pads for up to eight ESC connections. This PDB has an input voltage range of $7 < V < 51$ at a maximum amperage rating of $140\ A$. This power module can regulate battery consumption during flight and is also capable of communicating battery data to the FC through telemetry.

A Battery Management System (BMS) can be found in almost all battery-powered electric vehicles and is used as an interface manager between the battery pack and the components using its power. The implementation of a BMS within the *Airslipper's* Li-Ion battery pack provides the essential task of safely charging the individual cells. Features of a BMS typically include constant current/voltage charging and voltage balancing, which allows the vehicle to maximise the full voltage of the battery without damaging the pack.

Depending on the electronic design, a BMS can monitor several critical parameters of a battery pack, which aids the pack's effectiveness and overall health. *Figure 3-8* shows a basic illustration of how a BMS measurement controller can be used to collect and analyse the batteries data to optimize the performance of the system. This figure reveals how the batteries thermal behaviour and State of Charge (SOC) can be ascertained through the identification and measurement of each cell voltage. This method of power management significantly increases the functionality of the UAV whilst increasing the life cycle of the battery.
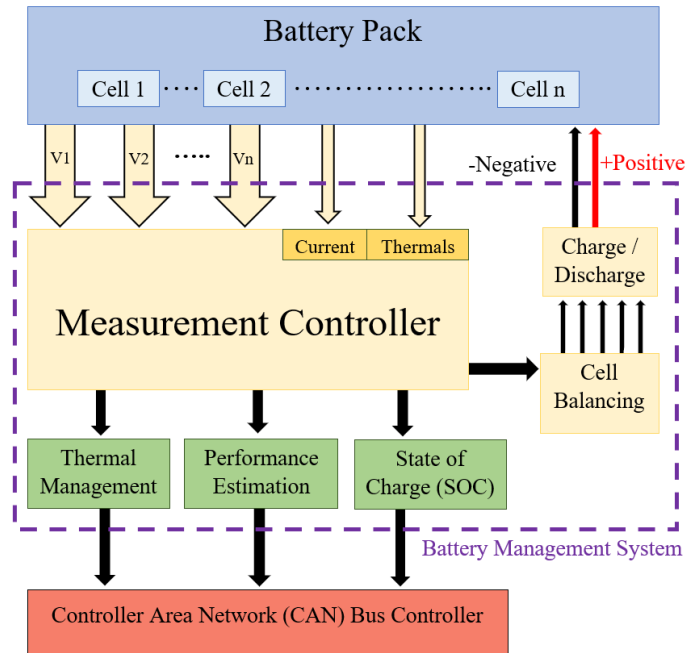
Figure 3-8: Systematic framework of BMS design

3.3.3.3 Wireless communication

Achieving the full capabilities of an unmanned aerial vehicle requires a continuous and stable connection of wireless communication between a Ground Control Station (GCS) and GPS satellite. The appropriate setup of a UAV's telemetry modules allows the vehicle to operate independently of human interaction which ensures position and control is maintained. *Figure 3-9* shows the fundamental process for attaining autonomous flight and reveals how each communication layer operates with each other.
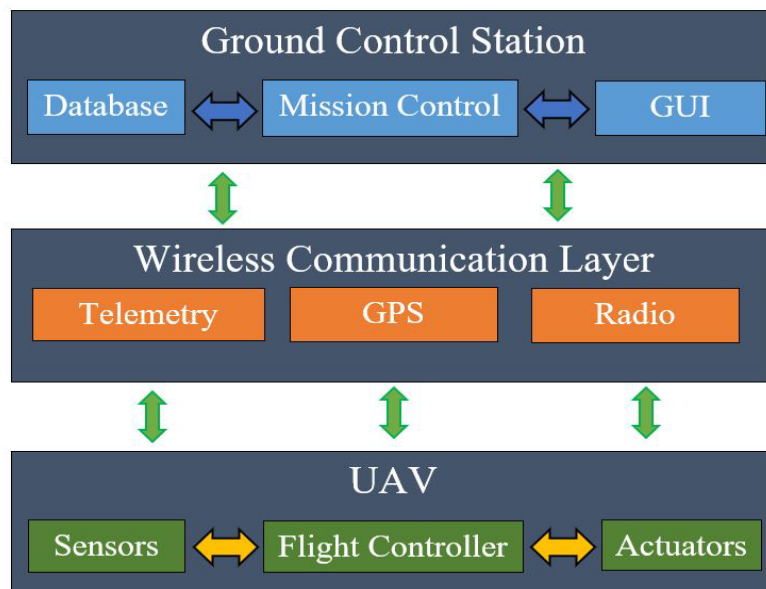
Figure 3-9: Communication layers for unmanned system operation

3.3.4 PX4 autopilot firmware

The PX4 autopilot firmware has been employed in several UAV configurations by major companies such as 'Google', 'Amazon' and 'DHL'. This firmware is an open-source project that has contributing developers from multiple countries and is managed by a company named 'Auterion'. The firmware is based on the 'NuttX' operating system and consists of two main layers, the flight stack and middleware. PX4 autopilot relies on uORB messaging within its system architecture. This protocol is an asynchronous publish and subscribe messaging Application Programming Interface (API) used for inter-thread/inter-process communication. *Figure 3-10* shows an overview of this high-level software architecture and reveals how each module interfaces with each other.

The flight stack is a compilation of navigation, guidance and control algorithms used for autonomous flight. This stack utilizes position and attitude controllers for achieving stabilization of various airframe configurations. *Figure A-2* in Appendix A shows an overview of this flight stack as a collection of building blocks and demonstrates a more straightforward process in which PX4 uses for controlling UAVs.
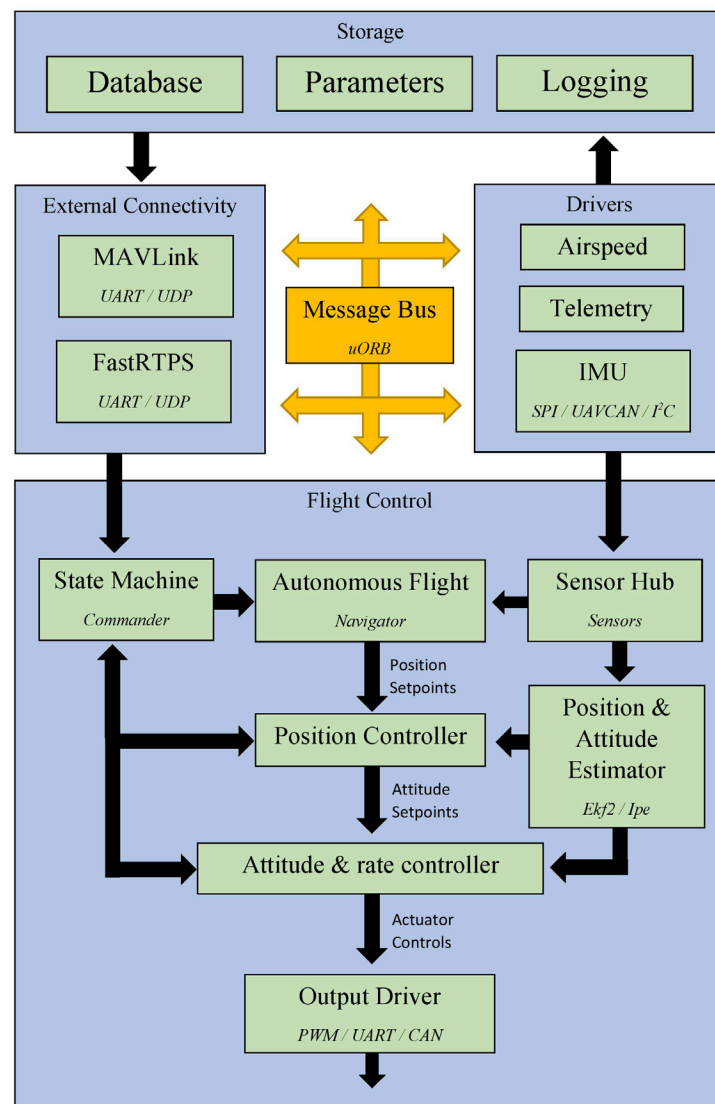
Figure 3-10: Architectural overview of PX4 autopilot firmware, adapted from [93]

3.3.4.1 Controllers

The PX4 autopilot follows a standard cascaded approach for Multicopter (MC) vehicle control, where a setpoint is required from the outer controller which results in an outputted actuator command. *Figure 3-11* shows this architecture as a combination of position, velocity, angle, and angular rate control. These control loops each operate at various refresh rates and use either P or PID control.
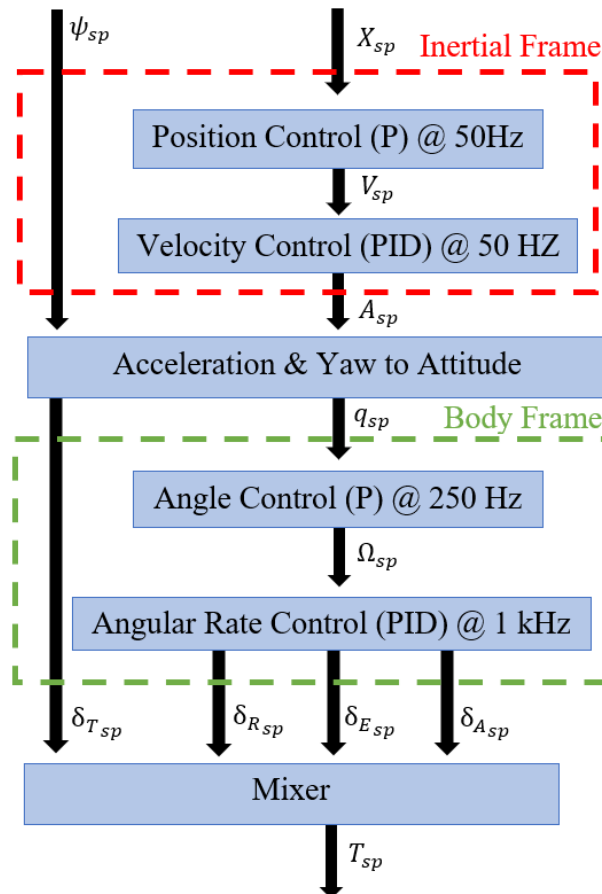
Figure 3-11: Position and attitude control module used in MC mode, adapted from [93]

FW position controller

The control architecture of FW vehicles is substantially more complex and contrasts from MC architecture by implementing a Total Energy Control System (TECS) in the position controller. The TECS approach mathematically manipulates sensor data from the IMU and GPS to output throttle and pitch setpoints. Due to the intricate nature of FW position control, TECS utilizes the total kinetic and total potential energies of the system rather than using setpoints. The TECS control loops operate by decoupling the initial setpoints and converting them into energy quantities which can then be controlled independently. This strategy alleviates the complications surrounding the analysis of true lift and pitch angles during operation. By combining a standard L1 controller for roll setpoint output, this FW position controller can provide the necessary attitude and thrust setpoints which can then be sent to the FW attitude controller. *Figure 3-12* illustrates the basic layout for the FW position controller, whilst *Figure 3-13* reveals the fundamental approach used within TECS.
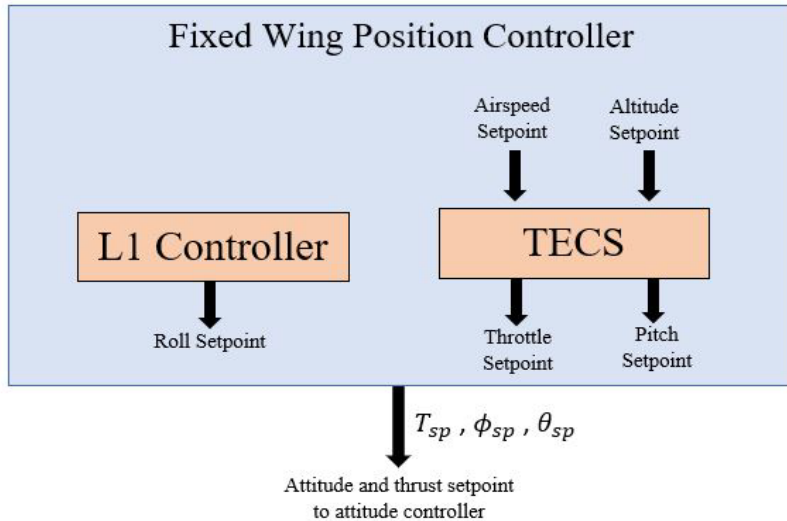
Figure 3-12: Position control module implemented in FW mode, adapted from [93]
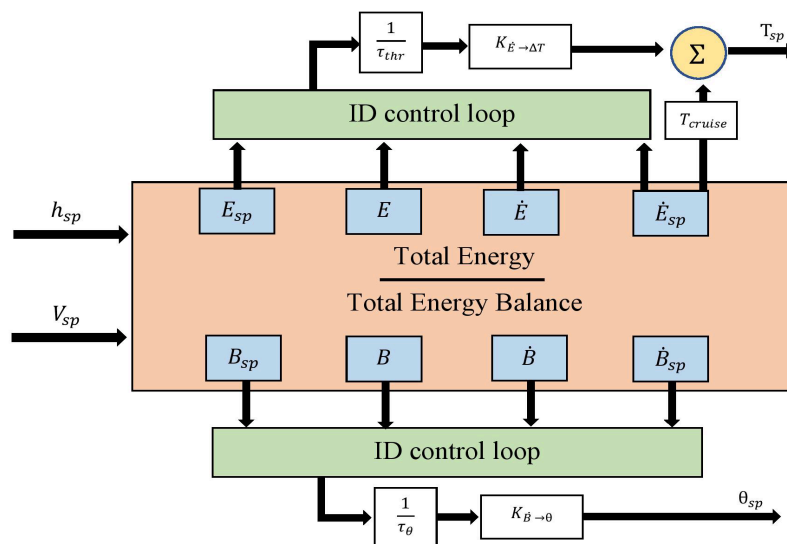
Figure 3-13: TECS approach used in FW position controller, adapted from [93]

FW attitude controller

The fixed-wing attitude controller has a similar architecture to MC, in that it also employs a cascaded loop approach. The entered thrust, pitch, and roll setpoints are taken from the position controller provides the outer loop with an error value between the actual attitude and estimated attitude. This is then multiplied by a gain from the P controller, which generates the corresponding rate setpoints. The inner loop then utilizes a PI controller to compute the error in rates and produces the desired angular and acceleration rates, respectively. This angular position is responsible for controlling the ailerons, elevators, rudders, and any other influencing aerodynamic surfaces. *Figure 3-14* shows the control architecture of this FW attitude controller. The feedforward term seen in this controller is used to compensate for aerodynamic damping whilst scalars are implemented for tuning purposes.
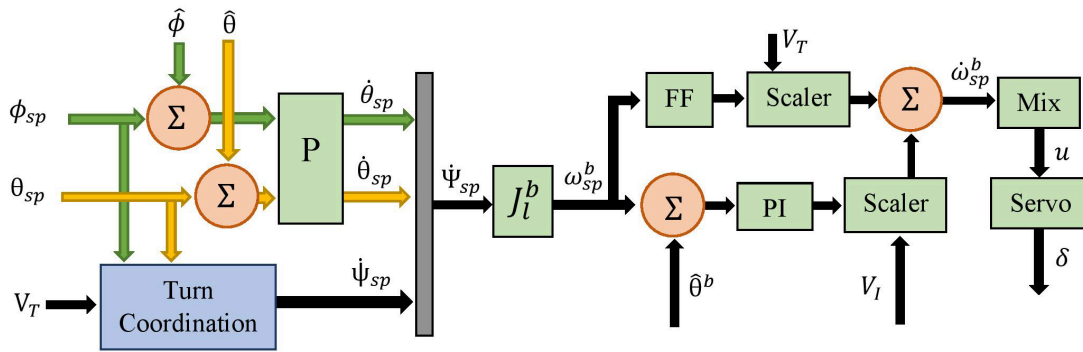
Figure 3-14: Attitude controller implemented in FW mode, adapted from [93]

VTOL controller

The VTOL control architecture used within the PX4 autopilot firmware is a combination of both MC and FW control. This implementation is utilized for vehicles that require transitioning between MC and FW flight modes, using either tilt-wing, tilt-rotor, tail-sitter, or hybrid vehicle configurations. *Figure 3-15* represents the VTOL controller as a parallel setup and demonstrates a simplified version of the control architecture which facilitates the necessary switching and blending of logic for these flight modes.

The input controls to the VTOL attitude controller are denoted by virtual setpoints, as some may be ignored depending on the current VTOL mode. Output actuator controls from the VTOL attitude controller are separated into torque and force commands for the MC and FW actuators. These commands are given by actuator control groups 0 and 1, which are handled by a specified mixer file within the autopilot's framework.
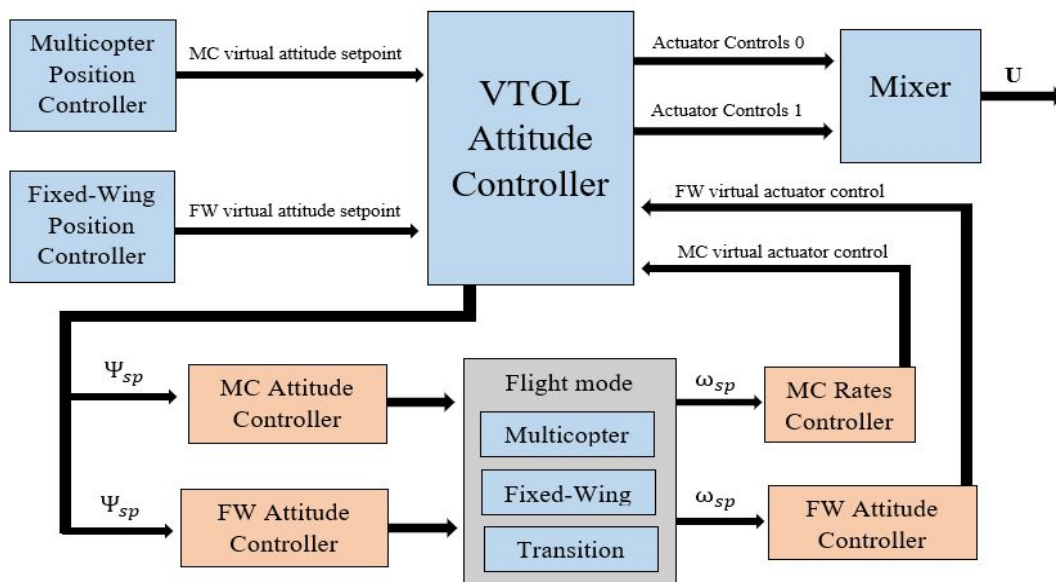
Figure 3-15: Position and attitude control module used in VTOL mode, adapted from [93]

3.3.4.2 Mixing

The mixing term referred to in the various flight controller diagrams is a force command that translates actuator commands into control for the vehicle. These actuators, represented by either a servo or BLDC motor, are given a prescribed number within the mixing file to assure the correct actuator is triggered when required. These numbers are then combined into a control group that defines the type of vehicle control needed. The PX4 firmware uses input and output control groups for assigning each actuator. These control groups are essentially the core flight instructions of the vehicle and act as a physical bus that outputs normalized commands to each actuator. These commands are mapped and scaled in the mixer file and indicate which actuator needs to perform which task for a given output from the controller. The output group utilizes communication protocols such as PWM and UAV Controller Area Network (CAN) to command the relevant actuators. The mixer file uses a combination of summing and multirotor mixers for achieving the desired control in a VTOL configuration.

Multirotor Mixer

This mixer combines the four inputs of roll, pitch, yaw and thrust into a set of BLDC actuator outputs which operate through the command signals received by the ESCs. The mixer is defined on a single line in the mixer file and given by the following syntax in *Figure 3-16*.

Figure 3-16: MC mixing file layout, adapted from [93]

Summing Mixer

This mixer is typically used for servo control during aerodynamic stabilization when a single servo actuator is required for more than one control output. The syntax given to the mixing technique is given by *Figure 3-17*.

Figure 3-17: Summing mixing file layout, adapted from [93]

Airframe and mixer file used for UAV

The control design of the *Airslipper* UAV uses the VTOL control architecture given by PX4 autopilot. However, due to the unique design of the *Airslipper,* this research created a custom airframe configuration and mixer file for controlling the necessary motor actuators. *Figures A-3* and *Figure A-4* in Appendix A illustrate the *Airslipper's* mixer file and also indicates some of the relevant parameters used for initiating the firmware on start-up.

3.4 Optimized aerodynamic and propulsion design

The exponential growth of UAV systems has significantly increased application versatility and vehicle operability. This progression had led to global demand, as more advanced systems are required with enhanced efficiency and functionality. As a result, designers have become increasingly aware of specific design parameters, that when correctly selected, can maximize a vehicle's performance for a given operation. The bulk of these influential parameters are present in central design features within the aerodynamic and propulsion system designs. Thus, for transport applications, obtaining an optimal vehicle design is necessary for achieving extended flight endurance capabilities. This characteristic is crucial in the medical aid delivery service and ensures continual development for this industry.

The successfulness of a medical aid delivery UAV is verified through the compatibility of its aerodynamic configuration and propulsion system. These individual design areas constitute the most extensive performance gain, therefore, achieving further efficiency improvements can become possible through a simultaneous optimization of both these designs. As seen by Chapter 2, specific aerofoil parameters considerably impact flight characteristics such as payload carrying capacity, flight speed and endurance. Thus, using the vehicles cruise flight condition, the aerofoil can be optimized in a manner that maximises the efficiency of the propulsion system. This process inherently reduces the amount of propulsion power needed to maintain stable flight and hence increase endurance.

Research in propeller-based propulsion systems has unravelled new and improved technologies, from innovations in Hybrid-Electric systems [75] to improved propeller aerodynamics and materials. These accomplishments, along with the progression of solar technology and fuel-cell power storage systems [76], have made propulsion systems advantageous. Although these technological breakthroughs have increased the performance of a particular subsystem, there still exist practical interfacing challenges that are apparent when combining the individual components.

Research such as [77] has approached the optimization of an entire propulsion system in the form of propeller aerodynamics and its operating conditions, whilst other research such as [78], has focused on propulsion system sizing and the effect it had on performance. However, these optimization techniques did not investigate the interlinking consequence that each component had on the system. Thus, a more reasonable approach for solving this particular challenge is through the implementation of an MDO technique. This method provides a more comprehensive array of design variables which can be related and optimized to create a more effective design.

The MDO section in Chapter 2, along with research in [79], describes the development of a complete tool for MDO design, which uses cost functions to define an electrically powered propulsion system in terms of its design parameters. Therefore, this research proposes to optimize the endurance of the *Airslipper* UAV by applying an MOEA to the aerodynamic and propulsion designs. Constraining the system to the applicational requirements enables this research to attain a Pareto front of individually optimized parameters which can be combined to form the most optimal setup for this vehicle and the medical aid delivery service application.

3.4.1 Aerodynamic design

The aerodynamic strategy focussed on the area S, aspect ratio AR, taper ratio λ and span l parameters of an aerofoil's planform, from a 2D perspective. One parameter, namely the aerofoils sweep angle, is not considered, due to its negative attributes in vehicle stability and its complications in the formulation. An additional aerodynamic parameter, the vehicle's cruise velocity V_{cruise}, is added to the strategy with the purpose of reinforcing the solution.

3.4.1.1 Parameter relations

A typical aircraft is judged aerodynamically steady when lift force L equals weight W, and when drag force D equals thrust force T_{FW}. These conditions are represented by *Equation 3-14* and *Equation 3-15*, which provide a mathematical approach to solving them using the associated parameters.

$$L = W = \frac{1}{2}\rho_{air}V_{flight}{}^2 SC_{L,vehicle} \tag{3-14}$$

$$D = T_{FW} = \frac{1}{2}\rho_{air}V_{flight}{}^2 SC_{D,vehicle} \tag{3-15}$$

The terms $C_{L,vehicle}$ and $C_{D,vehicle}$ are the vehicles lift and drag coefficients, respectively, whist ρ_{air} is the air density. V_{cruise} and S represent the vehicles cruise velocity and aerofoil area, respectively. The drag of an aircraft can then be expressed as a function of parasitic and induced drag components, as seen in *Equation 3-16*.

$$D = \frac{1}{2}\rho_{air}V_{cruise}{}^2 SC_{D0,aerofoil} + \frac{L^2 K}{\frac{1}{2}(\rho_{air}V_{cruise}{}^2 S)} \tag{3-16}$$

Where $C_{D0,airfoil}$ is the aerofoils profile drag constant and K represents the aerofoils induced drag constant, which can be further broken down by *Equation 3-17*.

$$K = \frac{1}{\pi ARe} \tag{3-17}$$

The parameter e is the Oswald efficiency factor of the aerofoil's profile whilst AR is the aspect ratio. Attaining the vehicles required power for the steady flight condition is obtained by substituting the drag of the vehicle into *Equation 3-16*. This yields *Equation 3-18,* and *Equation 3-19*, which represents the vehicles required power in terms of aerodynamic parameters.

$$P_{required,FW} = T_{FW}V_{cruise} = DV_{cruise} \tag{3-18}$$

$$P_{required,FW} = \frac{1}{2}\rho_{air}V_{cruise}{}^3 SC_{D0,aerofoil} + \frac{W^2 K}{\frac{1}{2}\rho_{air}V_{cruise}S} \tag{3-19}$$

Using these steady flight power requirements, one can obtain the vehicles optimal velocity for minimum power consumption. This is achieved by taking the derivative of *Equation 3-19* with respect to the vehicle's cruise velocity V_{cruise}, thus yielding *Equation 3-20*, which represents the flight velocity for maximum endurance.

$$V_{optimal} = \left[\frac{4}{3}\left(\frac{W}{S}\right)^2 \frac{1}{\rho_{air}{}^2 C_{D0,aerofoil}} \left(\frac{1}{\pi eAR}\right) \right]^{\frac{1}{4}} \tag{3-20}$$

Due to the nature of aerodynamic drag, flight endurance becomes a function of power and velocity. Therefore, introducing battery parameters in the form of the vehicles supplied power increases the effectiveness of this parametric design. So, to further develop the maximum endurance, battery parameters are formulated within the batteries output power term P_{out}. This can be achieved by making use of Peukert's law and modifying this to accommodate for battery discharge effects. However, the battery cells in consideration are not lead-acid, but are lithium instead, making Peukert's law obsolete. This is due to the self-heat regulation of lithium-ion cells and their ability to maintain high continuous current draw. Therefore, a simpler approximation of the battery parameters is used within the endurance formulation. The battery output power P_{out} is given by *Equation 3-21*.

$$P_{out} = V_{battery}\left(B_{capacity,actual}\right) = F_d S_f \tag{3-21}$$

Where $V_{battery}$ and $B_{capacity,actual}$ are the batteries nominal voltage and actual capacity, respectively. The terms F_d and S_f represent the batteries corrected and uncorrected capacity factors, which can be decoupled to form *Equation 3-22*.

$$P_{out} = V_{battery}(B_{capacity,actual})\left[(1 + d_f)(1 + t_f)(1 + c_f)(1 + a_f)\right] \tag{3-22}$$

The parameters d_f, t_f, c_f and a_f are the batteries design margin, temperature factor, state of charge and ageing factor, respectively. These values are determined based on an unused battery pack at full charge. Knowing that the batteries output power gets converted into propulsion power, relations may be used to determine the maximum endurance of the vehicle. *Equation 3-23* represents the endurance condition for the aerofoils profile drag component $C_{D0,airfoil}$.

$$C_{D0,aerofoil} = \frac{1}{3}KC_{L,aerofoil}^2 = \frac{2}{3}\left(\frac{KW}{S\rho_{air}V_{cruise}^2}\right)^2 \tag{3-23}$$

After applying a propulsion efficiency factor $\eta_{propulsion}$ due to electrical system losses along with combining the minimum power velocity condition, *Equation 3-24* shows the optimal endurance of a vehicle in terms of battery and aerodynamic parameters.

$$T_{flight,OPTIMAL} = \frac{\eta_{propulsion}V_{battery}B_{capacity,actual}(S_f)}{\left(\frac{2}{\sqrt{\rho_{air}S}}\right)C_{D0,aerofoil}^{1/4}\left(2W\sqrt{\frac{k}{3}}\right)^{3/2}} \tag{3-24}$$

As *Equation 3-20* and *Equation 3-24* are representative of the minimum power conditions for maximum endurance, any slight deviations in the parameters, which are not deemed variables, could result in inaccuracies after multiple optimization iterations. Therefore, as the aspect ratio AR is judged as a design parameter of interest and the induced drag constant K contains this parameter, an alternative approach is required to satisfy the vehicles parametrization. As such, authors of [80] and [81] managed to derive an equation that described the induced drag constant parameter. *Equation 3-25* represents this derivation and shows how the induced drag constant K can be represented in terms of the viscous P and inviscid Q drag factors of an aerodynamic surface. However, the authors could not find a definitive value for these factors due to the intricacies of aerodynamic design.

$$K = \frac{Q}{\pi AR} + P \tag{3-25}$$

Therefore, instead of redefining the induced drag factor, an approach was used to describe the Oswald efficiency factor in terms of the aerodynamic parameters needed. The author of [82] proposed to estimate the Oswald efficiency factor from the aircrafts geometrical parameters such as the taper ratio λ, sweep angle Λ and aspect ratio AR. *Equation 3-26* was developed, which defined the theoretical Oswald factor based on a fourth-order polynomial given in *Equation 3-27*.

$$e_{theoretical} = \frac{1}{1+f(\lambda - \Delta\lambda)AR} \tag{3-26}$$

$$f(\lambda) = 0.0524\lambda^4 - 0.15\lambda^3 + 0.1659\lambda^2 - 0.0706\lambda + 0.0119 \tag{3-27}$$

Where $\Delta\lambda$ is the shifted taper ratio from the $\frac{d}{d\lambda}f(0.45)$ of *Equation 3-27*. The 0.45 value is considered, according to the author, as the optimal taper ratio for wings with no sweep. It was understood that the theoretical value required compensation from fuselage drag, profile drag and Mach number influences. Thus, an overall estimated Oswald efficiency factor can then be given by *Equation 2-28*, which is dependent on the aerofoils taper ratio λ and aspect ratio AR.

$$e = e_{theoretical}.k_{e,F}.k_{e,D0}.k_{e,M} \tag{3-28}$$

The influencing factor values were determined based on a familiar aerodynamic shape, and due to the vehicle's application requirements, the Mach number factor $k_{e,M}$ can be neglected.

3.4.1.2 Aerodynamic mass parametrization

Obtaining an optimal aerodynamic configuration requires the mass of the vehicle to be parametrized, which allows the mass to be represented in terms of the desired design parameters and permits a more accurate optimization. The total estimated mass of the vehicle consists of several submodules, including the fuselage, aerofoil, battery, payload, and propulsion system. This aerodynamic parametrization assumes a constant fuselage design and propulsion system, thus a constant mass for both. Therefore, from the previous derivations, it can be noted that the aerofoil area and aspect ratio are dependent on the optimal velocity and endurance equations. Thus, a mass parametrization of the aerofoil is needed to satisfy these conditions. The aerofoil is assumed to be non-swept aft, meaning it employs a straight-line trailing edge. Given the aerofoils profile and FDM fabrication method, a unit mass length of $0.3\ kg/m$ is to be used. *Equation 3-29* reveals how the aerofoils span length l is determined, and *Equation 3-30* shows how the mass is calculated.

$$l = \sqrt{S.AR} \tag{3-29}$$

$$M_{aerofoil} = 0.3l = 0.3\sqrt{S.AR} \tag{3-30}$$

The aerofoils area S is resolved by keeping the root chord value at a constant $C_r = 0.28m$, due to vehicle design constraints. From this information, the aerofoils area can be represented in *Equation 3-31*, and the total mass can now be characterized in terms of aerofoil parameters in *Equation 3-32*.

$$S = 2\left(\frac{l}{2}(C_r - \lambda.C_r) + lC_r\lambda\right) \tag{3-31}$$

$$M_{aerofoil} = 0.3\sqrt{2(AR)\left[\frac{l}{2}(C_r - \lambda.C_r) + lC_r\lambda\right]} \tag{3-32}$$

3.4.2 Propulsion design

Propeller-based propulsion has formed an extensive gathering due to its simplistic implementation, and controllability. The popularity of this method in the UAV industry has allowed designers to explore various setups further. However, the complexities of component compatibility and integration make a propulsion system incredibly multifaceted. An electrically powered propulsion system commonly consists of a propeller, motor, and battery. As seen in Chapter 2, specific propeller parameters have a significant impact on vehicle performance. These parameters, along with others, are regarded as an essential aspect of vehicle design. Thus, for this optimization, the parameters of interest include propeller diameter d, propeller rotation speed n, battery voltage $V_{battery}$ and battery capacity $B_{capacity,actual}$.

3.4.2.1 Parameter relations

A propulsion system is a complicated set of interlinking components that influence the system's ability to produce its intended thrust force. Therefore, through a vigorous manipulation process, parameter relationships can be formed to satisfy flight conditions. As the propeller and motor are directly coupled, a constant and equal rotational speed is present for both. This rate can be ideally represented as a function of motor and propeller parameters by equating each of the generated torques. This is achieved by representing the motor torque Q_m in terms of motor parameters, as seen in *Equation 3-33*.

$$Q_{motor} = \frac{\left[\frac{V_{battery} - \frac{n}{KV}}{R}\right] - I_0}{KV} \tag{3-33}$$

Where $V_{battery}$ is the Open Circuit (OC) voltage and n represents the aforementioned rotational speed. KV, R and I_0 are motor constants and vary according to BLDC motor design. By equating this to the dimensional analysis definition of the rotation rate, a required rotational speed $n_{required}$ can be obtained as a function of both the motor and propeller parameters, as shown in *Equation 3-34* and *Equation 3-35*.

$$Q_{motor} = Q_{propeller} = C_Q\rho_{air}n^2d^5 = \frac{\left[\frac{V_{battery} - \frac{n}{KV}}{R}\right] - I_0}{KV} \tag{3-34}$$

$$n_{required} = KV[V_{battery} - R[C_Q\rho_{air}V^2KV^3d^5 + I_0]] \tag{3-35}$$

Knowing the required rotational speed for propeller and motor torque matching, there now exists an optimal rotational speed that satisfies the condition for maintaining steady flight of an aerial vehicle. By applying the condition of drag force D, must equal the generated thrust force T_{FW}, one can use the thrust definition of dimensional analysis to formulate an optimal rotational speed given by *Equation 3-36*.

$$n_{optimal} = \sqrt{\frac{\left(\frac{1}{2}\rho_{air}V_{cruise}^2SC_{D0,aerofoil} + \frac{W^2}{\frac{1}{2}\rho_{air}V_{cruise}^2S}\left(\frac{1}{\pi eAR}\right)\right)}{C_T\rho_{air}d^4}} \tag{3-36}$$

This equation now represents the optimal rotational speed in terms of propeller and aerodynamic parameters. However, to fully develop the optimal rotational speed, considerations must be made for a minimum power condition. By rearranging the efficiency of a propeller from the dimensional analysis theory and applying the induced power described by momentum theory, a relationship can be obtained that describes the induced propwash power as a function of propeller diameter, vehicle weight and cruise velocity in *Equation 3-37*.

$$T_{FW}V_{induced} = C_P\rho_{air}\left(\sqrt{\frac{(D)}{C_T\rho_{air}d^4}}\right)^3 d^5\eta_{propulsion} + T_{FW}V_{climb} \qquad (3\text{-}37)$$

This equation now represents the propwash power loss that a propeller endures when traversing through a medium. From these derivations, it is apparent that the required induced power to overcome the propwash is directly proportional to $\left(\frac{C_T^{\frac{3}{2}}}{C_P}\right)^{-1}$. Thus, minimizing the propwash effect means maximizing $\left(\frac{C_T^{\frac{3}{2}}}{C_P}\right)$. By applying the power coefficient C_P from blade element theory, which is represented by the inflow λ and solidity σ factors to the maximizing term, a suitable formulation can be formed that encompasses the thrust coefficient C_T, as seen in *Equation 3-38*.

$$\frac{C_T^{\frac{3}{2}}}{C_p} = \frac{C_T^{\frac{3}{2}}}{k\lambda C_T + \frac{1}{8}\sigma C_{Do,rotor}} \qquad (3\text{-}38)$$

Taking the derivative of *Equation 3-38* with respect to C_T yields the thrust coefficient of *Equation 3-39*. This interpretation can now be used for attaining the minimum induced power associated with the downwash.

$$C_T = \frac{\sigma C_{Do,rotor}}{8k\lambda} \qquad (3\text{-}39)$$

This thrust coefficient is now applied to the optimal rotational speed given previously, thus yielding an optimal rotational speed that accounts for the minimum propwash power consumption, therefore satisfying the minimum power condition. *Equation 3-40* now represents a rotational speed that optimizes the propeller's performance whilst satisfying the fundamental conditions.

$$n_{optimal} = \sqrt{\frac{\left(\frac{1}{2}\rho_{air}V_{cruise}^2 SC_{D0,aerofoil} + \frac{W^2}{\frac{1}{2}\rho_{air}V_{cruise}^2 S}\left(\frac{1}{\pi eAR}\right)\right)}{\rho_{air}d^4\left(\frac{\sigma C_{D0,rotor}}{8k\lambda}\right)}} \qquad (3\text{-}40)$$

3.4.2.2 Propulsion mass parametrization

It can be noted that the previously defined optimal rotational speed equation is dependent on propulsion and aerodynamic parameters but is also a function of the vehicle's weight. The masses used in this propulsion design parametrization match those of the aerodynamic design parametrization, except for the battery. Thus, the batteries mass can be represented by motor and propeller parameters in this section.

The batteries mass is solely based on the intended flight characteristics associated with the vehicle's application. Thus, battery parameters such as depth of discharge f_{DOD} and efficiency of discharge $\eta_{discharge}$ need to be understood to ensure battery safety and battery longevity. This knowledge is essential for determining the

vehicle's endurance $T_{flight,TOTAL}$, required propulsive $P_{propulsion}$ power and miscellaneous P_{misc} power. Equation 3-41 reveals the energy stored in the battery, whilst *Equation 3-42* shows the propulsive power required to maintain a given thrust.

$$E_{battery} = \frac{T_{flight,TOTAL}\ (P_{propulsion} + P_{misc})}{f_{DOD}\eta_{discharge}} \qquad (3\text{-}41)$$

$$P_{propulsion} = \frac{T_{FW}V_{cruise}}{\eta_{motor}\eta_{propeller}} \qquad (3\text{-}42)$$

Where η_{motor} and $\eta_{propeller}$ represent the efficiencies for the motor and propeller, respectively. The thrust term T_{FW}, is represented by *Equation 3-43* and the batteries total mass is then given by *Equation 3-44*.

$$T_{FW} = \left(\frac{\sigma C_{D0,rotor}}{8k\lambda}\right)\rho_{air}n_{required}^{2}d^{4} \qquad (3\text{-}43)$$

$$M_{battery} = \frac{[T_{flight,TOTAL}\ (P_{propulsion} + P_{misc})]}{\rho_{battery}f_{DOD}\eta_{dishcharge}} \qquad (3\text{-}44)$$

3.4.3 Optimization formulation

Attaining an optimized aerodynamic configuration and propeller-based propulsion system requires the formulation of two individual objective functions that are constrained to the vehicle's flight characteristics. This process is fundamental to the optimization and helps to evaluate the design parameters against crucial performance aspects. A successfully optimized design requires the objective functions to be minimized whilst satisfying the design restrictions and applicational requirements previously mentioned. Formulation of the aerodynamic objective function is comprised of three independent conditions that ensure optimality. These conditions include the vehicle's weight W be equal to the lift L produced by the aerofoils, the cruise velocity V_{cruise} be equal to the optimal velocity $V_{optimal}$ and the flight endurance $T_{flight,TOTAL}$ be equal to the optimal endurance $T_{flight,OPTIMAL}$. *Equation 3-45* reveals the aerodynamic objective function used for this optimization.

$$J_{aerodynamic}(S, AR, \lambda, V_{cruise}, l) = \quad |W - L| + |V_{cruise} - V_{optimal}| + |T_{flight,TOTAL} - T_{flight,OPTIMAL}| \quad (3\text{-}45)$$

Just like aerodynamic optimization, propulsion design optimization requires a similar objective function formulation. This function is based on the fundamental aircraft conditions, which states the thrust force T_{FW} equal the drag force D along with the required propeller rotation speed $n_{required}$ equal to the optimal rotation speed $n_{optimal}$. However, to fully define the formulation and optimize the system, another condition needs to be satisfied. This condition is valid for when the supplied power from the battery P_{out} equals the propulsions required power $P_{propulsion}$. Equation 3-46 shows this supplied power as a function of battery parameters.

$$P_{out} = \frac{f_{DOD}B_{cell,parrallel}V_{battery}B_{capacity,cell}}{T_{flight,TOTAL}} \qquad (3\text{-}46)$$

Where $B_{cell,parrallel}$ and $B_{capacity,cell}$ represents the number of parallel battery cells and cell capacity, respectively. The objective function can now give the final optimization formulation in *Equation 3-47*.

$$J_{propulsion}\left(V_{battery}, B_{cell,parrallel}, n, d\right) = |T_{FW} - D| + |n_{required} - n_{optimal}| + |P_{out} - P_{propulsion}| \quad (3\text{-}47)$$

3.4.4 Performance optimization results

The values and constants used in this optimization formulation were taken from the *Airslipper's* preliminary design and are shown in *Table 3-3*. Solving this optimization formulation required the proficiency of MATLAB's global optimization toolbox. By making use of the 'gamultiobj' function, which employs an elitist GA for greater solution accuracy, a Pareto front of the optimization problem was found. The objective function was initiated with double vector population sizes of 200, 2000 and 10000. The function was constraint dependent and had a crossover reproduction fraction and ratio of 0.8 and 1.0, respectively. The stopping criteria of the algorithm included no time limit and no fitness limit, which allowed a complete solution to be attained. The maximum number of generations was decided as 200 multiplied by the number of variables, which was 10. A function tolerance of 1e-6 was used whilst a constraint tolerance of 1e-5 was employed.

The optimization was performed on hardware that had an Intel® Core i5-7300HQ CPU that ran at 2.5GHz for the entire solution. A total of 12 gigabytes of memory was available for the optimization; however, only 8.67 gigabytes was needed. By utilizing the above problem and hardware setup, as well as the constants found in *Table 3-3*, solution of the fitness function gave results shown in *Figures 3-18*, *3-19* and *3-20*. The figures show the plot functions of the Pareto front, average Pareto spread and average Pareto distance for each corresponding population size. The optimized values found in *Table 3-4* are indicative of an optimized aerodynamic and propulsion design.

The findings of the optimization revealed a direct correlation between population size and average Pareto spread values. These outcomes demonstrated the importance of population size and indicated increased disparities in average Pareto distance for larger populations. It was also apparent that more generous population sizes resulted in a broader array of optimal solutions as well as smaller variations between solutions on the Pareto front. The individually optimized parameters clearly show small differences in values. However, this outcome is suggestive to the consistency and reliability in the algorithm of choice.

Table 3-4: Performance parameter values used in the optimization formulation

| Parameter	Unit	Value	Parameter	Unit	Value
Air density	ρ_{air}	1.225	No. of propeller blades	R_n	2
Gravitational constant	g	9.81	Empirical factor	k	1.13
Propeller profile drag	$C_{D0,propeller}$	0.02	Battery cell capacity	$B_{cell,parrallel}$	3000
Aerofoil root chord	C_r	0.4	Motor current	I_{motor}	35
Battery depth of discharge	f_{DOD}	0.8	Propulsion mass	$M_{propulsion}$	1.8
Battery discharge efficiency	$\eta_{Discharge}$	0.95	Fuselage mass	$M_{fuselage}$	3
Battery energy density	$\rho_{battery}$	170	Miscellaneous mass	M_{misc}	1
Propulsion efficiency	$\eta_{propulsion}$	0.8	Payload mass	$M_{payload}$	2.5
Propeller efficiency	$\eta_{propeller}$	0.8	Miscellaneous power	P_{misc}	30
Motor efficiency	η_{motor}	0.85	Propeller blade chord	c	0.04
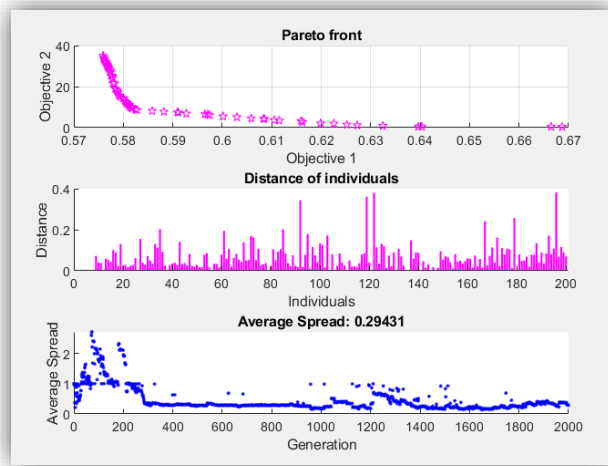
*Figure 3-18: Pareto chart for population size, 200*
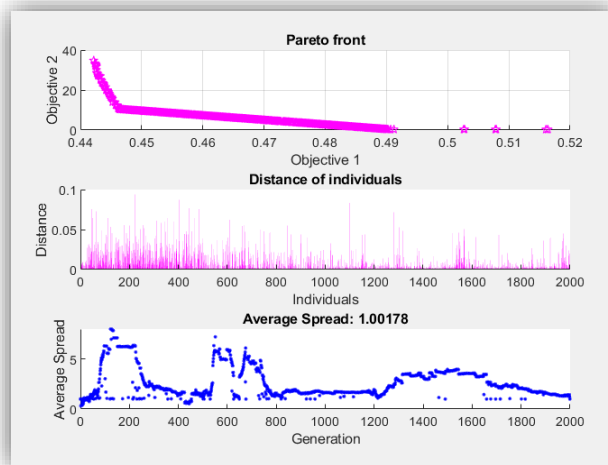
*Figure 3-19: Pareto chart for population size, 2000*
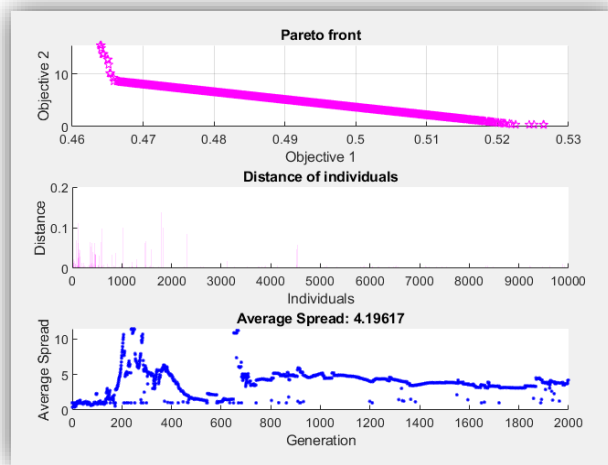
Figure 3-20: Pareto chart for population size, 10000

Table 3-5: Initial and optimized performance parameters with lower and upper bounds

Performance Parameter	Unit	Initial value	Lower bound	Upper bound	Parameter (200 Pop)	Parameter (2000 Pop)	Paramater (10000 Pop)
Cruise velocity	m/s	28	22	32	26.5	25.3	26.1
Aerofoil area	m^2	0.35	0.15	0.45	0.361	0.327	0.379
Aerofoil aspect ratio	-	13.82	6	14	11.98	11.61	11.85
Aerofoil taper ratio	-	5.2	3	7	4.45	4.82	4.66
Aerofoil span	m	2.2	1.5	2.5	2.08	1.94	2.12
Battery voltage	V	24	20	28	24	24	24
Flight endurance	s	720	450	950	762	752	820
Propeller diameter	m	0.45	0.35	0.5	0.393	0.442	0.431
Rotation speed	rpm	5740	4500	7000	6723	6422	6557
Parallel battery cells	$cells$	9	4	14	6	6	6

Regarding the actual optimized parameter values, it is evident that deviations are apparent against the initial parameter values and are within the lower and upper bounds. The outcome of this optimization revealed considerable changes for the propellers rotation rate, which increased by an average of **827 rpm**. This optimal rotation value allowed the aerofoil span to be slightly reduced whilst enabling a greater area through a reduction in taper ratio. It was evident that due to a decrease in the number of parallel battery cells required, battery mass diminished by a total of **800 g**, which allowed the vehicle to achieve lower cruise velocities. This optimized parameter combination significantly reduces drag and hence power consumption, which ultimately resulted in a **58 s** increase in flight endurance. This endurance increase, although minimal, is a substantial gain of **1.51 km** flight range, which is critically important when considering the medical aid delivery application. These findings reveal the potential for UAV optimization and demonstrate the effectiveness of MDO techniques for aerodynamic and propulsion system design.

3.5 Summary of Chapter 3

The *Airslipper* UAV was conceptualized through a design approach that factored in the FDM fabrication method and medical aid delivery application. This strategy provided a greater perspective on the *Airslipper's* operational conditions, which allowed for the systematic selection of propulsion and aerodynamic parameters. Results of an estimated calculation on an initial propulsion setup demonstrated confidence for the *Airslipper's* VTOL mode and provided valuable information on the vehicles flight characteristics. This chapter further explained the various power distribution, power management, and wireless communication techniques of UAVs. Implementation of the Pixhawk 4 flight controller and PX4 autopilot firmware offered an indication towards the control architecture and actuator mixing styles that were required by the *Airslipper* design. This chapter displayed the formulation of two parametric fitness functions for the relevant aerodynamic and propulsion designs. This multidisciplinary problem was constrained to the UAV's applicational requirements and initiated through an appropriate solver such as MATLAB's 'gamultiobj' function. Outcomes of this optimization revealed a Pareto front that showed an optimal set of individual parameter values for the given flight conditions. The parameter values exhibited deviation from the initial designs and showed improvements for vehicle weight and flight endurance.

4. AERODYNAMIC AND DESIGN ANALYSIS OF THE AIRSLIPPER

Analysing an aircraft forms a key aspect in aerial vehicle design and it is used to validate the performance associated with a proposed concept. The purpose of analysing the *Airslipper* UAV was to ensure the optimized propulsion setup was compatible with the optimized aerodynamic configuration, which is a vital process that confirms the design operates optimally and functions as intended. This chapter detailed the results of a stability and sensitivity analysis conducted on the aerodynamic surfaces of the *Airslipper* and graphically illustrated fluid behaviour during the vehicle's VTOL and FW flight modes. A CFD simulation was also conducted on a 3D modelled version of the *Airslipper* design, which revealed the critical airflow interaction and interference on the relevant design modules. This chapter concluded by executing an FEA simulation on the aerofoil and its supports with the intention of verifying the structural integrity of the FDM fabrication method.

4.1 Aerodynamic analysis

The use of an aerodynamic analysing program such as XFLR5 significantly benefits the competency of an aerial vehicle's design strategy. This program is capable of performing various analyses that include viscous and inertial effects, which enhances the real-world accuracy of the solution. The use of a direct foil analysis in conjunction with plane, stability, and sensitivity analyses provides a comprehensive array of results that can satisfy almost any vehicle configuration at a given flight condition. These analyses offer the necessary attributes of a design which ultimately characterizes the vehicle for its application.

4.1.1 XFLR5

Implementation of the XFLR5 analysing tool within this research enabled the *Airslipper's* aerodynamic surfaces to be thoroughly investigated. The XFLR5 program employs a unique modelling method that allows users to fully customize a design with any surface configuration and foil type. Therefore, the *Airslipper's* complete design was configured according to the specifications given by Chapter 3. Although the main aerofoil profile was selected in Chapter 3, this section must substantiate its characteristics against other profile options of similar capabilities. The programs expected outcome, within this dissertation, was to understand the influence these surfaces had on the stability and sensitivity of the vehicle when subjected to the specified flight conditions.

4.1.1.1 Direct aerofoil analysis

A direct foil analysis is fundamental to aircraft design, as it measures the foremost characteristics of an aerofoil profile at varying flight velocities, Reynolds numbers, and AoA. Furthermore, completing this type of analysis provides the program with a sufficient data set of foil polars which can be used to aid the accuracy of stability and sensitivity analyses. In order to determine which foil shape best suits the *Airslipper* and its application, a batch of three varying NACA foil profiles were chosen as potential candidates. These profiles are within a specified range of $\mathbf{10 - 16}$ % maximum thickness with a $\mathbf{2 - 6}$ % maximum camber. Selection of these foils was evaluated based on an operating Reynolds number of approximately $\boldsymbol{Re = 5.5x10^5}$ and are shown in *Table 4-1* with their relevant attributes.

Table 4-1: Thickness and camber attributes for NACA foils 2411, 4415, and 6412

NACA foils	Max thickness	Max camber
2411	11 % @ 30 % chord	2 % @ 40 % chord
4415	15 % @ 30 % chord	4 % @ 40 % chord
6412	12 % @ 30 % chord	6 % @ 40 % chord

The analysis of these foils was conducted using the batch foil analysis option in XFLR5. Forced transition locations for the top and bottom was set at $\frac{x}{c} = 1.00$ and the foils AoA was specified for a range of $-2.0^0 < AoA < 10^0$ with increments of 0.5^0 degrees. The analysis was executed as a Type 1 condition, which fixed the lift force associated with each foil. A maximum of 200 iterations was used for convergence and gave results given by *Figure 4-1* and *Figure 4-2*. The NACA 6412 foil depicted by the red contours showed superior performance for the lift coefficient and glide ratio at the specified Reynolds number. Although each foil exhibits potential for the *Airslipper* design, a maximum glide ratio of $\frac{C_L}{C_D} = 126$ at $AoA = 7^0$ for the NACA 6412 confirms its initial selection.


Figure 4-1: Performance curves for NACA foils 2411, 4415, and 6412
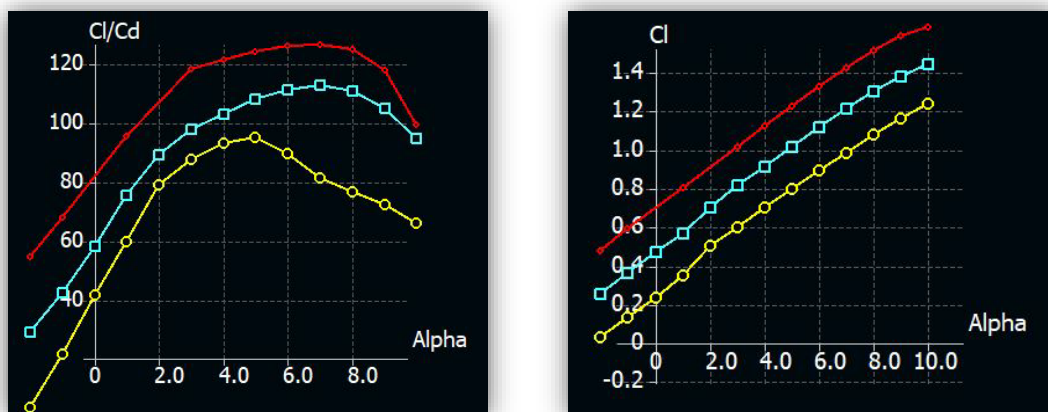
Figure 4-2: Glide ratio and lift coefficient for NACA foils 2411, 4415, and 6412

Noting that the NACA 6412 foil demonstrated more pertinent characteristics, a second direct foil analysis was conducted for only this foil to gauge its performance at varying Reynolds numbers, ranging from $2x10^5 < Re < 7x10^5$. This analysis was performed with the same criteria given to the previous study and gave results shown in *Figure 4-3*, which revealed a viscous-based polar set for the NACA 6412. The behaviour of this foil displayed consistency for the Reynolds number range and portrayed a linear relationship between the lift coefficient and AoA. It can also be noted that the foil produces maximum glide ratios at $AoA = 7^0$ degrees before the performance significantly degrades. *Figure 4-4* shows the lift force distribution and centre of lift of this foil profile and also reveals the boundary layer illustrated by a dotted red line.
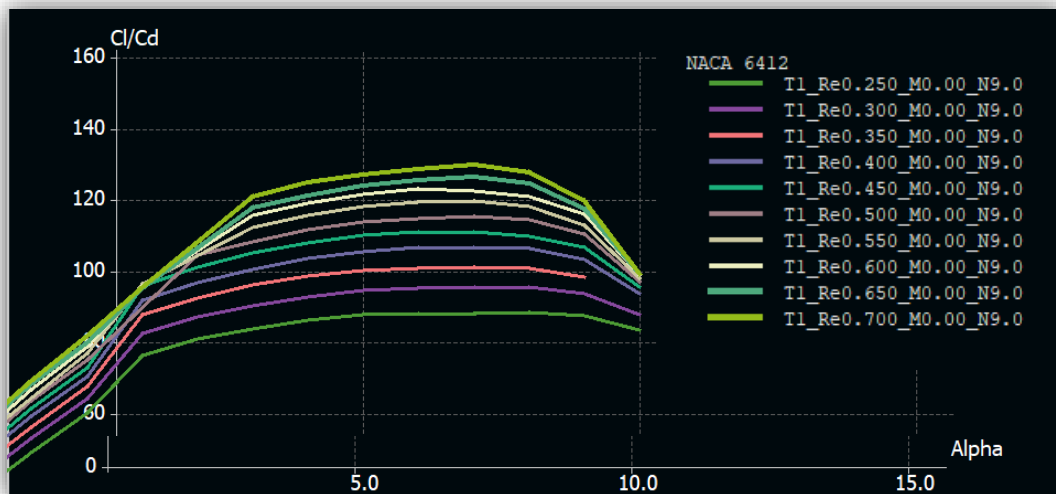
Figure 4-3: Glide ratio polar set for NACA foil 6412
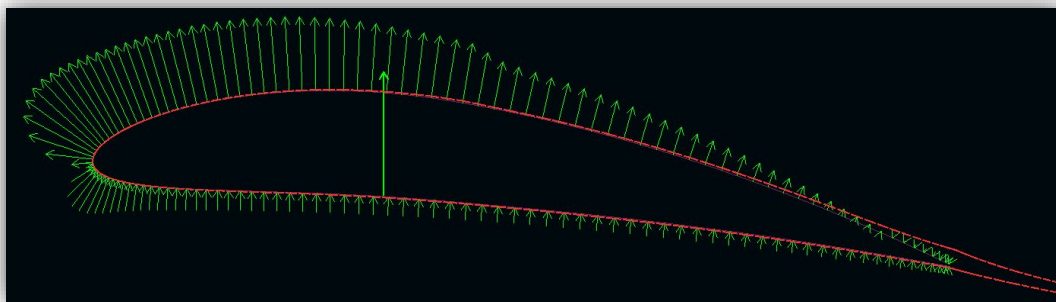
Figure 4-4: Pressure distribution of NACA foil 6412 at $AoA = 7^0$ and $Re = 5.5x10^5$

4.1.1.2 UAV Analysis

By understanding the viscous behaviour of the NACA 6412 at different Reynolds numbers, the main aerofoil and control surfaces can be modelled in 3-dimensional space using the XFLR5 modelling tool. However, placement of these surfaces, with relevance to each other, is integral for achieving the correct aerodynamic configuration. Ascertaining an accurate plane analysis also requires a comprehensive and accurate distribution of the associated point masses. These masses correspond to the electronic components and submodules within the *Airslipper's* design and ensure inertial effects are accounted for. *Table A-1* in Appendix A reveals these masses and shows

their location relative to the UAV's origin, which is positioned at the centre of the fuselage. Using this table information and the optimized design considered in Chapter 3, the *Airslipper* UAV was modelled and analysed using XFLR5's ring VLM analysis method. The attributes of the aerodynamic surfaces can be found in *Table 4-2*, whilst *Figure 4-5* illustrates a graphical representation of the experienced pressure coefficient. The reduced pressure exhibited by the rear control surface is a result of its negative inclination angle. This impact is reversed for the front control surface, so as to provide a lifting force nearer the design's front-end. These characteristics are subsequently needed to keep the vehicle in a stable position and ensure optimal performance for unmanned operation.

Table 4-2: Design parameters of aerodynamic surfaces and their corresponding attributes

Main aerofoil		Front control surface	
Foil profile	NACA 6412	Foil profile	NACA 0015
Inclination angle	$+7^0$	Inclination angle	$+4^0$
Span	$2.12\ m$	Root chord	$0.22\ m$
Area	$0.38\ m^2$	Span	$0.22\ m$
Taper ratio	4.667	**Rear control surface**	
Aspect ratio	11.855	Foil profile	NACA 0015
Root chord	$0.280\ m$	Inclination angle	-4^0
Mean aerodynamic chord	$0.205\ m$	Root chord	$0.22\ m$
Wing loading	$24.12\ kg/m^2$	Span	$0.22\ m$
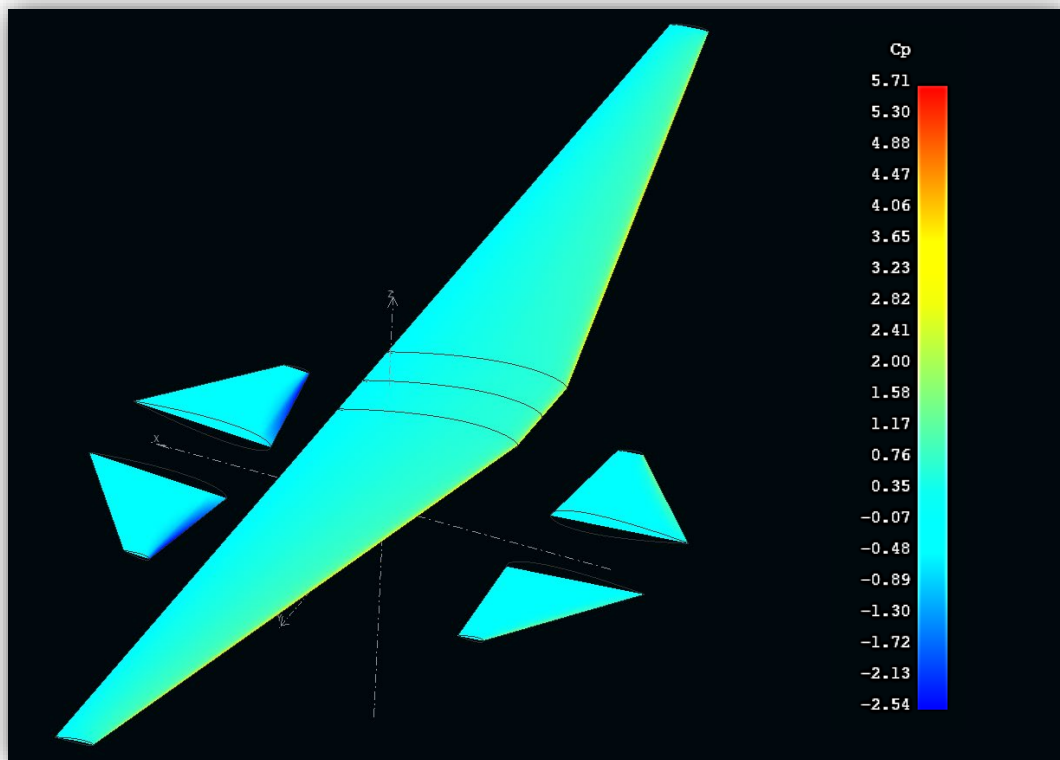
Figure 4-5: Pressure coefficient distribution on aerodynamic surfaces

To further assess the fluid's impact on these surfaces, *Figure 4-6* shows a plotted representation of the viscous drag for the main aerofoil at the analysed conditions. This figure reveals the drag values of each node on the aerofoil versus its spanwise length. It can be seen that an increase in drag closer to the aerofoil's tips is characteristic of an increased lifting force and hence, Reynolds number. This consequence is a result of a tapered aerofoil with reduced chord size.

Figure 4-7 further depicts the bending moment of the main aerofoil and reveals a peak bending moment value of **20 $N.m$** at the aerofoils centre, which demonstrates the required structural abilities of the FDM fabrication method for this component. This severe bending moment is due to the lift profile of the aerofoil, which can be seen in *Figure 4-8*. The same figure also provides the lift profile of the control surfaces, which are mirrors of each other and are essential for maintaining a neutral pitching moment at the specified flight velocities. The findings of this plane analysis are indicative of a controlled and stabilized configuration.
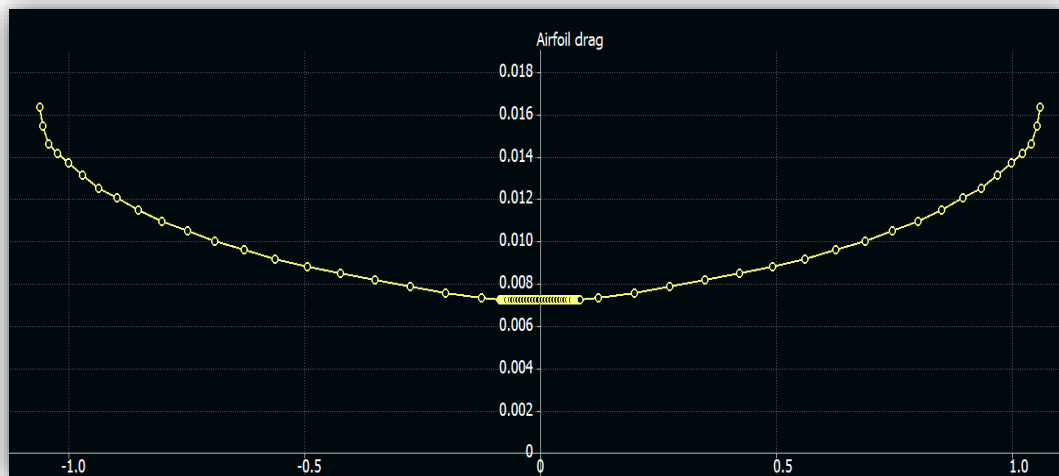
Figure 4-6: Spanned viscous drag associated with the main aerofoil
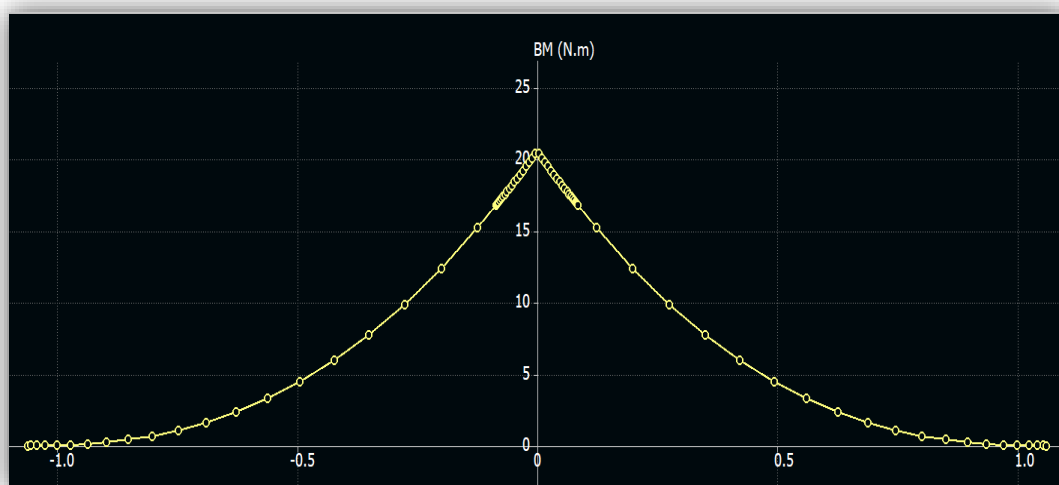
Figure 4-7: Spanned bending moment associated with the main aerofoil
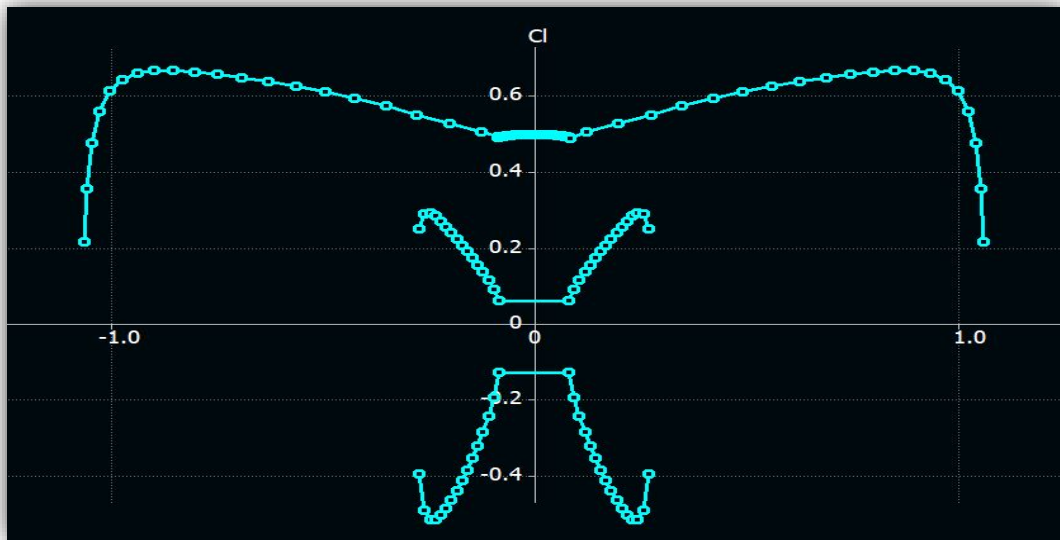
Figure 4-8: Spanned lift coefficient on aerodynamic surfaces

The dynamic pressure distribution of the *Airslipper's* aerodynamic configuration shown in *Figure 4-9* resembles the same lift profile shape across the main aerofoil. This figure is a front view of the analysis results and suggests a maximum negative pressure value of $-1094\,Pa$ is apparent at the peak of this lift profile. The figure also displays fluids streamlines surrounding the aerodynamic surfaces, which are visually represented in this figure by purple spirals. These streamlines reveal the undesired turbulent behaviour of the fluid during this flight condition and are significantly intensified nearer the tips of all the aerodynamic surfaces. Mitigating this turbulence is typically achieved by introducing winglets on the aerofoil, which aids the transition from laminar to turbulent flow at higher velocities. However, this research did not consider implementing this strategy as the FDM fabrication method could not provide the necessary stiffness required for these winglets.
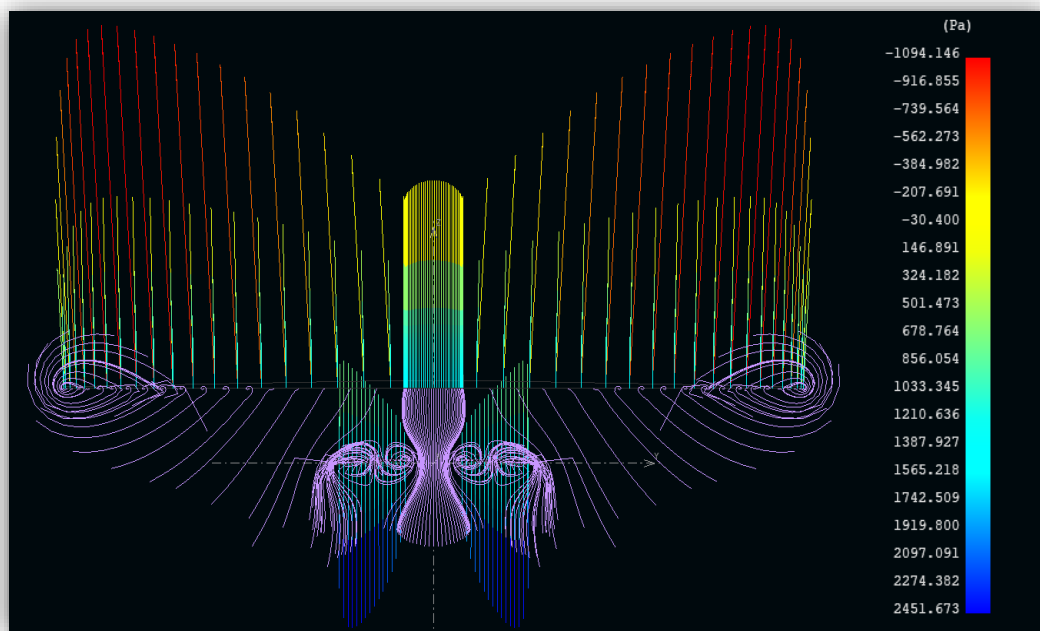
Figure 4-9: Dynamic pressure and fluid turbulence on aerodynamic surfaces

4.1.1.3 Stability and sensitivity Analysis

The stability of an aerial vehicle is an important consideration that impacts vehicle manoeuvrability, which consequently affects flight efficiency. Achieving stability can not only provide more vehicle control but can also increase the vehicle's endurance by reducing drag caused by excessive and continual actuator deflections. Therefore, attaining an aerodynamic configuration, that maintains steady flight in autonomous modes, is critical for ensuring optimal performance. However, for an aerial vehicle to become aerodynamically stable, certain prerequisites are required for confirming longitudinal and lateral stability. The first condition requires the vehicle's pitching moment C_m to have a negative slope relative to its AoA. This negative slope guarantees that any unnecessary pitching moment experienced by the vehicle due to wind gusts can be naturally damped, resulting in controlled flight.

The second condition is for the vehicle to have a positive lift coefficient C_L when $C_m = 0$. These prerequisites are essential for preserving accurate and consistent flight characteristics irrespective of environmental factors. These requirements can be seen in *Figure 4-10* and *Figure 4-11*, which depict the precise conditions for stable flight. The steepness of the negative slope found in *Figure 4-10* is suitable for this design and application; however, an aircraft that demands the utmost stability requires a more acute slope. It can also be seen that the aerodynamic configuration is most stable at an $AoA = 0.5^0$ and has a corresponding lift coefficient of $C_L = 0.56$. This positive lift coefficient ensures the vehicle remains airborne at the current conditions.

Figure 4-12 and *Figure 4-13* reveal the velocity and glide ratio of the aerodynamic surfaces versus the associated pitching moment. These results indicate that stable flight can be achieved at a cruise velocity of $V_{cruise} = 26\ m/s$, and at this speed, the vehicles corresponding glide ratio is $\frac{C_L}{C_D} = 23$. These outcomes provide confidence for the vehicle's aerodynamic configuration and foil selections.
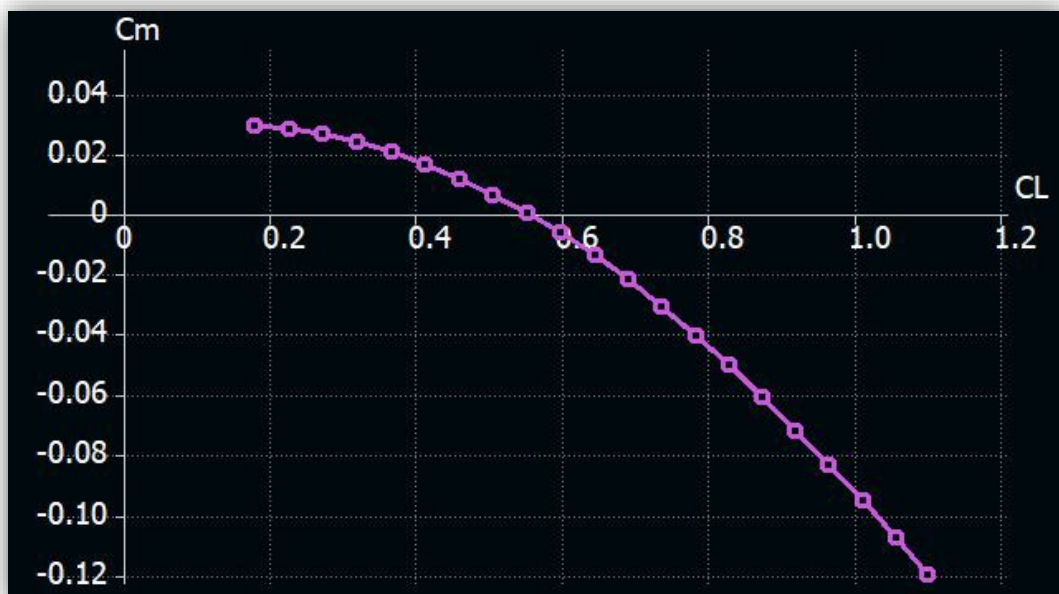
Figure 4-10: Pitching moment vs lift coefficient for Airslipper configuration
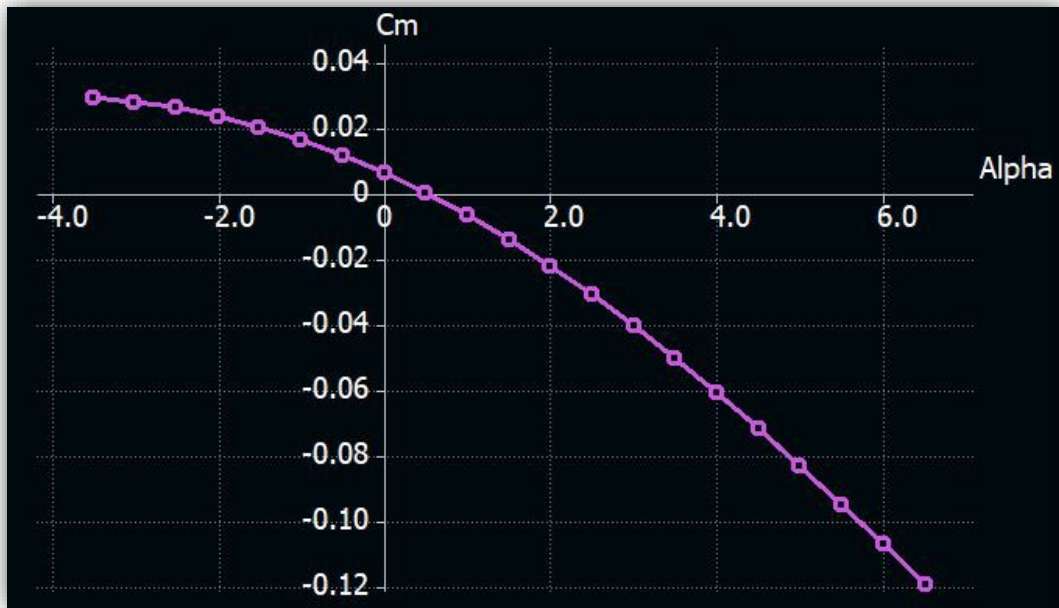
Figure 4-11: Pitching moment vs AoA for Airslipper configuration

However, genuinely gauging the longitudinal and lateral stability of a vehicle requires a focused stability analysis using XFLR5's eight natural damping modes. The longitudinal stability is comprised of phugoid and short period modes, whilst spiral, roll damping and Dutch roll modes are utilized for lateral stability. Combining these natural modes generates a comprehensive analysis of the vehicle's stability which can aid the control gains and response plots for stipulated controller implementations. Therefore, the stability analysis performed on the *Airslipper* design was conducted using the previously attained cruise velocity of $V_{cruise} = 26\,m/s$ at an inclination angle of $AoA = 0.5^0$.
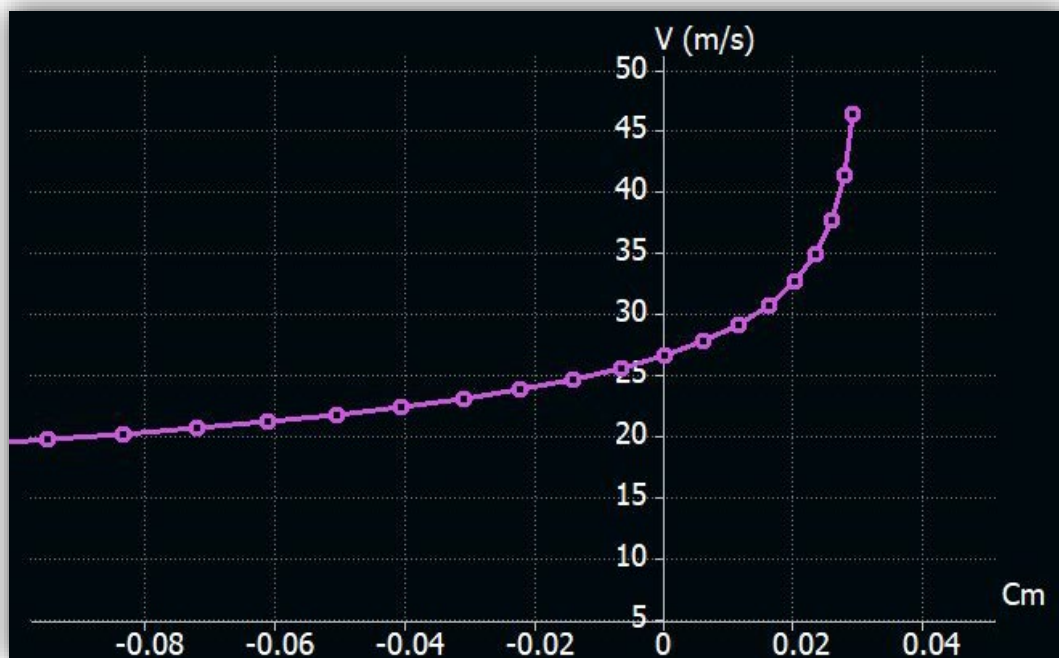
Figure 4-12: Cruise velocity vs pitching moment for Airslipper configuration
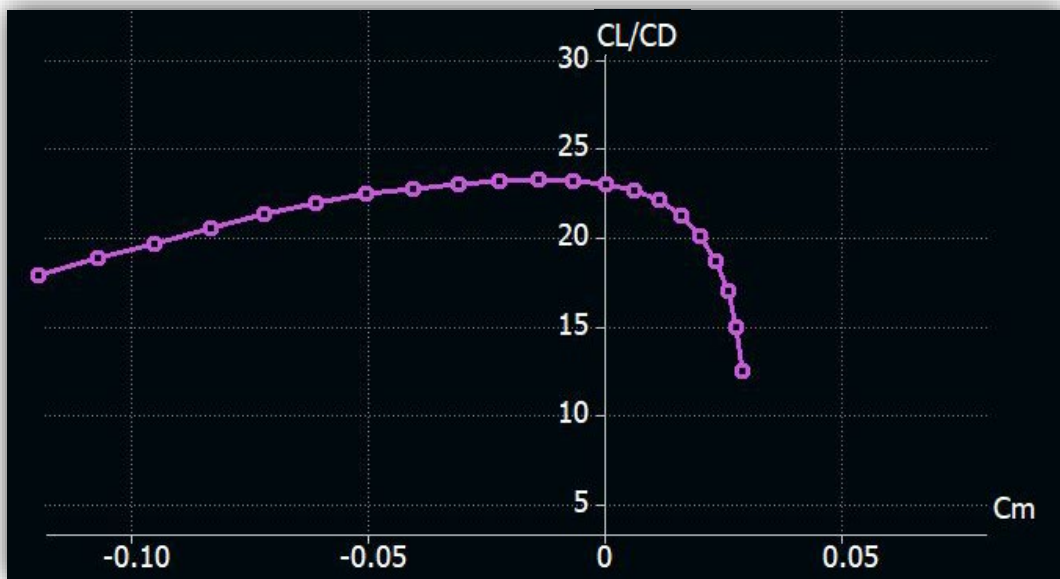
Figure 4-13: Glide ratio vs pitching moment for Airslipper configuration

However, to additionally assess the vehicles sensitivity and dynamic response during this stability analysis, the payload weight was assigned a gain value of $2.5\ kg$ per control, and the use of three control levels gave varying payload of $0kg, 2.5kg$ and $5kg$. This control gain allowed the vehicle to be analysed for an empty and overloaded flight. *Figure 4-14* and *Figure 4-15* reveal the complex eigenvalues of the longitudinal and lateral modes on a root-locus graph. The 'Real' axis represents the natural damping of the stability modes, whilst the 'Imaginary' axis represents the associated oscillating frequencies.
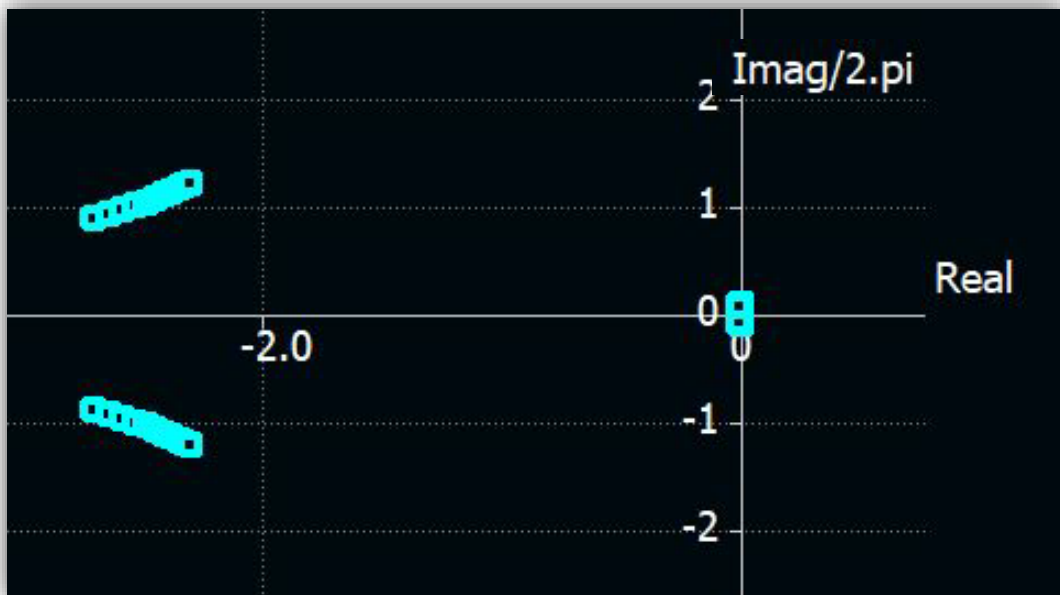
Figure 4-14: Complex eigenvalues for payload sensitivity on longitudinal root-locus

Figure 4-15: Complex eigenvalues for payload sensitivity on lateral root-locus

The results illustrate negative damping for both longitudinal and lateral stability modes, indicating the vehicle is dynamically stable at the current configuration. It can also be seen that as the payload weight increases, the vehicle becomes less stable but subsequently has a more pronounced response frequency. These findings are verified by the time responses of the short period longitudinal mode seen by *Figure 4-16* and *Figure 4-17*. These figures show the underdamped pitch and pitch rate responses of this mode and substantiate the increased stability performance for a lighter payload weight. *Figure 4-18* shows the cruise velocity-time response of both the short period and phugoid modes and suggests a significant difference in their numerical frequencies, which confirms these modes do not conflict with each other. This result suggests that the *Airslipper* design, and its flight conditions, provide a suitable and stable configuration for unmanned operation.
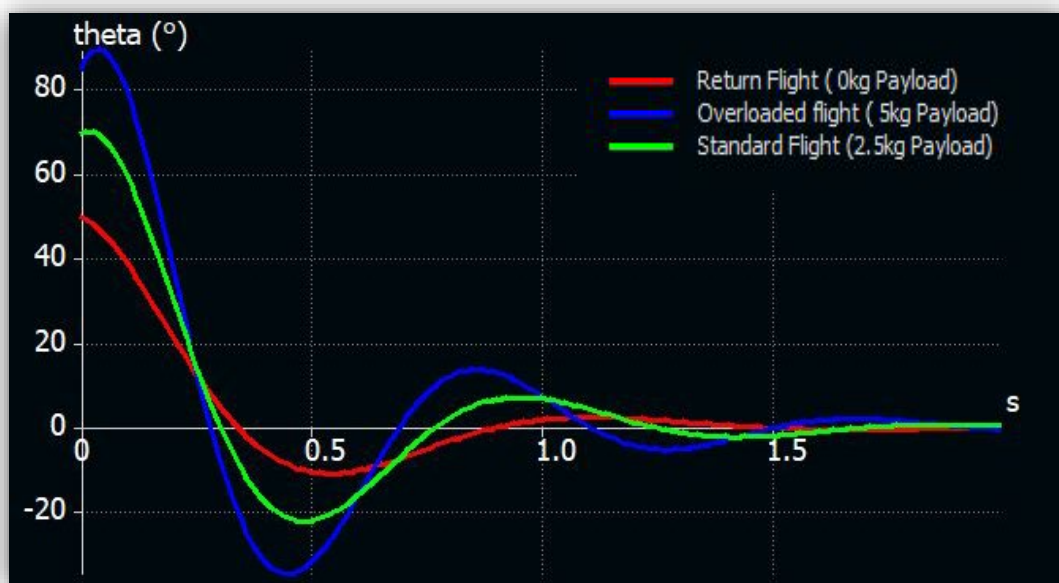
Figure 4-16: Pitch angle time response of short-period mode for payload sensitivity
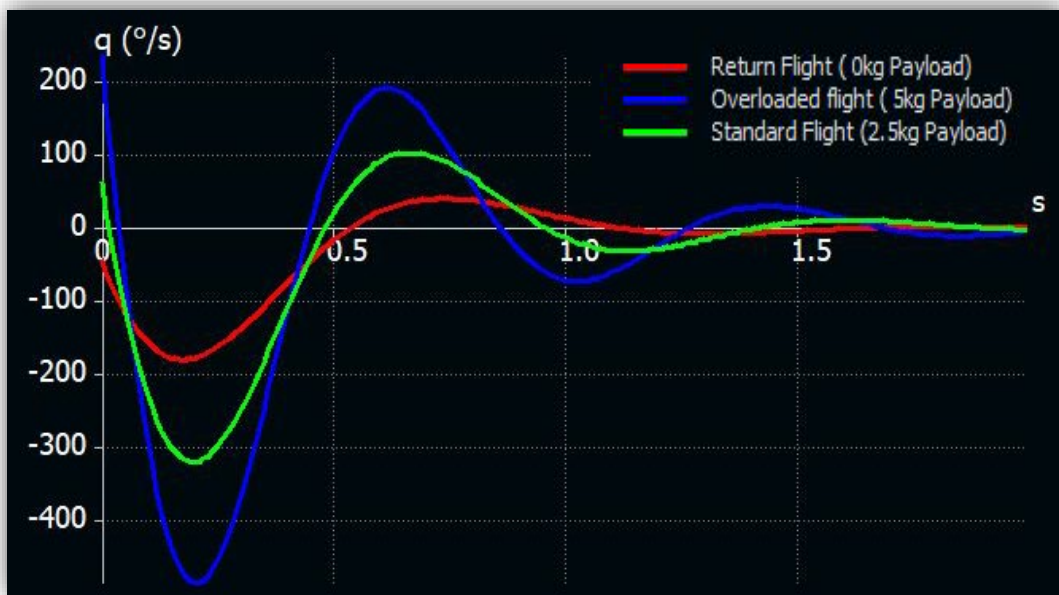
Figure 4-17: Pitch rate time response of short-period mode for payload sensitivity
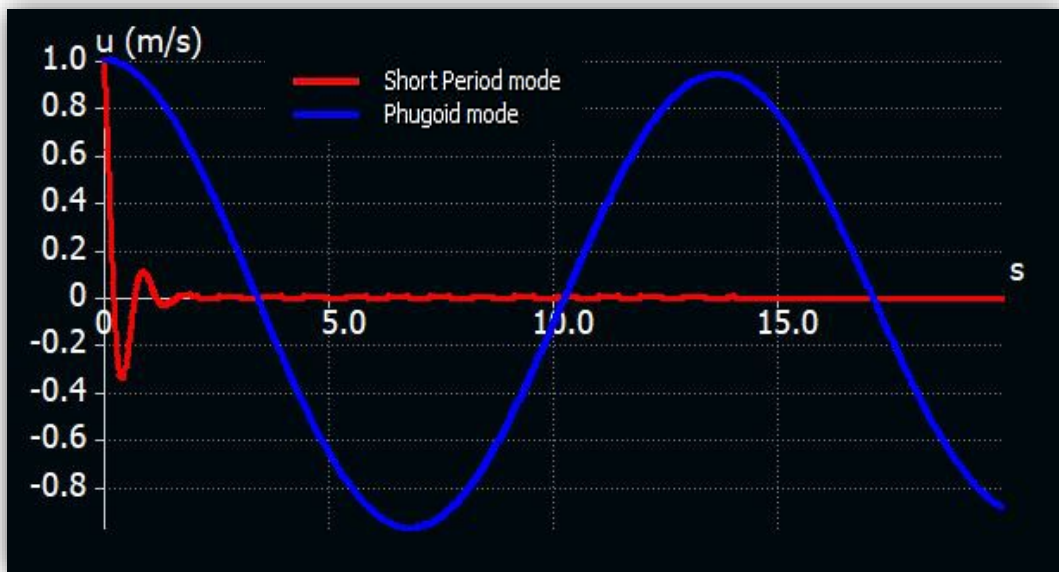
Figure 4-18: Flight velocity time response on longitudinal stability mode

4.2 Final design

From outcomes of the relevant analyses and considerations given by Chapters 2 and 3, the final *Airslipper* design was established. This design combined the necessary features of an unmanned system which conformed to legislation standards and applicational requirements. The *Airslipper* was 3D modelled in the SolidWorks CAD software package and was constructed in a technique that justified the FDM fabrication method. This meant certain parts were segmented to account for easier manufacturing and some parts were adapted to fit specific hardware limitations. This section provides a visual impression of the final design through detailed assembly renders. These graphics demonstrate the positioning of the *Airslipper's* components and offer various perspective views.

4.2.1 Full assembly renders

Figures 4-19 to *4-26* illustrate the renders of the *Airslipper* design. However, these renders only show the parts and modules that require FDM fabrication, except for the motors, servos, and propellers, which are considered off-the-shelf components. The colours associated with these figures are not representative of the final prototype but are instead used to clarify the positioning of individual components.
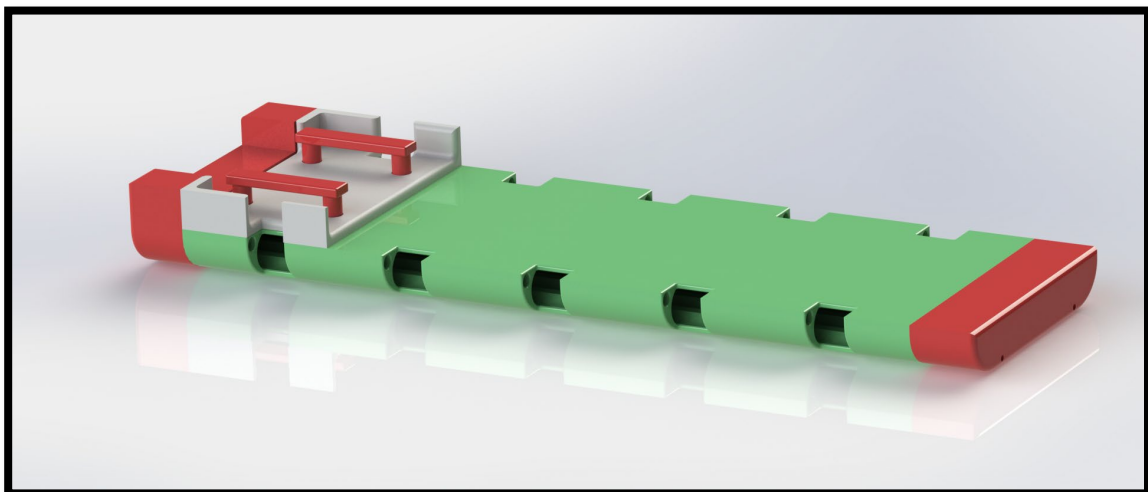
Figure 4-19: Render of the 18650 Li-Ion battery pack module
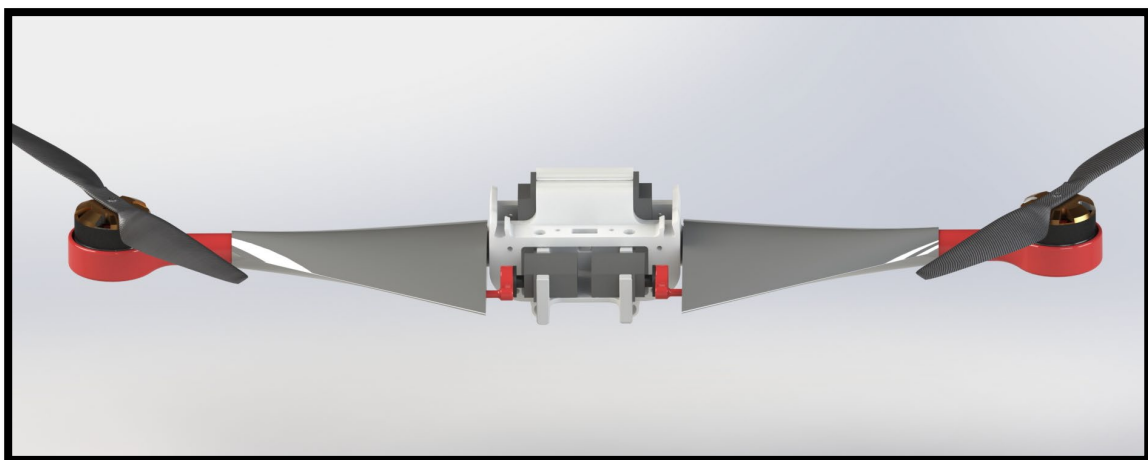
Figure 4-20: Render of the propulsion system and aerodynamic control surfaces
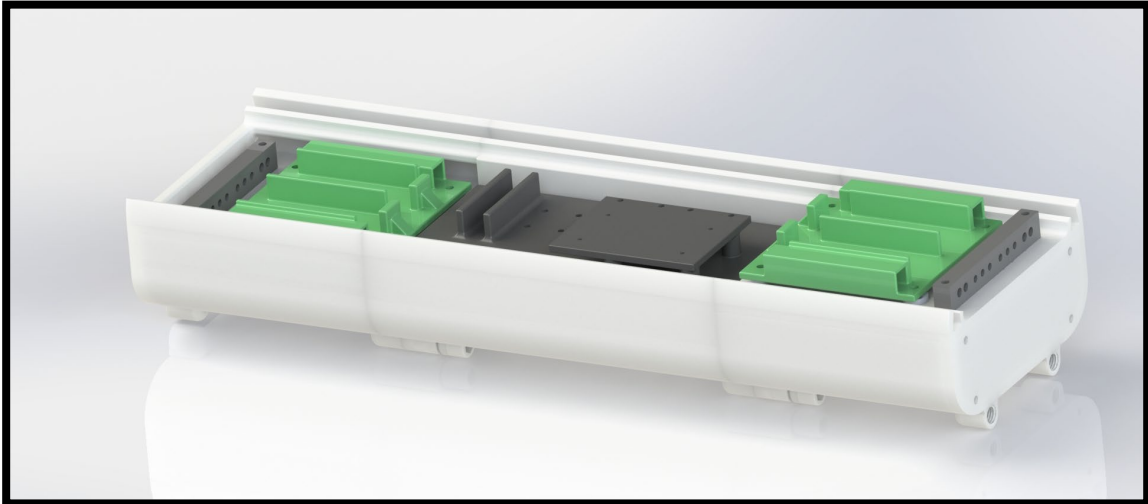
Figure 4-21: Render of the bottom fuselage with electronic housing compartments
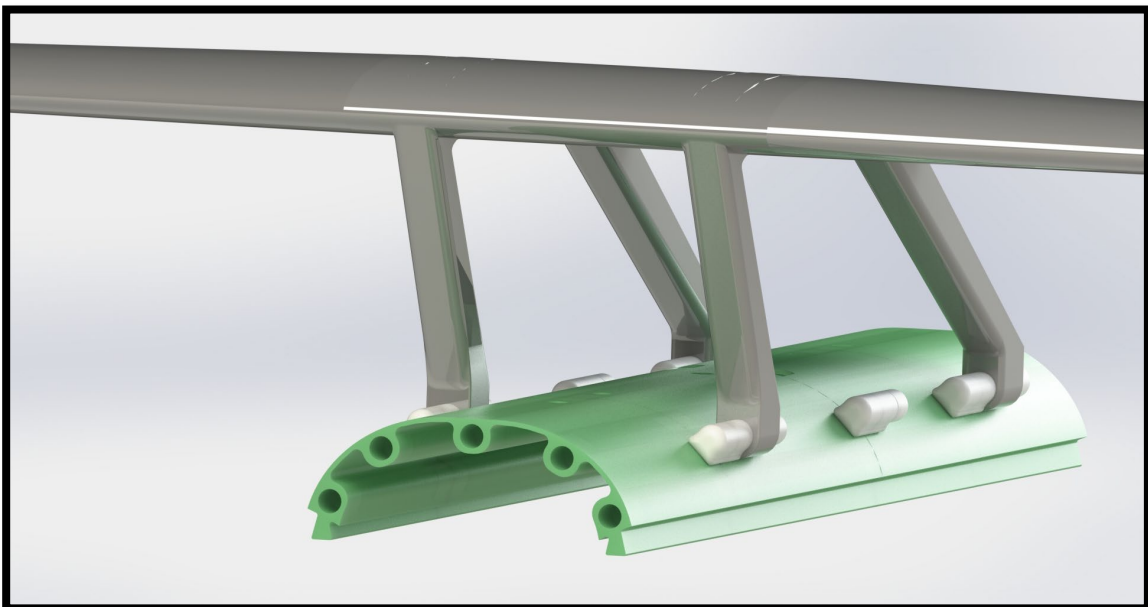
Figure 4-22: Render of the top fuselage with aerofoil supports and M10 bolt connectors
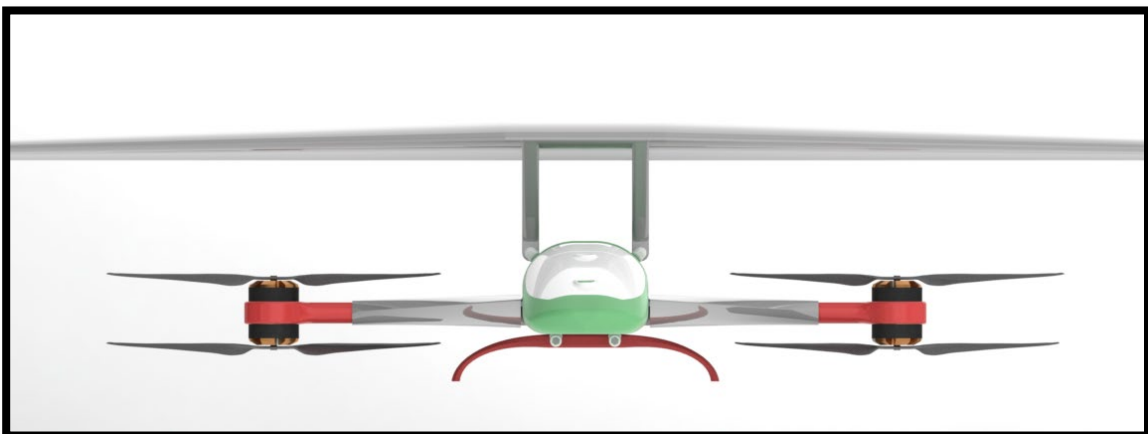
Figure 4-23: Full assembly front view render of Airslipper in VTOL mode

Figure 4-24: Full assembly below view render of Airslipper in VTOL mode
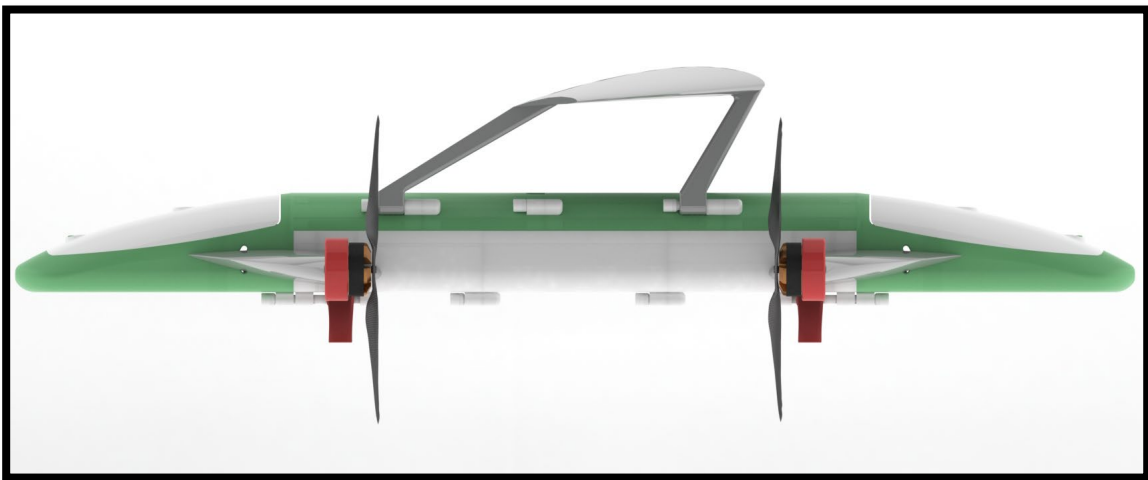
Figure 4-25: Full assembly side view render of Airslipper in FW mode

Figure 4-26: Full assembly behind view render of Airslipper in FW mode

4.2.2 CFD simulations

The purpose of conducting an array of CFD analyses within this research was to gain an understanding of fluid interaction and fluid interference for the *Airslipper* design. The analyses were conducted using the SolidWorks flow simulation toolbox and were setup to match the flight conditions of the previous plane analyses. Due to the FDM fabrication method and the literature given in Chapter 2, a surface roughness value of $105\mu m$ was used in conjunction with a gravity component to reinforce solution accuracy. A climb velocity of $V_{climb} = 2.5\,m/s$ and cruise velocity of $V_{cruise} = 26\,m/s$ was set to the corresponding flight modes and provided a full spectrum of results for the *Airslipper's* operation. Outcomes of the simulations were graphically represented by a combination of cut plots, surface plots and flow trajectories to fully gauge the interaction of fluid over the different aerodynamic surfaces and modules.

4.2.2.1 Fuselage

The fuselage of the *Airslipper* followed the design approach of Chapter 3 and is comprised of several individual parts that are fastened to achieve a final fuselage. Although this design strategy can become problematic, it allowed for simplified manufacturing and assembly whilst maintaining aerodynamic and structurally abilities. Assessing the competency of this fragmented design required the conduction of a CFD simulation on the fuselage with the inclusion of control surfaces. Results of the analysis are shown in *Figure 4-27* and reveal increased surface pressure zones at the leading edges of both the fuselage and control surfaces. A further inspection exposes the low-pressure pockets along the top of the control surfaces. These negative pressure regions are understandable and correspond to the previously attained XFLR5 plane analysis results.

Due to the unique fuselage design and placement of the aerodynamic controls, this analysis demonstrated control surface interference through an increase in fluid vorticity. This vorticity development is a result of extreme turbulence and boundary layer formation near these contact regions and thus became a concern for the *Airslipper's* performance. However, the Global Goal (GG) results of *Table 4-3* reveals a maximum turbulence intensity of 0.524 % at a maximum turbulent energy of $0.029\,J/kg$. These outcomes indicate complete fluid recovery from a turbulent to laminar flow state before reaching the leading edge of the second control surface. These findings mitigate the control placement concerns and express confidence for minimal performance deviations. *Figure 4-28* shows the same CFD simulation but from a front-on view. The pressure contours in the fluid reveal no significant variations, but slightly higher values can be seen at the leading edges of the fuselage and control surfaces. The fluids vorticity is greatest nearer the upper and lower regions of the fuselage. However, this increase is mostly due to the surface roughness associated with the FDM fabrication method.

Table 4-3: CFD simulation GG results of the fuselage during FW mode

| Global Goals (GG)	Unit	Value
Average dynamic pressure	MPa	396.76
Average fluid shear stress	MPa	0.73
Average fluid friction force	N	4.78
Maximum turbulent energy	J/kg	0.029
Maximum turbulence intensity	%	0.524

Surface and Fluid Contours

Fluid Streamlines

101151.58   101452.45

146.02   178.29

Pressure [Pa]

Vorticity [1/s]
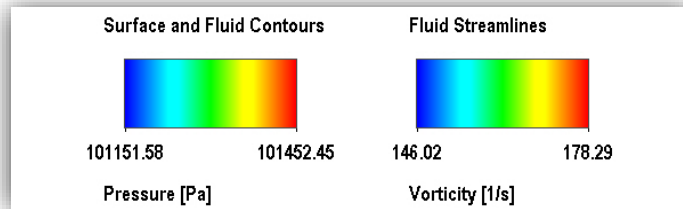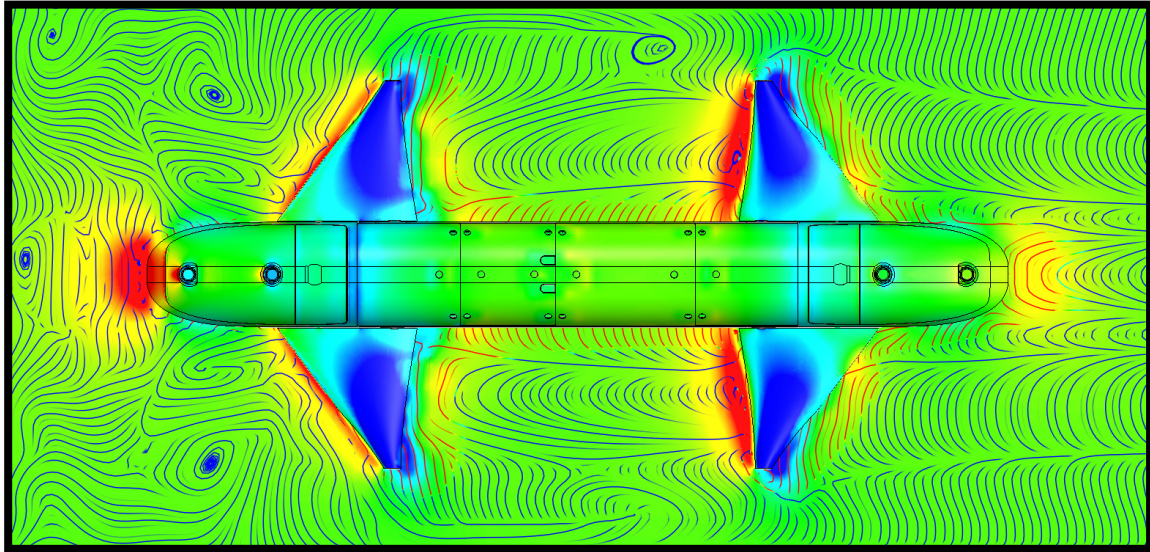
Figure 4-27: Top view CFD graphical results of the fuselage during FW mode

Surface and Fluid Contours

Fluid Streamlines

101151.58   101452.45

-2.58   20.00

Pressure [Pa]

Vorticity [1/s]
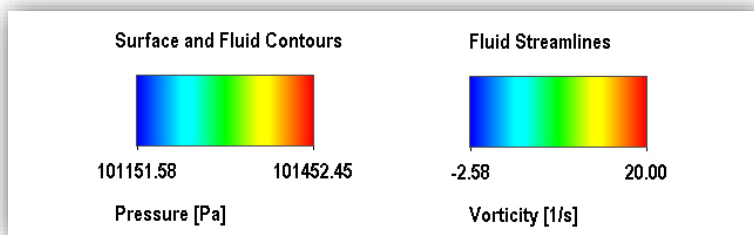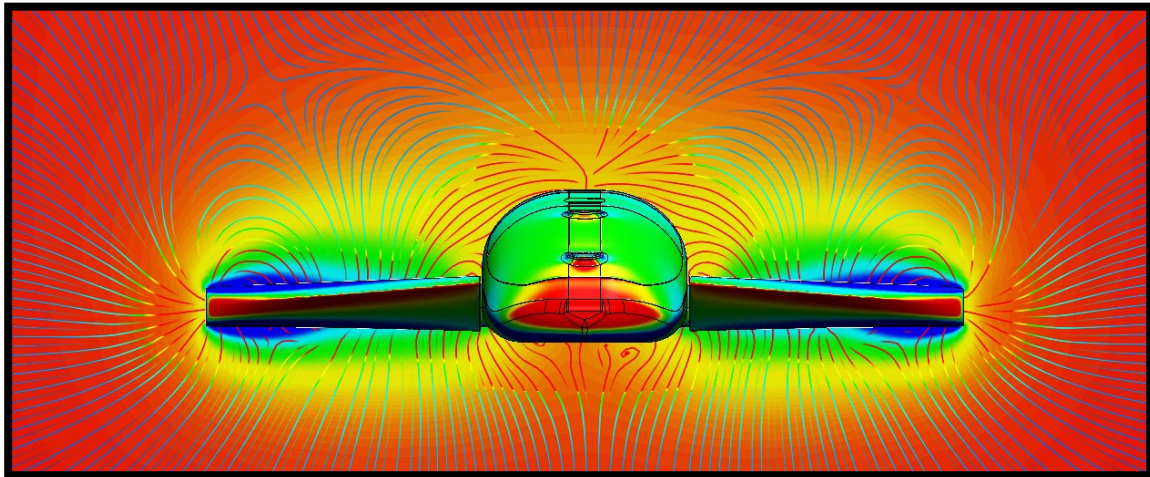
Figure 4-28: Front view CFD graphical results of the fuselage during FW mode

4.2.2.2 Propulsion system in VTOL mode

The final propulsion system of the *Airslipper* was arranged to mimic the results of the optimization previously attained in Chapter 3. By implementing this information, a CFD simulation was conducted on the propulsion system during its VTOL flight mode. The climb velocity was set to $V_{climb} = 2.5\ m/s$ and the propellers rotation rate was set at $n = 6570\ rpm$ to provide an understanding of the fluid behaviour during take-off procedures. Results of the simulation are shown by *Figure 4-29* and *Figure* 4-30, which reveal cut plots of the top and side views, respectively. Equally to the fuselage simulation, a concern of airflow disturbance over the control surface was apparent. These figures demonstrate an increase in vorticity and surface pressure near these regions, which is indicative of fluid interference. However, the GG results shown in *Table 4-4* reveal negligible comparison between generated thrust forces and fluid shear stress values for a configuration that contains the control surface and for one that does not. These findings suggest that the reduced area exposed to the propeller's downforce minimizes force exerted on this location, which assures minimal influence in propulsion performance.

Table 4-4: CFD simulation GG results of the propulsion system during VTOL mode

Global Goals (GG)	Unit	With control surface	Without control surface
Average dynamic pressure	MPa	86.23	19.85
Average fluid shear stress	MPa	6.64	4.43
Maximum normal force (thrust force)	N	28.62	31.74
Maximum turbulent energy	J/kg	0.008	0.006
Maximum turbulence intensity	%	11.64	3.6
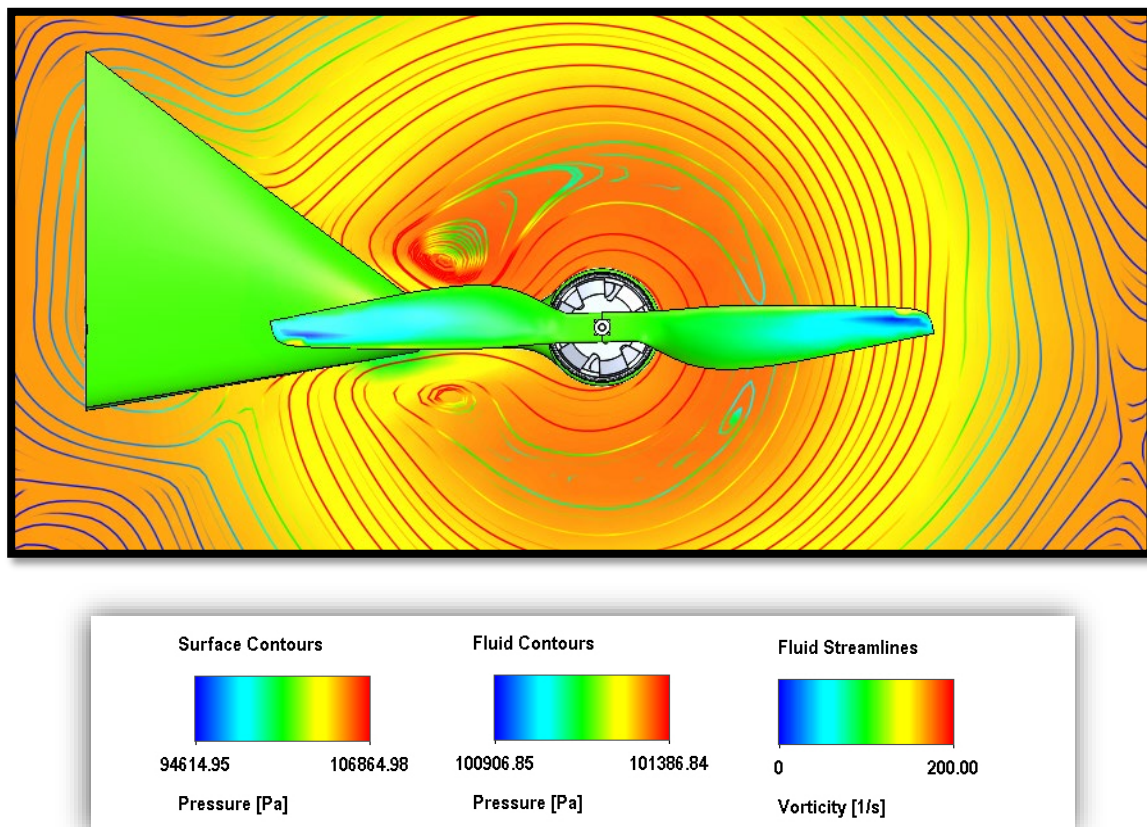
Figure 4-29: Top view CFD graphical results of the propulsion system during VTOL mode
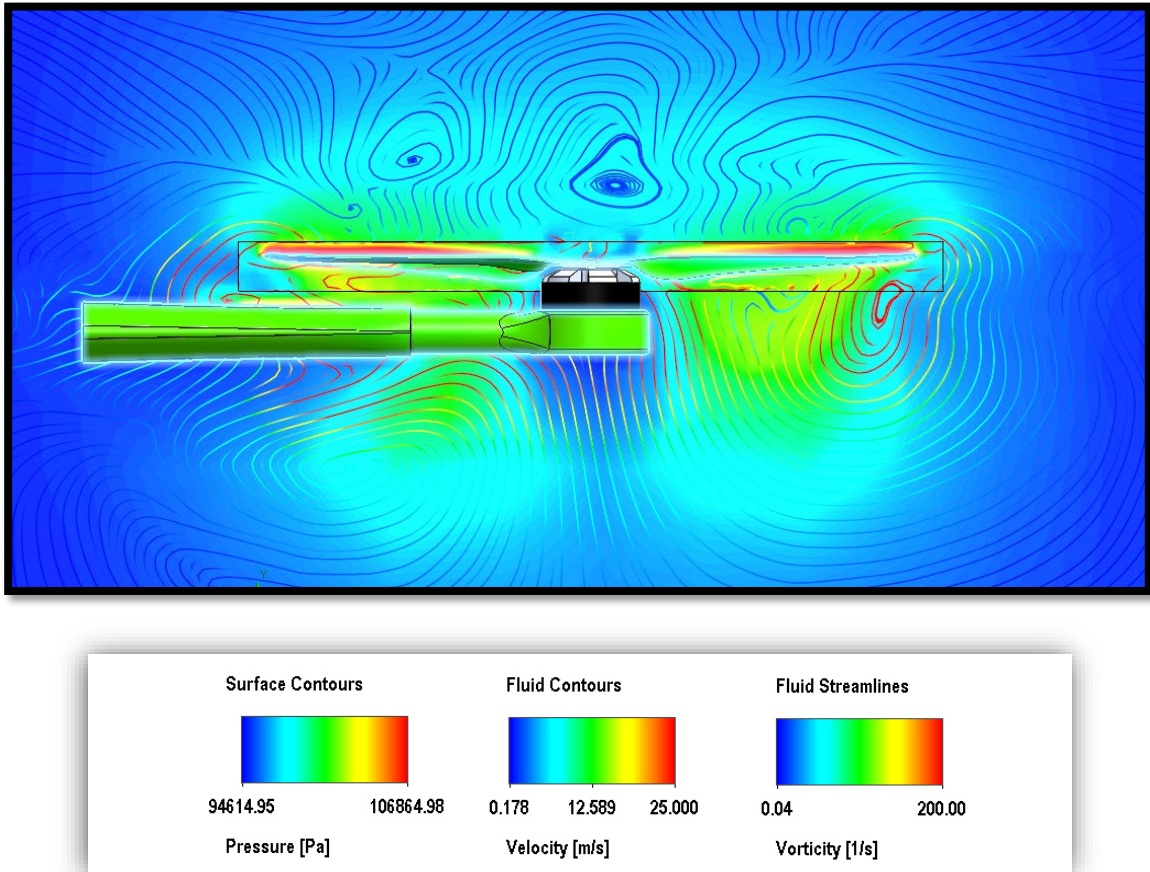
Figure 4-30: Front view CFD graphical results of the propulsion system during VTOL

4.2.2.3 Propulsion system in FW mode

Setting the cruise velocity to $V_{cruise} = 26\,m/s$ and tilting the propeller to its forward position, the propulsion system was CFD simulated for FW mode. Results are shown in *Figure 4-31,* and *Figure 4-32*, which reveal cut plots of the system and illustrate a reduction in fluid pressure within the propellers operating region. *Table 4-5* displays the GG values of the simulation for the current setup and for one that does not have the control surface attached. It can be noted that an additional $3N$ of maximum thrust force is present for a setup without any control surface. However, these findings suggest no significant disruption in fluid behaviour and are considered minimal for the application. Thus, the impact of control surfaces within this design does not interfere with the *Airslipper's* flight characteristics or performance.

Table 4-5: CFD simulation GG results of the propulsion system during FW mode

Global Goals (GG)	Unit	With control surface	Without control surface
Average dynamic pressure	MPa	402.36	395.17
Average fluid shear stress	MPa	9.74	6.84
Maximum normal force (thrust force)	N	9.85	12.79
Maximum turbulent energy	J/kg	0.042	0.03
Maximum turbulence intensity	%	0.34	0.28

Surface Contours
87753.41   110859.45
Pressure [Pa]

Fluid Contours
92339.43   102764.93
Pressure [Pa]

Fluid Streamlines
0   20.00
Vorticity [1/s]
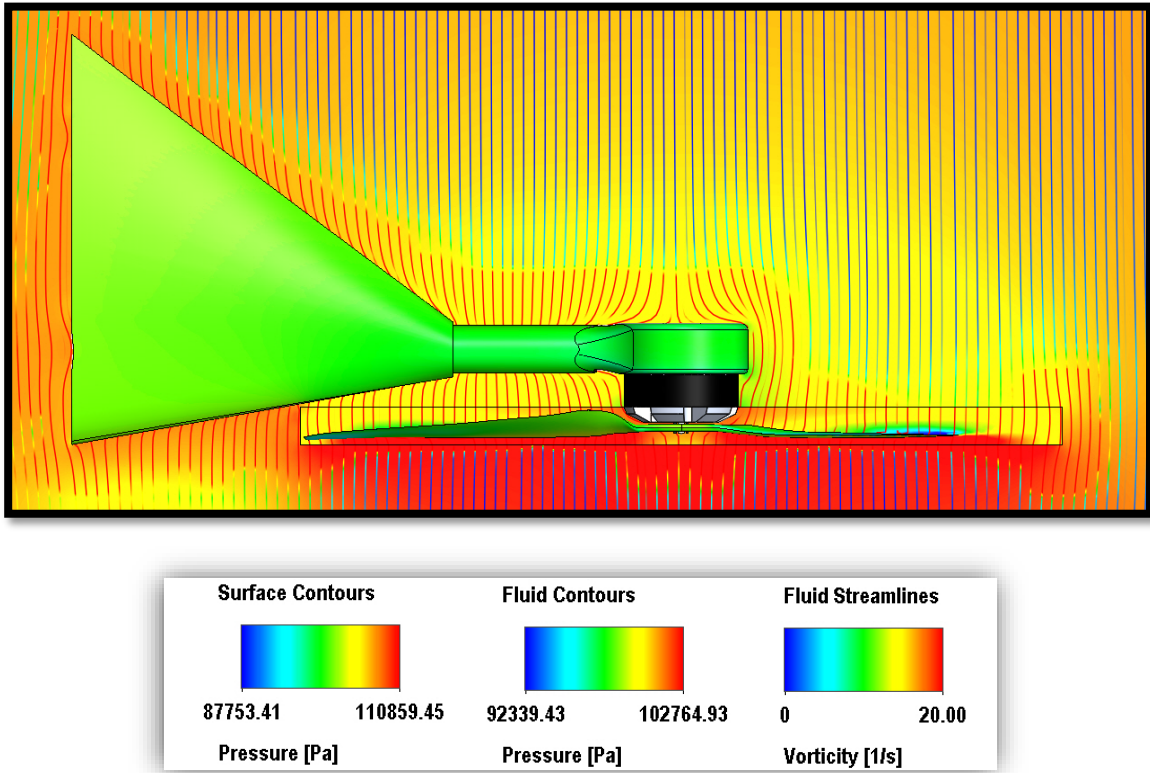
Figure 4-31: Top view CFD graphical results of the propulsion system during FW mode

Surface Contours
94204.20   101571.89
Pressure [Pa]

Fluid Contours
87753.41   110859.45
Pressure [Pa]

Fluid Streamlines
0   20.00
Vorticity [1/s]
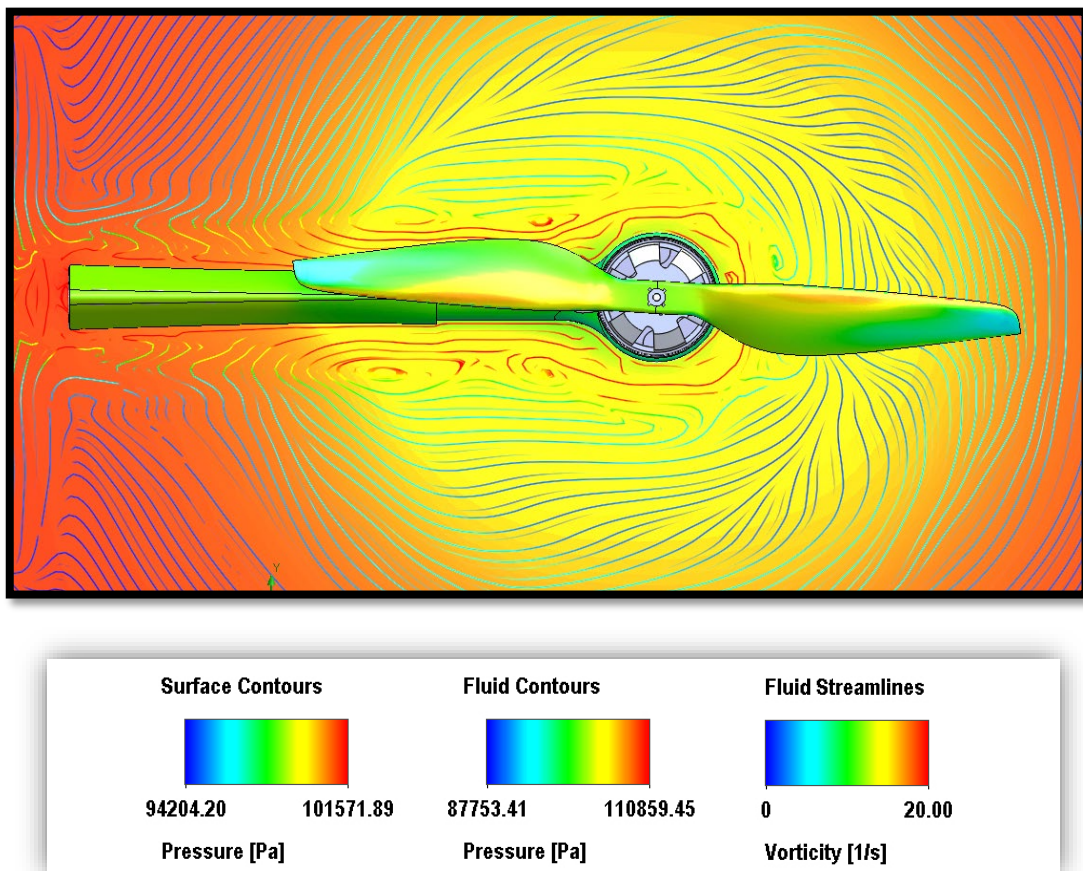
Figure 4-32: Front view CFD graphical results of the propulsion system during FW mode

Due to the propellers co-axial configuration and proximity to the aerofoil in FW mode, a validation simulation was conducted to ensure no interference was present. The simulations setup parameters were identical to the previous, and results are shown in *Figure 4-33*. The fluid exiting the leading propeller experiences extreme turbulence and vorticity, just as the previous simulation. However, due to the relatively large air gap between the co-axial propellers, the fluid manages to recover from a turbulent to normal state before entering the second propulsion system. This outcome is backed by the literature found in Chapter 2 and indicates no performance deviations for this type of configuration with this amount of air gap. The concern surrounding the aerofoil's interference with this current configuration is apparent; however, the figure displays no extreme variations in fluids pressure contours or vorticity. These findings signify a capable design at the stipulated FW mode and should theoretically operate as intended.
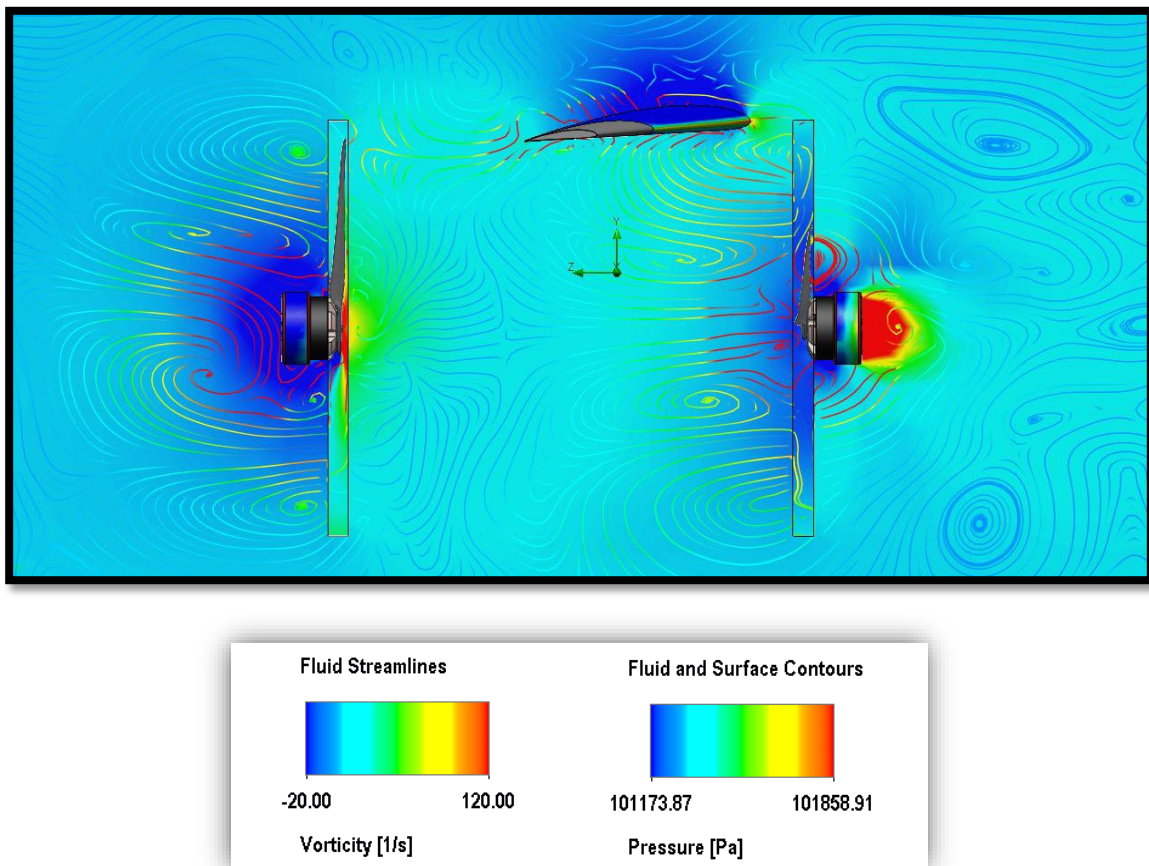
Figure 4-33: Side view CFD graphical results of the fluid disturbance in FW mode

4.2.2.4 Aerofoil

Performing a CFD simulation on an aerofoil is necessary for ensuring the correct flight characteristics are observed before conducting any experimental testing. Therefore, due to the *Airslipper's* design, a CFD simulation was used to investigate fluid interaction between the fuselage's top surface and aerofoil's bottom surface. *Figure 4-34* reveals a cut plot of these results and shows the development of boundary layers at the outer surfaces of both components. This boundary layer formation consequently generated higher vorticity and velocity values in these regions. However, due to the consistently parallel streamlines within the fluid, these boundary layers never intersect. These findings are reinforced by the GG values seen in *Table 4-6*, which show steady dynamic pressures

and lift forces of **407.63 MPa** and **106.32 N**, respectively. These results imply no fluid disturbance between the fuselage and aerofoil is present during this flight mode and also correspond with the previously attained plane analysis results.

Table 4-6: CFD simulation GG results of the aerofoil during FW mode

Global Goals (GG)	Unit	Value
Average dynamic pressure	MPa	407.63
Average fluid shear stress	MPa	1.13
Maximum normal force (lift force)	N	106.32
Maximum turbulent energy	J/kg	0.001
Maximum turbulence intensity	%	0.114
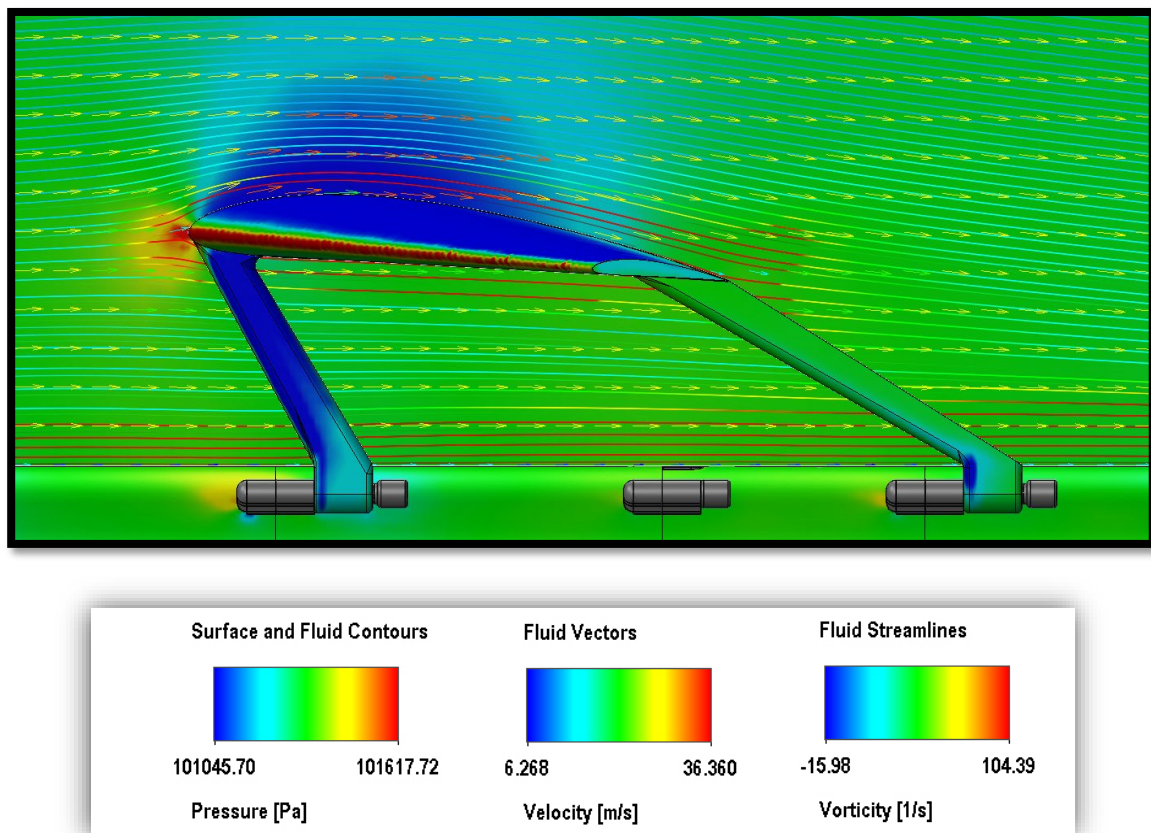
Figure 4-34: Side view CFD graphical results of the aerofoil during FW mode

Figure 4-35 shows a cut plot of the aerofoils front view during the vehicles cruising mode. This figure demonstrates the fluid's interaction and illustrates pressure intensities which are consistent with a standard foil design. The simulation also shows how the aerofoil experiences extreme turbulence and vorticity at both ends of its tips, representative of the fluid streamlines in the XFLR5 analyses. The low-pressure pockets located near the tips are an indication of the aerofoils lifting line, which are consistent with the previous outcomes. These CFD findings are suggestive of a fully functional aerofoil design and confirm the aerofoils implementation within the *Airslipper's* design. However, the XFLR5 plane analysis specifically displayed a sizeable bending moment experienced by the aerofoils middle section. This moment creates high-stress concentrations and localised

shearing forces in this region. As a result, the next section performs an FEA on the aerofoil to investigate this bending moment and confirm the viability of the FDM fabrication method.
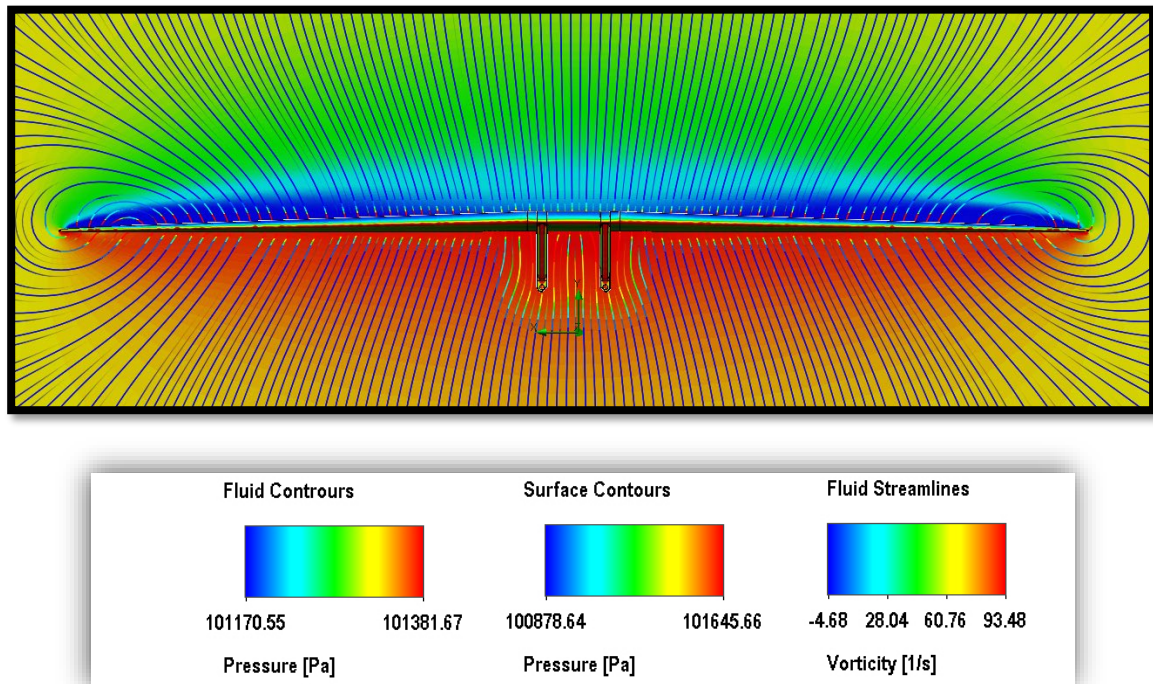
Figure 4-35: Front view CFD graphical results of the aerofoil during FW mode

4.2.3 FEA simulation

Due to the anisotropic nature of FDM fabrication, components that experienced localised pressure and stress variations in the CFD simulations require further structural analysis. This is needed to verify the strength and robustness of a part before undergoing real-world applications. The areas of interest within the *Airslipper's* design include the aerofoil and its supports. These parts are fundamental to the UAV's operation and thus need to prove their structural integrity against the fabrication's material properties.

4.2.3.1 Structural analysis of Aerofoil

As previously mentioned, the extreme pressures encountered by an aerofoil during flight results in a high bending moment at its centre section. The quantity of this bending moment is directly proportional to the aerofoils lift generation and lift distribution profile. Therefore, it can be noted that the aerofoils associated geometrical parameters and the vehicles flight velocity constitute the greatest threat to the aerofoil's integrity. The FEA simulation was conducted on the *Airslipper's* aerofoil at cruise conditions, and the fluid shear stress values were imported from the CFD simulation, which provided the necessary bending moments. *Figure 4-36* and *Figure 4-37* reveal the results of the 1st and 3rd principle stresses experienced by this component. The simulation outcomes graphically illustrate the areas of concern, as the maximum tensile and compressive stress values of $\mathbf{1.28\,MPa}$ and $\mathbf{0.19\,MPa}$ are indicated, respectively. These results, however, are below the $\mathbf{26.4\,MPa}$ Ultimate Tensile Strength (UTS) of the material and thus suggest proficiency in the PLA fabrication material and design.
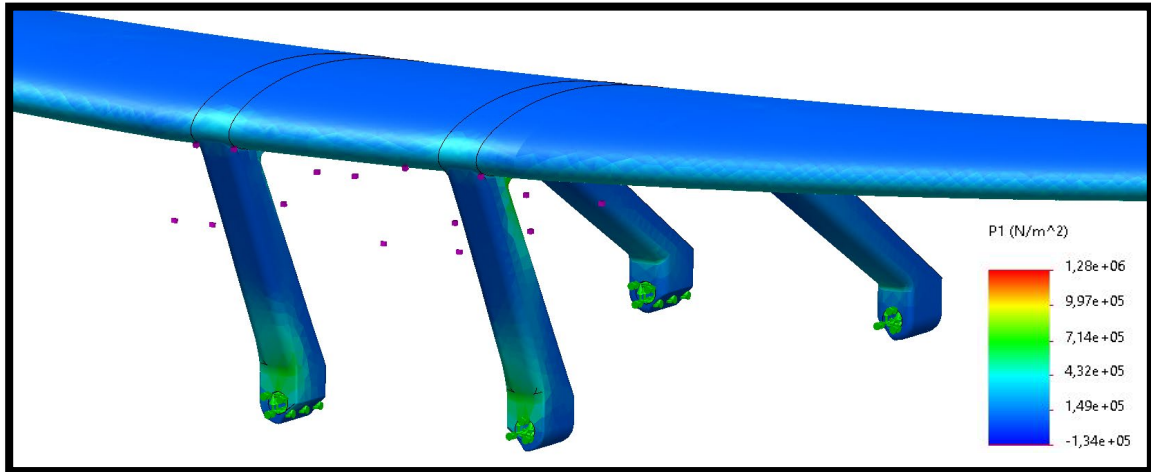
Figure 4-36: Graphical FEA 1ˢᵗ principle stress results of the aerofoil during FW mode
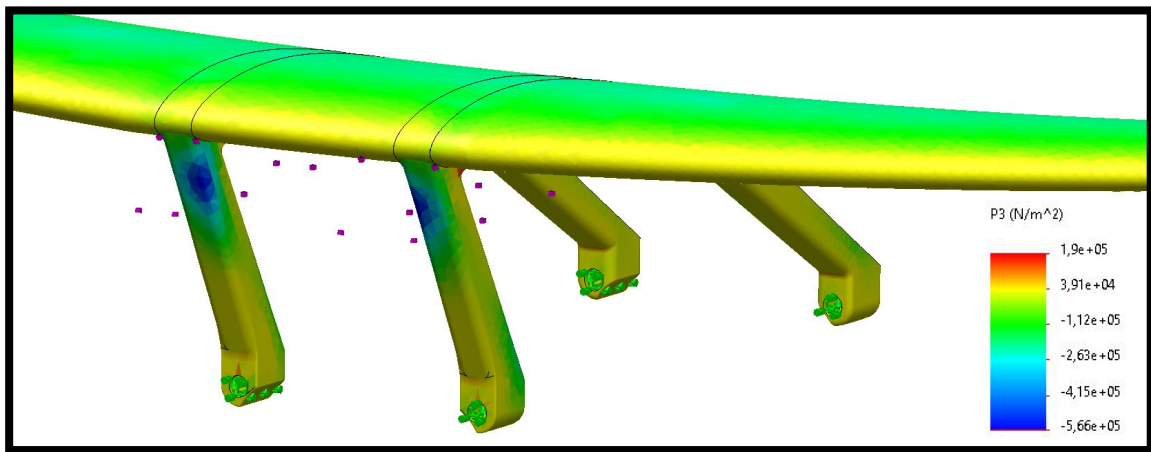
Figure 4-37: Graphical FEA 3ʳᵈ principle stress results of the aerofoil during FW mode

4.3 Summary of Chapter 4

The analysis and simulation results attained in this chapter provided critical airflow information during the vehicles flight VTOL and FW flight modes. The execution of XFLR5's stability and sensitivity analysis on the *Airslipper's* aerodynamic surfaces confirmed vehicle's stability for both return and overloaded flight scenarios. The results also demonstrated that the configuration exhibited the most stable flight at an $AoA = 0.5^0$ and at cruise velocity of $V_{cruise} = 26\,m/s$. These findings, along with longitudinal mode time response graphs, reassured the design for controlled flight in an unmanned mode. This chapter also displayed several perspective renderings of the *Airslipper* design. This CAD model also allowed for an array of CFD simulations to be performed on the fuselage, propulsion system and aerofoil. Outcomes indicated consistent and expected fluid behaviour and concern of fluid interference surrounding the control surfaces in both VTOL and FW flight modes was mitigated by the GG performance results. An additional FEA simulation was conducted on the aerofoil, and the 1ˢᵗ and 3ʳᵈ principle stress results were graphically represented. These simulation findings correspond to the XFLR5 analyses, which confirms the *Airslipper's* operational characteristics for the intended application.

5. *FABRICATION, TESTING AND EVALUATION OF THE AIRSLIPPER*

After discussing the fundamental aspects of FDM and UAV technologies in Chapter 2, an initial design was conceptualized and optimized in Chapter 3. Chapter 4 then provided a full investigation on the *Airslipper's* aerodynamic surfaces and verified the vehicle's flight characteristics through a series of plane, stability, and sensitivity analyses. However, this chapter focussed on the FDM fabrication method and revealed the significance each critical FDM parameter had on a parts resilience to failure. Based on experimental results, the individual components within the *Airslipper* design were assigned a set of parameter values that considered attributes such as replaceability, dimensional accuracy, aerodynamics, and robustness. This process enabled the *Airslipper* to be successfully manufactured and assembled with the relevant electronic modules. By initializing a simple mission setup through a suitable GCS, the *Airslipper* UAV was experimentally tested in VTOL mode and provided the necessary results for validating the proficiency of this design. This chapter concluded by evaluating qualities associated with the *Airslipper* UAV against the application requirements and FDM fabrication method.

5.1 Influence of FDM printing parameters

The FDM fabrication method is distinctly different from routine UAV manufacturing processes, as aspects such as cost, modularity, flexibility, and recyclability significantly promote the choice of this method and reveal the continual development of this technology. However, as with most manufacturing techniques, FDM printing parameters have certain influential features that considerably impact the mechanical qualities of specific components. Therefore, implementing the FDM method within the *Airslipper* design requires individual components to be strategically set up to ensure the necessary qualities are attained. Achieving these standards for UAV production means executing a strategy that adds structural integrity and aerodynamic capabilities whilst minimizing additional complexities and undesirable effects.

5.1.1 Experimental correction factor for an FDM printed aerofoil

The advancement in FDM technology has progressed so rapidly that there does not currently exist any reliable FEA analysing platforms that are capable of replicating the intricacies associated with FDM fabricated parts. The most pertinent cause of this limitation is due to the apparent number of permutations that can occur when varying FDM parameters and setup strategies are selected. Other problematic issues are related to the inconsistencies between FDM printers and the materials they use. These challenging facets prohibit and discourage any form of FEA simulation for parts produced by this method.

However, this research aims to combat this problematic area through an experimental setup that couples a correction factor with a specific combination of printing parameters. Due to the findings of Chapter 4, a part that can substantially benefit from this strategy would be the *Airslipper's* aerofoil, which experiences high-stress concentrations and bending forces as seen in the previous CFD simulations and XFLR5 analyses. Due to the concern directed towards the layer adhesion capabilities of FDM printed parts, this experiment focussed on the layer shearing strength and resilience of a downscaled aerofoil section when exposed to these excessive bending moments.

By assigning a root chord value of $C_{r,experimental} = 80 \, mm$ to the aerofoil section, the experiment was conducted with nine individual specimens that shared the same geometric dimensions but varied in FDM parameters values. Each specimen was subjected to a shearing force at a predetermined location, and results were observed when the parts experienced failure. This failure point was adjudged valid for when specimens exhibited shearing of its layers or when significant plastic deformation occurred in terms of buckling. The failure load measured by each specimen was considered the new yield strength for that parameter combination, which can then be utilized within an FEA simulation to ascertain a correction factor. This correction factor is applied to the aerofoil so as to verify the design and fabrication method against the predefined stresses.

The experimental setup employed for this testing featured a precisely designed dual-leadscrew system that increased the force on the specimen, incrementally. This applied force generated a localized bending moment along the specimen's Z-axis, which allowed for consistent results. The nine uniquely built specimens were segmented into three smaller Batches that corresponded to a different layer height for each Batch. Batch 1 and 2 differed in infill percentage and wall thickness, whilst Batch 3 kept a constant wall thickness for determining the impact infill percentage had on the failure force. *Table 5-1* shows the experimental results for Bathes 1 and 2, whilst *Figure 5-1* displays these results in a graphical manner.

Table 5-1: Experimental failure testing results for Batch 1 and 2 specimens

		Batch 1			Batch 2		
Parameters	**Unit**	**1**	**2**	**3**	**4**	**5**	**6**
Layer height	*mm*	0,15	0,15	0,15	0,25	0,25	0,25
Wall thickness	*mm*	1,2	0,9	0,6	1,2	0,9	0,6
Infill percentage	%	10	15	20	10	15	20
Weight	*g*	64	66	68	64	66	68
Build time	*hours*	12,5	12,5	12,5	7,5	7,5	7,5
First failure load	*kg*	63.2	52.4	41.7	29.3	32.6	35.4
Second failure load	*kg*	61.1	49.8	43.9	30.9	34.5	37.5
Average failure load	**kg**	**62.1**	**51.1**	**42.8**	**30.1**	**33.5**	**36.5**
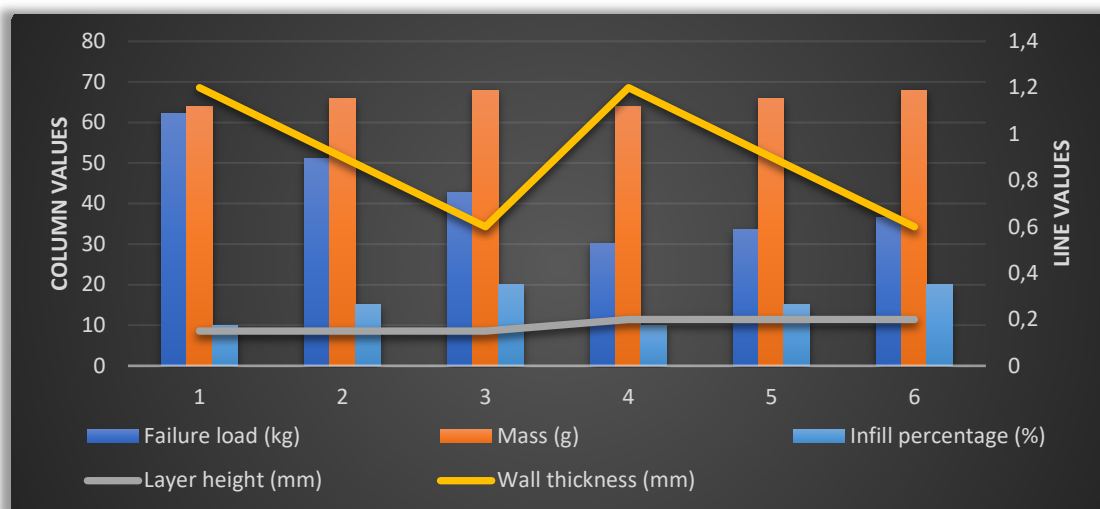
Figure 5-1: Graphical representation of specimen failure testing results for Batch 1 and 2

Each specimen was failure tested twice to guarantee fabrication accuracy and to attain a broader set of data points. The initial results of Batch 1 revealed a direct positive correlation between a specimen's wall thickness and failure load. However, the findings of Batch 3 demonstrated a negative correlation for the same test. This strange behaviour was a consequence of the increased layer, which, according to this experiment, is detrimental to a part's structural integrity. It can thus be noted that a reduction in layer height increases layer adhesion, but subsequently requires more printing time.

The results of Batch 3, seen in *Table 5-2* and *Figure 5-3*, indicate a similar failure pattern to Batch 2. However, the outcomes reveal improved failure loads for increased infill percentage, which suggests that its infill percentage directly influences the resistance of a part to shear, but so is its weight and printing time. *Figure 5-2* reveals the results of Batch 1 and demonstrates the variations in the specimen's infill percentage and wall thickness, respectively.

Table 5-2: Experimental failure testing results for Batch 3 specimens

Parameters	Unit	Batch 3		
		7	8	9
Layer height	*mm*	0,2	0,2	0,2
Wall thickness	*mm*	0,9	0,9	0,9
Infill percentage	%	10	15	20
Weight	*g*	56	66	76
Build time	*hours*	9,5	10.5	11.5
First failure load	*kg*	40.6	47.8	54.3
Second failure load	*kg*	42.4	47.4	55.7
Average failure load	***kg***	**41.5**	**47.6**	**55.1**
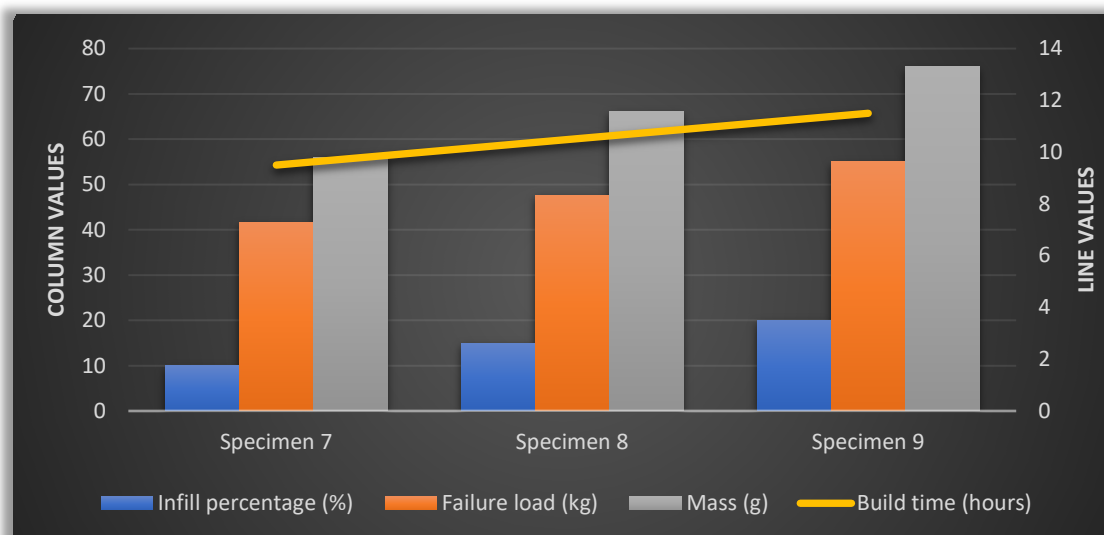
Figure 5-2: Graphical representation of specimen failure testing results for Batch 3
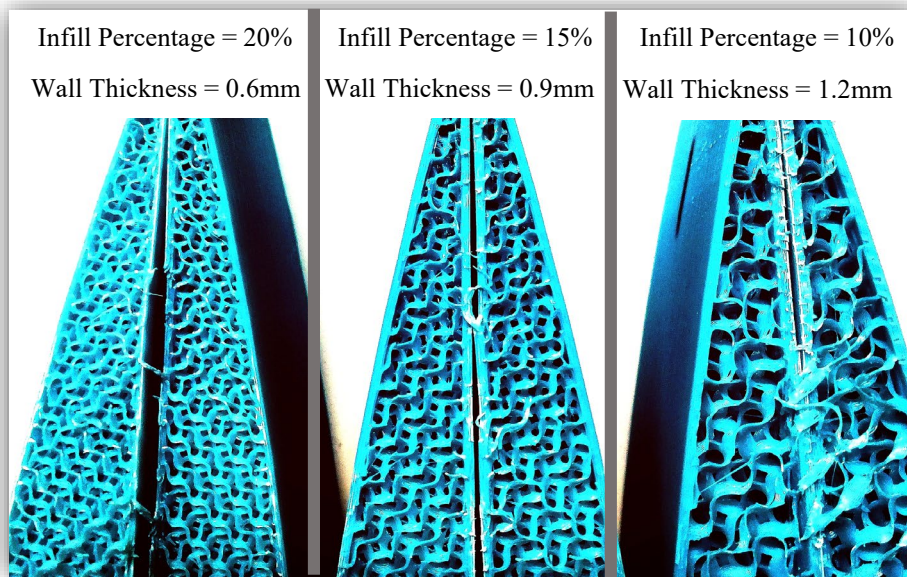
Figure 5-3: Specimen infill percentage and wall thickness differences for each Batch

The discoveries made in this experiment communicate the importance of combining the correct FDM parameters for achieving increased strength and resistance to shearing. The results proved that layer heights greater than $0.3\ mm$ do not contribute towards a part's structural integrity in either a shearing or bending manner. The experimental outcomes also alluded to an apparent relationship between the specimen's mass and build time, which were directly influenced by increased infill percentage and layer thickness.

The obtained failure loads for each Batch were used within an FEA simulation to determine the specimens new yield strength. *Table 5-3* shows the maximum Von Mises stresses experienced by each specimen along with the corresponding correction factors. These correction factor values are now representative of FDM parameter combinations and can thus be applied to the *Airslipper* design to validate its mechanical qualities. This experiment revealed that obtaining a minimum correction factor value of 12.14 requires reduced layer heights with increased wall thickness and infill percentages. However, compromises must be made to account for weight and build time for a given set of parameters.

Table 5-3: Specimen's new calculated correction factor based on FDM parameter combination

Batch number	Specimen number	New yield strength (MPa)	Correction factor (Yield/New)
	1	4.12	12.14
Batch 1	2	3.39	14.75
	3	2.84	17.61
	4	2.02	24.75
Batch 2	5	2.23	22.42
	6	2.42	20.66
	7	2.77	18.05
Batch 3	8	3.16	15.82
	9	3.69	13.55

5.2 Selection of FDM parameters

Observing results from the previous experiment has enabled this research to optimally select the layer height, wall thickness, and infill percentage parameter values within a design. This knowledge provided a baseline for successfully manufacturing components with the purpose of yielding increased strength and resistance to shear. However, the required qualities of UAV components are not only limited to strength, but are inclusive of factors such as surface finish, rigidity, replaceability, dimensional accuracy, and durability. These factors define a components usefulness for a UAV design and thus requires further addressing with regards to parameter choice. Therefore, this research must evaluate the importance of each component within the *Airslipper* against these factors. This process, shown in *Table 5-4*, forms a selection matrix that weighs FDM parameters against component qualities using a simple importance rating technique.

Table 5-4: Importance rating selection matrix for FDM parameters versus UAV attributes

	Surface finish	Rigidity	Replaceability	Dimensional accuracy	Durability
Layer height	A	A	B	A	A
Wall thickness	C	A	A	C	A
Infill percentage	C	B	B	C	B
Nozzle diameter	B	C	A	A	C
Print speed	A	B	B	A	A
Importance rating					
A – Extremely important (parameter has direct influence on the parts performance and efficiency)					
B – Moderately important (parameter has some influence on the parts functionality)					
C – Less important (parameter does not contribute towards a parts fabrication or use in the design)					

This selection matrix explicitly illustrates the importance of particular FDM parameter and shows how some are more pertinent than others for particular qualities. This breakdown allows the fabricated components of the *Airslipper* to have maximized performance qualities for its intended operation. This research refers to components as segments, and multiple segments make up a design module. *Table 5-5* reveals the various segments of the design and their corresponding parameter values which are utilized in the manufacturing of the *Airslipper* UAV.

Table 5-5: FDM parameter combination value selection per Airslipper segment

	Layer height (mm)	Wall thickness (mm)	Infill percentage (%)	Nozzle diameter (mm)	Print speed (mm/s)
Payload compartment	0.15	1.2	10	0.4	50
Fuselage top	0.12	0.8	20	0.4	60
Fuselage bottom	0.15	0.8	10	0.4	50
Servo brackets	0.18	0.6	15	0.6	60
Motor arms	0.12	1.8	15	0.6	45
Battery pack	0.2	0.8	10	0.4	60
Aerofoil	0.15	1.2	10	0.6	45
Aerofoil supports	0.12	1.2	25	0.6	50
Control surface	0.18	1.2	12	0.6	70
Bolt connectors	0.1	2.4	60	0.6	50
Electronics housing	0.2	1.2	20	0.4	65

As previously mentioned, the design modules of the *Airslipper* are broken down into segments, and due to the limitations on FDM technology, these segments are further partitioned into multiple parts. *Table 5-6* shows a breakdown of these modules and segments along with the associated printing times and weight for each. *Figure 5-4* reveals a graphical representation of this module and segment breakdown and also illustrates the total printing time, the total number of parts and weight of each design module. These numbers indicate the complexity and strategy implemented within the *Airslipper* design.

Table 5-6: Airslipper segment printing time and weight breakdown for each design module

~Module~ segment	Segment printing time (*hours*)	Segment weight (*grams*)	No. of parts that make up segment	Quantity of segments in UAV
~Fuselage~				
Payload compartment	58.8	458	3	2
Fuselage bottom	33.8	223	3	1
Fuselage top	18.1	123	4	1
Control servo brackets	6	46	1	2
~Propulsion system~				
Motor arms	11.1	95	1	4
Battery pack	51.5	366	4	1
Servo brackets	17.5	148	4	2
~Aerodynamic surfaces~				
Aerofoil	57.3	834	4	2
Aerofoil supports	9.6	121	1	2
Control surface	14.8	154	1	4
~Miscellaneous~				
Fuselage bolt connectors	3	10	3	12
Payload bolt connectors	5.3	26	3	4
Deployment feet	5.5	57	1	2
Electronics housing	8.4	75	2	1
ESC housing	4.5	37	1	2
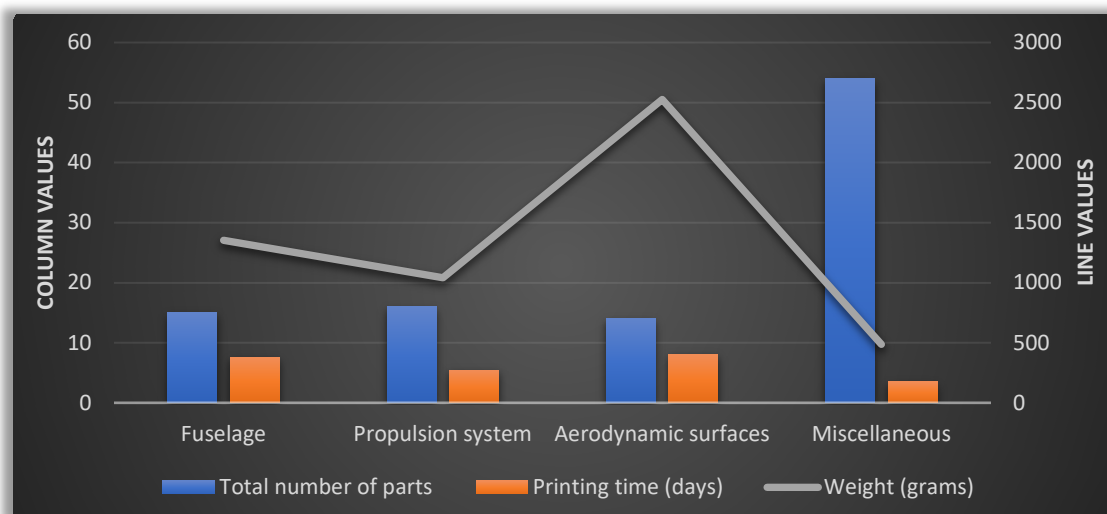
Figure 5-4: Graphical representation of Airslipper printing time and weight breakdown

5.3 Off-the-shelf components used in the design

The mechatronic design of the *Airslipper* was investigated in Chapter 3, and the relevant electronic component characteristics were systematically selected for an initial evaluation. Using this evaluation as a guideline and noting the optimization results obtained previously, a list of necessary components can be purchased. *Table 5-7* shows these components, along with their quantity, brand names, specifications, and costings.

Table 5-7: Airslipper's required component quantity, brand, specifications, and costs

Component	Quantity	Brand	Specification/Model	Total Cost
Propellers	4	T-Motor	Carbon fiber 18x6.1	R 2713
BLDC Motors	4	T-Motor	MN 5208 KV340	R 6539
ESC's	4	T-Motor	2-6S LiPo with UBEC (60 Amp)	R 1961
Control surface servo's	4	FEETECH	180-Deg 6V Analog @ 10 kg.cm	R 1986
Motor arm servo's	4	FEETECH	180-Deg 6V Analog @ 30.1 kg.cm	R 4448
FC	1	Holybro	Pixhawk 4	R 3849
PDB	1	Holybro	PM07	R 749
GPS	1	Holybro	UBLOX NEO-M8N	R 1049
Telemetry	1	Holybro	500mW @ 433Mhz	R 735
Radio control	1	Flysky	FS-i6X	R 1235
Battery cells	36	Samsung	30Q 18650 3000mAh	R 4500
BMS	2	Unknown	6S Li-Ion 60A	R 168

5.4 The final build of the *Airslipper*

This section graphically illustrates the systematic process of constructing and assembling the *Airslipper* UAV. All printed parts employed in this design were fabricated using the 'BCN3D' Sigmax R19 printer. This machine is a high-end desktop printer that features an IDEX system for dual extrusion. The build area of this printer has a maximum volume of $420 \ x \ 297 \ x \ 210 \ mm$ and utilizes a heated glass bed for better adhesion. *Figure 5-5* shows the printer in operation during the development of the *Airslipper's* aerofoil.
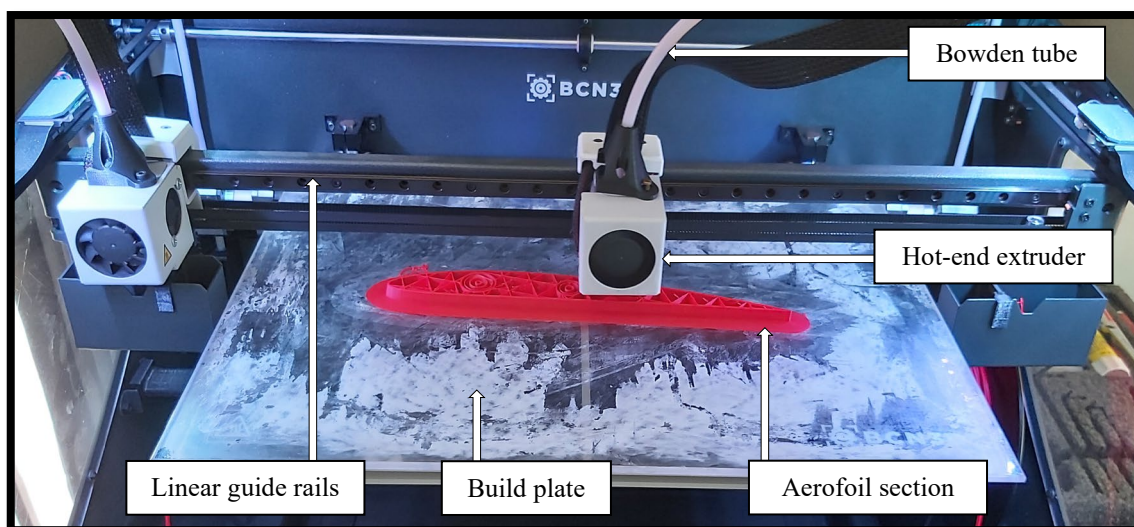
Figure 5-5: BCN3D Sigmax R19 printer in operation with Airslipper aerofoil section

The precise linear guide rails and superior hot-ends used within the BCN3D machine provided the printed parts with a reasonable surface finish. Therefore, the exteriors of most parts did not require any form of post-processing, with the exception of parts that needed additional adhesive to produce the desired segment. The following figures demonstrate the placement of each off-the-shelf component within the *Airslipper* design. This positioning offers an indication to the mechatronic design layout used in this research and also reveals how the printed segments contribute to the UAV's functionality. *Figure 5-6* shows the interaction of the $\mathbf{0.1\ kg.m}$ FEETECH servos and control surfaces. Deflection of these surfaces is achieved through a mechanical slot interface that is slightly offset to allow for greater inclination angles. The neutral position for these control surfaces corresponds to $\mathbf{+4^0}$ for the front and $\mathbf{-4^0}$ at the back. These settings, along with a $\mathbf{0.1\ kg.m}$ holding torque enables the vehicle to maintain stability and control during FW flight mode.
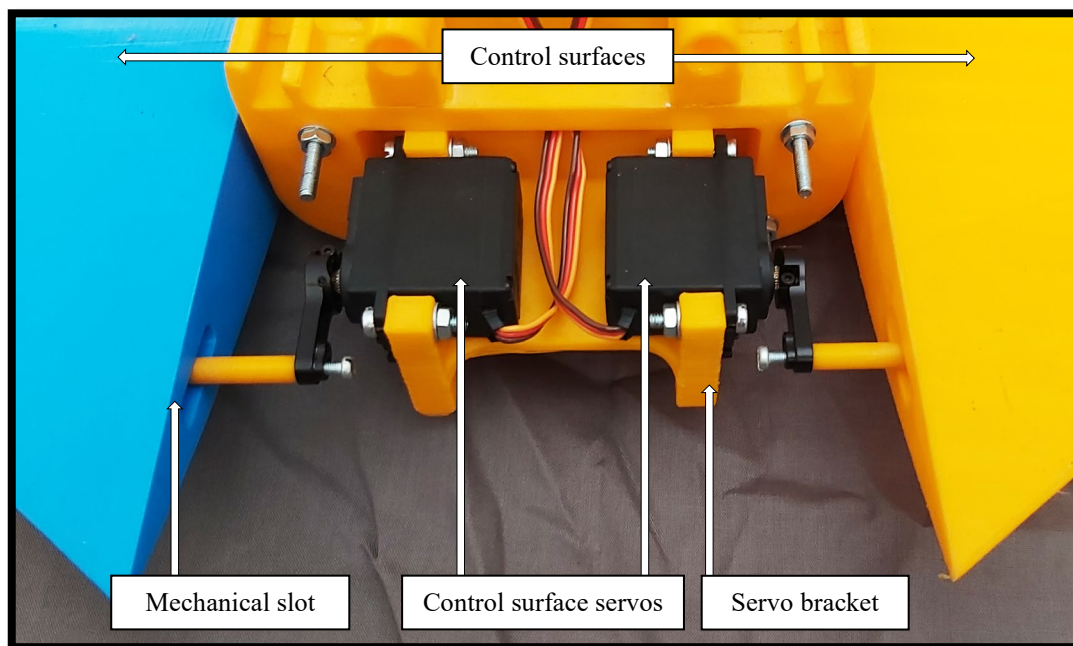
Figure 5-6: Front view subassembly of the control surface servo operating region

Figure 5-7 displays a partially assembled back part of the fuselage, with all necessary electronics responsible for actuating the motor arms, control surfaces and BLDC motors. The individual $\mathbf{0.301\ kg.m}$ servo motors are housed within the fuselage and are directly coupled to the motor arms by a servo horn. This approach allows the motor arms to have a 1:1 rotation ratio with the servos, which increases movement accuracy whilst reducing mechanical complexities. Implementation of XT-60 connectors is the preferred choice of power distribution for this system. These connectors aid the maintenance and repair strategies and are employed for the ESC's, PDB, servos and battery pack. The main electronics seen in *Figure 5-8* are housed on a single submodule within the fuselage, which is needed to facilitate sensor calibration of the FC. These components are accountable for controlling the vehicle in unmanned operation and also ensure the correct communication signals are received. This electronic module contains the Pixhawk 4 FC and the relevant 'Holybro' PDB, GPS and telemetry units. The use of external PWM and FMU interfacing pins for the FC's outputs simplifies adjustments and accessibility during the calibration phase.
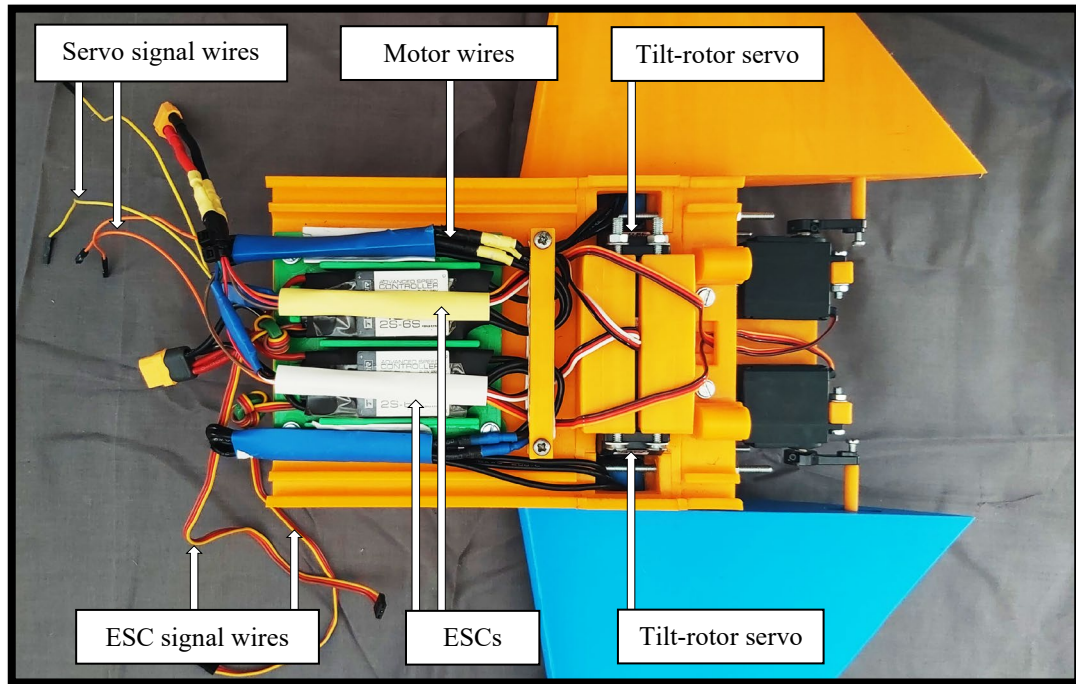
Figure 5-7: Top view subassembly of the tilt-rotor servos and ESC wiring
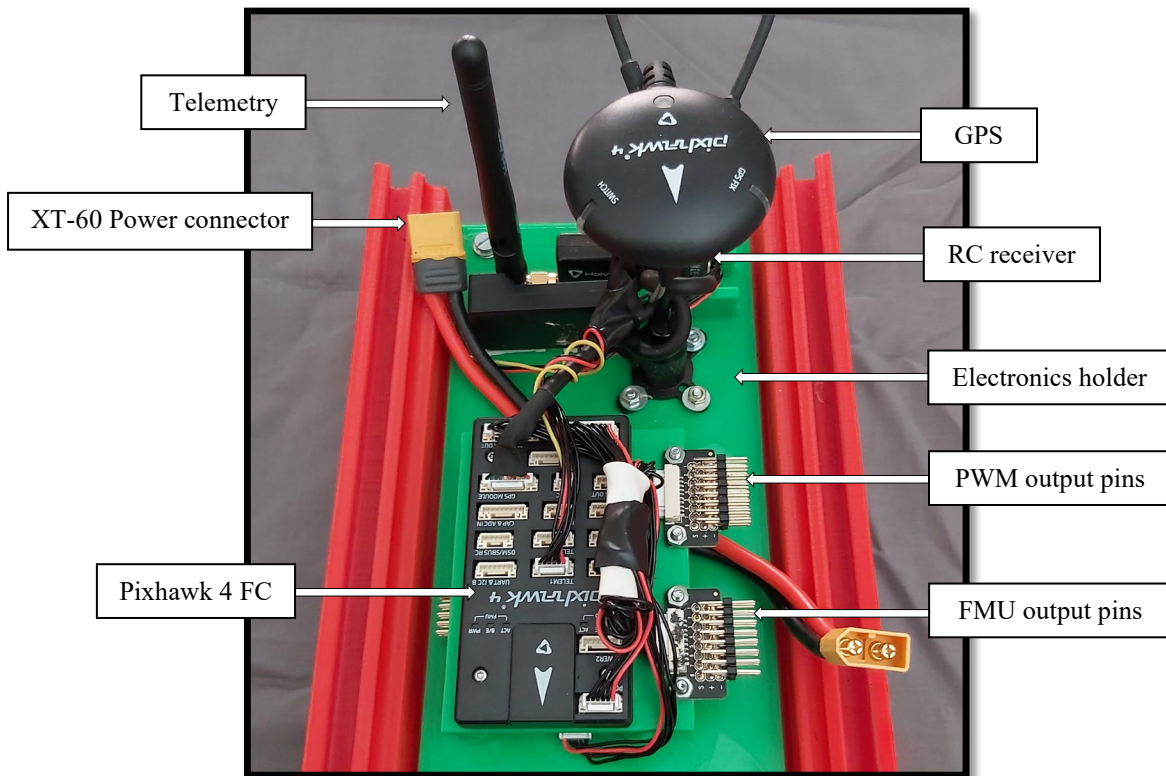
Figure 5-8: Top view subassembly of the main electronic components and their housings

The completed battery pack assembly is shown in *Figure 5-9* displays the 6S6P spatial configuration of the 18650 Li-Ion cells. A BMS is implemented for power management and uses balanced charging to guarantee battery safety. The unique design of this battery module allows the individual cells to slide into their allocated position and secures them via end caps. The periodically spaced slots in the design permits easier assembly and

maintenance, but most importantly allows the cells to be passively cooled from the surrounding airflow. This feature is critical for sustaining the life cycle of a Li-Ion battery pack and ensures temperatures are kept below the cell's limits. A top view of the rear propulsion system, including the T-Motor propellers and BLDC motors, is shown in *Figure 5-10*. This perspective provides a sense of scale for the design and shows the positioning of the propellers in relation to the fuselage and control surfaces.
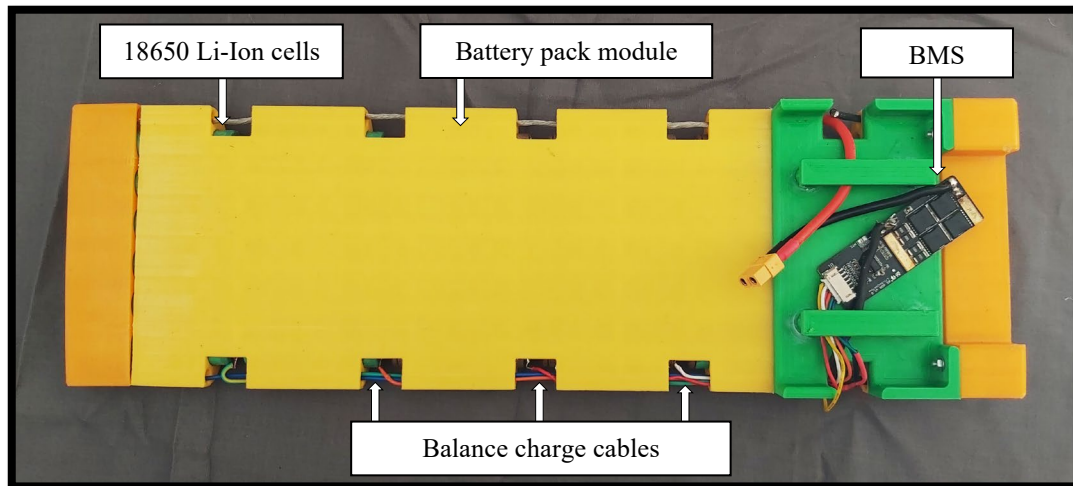
Figure 5-9: Top view assembly of 18650 Li-Ion battery pack with BMS
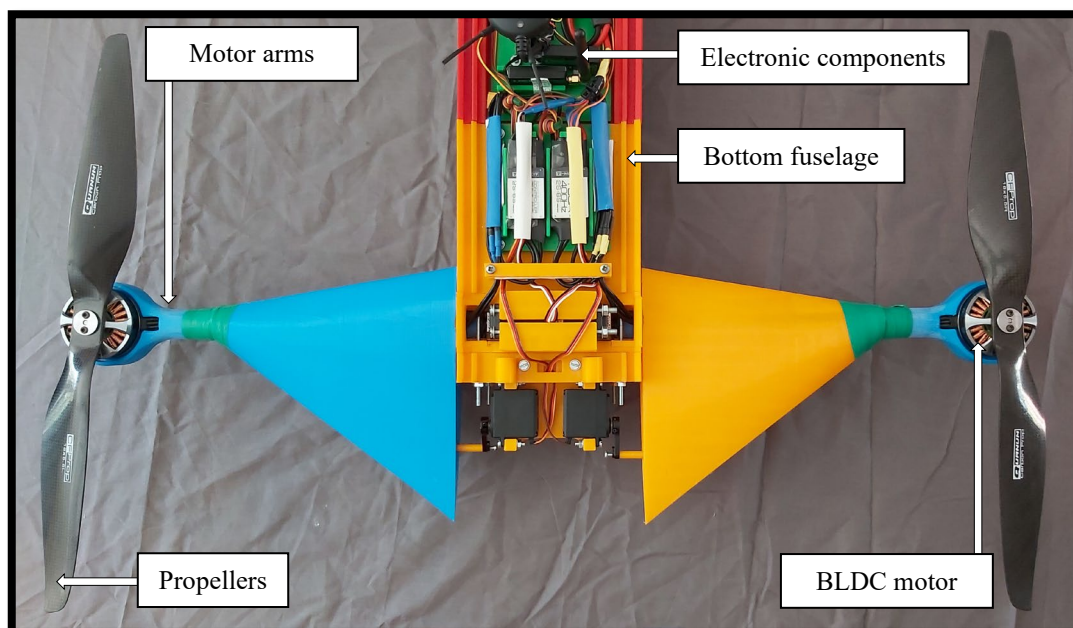
Figure 5-10: Top view of the propulsion system attached to the fuselage

Figure 5-11 reveals the fully completed electronic design, setup, and wiring of the *Airslipper*. For organizational purposes, all components within this section have a designated placement and are secured via M4 bolts. The servo, ESC, and BLDC motor wires are fastened into a dedicated clamp. This structured positioning provides a methodical system which enables straightforward component identification and maintenance. The vehicle's battery, although not shown, is slotted into the fuselage's lower compartment below the electronics. This location offers the design greater rigidity and allows for easier assembly.

The payload compartment seen in *Figure 5-12*, is a single part that uses the assembly rails to slide directly over the control surface interfacing rods to create a flush connection with the fuselage body. This compartment allows the payload to keep separate from the electronics and is secured via four FDM printed bolts.
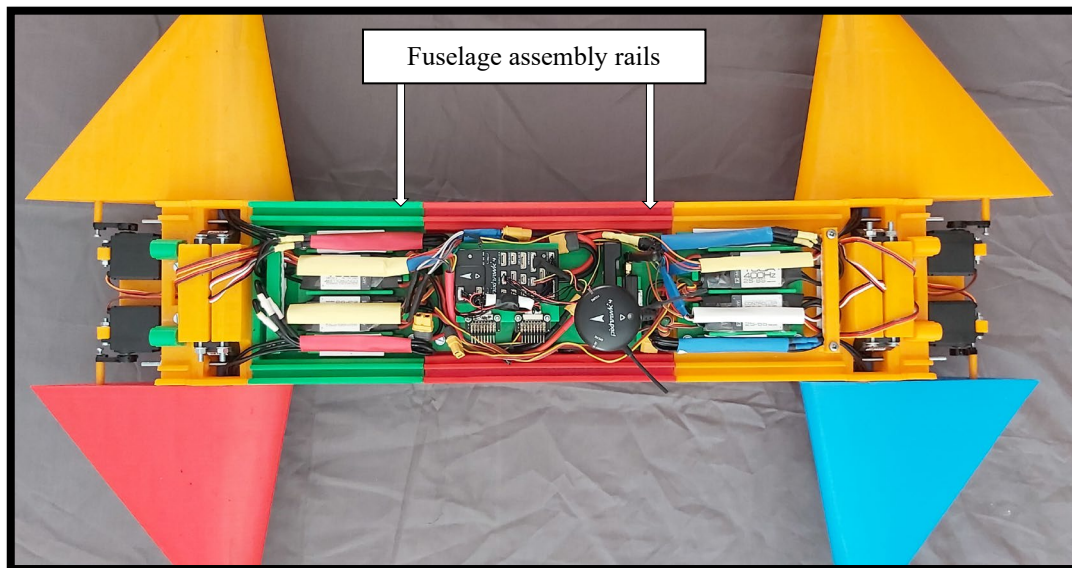
Figure 5-11: Top view assembly of all the electronic components within the fuselage
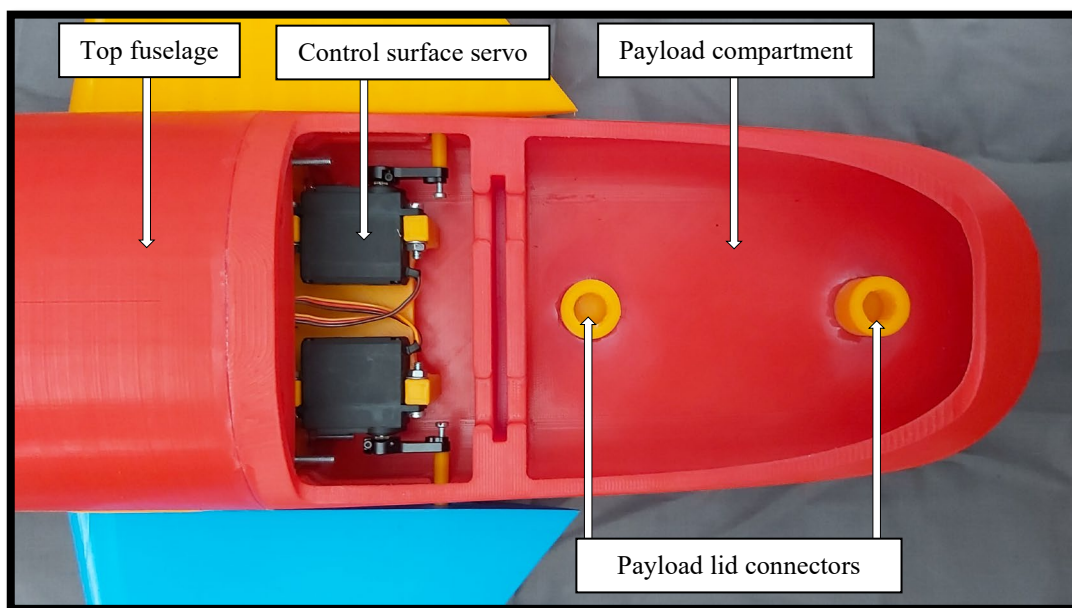
Figure 5-12: Top view of the payload compartment attached to the fuselage

Figure 5-13 and *Figure 5-14* displays the complete assembly of the *Airslipper* with its propulsion system, fuselage, and electronic modules attached. The payload lid and its associated bolt connectors are shown in conjunction with the control surface servo cover, which is secured using printed M10 bolts. The fuselage and aerofoil fastening points are also shown, which indicates the position of the aerofoil. The overall shape and design of the *Airslipper* resembles the initial concept considered in Chapter 3. However, the limitations of FDM fabrication has proven its difficulties in many aspects. One of the most pertinent aspects, the designs segmentation,

can be visually noted within these figures by the number of individual parts required to achieve an assembled UAV.
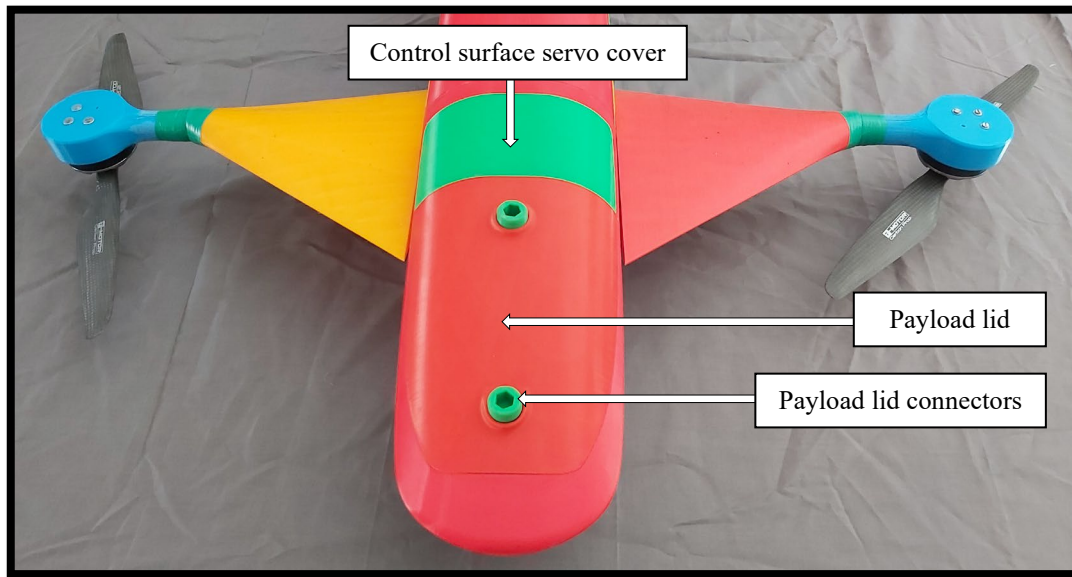
Figure 5-13: Front view of the Airslipper with the payload lid attached
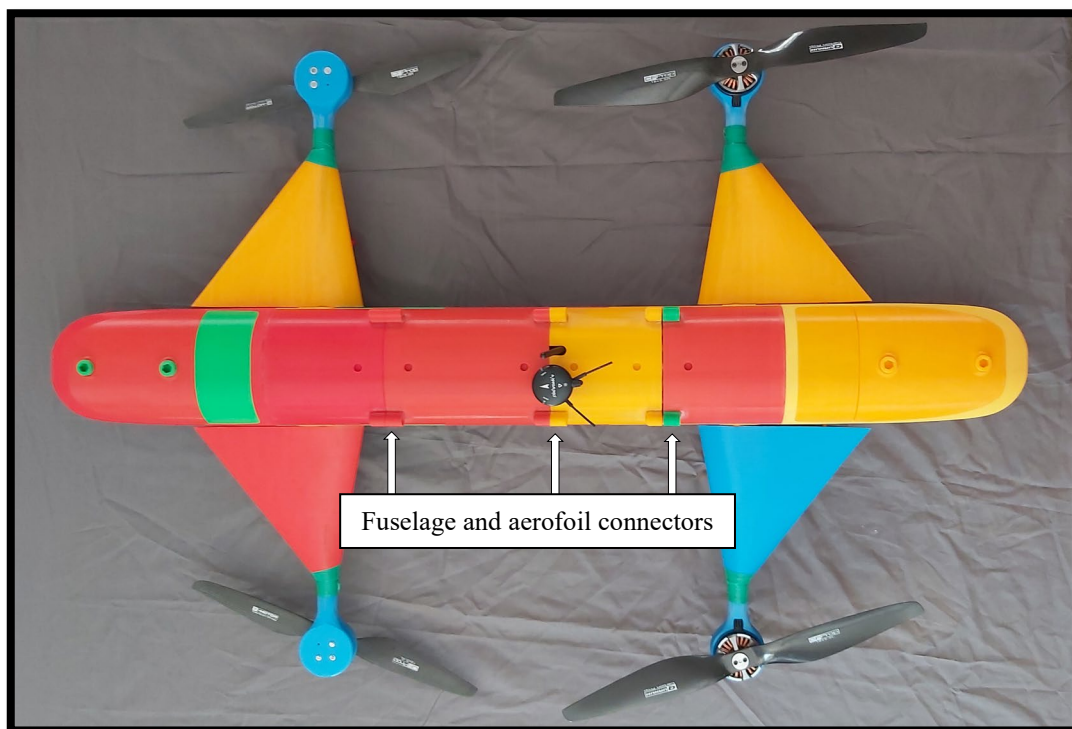
Figure 5-14: Top view of the Airslipper without its aerofoil

Fabricated assemblies of the aerofoil and its supports are presented in *Figure 5-15* and *Figure 5-16*. The implementation of cylindrical struts for aerofoil bracing allows for faster assembly and aids the aerofoils in resisting the aforementioned bending moment. Attaching the aerofoil and its supports to the fuselage is achieved by tightening four M10 printed bolts through the same fastening points stated previously. Due to design

partitioning, each aerofoil section comprised of four individual parts that required an epoxy resin to complete the final component.
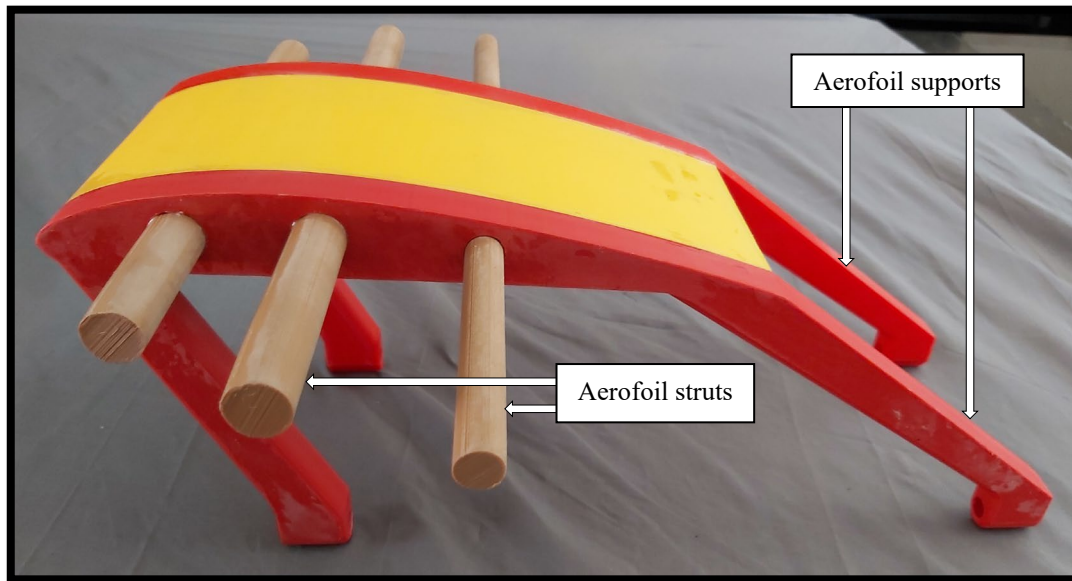
Figure 5-15: Side view of the aerofoil supports

Figure 5-16: Top view assembly of the completed aerofoil

Due to the previously mentioned FDM parameter selection strategy, each printed segment of the design contributes to the overall cost, manufacturing time, aerodynamic efficiency, and robustness of the *Airslipper*. This strategy has also permitted effortless replaceability for the individual parts of a module, thus leading to a more sustainable and reliable design. These factors have greatly improved the flight characteristics of this prototype and have enhanced the general qualities of this design, considering the operating environment, and intended application.

Assembly of the *Airslipper* was a straightforward process that only required tightening of twelve printed bolts to secure the vehicle thoroughly. This simplicity was made possible by the design approach and structured component placements considered in Chapter 3. *Figures 5-17* to *5-20* depicts the completed *Airslipper* design with all the necessary elements for attaining both VTOL and FW flight modes. Construction of the two individual feet offered the vehicle a sufficient amount of ground clearance for take-off, whilst maintaining an aerodynamic profile.

Figure 5-17: Side perspective view assembly of the completed Airslipper in VTOL mode

Figure 5-18: Top view assembly of the completed Airslipper in VTOL mode

Figure 5-19: Front view assembly of the completed Airslipper in VTOL mode

Figure 5-20: Side perspective view assembly of the completed Airslipper in FW mode

5.5 Propulsion system testing

Before deploying the *Airslipper* for operational use, thrust testing the propulsion system is required for validating its performance and confirming the optimization results attained in Chapter 3. This experimental testing also ensures the fundamental design requirements are satisfied, and the relevant safety measures are put in place before a flight. The propulsion system testing conducted in this research focussed on understanding the thrust generation and power consumption for different propeller combinations. The T-Motor 5208 BLDC motor was utilized in conjunction with nine varying propeller models that differed in diameter, pitch, and material. This array provided a broader set of results that can be used to assess further the validity of performance outcomes obtained in Chapter 3. The testing was performed on an accurate and well-calibrated thrust stand setup from RCbenchmark, which is capable of obtaining several independent measurements, including thrust, vibration, torque, rotation rate, and electrical power. The testing stand was limited to a maximum thrust force of 5kg and up to 60 Amps of continuous current draw.

The experiment was executed using a standard PWM signal value of $1750\mu s$, as this value was the limiting factor for the polymer-based propellers. *Table 5-8* reveals the results of these propeller setups and demonstrates a performance correlation between generated thrust force and power consumption. It can be noted that the diameter of a propeller had a direct influence on the amount of power consumed and a relationship between the thrust and propeller pitch was evident. These findings were consistent with the propeller theory of Chapter 2. Although the polymer-based propellers shown in experiment number 7, 8 and 9 yielded similar performance in comparison, their capabilities are restricted to these thrust values due to the lack of rigidity associated with the properties of the material. Therefore, this research disregarded the polymer propellers and only considered the CF for the *Airslipper's* use. *Figure 5-21* show a graphical representation of the CF propeller results and introduces a Power-to-Thrust ratio, which adds relevance to the propeller's proficiency.

Table 5-8: Performance results for the propeller thrust stand experiment

	Diameter (inch)	Pitch (inch)	Material	Thrust (N)	Power (W)	Vibration (g)	Torque (Nm)
Propeller 1	13	4.4	Carbon Fibre	11.16	147.61	0.427	0.187
Propeller 2	15	5	Carbon Fibre	17.08	228.22	1.188	0.317
Propeller 3	16	5.4	Carbon Fibre	20.15	275.82	1.099	0.391
Propeller 4	17	5.8	Carbon Fibre	26.46	367.81	1.218	0.581
Propeller 5	18	5.5	Carbon Fibre	23.42	439.31	1.511	0.704
Propeller 6	18	6.1	Carbon Fibre	32.64	463.36	1.647	0.719
Propeller 7	13	5	Polymer	12.11	162.456	0.796	0.215
Propeller 8	15	5.4	Polymer	17.41	241.76	1.012	0.340
Propeller 9	17	6.5	Polymer	23.74	358.94	1.029	0.549
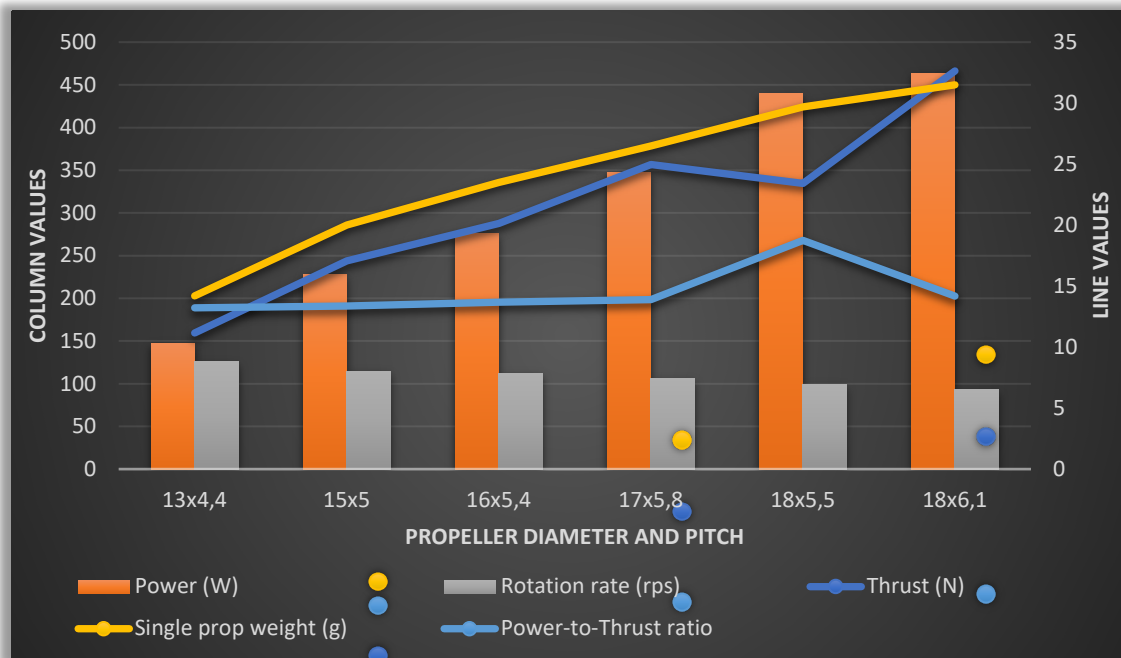
Figure 5-21: Graphical representation of the results for the CF propellers

The graphic illustrates the linear behaviour of this ratio for all propeller variations. However, due to the insufficient 5.5-inch pitch associated with the 18-inch diameter of propeller 5, this ratio is negatively emphasized. This incompetence in propulsion performance rules out the 18x5.5 propeller from the design. These results are indicative of CF-based propeller performance and suggest the utilization of the 18x6.1 propeller for the *Airslipper*, as its capabilities suffice the intended design requirements. This propeller choice also matched the optimized propulsion design of Chapter 3 in both thrust generation and power consumption.

5.5.1 Discrete propulsion system testing

Determining the complete effectiveness of a propeller throughout its performance range requires a discrete step-by-step testing setup. This process assures the propeller operates at the desired conditions and provides the necessary propeller information which characterizes the thrust at different intensities. This test used the same

RCbenchmark thrust stand equipment, but instead of specifying a PWM value, an array of throttle percentages was employed. These percentages were executed through the implementation of a predefined script code that initialized a systematic process of testing the propeller. The script logged 100 sampling values for each percentage step and averaged them to reduce noise interference and improve testing accuracy. The script was set to record 6 data values with a 3 second settling time between each data point. The range of throttle percentages displayed a broad set of results for the 18x6.1 propeller and are seen in *Table 5-9*. These values were verified by the performance testing done by the T-Motor company [83] and showed minimal deviation, which confirms the legitimacy of these findings.

These results are graphically represented in *Figure 5-22* and show an inverse correlation between thrust and efficiency. However, this phenomenon is customary for propellers that operate statically. It is worth noting that the maximum drawn current and power consumption of this propeller is less than the stipulated requirements. These outcomes are suggestive of a practical propulsion system for the *Airslipper* design, which ensures functionality for the different operating conditions.

Table 5-9: Discrete performance results for the 18x6.1 CF propeller

	Unit	Values				
Throttle Percent	%	55	65	75	85	100
Thrust	N	16.33	21.87	27.71	32.86	40.46
Torque	Nm	0.359	0.478	0.602	0.712	0.871
Power	W	186.2	285.4	411.1	538.8	747.4
Current draw	A	7.8	11.9	17.1	22.5	31.1
Rotation rate	rps	66.92	77.35	86.85	93.81	103.15
Efficiency	-	89.94	78.14	68.73	62.27	55.97
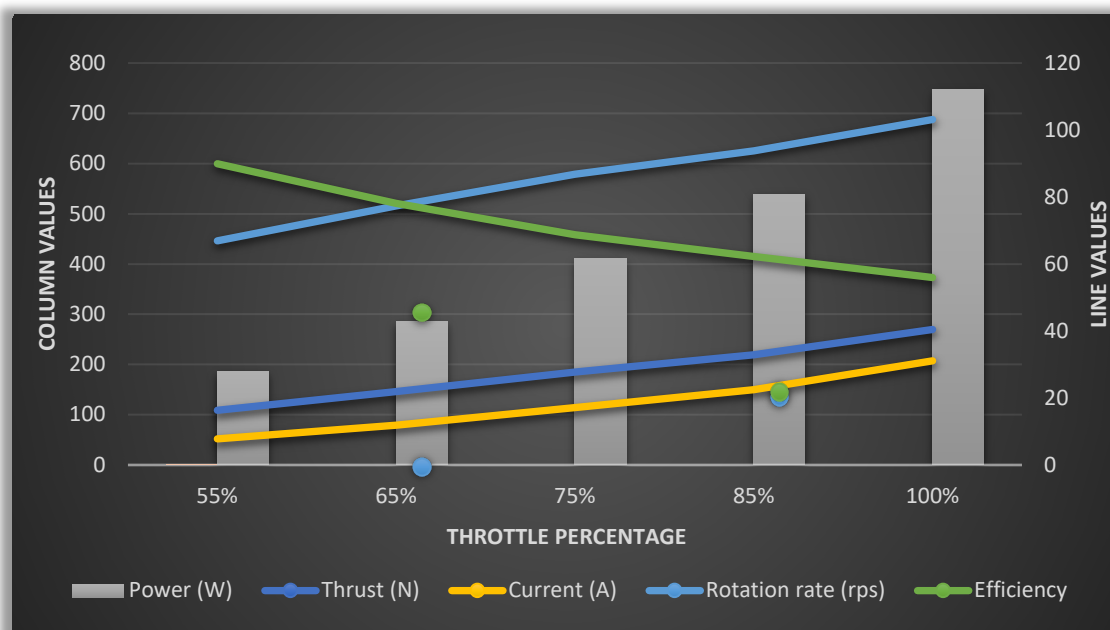
Figure 5-22: Graphical representation of the results for the of 18x6.1 CF propeller

5.6 *The Airslipper's* flight characteristics during VTOL testing

The current results, outcomes, and findings of this research have provided sufficient data to confirm the functionality and effectiveness of this UAV design from a theoretical and experimental perspective. However, to fully comprehend the *Airslipper's* performance, an examination of the vehicles, flight characteristics are required during operational conditions. Due to legislative requirements and limitations within South Africa, the vehicle is only operable in VTOL mode, as FW mode would require RPAS and RTO certification, which is not possible during this research period. Although these factors hinder the full range of flight modes, it is still possible to evaluate the performance of the *Airslipper* during a series of automated hovering tests.

The testing process supports the analysis of the *Airslipper* without compromising any regulations and is used to validate further the vehicles mechanical construction, controller response and propulsion system design. Performing the tests can be executed through a GCS program known as 'QGroundControl' (QGC), which is a common platform for UAV mission planning and parameter configuration. The tests runs were limited to **120 s** of flight time at an altitude of approximately **4 m**. *Figure 5-23* reveals an image of the *Airslipper* during the Test Run (TR) 3, whilst *Table 5-10* shows the necessary vehicle information for all three TRs. As this test only required VTOL mode, the aerofoil was not considered pertinent and thus was not attached.

Figure 5-23: Photograph of the Airslipper during hover TR 3

Table 5-10: General vehicle and mission information during the three TRs

Test information	Units	Test Run 1	Test Run 2	Test Run 3
Logging duration	s	131	145	137
Vehicle flight time	s	120	120	120
Total distance traveled	m	10.6	6.87	18.69
Maximum altitude	m	4.12	4.05	4.17
Maximum vertical speed	m/s	3.6	4.2	2.4
Maximum tilt angle	°	13.9	14.5	12.3

5.6.1 Data logging results

The data logging results shown in this section were made possible by the embedded feature within the Pixhawk 4 FC. These logs allow specific knowledge to be captured during vehicle operation, which enables developers to adjust specific parameters and tune the necessary controls for obtaining maximum performance. The log results of the hovering TR 3 are displayed in this section and shows the relevant plots pertaining to the vehicles control response, actuator outputs, vibration metrics and power.

5.6.1.1 General

The GPS projected and estimated flight path of the *Airslipper* during this hovering test is revealed in *Figure 5-24*. This figure depicts slight deviations throughout the test, but the most prominent disturbance in flight occurs within the first $30\ s$ of the test, which is shown by the outlying path. This abnormality was a result of a wind gust that caused the vehicle to drift away from the original take-off point slightly. However, once the environmental conditions steadied, the vehicle returned to a more stabilized flight. Due to this wind gust, the autopilot firmware misaligned the initial take-off position and ended up landing approximately $1.35\ m$ adrift. Although this distance may seem high, it is perfectly acceptable given the setup parameters, frame rigidity, and flight time. *Figure 5-25* shows the corresponding vehicle velocities for the X, Y, and Z directions and also demonstrates the wind disturbance by a prominent spike in Z velocity. This plot resembles a relatively stable flight with velocities rarely exceeding $0.5\ m/s$ in all directions.
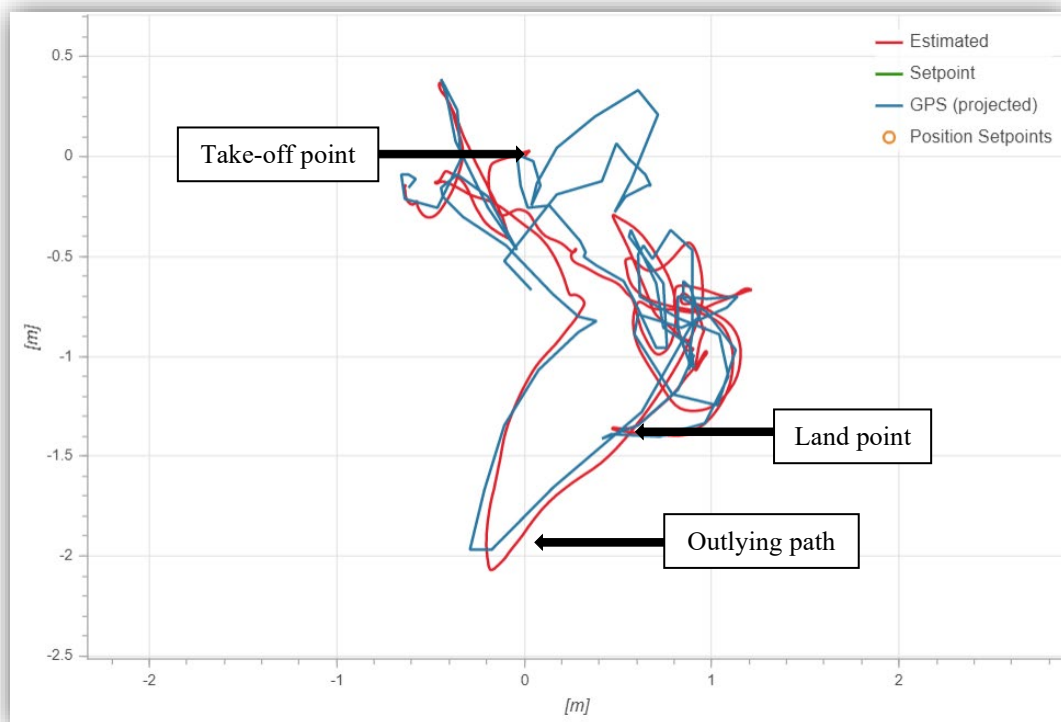
Figure 5-24: Flight path of the Airslipper during hover TR 3

Figure 5-25: Velocity of the Airslipper during hover TR 3 in 3D space

5.6.1.2 Control response

The employed PID controller used by the *Airslipper* UAV requires precise tuning of the relevant parameters in order to achieve controlled flight. This continuous adjustment ensures the setpoint values outputted from the rate controllers match the estimated values. *Figure 5-26* demonstrates this matching with a close-up view of the roll angle during a six-second period of the TR 3. It can be noted that the roll setpoint line in green mimics the roll estimated line in red, which is indicative of a well-tuned controller. *Table 5-11* shows the PID gain values used to achieve the desired response of the *Airslipper*.

Figure 5-26: Close-up view of the Airslipper's roll angle during hover TR 3

Table 5-11: Airslipper's P-I-D tuning setup used for TR 3

Tuning axis	P-gain	P-rate	I-rate	D-rate	Feedforward
Roll	8.0	0.5	0.15	0.005	0.0
Pitch	10.2	0.4	0.15	0.006	0.0
Yaw	4.0	0.5	0.06	0.000	0.0

The graphics displayed in *Figures 5-27* to *5-32* reveal the angular rate and step response plots for each roll, pitch, and yaw axis, respectively. The step response plot for roll rate demonstrates a fast-reacting controller with a settling time just over $0.2\ s$. Although the substantial overshoot of this response is indicative of uncontrollable oscillations, it is necessary to balance the segmented frame design of this vehicle when external perturbations occur.

The pitch rate step response reveals a more subdued reaction, which results in a smoother convergence but subsequently required a longer settling time. However, the intense pitch angular rate within the first $30\ s$ of flight, validates the vehicle's pitch response capabilities, as angular rates become restrained a few seconds later. These visuals offer a greater understanding of the PID control architecture and tuning setup utilized by the *Airslipper* during the entirety of TR 3.
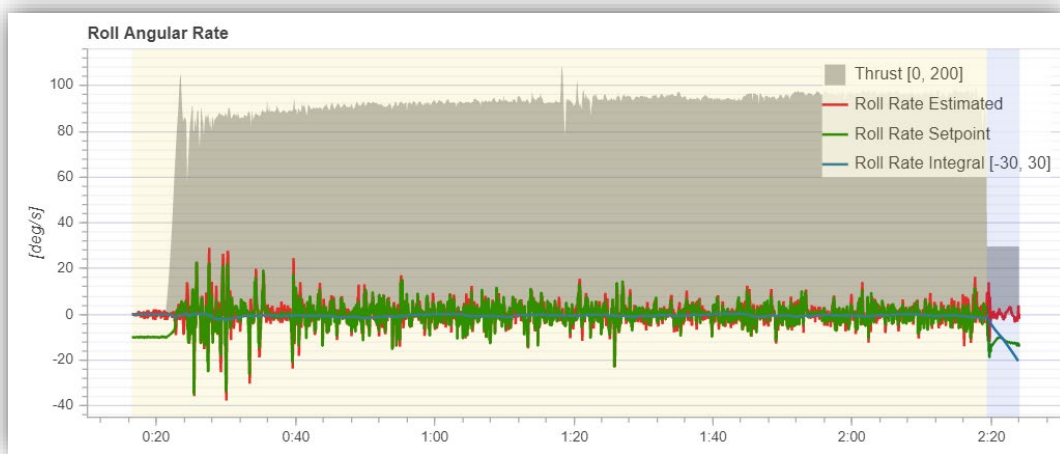
Figure 5-27: Roll angular rate for TR 3
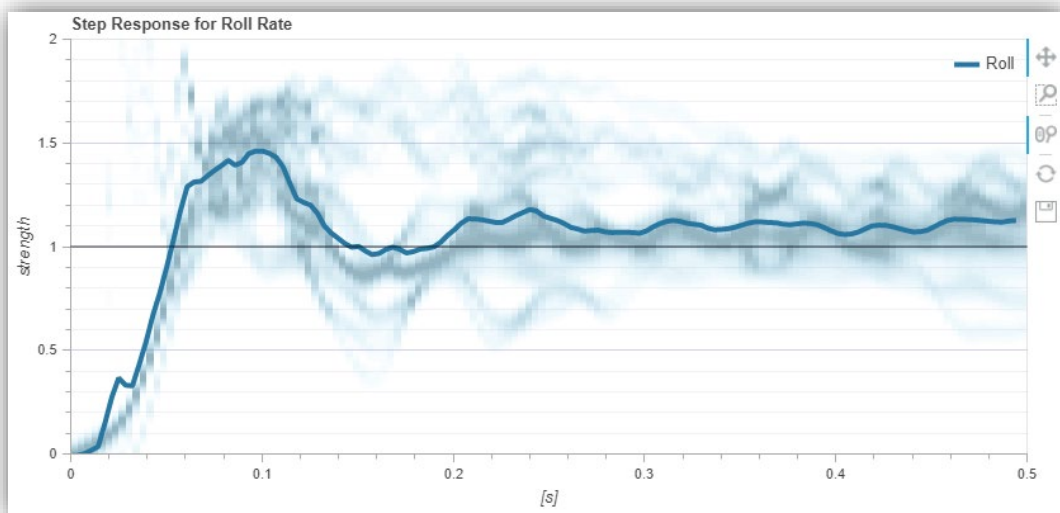
Figure 5-28: Step response plot for the roll rate
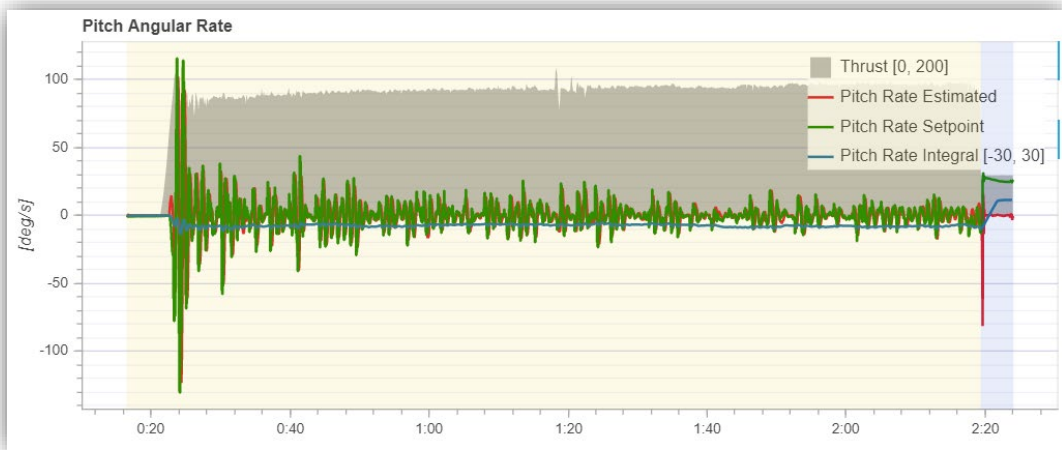
Figure 5-29: Pitch angular rate for TR 3
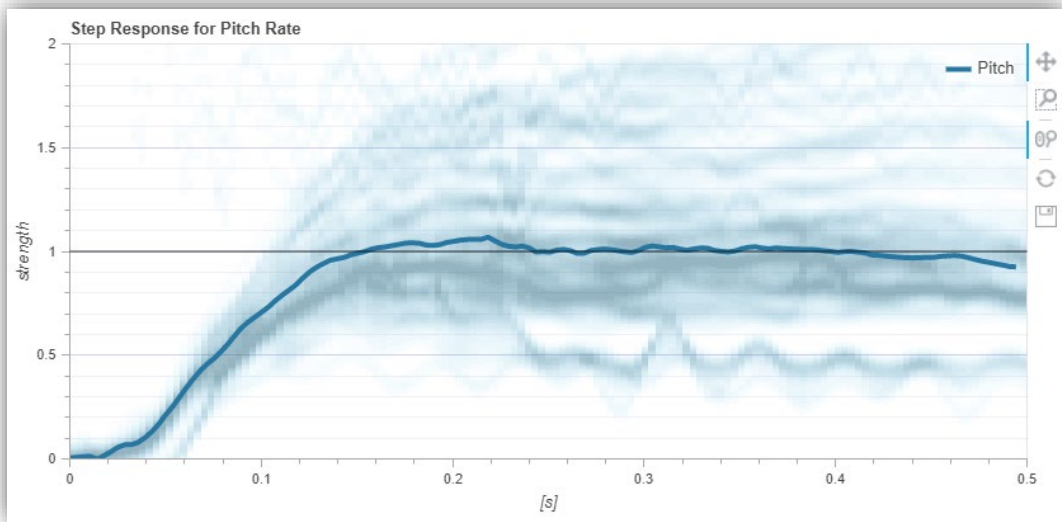
Figure 5-30: Step response plot for pitch rate
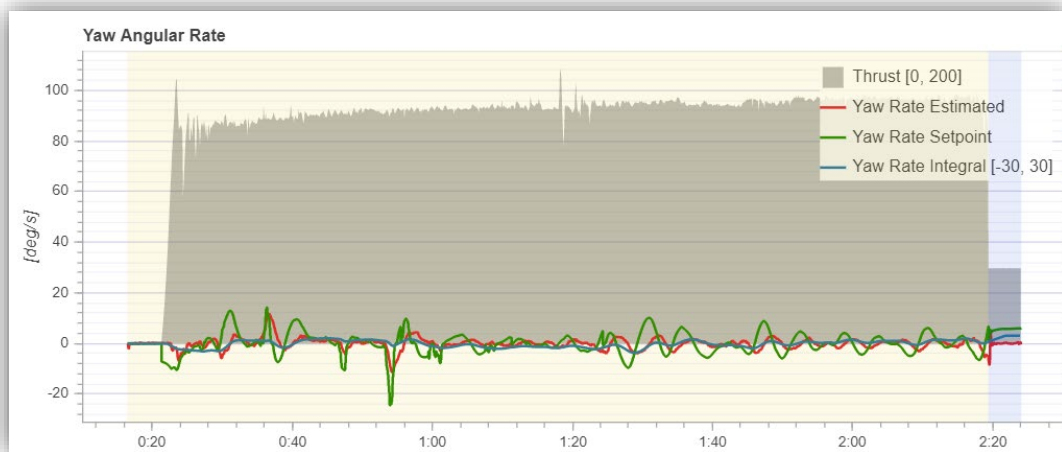
Figure 5-31: Yaw angular rate for TR 3
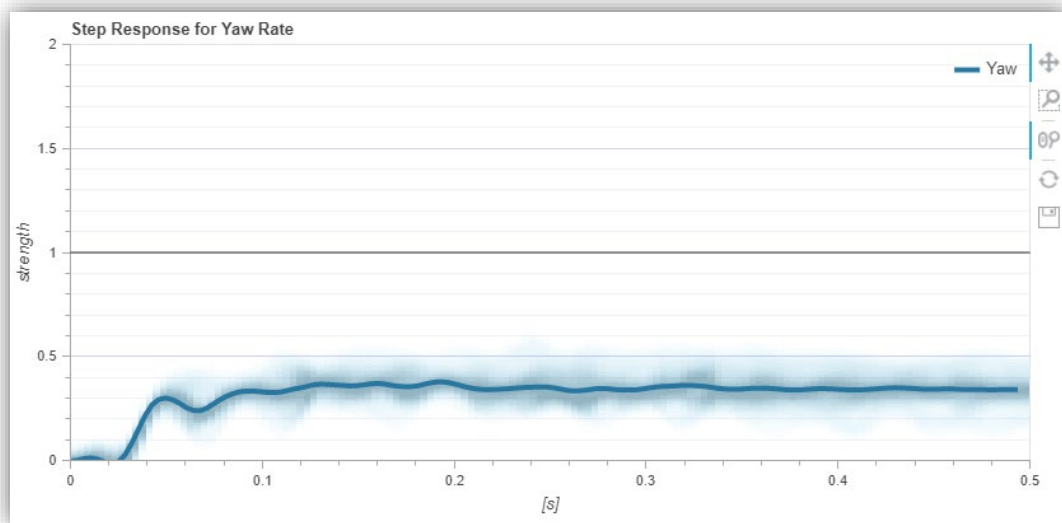
Figure 5-32: Step response plot for yaw rate

5.6.1.3 Actuator outputs and control

The actuator output signals sent to the BLDC motors for this hovering test are given by *Figure 5-33*. These signals are PWM values that correspond to **$1500\mu s$**, which is set as the vehicles throttle value for hover mode. The actuator outputs 0, 1, 2, and 3, correspond to the four-motor setup used by the *Airslipper,* and as seen in the figure, all signals are within a specified range. The overlapping of these command signals indicates that the propulsion system is operating flawlessly and also signifies that the vehicle is critically balanced. The lack of noise amplitude throughout this hover test justifies the PID gains and suggests vehicle vibrations are minimal. *Figure 5-34* portrays the actuator controls of the *Airslipper's* flight, which is a result of the raw angular speeds from the on-board gyroscope shown in *Figure 5-35*. These outcomes confirm the validity of the mixer file used *Airslipper* but also demonstrate the severity of the wind gust experienced by the vehicle in the first **$30\ s$** of flight.
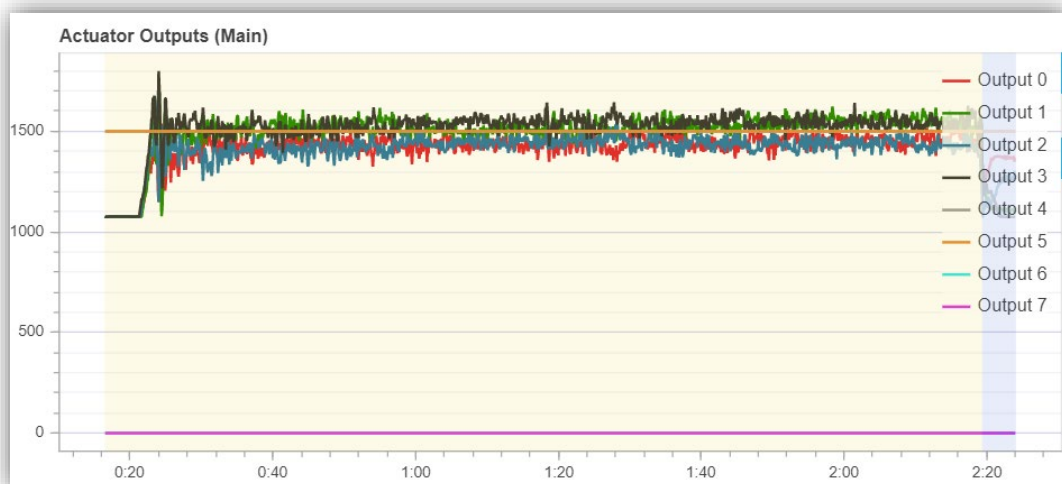
Figure 5-33: The main actuator outputs for the Airslipper's BLDC motors during TR 3

Figure 5-34: Actuator controls for the Airslipper

Figure 5-35: The raw angular speed from the Pixhawk 4 onboard gyroscope

5.6.1.4 Vibration

The vibration associated with a propeller-based aerial vehicle forms a particular facet that can affect aerodynamic performance, efficiency, and flight time. In extreme circumstances, insufficient vibration levels can lead to position estimation failures and sensor clipping, which is detrimental to autonomous flight modes. The range of suitable vibration levels heavily depends on vehicle size, inertia, and rigidity. These factors, when incorrectly set up, are often the cause of degraded control response and increased actuator noise. *Figure 5-36* displays the vibration metrics of the *Airslipper* and illustrates satisfactory delta velocity levels for a vehicle of this size. The graph of *Figure 5-37* reveals a frequency plot for the roll, pitch, and yaw axis, which are based on the actuator control signals given previously. This graph is typically used to aid the identification of frequency peaks during a test flight and helps configure the necessary software filters within the autopilot firmware. The vibration characteristics of this plot reveals a reduced cut-off frequency for the gyroscope, which creates higher control latency. However, considering the application and fabrication method, these values are appropriate.
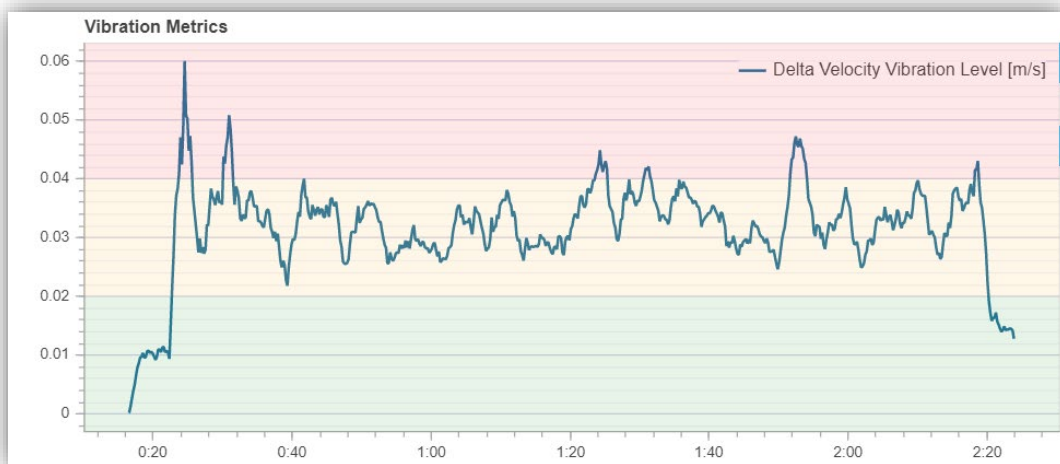
Figure 5-36: Vibration metrics of the Airslipper during hover TR 3
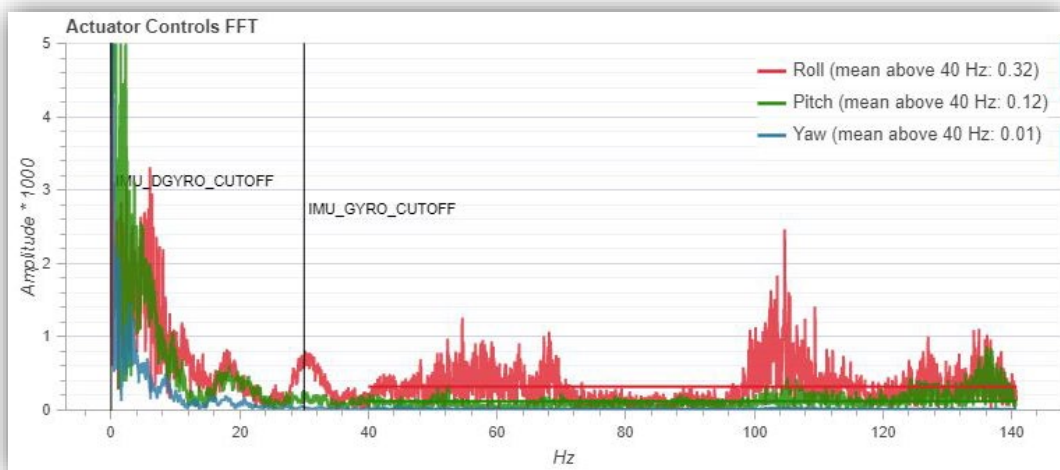
Figure 5-37: Actuator controls Fast Fourier Transform (FFT) for the Airslipper

The raw accelerations shown in *Figure 5-38* are also a measure of vehicle vibration and is commonly used to validate the FFT results should any discrepancies arise. The values of this graph signify acceptable accelerations for the X and Z axis of the *Airslipper*. However, the Y-axis experiences a brief spike in acceleration due to the mentioned wind gust. Nevertheless, the Z acceleration line is situated below the corresponding X and Y lines, which is considered a tolerable format and should not impede the performance of the vehicle in any way.

The 2D frequency plot of *Figure 5-39* is a method of representing the IMU's raw accelerometer data over the flight test period. This graph, known as an acceleration power spectral density plot, displays the frequency response of *Airslipper* with respect to its X, Y, and Z-axis. An ideal spectral density should reveal a majority of blue and green shading throughout the plot with the lower frequencies exhibiting a yellower tinge. However, the results of the hover test demonstrate a strong frequency response at around **80 Hz**. Although these findings may indicate potential issues, it is typical for propeller blade passing frequencies to be **100 Hz**, which subsequently coincides with the plot. Therefore, through an analysis of these figures and accounting for the FDM fabrication process, vibration levels of the *Airslipper* are considered satisfactory.
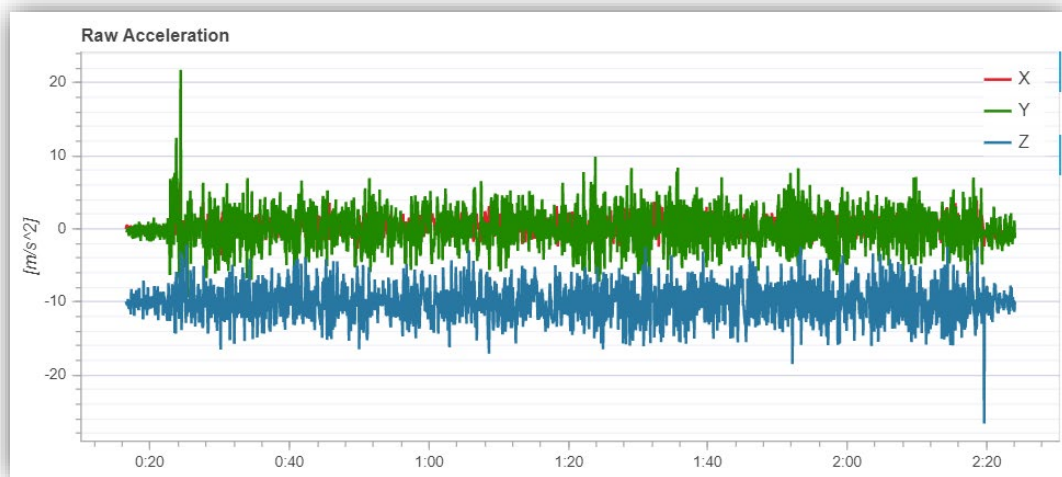
Figure 5-38: Raw acceleration of the Airslipper during hover TR 3
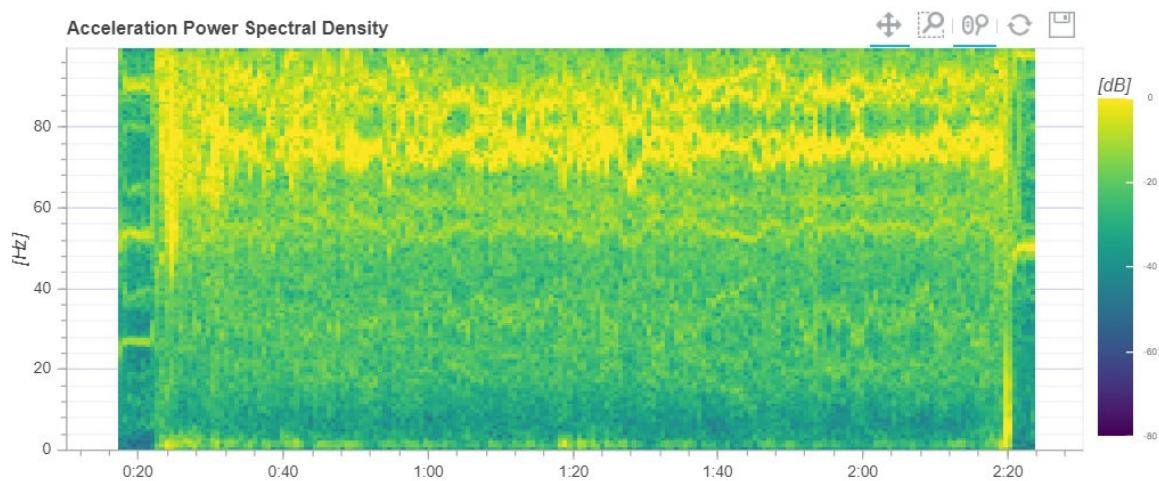
Figure 5-39: Acceleration power spectral density of the Airslipper during hover TR 3

5.6.1.5 Power

The associated power information during the test is given by *Figure 5-40*, which provides an indication to the propulsion systems power needs at hover conditions. The grey spiked line at the bottom of the graph signifies the current draw of the vehicle, whilst the batteries voltage and filtered voltage are shown by the red and blue lines, respectively. Evidence of the abovementioned wind gust can be seen by successive current and voltage spikes before the thirty-second flight time mark. This increased current demonstrates the excessive workload of the BLDC motors in an attempt to counteract the undesired disturbance and return to a more neutral position.

Although not shown clearly, the **120 s** flight duration yielded an average battery current draw of **60 A**, which equates to **2000 mAh** of battery discharge. Noting an averaged filtered battery voltage of **22.36 V**, the vehicle necessitated a power consumption of **44.72 Wh**. These results give the *Airslipper* a specific thrust value of **7.11 g/W,** which is deemed suitable for this type of configuration.

Figure 5-40: Power metrics associated with the Airslipper during hover TR 3

5.7 *Airslipper* evaluation

Experimentally validating the propulsion system offered the necessary findings to confirm a propeller choice for the *Airslipper*. By exploiting these results, the vehicle was hover tested in VTOL mode to ensure the correct flight characteristics were present. Outcomes displayed sufficient control response, vibration levels, and power consumption, which demonstrated a successful unmanned system design, given the vehicles fabrication method. However, conditions of this research and the medical aid delivery application requires the execution of dominant features within the *Airslipper's* operating environment. This ensures the practical functionality of the vehicle during working circumstances and guarantees proficiency of the relevant design elements when critical situations arise.

5.7.1 Deployment

The deployment and retrieval strategies for an unmanned delivery system forms an integral feature that requires the utmost precision to reassure the intended supplies are protected during transit. This feature also determines the vehicle's operational success, as faster deployment times results in faster medical aid delivery. Designing the *Airslipper* for on-demand deployment required each module of the design to have a normalized attachment procedure so that assembly complexities are alleviated during emergencies.

The implementation of specific check routines on the propulsion, fuselage, payload, and aerofoil modules ensured complete segment compatibility and security. This process was achieved through a combination of visual and contact verification steps that rigorously examined the bolts and mechanical interfaces throughout the vehicle's assembly. Each bolt used in the assembly is Polytetrafluoroethylene (PTFE) coated, intending to provide ample clamping force that also resists external vibrations. The addition of a thin silicone coating around the payload lid allows the payload compartment to become watertight and dust resistant, resulting in a decontaminated area for medical use.

5.7.2 Maintenance and repair

As mentioned previously, the *Airslipper* has a partitioned design due to the limiting factors associated with FDM fabrication. This process required each segment of the design to be fastened to create the desired component, which ultimately compromises the structural and aerodynamic capabilities of the vehicle. However, this consequential adaption has made the design extremely proficient in terms of maintenance and repair strategies. Since FDM offers rapid and flexible fabrication, parts can be effortlessly substituted without replacing the entire module, which saves production time and costs. Having a deconstructed design has also enabled parts to become easier to manufacture, which has made assembly more intuitive.

Throughout this research, the unique segmented design of the *Airslipper* has made the inspection, identification, and modification process of components an uncomplicated process. This simplistic design strategy was made possible by employing a guide rail within the fuselage design, with the intention of allowing quick access to the internal electronics. This feature benefits the development of any new prototype and is exceptionally useful during testing phases. The shortcomings of this fabrication method have significantly altered the *Airslipper's* design approach but have subsequently improved the overall operation and cost of the vehicle, making replacement parts more accessible, affordable, and manageable for any demanding situation.

5.7.3 Sustainability

UAV systems are an effective and efficient tool for completing tasks that were once regarded as impractical. The continues requirement demand for this technology has altered the design strategies for these systems. It thus necessitates this research to not only focus on the delivery of medical aid supplies but to also emphasize the sustainability of this applications solution. The conceptualized *Airslipper* UAV prototype discussed in this dissertation is considered fully sustainable in terms of its fabrication method and fabrication material.

Over the last decade, the cost of FDM fabrication equipment and material has drastically reduced. This affordability has prompted further growth of the industry, which has allowed this method to expand its capabilities to incorporate more interesting materials and mechanical components. These beneficial qualities demonstrate the proficiency of FDM and allow for increased flexible production whilst minimizing the associated tooling costs. This factor is particularly significant in locations that are not capable of maintaining industrial-grade plants or facilities for UAV manufacturing. With naturally sourced materials such as PLA, biodegradability and reusability of this method exemplifies the sustainability for this technique for UAV production.

5.8 Summary of Chapter 5

The experimental investigations conducted in this chapter confirmed the structural capabilities of the FDM fabrication method and subsequently provided optimal FDM parameter combinations for the individual segments of the *Airslipper* design. The execution of this factor-driven selection matrix strategy, in conjunction with the off-the-shelf electronic components, allowed for a straightforward UAV fabrication and assembly. Due to legislative reasonings, the *Airslipper* was unable to operate in the intended FW mode. However, the utilization of QGC and a simple hovering test enabled this research to evaluate the performance characteristics of the design during a 120-

second experiment. Data logging results displayed in this chapter demonstrated a proficient vehicle that was capable of maintaining stabilized flight with minimal vibration, power, and control response issues. These findings reassured the *Airslipper's* fabrication method and offered confidence to a functional prototype for the envisioned medical aid delivery application.

6. DISCUSSION

The increasing population of underdeveloped communities within the rural areas of South Africa has undoubtedly been a contributor to the rise of disease and illness. This threatening development has put an excessive strain on the limited medical infrastructure of SA and has impacted the living conditions of many individuals. Thus, for the sake of human health, contending this challenge required a rapid health care response approach which could assist a community's well-being without causing economic instability. The aim of this dissertation proposed to find a solution for the task of delivering emergency medical aid supplies to these aforementioned areas. This research focussed on implementing technologies within the 4th industrial revolution to create a more sustainable and practical system that could maintain the growth and prosperity of individuals for future generations.

6.1 The delivery of medical aid supplies with UAV and FDM technologies

Progression of modern civilization has provided a multitude of technological breakthroughs and innovative opportunities. Among these triumphs are FDM printing and UAV systems, which have modernized industry standards and pushed the technological envelope to an extreme. The globalization of both these technologies has ultimately increased product accessibility and affordability whilst maintaining superior quality. Continuous research and development have transformed these complex systems into ubiquitous consumer tools that have become synonymous with flexible manufacturing, prototyping and autonomous operation. The associated attributes and dedicated features of these systems have allowed enthusiasts, academia, and even specialists to enhance their productivity and scope in a variety of disciplines. The research shown in this dissertation demonstrated the proficiency of these discrete technologies and offered an understanding to the array of functionality that can become once combined, specifically as a medical aid delivery system.

This form of delivery demanded the utmost care from a legislative perspective, as SACAA regulations necessitated certification and licensing for operating RPAS vehicles with commercial gain. The *Airslipper* prototype, which was classified as Class 1C, needed to operate below an altitude of $122\ m$ and have an MTOW of less than $20\ kg$. These provisions form an essential factor when considering the delivery destinations are distant from metropolitan cities and hospitals. With 84% of citizens relying on the public health sector for medical assistance, current support strategies within SA cannot facilitate those who need it most. Therefore, providing a solution to the medical aid delivery challenge required the full aptitudes of both UAV and FDM technologies.

The humanitarian nature of this medical application has ignited the compassionate side of corporations and government organizations, leading to project funding and additional resources. These generous contributions have allowed engineers and designers to fully express their innovative ideas, which has progressed the technological prowess of these tools, specifically in the biopharmaceutical industry. The dissemination of medical supplies by UAV's has gained significant research interest, and through experimental exploration, researchers of MIT have shown positive economic results for distributing large quantities of vaccines within the inaccessible areas of Africa. Findings of this research demonstrated feasibility from a supply chain management standpoint and the author's proposed continual use of UAV's for on-demand delivery, with the purpose of off-setting the initial outlay costs. These studies were backed by the implementation and operation of an established medical delivery

service named ZipLine, which has already developed a network of UAVs within Rwanda and Ghana. These case studies have shown the advancements in UAV technology and have indicated a considerable transformation of the biopharmaceutical industry with substantial growth for medical aid delivery by UAV.

Literature ascertained in this report uncovered the elementary principles associated with UAV technology and research suggested that the efficiency of an autonomous system relied heavily on the fundamental characteristics of aerodynamic surfaces and propeller-based propulsion. These elements significantly contributed to the UAV's cause and had a direct correlation to endurance, as seen by the optimization outcomes of Chapter 3. This research also signified the importance of employing aerodynamic analysing programs such as XFLR5 and AVL, which have become an essential means of theoretically evaluating the performance of an aircraft's design. The execution of these programs within this report alluded to the stability and sensitivity flight characteristics of the *Airslipper* and demonstrated success before experimental testing was performed.

This work further explored the possibilities of fabricating large UAV components using the FDM method. The challenges of this technique were expressed in a manner that considered the attributes of a part's functionality. These concerning factors led to literature pertaining to the surface finish qualities and structural abilities of FDM printing. However, through other research and experimental investigations conducted in this dissertation, optimal FDM parameter combinations have shown noteworthy results for enhancing the performance qualities of printed parts. Sustainability of this method came into fruition through the utilization of a biodegradable polymer such as PLA. This material has comparable mechanical characteristics and is considered the least expensive and most abundant material for FDM printing. Other factors such as RepRap and IDEX have heightened the quality of FDM, which further necessitates the need for this method in UAV production. These improvements, along with the investigations conducted in Chapter 5, provided the necessary foundation for fabricating a functional UAV prototype using FDM.

6.2 The design and optimization of *Airslipper*

Development of the conceptualized *Airslipper* UAV required the formation and execution of a specific design approach that satisfied the flight conditions of the application and contended limitations of the FDM fabrication method. Due to the obligations of a medical aid delivery system operating in SA, this research defined the working circumstances of the application and proposed the vehicle have a payload capacity of $2.5\ kg$ with a total service distance of $12\ km$. These flight restrictions provided the best compromise between design complexity, vehicle stability and legislative regularity. Throughout the design phase, it was evident that attaining maximum endurance of an aerial vehicle could be achieved through the employment of an FW assembly. Therefore, the propulsion system needed to combine two distinct flight modes to transition to the desired outcome. The *Airslipper* UAV, which is constructed with an independent tilt-rotor setup, enabled the system to achieve VTOL and FW flight modes whilst maintaining the necessary controllability and manoeuvrability. This arrangement gave the UAV an extended flight envelope, which remains critical for an emergency delivery.

The mechatronic nature of unmanned systems formed an integral aspect of the *Airslipper's* initial design strategy, as modules needed to be systematically selected to ensure the most conceivable setup was achieved. The

mechatronic illustration shown in this research described the pivotal operation of a tilt-rotor VTOL UAV, which combined hardware requirements, SACAA regulations, and FDM fabrication constraints to form an outline of the final design. These reasonings provided a methodical approach for attaining the relevant electronic, electrical, and mechanical components, which were centred around an estimated weight value of the vehicle. By appropriately calculating the required thrust for each VTOL and FW flight mode, a suitable propeller diameter of $d = 450\ mm$ at an approximated VTOL rotation rate of $n_{VTOL} = 5741\ rpm$ was recognized. The utilization of a Li-Ion battery pack was the preferred power source for this research, as it offered higher energy density and appreciable spatial volume customizability. Aiming for a total flight time of $T_{flight,TOTAL} = 10.75\ minutes$, a Li-Ion battery cell configuration of 6S6P was chosen. This ideal setup gave the *Airslipper* a maximum charge capacity of $B_{capacity,actual} = 27\ 160\ mAh$ and allowed for the selection of a motor rotation constant of $KV = 360$.

Performance of the propulsion system was measured using an online program and gave characteristics such as a $T_{flight,calaculated} = 13.1\ minute$ flight time and a $\gamma_{VTOL} = 1.4$ maximum thrust-to-weight ratio. These initial findings satisfied the application's objectives which confirmed the current propulsion setup. However, obtaining the maximum flight endurance required a strategy that could simultaneously optimize the aerodynamic configuration and propulsion system of the *Airslipper* without compromising the FDM fabrication constraints.

This research accomplished an optimized UAV design by investigating the literature of various MDO techniques and numerically formulating two objective functions which contained the critical parameters of an aerodynamic and propulsion design. The solution of these functions, which were subjected to applicational constraints, resulted in a set of Pareto points along a Pareto front. The 10 individually optimized parameters provided an increased flight endurance of 5% when compared to the traditional methods. This development corresponded to $58\ s$ of extra flight time with $1.51\ km$ of additional flight range, which critically influences the delivering capabilities of a medical aid delivery system. This improved functionality demonstrated the competency of MDO within UAV design and suggested further research can be completed on other practical aspects, to enhance particular flight characteristics for supplementary duties.

6.3 Using aerodynamic analysis to verify the functionality of the *Airslipper* design

Optimization of the *Airslipper* design provided the fundamental performance parameters that enhanced the vehicles flight endurance. However, these parameter combinations disregarded component placement and aerodynamic interference, which are critical aspects of aircraft stability and performance. Therefore, this research conducted an array of aerodynamic analyses and CFD simulations to confirm the correct characteristics were exhibited by the vehicle's aerodynamic surfaces, which included the control surfaces and main aerofoil.

The open-source XFLR5 program was used to conduct the various plane, stability, and sensitivity analyses on the *Airslipper* design. Pressure coefficient distribution results on all aerodynamic surfaces were graphically displayed and provided valuable information towards the choice of the vehicle's aerofoil chord, profile shape, and aerodynamic surface positioning. The associated lift coefficient contour and the corresponding bending moment contour demonstrated the required structural abilities of the main aerofoil. However, the experimental outcomes

of Chapter 5 validated the use of FDM fabrication for the main aerofoil and offered correction factors for unique FDM parameter combinations.

Throughout the analyses, the *Airslipper* design confirmed to have stability attributes that guaranteed the vehicle had a zero-pitching moment $C_m = 0$ at an $AoA = 0.5^o$ and at a cruising velocity of $V_{cruise} = 26\ m/s$. The sensitivity analysis performed in this research offered insight into the maximum payload carrying capacity of the vehicle. Results proved that an overloaded UAV, with the designed aerodynamic setup, exhibited substantial-frequency response but subsequently became less stable due to higher inertial effects. These findings were backed by the longitudinal and lateral time responses of pitch angle and pitch rate, which displayed overshooting for larger payload masses. Therefore, a payload capacity of $2.5\ kg$ and less presented adequate aerodynamic control for the given configuration, which is representative of the applications flight conditions. Outcomes of these analyses proved to be sufficiently effective for the medical delivery requirements, and due to the *Airslipper's* stabilized traits, excessive actuator deflections can be minimized, which reduces power consumption and improves vehicle endurance.

Based on the optimization results and aerodynamic validation analyses, a CAD model of the final *Airslipper* design was constructed, and CFD simulated using the SolidWorks flow simulation toolbox. A combination of surface and fluid contours, in conjunction with fluid streamlines, created graphical representations of the fluid's behaviour surrounding the *Airslipper's* fuselage, aerofoil, and propulsion system, respectively. Illustrations of cut and surface plots gave indications towards the fluids pressure, velocity, and vorticity during VTOL and FW flight phases. Concern regarding fluid interference between propeller and control surface was negated by the results of these CFD simulations, as findings revealed an insignificant fluid disturbance and an inconsequential decline in the propeller performance. Aerofoil simulation outcomes displayed extreme turbulence and vorticity nearer the tips, which is demonstrative of increased induced drag. However, these fluid simulation outcomes were typical for the intended flight conditions and offered the necessary validation that confirmed the functionality of the vehicle for unmanned flight, for this aerodynamic configuration.

6.4 The fabrication, assembly and testing of *Airslipper*

Traditional methods of fabricating strong, lightweight, and aerodynamic aircraft parts, using precision machining and complex tooling, form a practical technique in high-performance designs. Although these conventional practices are feasible for UAV production, initial equipment outlay costs and operating costs are unrealistic for small UAV production companies and thus become extraordinarily unappealing when prototyping new configurations. This predicament has challenged designers to find a solution that exhibits similar properties and characteristics to traditional parts but has a more sustainable and economic footprint. This research revealed the capabilities of using the FDM fabrication method for the *Airslipper* design and demonstrated what steps were necessary for achieving a successful prototype that portrayed similar attributes to other UAV designs.

The FDM fabrication method possesses unique features that cannot be replicated by any other manufacturing technique and displayed many qualities that were extremely beneficial when implemented correctly. However, the anisotropic behaviour of a printed part undoubtedly produces weak adhesion points along a parts build

direction. This undesirable factor creates concern for the structural integrity and durability of a part that experiences a concentrated force in that same direction. This phenomenon was displayed within this dissertation through an experimental investigation of an FDM printed aerofoil section that aimed to determine the effect critical parameters had on a parts ability to withstand these forces. Results showed that a part's shear strength simultaneously increased with wall thickness and layer height. Outcomes also alluded to an apparent relationship between a part's mass and build time, which were directly impacted by infill percentage and layer height. These findings suggested that a layer height above 0.3mm exhibited no layer adhesion and thus did not contribute to the overall integrity or rigidity of the part.

By making use of the literature and experimental data attained in this research, the final manufacture and assembly procedure of the *Airslipper* was performed. The partitioned design of *Airslipper* was a result of the limited build volume associated with desktop FDM printing and forced the elemental modules to be constructed into different segments. Although these individual segments compromised the vehicles structural integrity and durability, attributes such as maintenance, deployment and sustainability all benefitted from a deconstructed design. The optimal parameter combination of each printed part made assembly of the vehicle intuitive and allowed the particular segments to become more functional. A total of 99 separately printed parts, constituting 21 days of continuous printing, made up the completed *Airslipper* design. The precise positioning of each segment was recognized, and the employment of a structured bolt assembly approach made accessing the electronics a simple task, which inherently allowed for easier repair and controller tuning.

Prior to the commencement of any flight testing, the propulsion system of the *Airslipper* was experimentally verified. This process ensured the performance of the relevant components provided a sufficient lifting force and made sure results matched the optimization findings of Chapter 3. However, due to the lack of diameter and pitch matching for the 18x5.5 propeller, performance significantly decreased when compared to the other propellers. Nevertheless, testing results noticed that the thrust and power values associated with the 18x6.1 propeller provided the best outcomes for the design and were within the hardware limitations. This propeller diameter, pitch and rotation speed combination also satisfied the optimization parameters, thus making this propeller the best-suited choice for maximizing the *Airslipper's* flight endurance. The performance testing of these propellers demonstrated the benefits of using carbon fibre over the polymer variants, as they provided greater rigidity and increased maximum lift.

Flight testing the *Airslipper* UAV was achieved by tuning the necessary PID gains of the controller and executing a simple hover test using the QGC software. The logged results of three different TR's provided critical information on the vehicles roll, pitch and yaw response rates. These findings justified the controllers tuning selection and also validated the rigidity of the design. Actuator output graphics showed consistent signal yield, which provided confidence for the *Airslipper's* airframe configuration file and mixer file used by the PX4 autopilot firmware. Vibration metrics during the hover test revealed satisfactory levels, with no degradation in flight performance or manoeuvrability. With considering the partitioned design and fabrication method, these logging outcomes were acceptable for the medical aid delivery application.

6.5 Recommendations and improvements for *Airslipper* design

The results attained from the various simulations, analyses, and experimental investigations within this dissertation provided the necessary evidence to confirm the functionality of the *Airslipper* design and FDM fabrication method. The initial design approach, component selection strategy and optimized parameter combinations, yielded an appropriate outcome in regard to the UAV's capabilities of delivering medical aid supplies. Although this vehicle satisfied all objectives set out by this research, certain features associated with the design and fabrication method could have been improved to enhance the operational characteristics of the system further.

The unique design of the *Airslipper* UAV featured a propulsion system that individually actuated each motor arm for attaining VTOL and FW flight modes. This allowed for the addition of an aerofoil that enabled the vehicle to achieve greater flight velocities and endurance, which resulted in a much more comprehensive service radius and superior flight envelope. However, due to the FDM fabrication method and its compromises in structural integrity with concentrated and localised forces, traditional aerofoil mounted control flaps were not plausible. Therefore, the *Airslipper* placed the corresponding aerodynamic control surfaces directly on the motor arms, which formed a distinctive configuration that maintained full control of the vehicle. Although this setup allowed these surfaces to become customizable, the stability analysis conducted on this design indicated potential improvements for a more stabilized and controlled vehicle. Achieving this enhanced attribute could have been obtained by positioning the control surfaces farther away from the fuselage body and aerofoil, so as to generate larger control moments around the vehicles COG. This incremental development could potentially increase the sensitivity and response of the vehicle to wind disturbances, which ultimately benefits the vehicle's functionality in varying environmental conditions.

Implementing the FDM method within UAV fabrication proved complicated, as it required the *Airslipper* design to be entirely fragmented into multiple segments, which required further fastening to form larger modules. However, once the optimal build strategy was obtained in Chapter 5, parts became more comfortable to correctly setup and fabricate. This systematic process alleviated the difficulties associated with FDM and enabled for faster printing with a more consistent production flow. However, the same constraining limitations of FDM plagued the surface finish of the *Airslipper's* fuselage and payload compartment. This negative quality impacted the accuracy of the outer surface, which degraded the aerodynamic compatibility of the two segments when fastened together.

Other complexities were apparent when two concentric parts required small clearances for rotation. This effect was witnessed in this design by rotation of the individual motor arms within their housings. Additional tolerance problem areas included the assembly guide rail between the top and bottom fuselages, where any slight part deviation caused sticking during the sliding action. Negating these issues for this research required extreme amounts of post-processing and supplementary lubricants. However, potential improvements for combatting these concerns would be to either implement a design that negated concentric tube rotation or use lightweight aluminium bushings to help ease the rotation. These enhancements would increase the controllability of the vehicle and make assembly more effective, due to the absence of post-processing needed.

7. CONCLUSION

The need for a reliable, economical, and sustainable method of delivering medical aid supplies to underdeveloped areas within South Africa was apparent. Therefore, this dissertation aimed to combine the unique characteristics of FDM printing with the capabilities of UAVs in order to conceptualize a vehicle that assisted this delivery solution. The research conducted in this report revealed sufficient evidence to confirm the proficiency of using FDM as the fabrication method for a prototype VTOL UAV named *Airslipper*. The practical testing outcomes, along with experimentally investigative results, demonstrated a functional design that displayed all the necessary traits of an aerial vehicle. This research set out operational characteristics for this solution, and considerations were made for the systems payload carrying capacity, deployment strategy, maintenance plan, legislative requirements, and cost-effectiveness. These aspects formed the fundamental conditions for the delivery application within SA and were essential for maintaining the longevity of this solution.

The objectives portrayed in this research provided the primary direction for obtaining a complete dissertation that answered the research question. The central necessities of each objective defined the relevant chapters within this document and made continuous regard to the fundamental workings of both FDM and UAV technologies. The literature described throughout this work discussed the current legislative challenges facing the UAV industry and accentuated on the medical assistance needed within SA. Potential benefits of using UAV's to transport and distribute large quantities of vaccines to underdeveloped communities was made with relevance to the transformation of the biopharmaceutical industry. These literature findings confirmed the possibilities of this application and provided a practical comparison to some of the current strategies for effectively delivering emergency supplies within Rwanda and Ghana.

This research placed emphasises on the importance of an optimized aerodynamic configuration and propulsion system design, with the intention of attaining enhanced endurance capabilities. Results of a specifically formulated MDO problem, which contained critical performance parameters, allowed the *Airslipper* UAV to achieve an optimal parametric design that facilitated $58\,s$ of additional flight time. This outcome enabled for an extended flight service radius of $1.51\,km$ and demonstrated the effectiveness of the MDO technique for UAV design.

This research assessed the challenges associated with FDM printing alongside the upcoming developments in this field. Although continual advancements in the FDM industry has led to heightened equipment, modified material properties and innovative build strategies, particular evidence to the constraining factors of FDM hindered conventional aircraft design. Therefore, literature proposed an adaptive FDM build strategy for UAV production, that considered the applicational conditions and optimized aerodynamic design. This strategy forced the *Airslipper* design to have a partitioned construction that required fastening of 99 individual parts to form the complete assembly. As a result, and due to the vulnerabilities of FDM, traditional placement of control flaps on the aerofoil was not plausible. Thus, the *Airslipper* employed control surfaces that were positioned on the separate motor arms, which negated standard stress concentration and allowed for enhanced controllability with improved customizability.

However, this unique design strategy consequently created concern for the structural integrity, mechanical robustness, and fluid interference of the implemented strategy. Thus, the vehicle required a performance validation of all its aerodynamic surfaces, to appraise the successfulness of the design and optimization method. The outcomes of several aerodynamic analyses and CFD simulations revealed significant results, which pertained to the operational qualities of the *Airslipper* during both VTOL and FW flight modes. Findings suggested the vehicle was stabilized at the stipulated flight conditions and that control response degraded with additional payload weight. The apprehension of airflow disturbance between propeller, control surface, fuselage and aerofoil was negated by the results of a CFD simulation conducted on an *Airslipper* model. Discoveries proved noticeable deviations in flow trajectories and vorticity levels, but performance values demonstrated insignificance in generated propulsion force and aerofoil lift force. These findings concluded the decisive characteristics of the design and installed confidence in the *Aislirpper's* functionality for the given flight conditions.

By recognizing the localized bending moment experienced by the *Airslipper's* aerofoil, this research experimented with substantiating the anisotropic properties of an FDM printed part when subjected to variations in FDM parameter combinations. The corresponding aerofoil durability results showed extraordinary shear strength abilities for increased wall thicknesses and infill percentage parameters. A direct correlation between structural integrity and layer height allowed this experiment to exclude $0.3\ mm$ or above layer heights from the *Airslipper's* development, as they offered no layer adhesion and did not contribute to structural integrity. Outcomes of this experiment were used in conjunction with an importance selection matrix to assign design segments with an optimal set of FDM parameters. This process permitted ideal aircraft attributes to be incorporated with the individual printed parts of the *Airslipper's* construction.

Assembly of the various electronic and mechanical components, together with the printed segments, was made intuitive through the development of a uniform bolt attachment approach that enabled the *Airslipper* to be structurally static whilst being easily accessible for maintenance and repair. Validating the operational characteristics of this prototype required a comprehensive examination of the $120\ s$ hovering test results. Flight log data demonstrated consistent angular rate and step response for the relevant roll, pitch, and yaw axis, which indicated adequate tuning of the PID controller. Overall, with acceptable actuator output signals and considerably manageable vibration metrics, the *Airslipper* UAV satisfies the applicational requirements and yields comparable qualities when compared to other vehicle types.

An evaluation of the *Airslipper's* design and performance characteristics indicated the deployment capabilities, maintenance and repair strategies, and sustainability attributes of this FDM fabrication method. In conclusion, the appraisal given by this dissertation, along with the potential improvements for future research, suggested that fabricating a transitional VTOL UAV using FDM methods is possible. This manufacturing method is also encouraged, as it further facilitates support for underdeveloped communities.

REFERENCES

[1] S. L. Donaldson, "Healthier, fairer, safer: the global health journey 2007–2017," World Health Organization 2017, Geneva, Switzerland, 2017.

[2] J. F. K. a. S. S. Carr, "A Brief History of Early Unmanned Aircraft," *JOHNS HOPKINS APL TECHNICAL DIGEST,* vol. 32, no. 3, pp. 558-571, 2013.

[3] A. A. M. Hassanalian, "Classifications, applications, and design challenges of drones: A review," *Progress in Aerospace Sciences,* vol. 91, pp. 99-131, 2017.

[4] D. Peter, "Eighth amendment of the civil aviation regulations, 2015," *Department of transport,* pp. 6-34, 27 May 2015.

[5] S. A. C. A. Authority, "RPAS regulations (Part 101) - SACAA," 2020. [Online]. Available: http://www.caa.co.za/Documents/RPAS/Part%20101%20-%20RPAS%20Workshops.pdf. [Accessed 7 July 2020].

[6] B. R. B. Winnie T. Maphumulo, "Challenges of quality improvement in the healthcare of South Africa post-apartheid: A critical review," *Curations 2019,* vol. 42, no. 1, 2 October 2019.

[7] B. K. Hecht, "First Aid: From Witchdoctors & Religious Knights to Modern Doctors," MedicineNet, [Online]. Available: https://www.medicinenet.com/first_aid_witchdoctors_and_religious_knights/views.htm. [Accessed 24 September 2020].

[8] P. K. S. L. C. C. M. B. S. A. S. Connie A. Line, "Drone delivery of medications: Review of the landscape and legal considerations," *American Journal of Health-System Pharmacy,* vol. 75, no. 3, pp. 153-158, 2018.

[9] S. T. M. F. E. B. M. S. A. W. R. A. V. S. D. L. B. Y. Leila A.Haidari, "The economic and operational value of using drones to transport vaccines," *Vaccine,* vol. 34, no. 34, pp. 4062-4067, 2016.

[10] D. Schlenoff, "Aerial Resupply Invented, 1916," Scientific American, 2016.

[11] B. Y. Lee, "Drones to the Rescue," MIT Technology Review, Baltimore, Maryland, 2017.

[12] D. O'Driscoll, "UAVs in Humanitarian Relief and Wider Development Contexts," UK Department for International Development , Manchester, United Kingdom, 2017.

[13] D. Guthrie, "History of stereolithography," Prototech Asia, 2018. [Online]. Available: https://prototechasia.com/en/stereolithography/history-of-stereolithography#:~:text=Invention%20of%20stereolithography&text=The%20first%20version%20of%20this,light%20to%20cure%20photosensitive%20polymers.. [Accessed 2 August 2020].

[14] T. J. H. a. O. L. A. Harrysson, "Overview of current additive manufacturing technologies and selected applications," *Science Progress,* vol. 95, no. 3, pp. 255-282, 2012.

[15] K. V. W. a. A. Hernandez, "A Review of Additive Manufacturing," *International Scholarly Research Network,* vol. 2012, pp. 1-10, 2012.

[16] M. C. L. Nannan GUO, "Additive manufacturing: technology, applications and research needs," *Frontiers of Mechanical Engineering,* vol. 8, no. 3, pp. 215-243, 2013.

[17] M. F. a. A. E.T., "Basics of Fused Deposition Modelling (FDM)," in *Fused Deposition Modeling*, Springer, Cham, 2020, pp. 1-15.

[18] N. R. D. S. S. L. Hai-Chuan Song, "Anti-aliasing for fused filament deposition," *Computer-Aided Design,* vol. 89, no. 1, pp. 25-34, 2017.

[19] H. A. K. F. K. M. A. E. A. Barari, "On the surface quality of additive manufactured parts," *The International Journal of Advanced Manufacturing Technology ,* vol. 1, no. 89, pp. 1969-1974, 2017.

[20] S. A. G. L. G. V. D. S. L. S. W. Y. Y. G. D. Goh, "Additive manufacturing in unmanned aerial vehicles (UAVs): Challenges and Potential," *Aerospace Science and Technology,* vol. 63, no. 1, pp. 140-151, 2017.

[21] R. K. O. S. S. M. Anoop K. Sood, "Experimental investigation and empirical modelling of FDM process for compressive strength improvement," *Journal of Adcanced Research,* vol. 3, no. 1, pp. 81-90, 2012.

[22] C.-c. W. S.-c. C. Wei-chen lee, "Development of a hybrid rapid prototyping system using low-cost fused deposition modeling and five-axis machining," *Journal of Materials Processing Technology,* vol. 214, no. 11, pp. 2366-2374, 2014.

[23] Z. W. X. W. J. W. Z. C. Jun Du, "An improved fused deposition modeling process for forming large-size thin-walled parts," *Journal of Materials Processing Technology,* vol. 234, no. 1, pp. 332-341, 2016.

[24] R. M. e. al, "Three-dimensional printing of continuous-fiber composites by in-nozzle impregnation," Scientific Report, 2016.

[25] J. S. A. M. E. N. R. S. K. a. G. P. H. Michael Arthur Cuiffo, "Impact of the Fused Deposition (FDM) Printing Process on Polylactic Acid (PLA) Chemistry and Structure," *Applied Sciences,* vol. 7, no. 6, pp. 579-593, 2017.

[26] C. R. M. M. P. David A. Roberson, "Evaluation of 3D Printable Sustainable Composites," in *26th Annual Solid Freeform Fabrication Symposium*, Austin, Texas, 2015.

[27] D. M. P. M. a. L. L. Jukka Pakkanen, "About the Use of Recycled or Biodegradable Filaments for Sustainability of 3D Printing," in *International Conference on Sustainable Design and Manufacturing*, Turin, Italy, 2017.

[28] P. H. E. S. P. I. V. O. C. P. a. A. B. Rhys jones, "RepRap – the replicating rapid prototyper," *Robotica,* vol. 29, no. 1, pp. 177-191, 2011.

[29] S.-Y. L. Sheng-Jye Hwang, "Evaluation of Surface Finish Affect on Aerodynamic Coefficients of Wind Tunnel RP Models Production with ABSi Material," *Materials Science Forum,* pp. 255-260, August 2008.

[30] P. N. e. al, "Dimensional and surface texture characterization in Fused Deposition Modelling (FDM) with ABS plus," in *The Manufacturing Engineering Society International Conference*, Spain, 2015.

[31] R. H. e. al, "Effect of Build Orientation on FDM Parts: A Case Study for Validation of Deformation Behaviour by FEA," in *International Conference on Design and Concurrent Engineering* , Melaka, Malaysia, 2010.

[32] H. Klippstein, "Additive Manufacturing of Porous Structures for Unmanned Aerial Vehicles applications," *Advanced Engineering Materials,* vol. 20, no. 9, pp. 1-30, 2018.

[33] M. G. a. al, "Anisotropic Mechanical Properties of ABS Parts," in *Mechanical Engineering*, Rijeka, Croatia, InTech, 2012, pp. 160-185.

[34] J. Baez, "The Butterfly, the Gyroid and the Neutrino," University of California, Riverside, 13 August 2015. [Online]. Available: https://math.ucr.edu/home/baez/butterfly.html. [Accessed 6 Aufust 2020].

[35] D. M. M. P. Ognjan Lužanin, "EFFECT OF LAYER THICKNESS, DEPOSITION ANGLE, AND INFILL ON MAXIMUM FLEXURAL FORCE IN FDM-BUILT SPECIMENS," *Journal for Technology of Plasticity,* vol. 39, no. 1, pp. 49-58, 2014.

[36] J. Torres, "Mechanical Property Optimization of FDM PLA in Shear with Multiple Objectives," *JOM,* vol. 67, no. 5, pp. 1183-1193, 2015.

[37] L. Baich, "Impact of Infill Design on Mechanical Strength and Production Cost in Material Extrusion Based Additive Manufacturing," OhioLINK ETD Center , Youngstown, 2016.

[38] M. Fernandez-Vicente, "Effect of Infill Parameters on Tensile Mechanical Behavior in Desktop 3D Printing," *3D Printing and Additive Manufacturing,* vol. 3, no. 3, 2016.

[39] H. O. B. G. a. I. C. Justin Winslow, "Basic Understanding of Airfoil Characteristics at Low Reynolds Numbers (104–105)," *JOURNAL OFAIRCRAFT,* vol. 55, no. 3, pp. 1050-1061, 2018.

[40] J.-W. H. H.-J. L. B.-S. K. a. J. L. Kyoungwoo Park, "Optimal Design of Airfoil with High Aspect Ratio in Unmanned Aerial Vehicles," *International journal of Aerospace and Mechancical Engineering,* vol. 2, no. 4, pp. 381-388, 2008.

[41] T. R. Ahmad. A.A, "Aerofoil Design for Unmanned High-Altitude Aft-Swept Flying Wings," *Journal of Aerospace Technology and Management,* vol. 9, no. 3, 2017.

[42] J. F. a. M. Friswell, "Aerodynamic optimisation of a camber morphing aerofoil," *Aerospace Science and Technology,* vol. 43, pp. 245-255, 2015.

[43] C. H. e. al, "Piezoelectric Morphing versus Servo-Actuated MAV Control Surfaces," in *Structural Dynamics and Materials Conference*, Honolulu, Hawaii, 2012.

[44] O. D. a. M. Vahora, "Comparison of Aerodynamic Characterization Methods for Design of Unmanned," in *American Institute of Aeronautics and Astronautics*, Kissimmee, Florida, 2018.

[45] K. Budziak, Aerodynamic Analysis with Athena Vortex Lattice (AVL), Hamburg: Creative Commons, 2015.

[46] R. Austin, Unmanned Aircraft Systems, Chippenham, Wiltshire, UK: John Wiley & Sons Ltd, 2010.

[47] P. Z. S. Spakovsky, "16. Unified: Thermodynamics and Propulsion".

[48] B. T. e. al, "Influence of propeller configuration on propulsion system efficiency of multi-rotor UAV," KU Leuven, Leuven, Belgium.

[49] C. B. a. C. B. D. Felix Finger, "A Review of Configuration Design for Distributed Propulsion transitioning VTOL Aircraft," in *Asia-Pacific International Symposium on Aerospace Technology*, Seoul, Korea, 2017.

[50] W. Z. e. al, "An experimental Investigation on Rotor-to-Rotor interactions of small UAVs," in *35th AIAA Applied Aerodynamic Conference*, Denver, Colorado, 2017.

[51] J. R. R. A. M. a. A. B. Lambe, "Multidisciplinary Design Optimization: A Survey of Architectures," *American Institute of Aeronautics and Astronautics, Inc.,* vol. 51, no. 9, 2013 .

[52] M. N. a. T. H. P. David W. Zingg, "A comparative evaluation of genetic and gradient-based algorithms applied to aerodynamic optimization," *European Journal of Computational Mechanics ,* pp. 103-126, 2008.

[53] D. D. S. B. K. G. C. A. D. a. J. P. Michael Meheut, "Gradient-Based Single and Multi-points Aerodynamic Optimizations with the elsA Software," in *AIAA Aerospace Sciences Meeting*, Kissimmee, Florida, 2015.

[54] M. E. a. A. Jahangirian, "Aerodynamic Optimization of Airfoils Using Adaptive Parameterization and Genetic Algorithm," *Journal of Optimization Theory and Applications,* pp. 257-271, 2013.

[55] A. A. a. H. G. A.F.P. Ribeiro, "An airfoil optimization technique for wind turbines," *Applied Mathematical Modelling,* pp. 4898-4907, 2012.

[56] S. G. a. C. T. Trinh, "Comparison of Multi-Objective Evolutionary Algorithms to Solve the Modular Cell Design Problem for Novel Biocatalysis," *Process 2019,* vol. 361, no. 7, pp. 1-13, 11 June 2019.

[57] A. P. S. A. a. T. M. K. Deb, "A Fast and Elitist Multiobjective Genetic Algorithm: NSGA-II," *IEEE TRANSACTIONS ON EVOLUTIONARY COMPUTATION,* vol. 6, no. 2, pp. 182-197, 2002.

[58] M. L. a. L. T. Eckart Zitzler, "SPEA2: Improving the Strength Pareto Evolutionary Algorithm," in *TIK-Report*, Switzerland, Zurich, 2001.

[59] S. R. a. R. Ganguli, "Multidisciplinary Design Optimization of a UAV Wing using Kriging based Multi-Objective Genetic Algorithm," in *50th AIAA/ASME/ASCE/AHS/ASC Structures, Structural Dynamics, and Materials Conference*, Palm Springs, California, 2009.

[60] O. Magnussen, "Multirotor Design Optimization: The Mechatronic Approach," University of Agder, Kristiansand, 2015.

[61] T. H. P. M. a. C. S. Minh-Duc Hua, "A control approach for thrust-propelled underactuated vehicles and its applications to VTOL Drones," *IEEE Transactions on Automatic Control,* vol. 54, no. 8, pp. 1837-1853, 2009.

[62] B. Wingo, "Mathematical Modeling of Quadcopter Dynamics," Rose-Hulman Undergraduate Research , 2016.

[63] E. Biever, "Controlling of an single drone," TU/E Eindhoven, 2015.

[64] T. Luukkonen, "Modelling and control of quadcopter," Aalto University, Aalto, 2011.

[65] A. B. Y. S. I. a. J. M. D. Adnan Salem Saeed, "A Review on the Platform Design, Dynamic Modelling and Control of Hybrid UAVs," Khalifa University, Abu Dhabi, 2014.

[66] T. H. e. a. Minh-Duc Hua, "Introduction to Feedback control of underactuated VTOL vehicles," *IEEE control systems magazine,* p. 15, 17 January 2013.

[67] e. a. Hossein Bolandi, "Attitude Control of a Quadrotor with Optimized PID Controller," *Intelligent Control and Automation,* vol. 4, pp. 335-342, 2013.

[68] e. a. Glen Bright, "Quad-Rotor Unmanned Aerial Vehicle Helicopter Modelling and Control," Intech , Durban, 2011.

[69] T. O. e. al, "Control concept of a tiltwing UAV during low speed manoeuvring," in *International congress of the aeronautical sciences*, Germany, Aachen, 2012.

[70] D. C. C. S. P. Casau, "Autonomous transition flight for a vertical take-off and landing aircraft," in *50th IEEE Conference on Decision and Control and European Control Conference*, Orlando, Florida, 2011.

[71] P. R. B. a. F. Wong, "Modeling and control of a hovering mini tail-sitter," *International journal of micro air vehicles,* vol. 2, no. 4, pp. 211-220, 2010.

[72] J. M. O. Barth, "Fixed-wind UAV with transitioning flight capabilities: Model-Based or Model-Free Control approach," in *International Conference on Unmanned Aircraft Systems*, Dallas, Texas, 2018.

[73] K. C. a. H. Eren, "UAV fuel preferences for future cities," in *6th International Istanbul Smart Grids and Cities Congress and Fair (ICSG)*, Istanbul, Turkey, 2018.

[74] M. Muller, Interviewee, *eCalc & EV Range Simulator | Interview with Markus Müller.* [Interview]. 7 August 2019.

[75] J. Hung, "On parallel hybrid-electric propulsion system for unmanned aerial vehicles," *Progress in Aerospace Sciences,* vol. 51, pp. 1-17, 2012.

[76] P. T. P. W. M. K. P. B. a. B. L. Magdalena Dudek, "Hybrid Fuel Cell – Battery System as a Main Power Unit for Small Unmanned Aerial Vehicles (UAV)," *International Journal of ELECTROCHEMICAL SCIENCE,* vol. 8, pp. 8442-8463, 2013.

[77] O. G. a. A. Rosen, "Optimizing Electric Propulsion Systems for Unmanned Aerial Vehicles," *Journal of Aircraft,* pp. 1340-1353, 2009.

[78] S. H. a. E. N. J. Dmitry Bershadsky, "Electric Multirotor UAV Propulsion System Sizing for Performance Prediction and Design Optimization," in *57th AIAA/ASCE/AHS/ASC Structures, Structural Dynamics, and Materials Conference*, San Diego, California, 2016.

[79] A. R. a. O. Gur, "Optimization of Propeller-Based Propulsion System," *Journal of Aircraft,* vol. 46, no. 1, pp. 95-106, 2009.

[80] B. McCormick, Aerodynamics, Aeronautics and Fluid Mechanics, 1st ed., Ney York: John Wiley, 1995.

[81] S. R. D., The Elements of Aircraft Preliminary Design, 1st ed., Santa Ana, CA: Aries, 2000.

[82] D. S. M. Nita, "Estimating the Oswald Factor from Basic Aircraft Geometrical Parameters," Hamburg, Germany, 2012.

[83] T-Motor, "MN5208 Test Report," T-Motor, [Online]. Available: https://store-en.tmotor.com/goods.php?id=353. [Accessed 24 July 2020].

[84] W. M. Mickel. K, "Tailless aircraft in theory and Practice," American Institute of Aeronautics and Astronautics, Washington, 1994.

[85] J. M. P. Ben Wittbrodt, "The Effects of PLA Color on Material Properties of 3-D Printed Components," *Additive Manufacturing,* vol. 8, no. 1, pp. 110-116, 2015.

[86] J. A, "Optimum Aerodynamic Design Using CFD and Control Theory," in *AIAA 12th Computational Fluid Dynamics Conference*, 1995.

[87] N. A. P. a. L. M. A. Jameson, "Optimum Aerodynamic Design Using the Navier–Stokes Equations," in *35th Aerospace Sciences Meeting and Exhibit*, 1997.

[88] G. K. C., "Design of Optimal Aerodynamic Shapes Using Stochastic Optimization," *Progress in Aerospace Sciences,* vol. 38, no. 1, pp. 43-76, 2002.

[89] L. D. K. S. L. F. Gonzalez, "Aero-Structural Optimisation of Unmanned Aerial Vehicles Using a Multi-Objective," in *Proceedings of the 2nd Australasian Unmanned Air Vehicle System Conference Evolutionary Algorithm*, 2009.

[90] K. D. e. al, "A Fast and Elitist Multiobjective Genetic Algorithm: NSGA-II," *IEEE TRANSACTIONS ON EVOLUTIONARY COMPUTATION,* vol. 6, no. 2, pp. 182-197, 2002.

[91] E. Z. e. al, "SPEA2: Improving the Strength Pareto Evolutionary Algorithm," in *TIK-Report*, Switzerland, Zurich, 2001.

[92] J. V. F. L. a. A. S. Pedro Gamboa, "Design and Testing of a Morphing Wing for an Experimental UAV," in *Platform Innovations and System Integration for Unmanned Air, Land and Sea Vehicles*, Neuilly-sur-Seine, France, 2007.

[93] Auterion, "Controller Diagrams," Dronecode, 2020. [Online]. Available: https://dev.px4.io/v1.8.0/en/flight_stack/controller_diagrams.html. [Accessed 17 July 2020].

1. Power module 1
2. Power module 2
3. Telemetry 1 (radio telemetry)
4. USB
5. Telemetry 2 (companion computer)
6. CAN1 (controller area network) bus
7. I^2C (for I^2C splitter to use additional sensors)
8. CAN2 (controller area network) bus
9. S.BUS out for S.Bus servos
10. Radio Control Receiver Input (PPM)
11. Main outputs (I/O PWM out)
12. UART and I2C (for additional GPS)
13. Radio Control Receiver Input (DSM/SBUS)
14. Input Capture and ADC IN
15. GPS module
16. SPI (serial peripheral interface) bus
17. AUX outputs (FMU PMU out)

1. Micro-USB Port
2. IO Reset button
3. SD card
4. FMU Reset button

*Figure A-1: Pixhawk 4 FC interface connectors [93]*
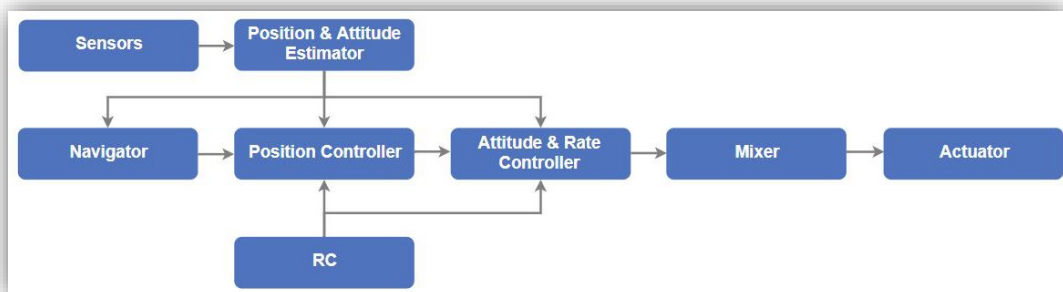
Figure A-2: PX4 autopilot simplified flight stack [93]

```
# @name Airslipper

# @type VTOL tilt-rotor
# @class VTOL

# @output MAIN 1 Motor front right
# @output MAIN 2 Motor back left
# @output MAIN 3 Motor front left
# @output MAIN 4 Motor back right
# @output MAIN 5 Tilt servo front right
# @output MAIN 6 Tilt servo front left
# @output MAIN 7 Tilt servo back right
# @output MAIN 8 Tilt servo back left

# @output AUX 1 feed-through for front right control surface
# @output AUX 2 feed-through for front left control surface
# @output AUX 3 feed-through for back right control surface
# @output AUX 4 feed-through for back right control surface

if [ $AUTOCNF = YES ]
then

        param set FW_AIRSPD_MAX            28
        param set FW_AIRSPD_MIN            20
        param set FW_AIRSPD_TRIM           25

        param set MC_ ROLL_ P_GAIN       8.0
        param set MC_ ROLLRATE _P_TERM     0.5
        param set MC_ ROLLRATE _I_TERM     0.15
        param set MC_ ROLLRATE _D_TERM     0.005
        param set MC_ROLLRATE_MAX           80

        param set MC_ PITCH _ P_GAIN      10.2
        param set MC_ PITCHRATE _P_TERM    0.4
        param set MC_ PITCHRATE _I_TERM    0.15
        param set MC_ PITCHRATE _D_TERM    0.006
        param set MC_PITCHRATE_MAX          80

        param set MC_ YAW_ P_GAIN         4.0
        param set MC_ YAWRATE _P_TERM     0.5
        param set MC_ YAWRATE _I_TERM     0.06
        param set MC_ YAWRATE _D_TERM     0.000
        param set MC_YAWRATE_MAX            20


set MAV_TYPE 21

set MIXER Airslipper.Mix

set PWM_OUT 12345678
set PWM_AUX_OUT 1234
```

Figure A-3: Airslipper airframe configuration file for PX4

```
# Airslipper main Mixer file

Quad motors 1 - 4
--------------------------
R: 4x 10000 10000 10000 0


Tilt mechanism servo mixer
--------------------------
# FRONT RIGHT
M: 1
O:              10000       10000       0       -10000      10000
S: 1      4     8000        8000        0       -10000      10000

# FRONT LEFT
M: 1
O:              10000       10000       0       -10000      10000
S: 1      4     8000        8000        0       -10000      10000

# BACK RIGHT
M: 1
O:              10000       10000       0       -10000      10000
S: 1      4     8000        8000        0       -10000      10000

# BACK LEFT
M: 1
O:              10000       10000       0       -10000      10000
S: 1      4     8000        8000        0       -10000      10000


Elevon mixers
-------------
#Right
M: 1
O:              10000       10000       0       -10000      10000
 S: 1     0     7500        7500        0       -10000      10000

M: 1
O:              10000       10000       0       -10000      10000
 S: 1     0     7500        7500        0       -10000      10000

#Left
M: 1
O:              10000       10000       0       -10000      10000
 S: 1     1     -7500       -7500       0       -10000      10000

M: 1
O:              10000       10000       0       -10000      10000
 S: 1     1     -7500       -7500       0       -10000      10000
```

Figure A-4: Airslipper mixer file for PX4

Table A-1: Point mass distribution of design modules for the Airslipper

Design module	Mass (kg)	X (m)	Y (m)	Z (m)
Payload	2.5	0.44	0	-0.06
Battery	2.2	0.1	0	-0.06
Fuselage Frame	1.2	0	0	0.0
Control Electronics	0.2	0.05	0	0.05
Main Aerofoil	1.2	0.22	0	0.24
Front Control Surfaces	0.6	0.26	0	0.0
Rear Control Surfaces	0.6	-0.26	0	0.0
Front Right Propulsion system	0.56	0.26	0.37	0.0
Back Right Propulsion system	0.56	-0.26	0.37	0.0
Back Left Propulsion system	0.56	-0.26	-0.37	0.0
Front Left Propulsion system	0.56	0.26	-0.37	0.0
Vehicle COG	**9.54**	**0.202**	**0**	**0.145**